Impact of large spoilers on a wind turbine blade using full scale and unsteady CFD simulations

Thomas Potentier

THESE DE DOCTORAT DE

L'ÉCOLE CENTRALE DE NANTES

ECOLE DOCTORALE N° 602
Sciences pour l'Ingénieur
Spécialité : Mécanique des Milieux Fluides

Par
Thomas POTENTIER

Impact of large spoilers on a wind turbine blade using full scale and unsteady CFD simulations

Thèse présentée et soutenue à Ecole Centrale de Nantes, le 15 Décembre 2022
Unité de recherche : UMR 6598, Laboratoire de recherche en Hydrodynamique, Énergétique et Environnement Atmosphérique (LHEEA)

Rapporteurs avant soutenance :

Niels NORMARK SORENSEN Professor, Danmarks Tekniske Universitet, Danemark
Carlos SIMAO FERREIRA Professor, Technische Universiteit Delft, Pays-Bas

Composition du Jury :

Président : Gerard SCHEPERS Professor, Hanzehogeschool Groningen, Pays-Bas
Examinatrice : Sandrine AUBRUN Professeure des universités, École Centrale de Nantes
Dir. de thèse : Caroline BRAUD Chargée de recherche HDR CNRS, École Centrale de Nantes
Co-encadrant : Emmanuel GUILMINEAU Chargé de recherche CNRS, École Centrale de Nantes

Invité
Arthur FINEZ Ingénieur acoustique expert, ENGIE Green, Lyon

Acknowledgement

Pursuing a doctoral degree was in the back of my mind soon after I started working. After five happy and fruitful years in the wind energy industry in the United Kingdom, I had the opportunity to finally do it and coming back home at the same time. First, I would like to express my gratitude to my industrial sponsor ENGIE Green and academic partner Centrale Nantes (especially the LHEEA Lab) for proposing a thesis which seemed tailored for me. It goes without saying that those entities are well functioning thanks to the people in them. Many thanks to Colin Le Bourdat and Dr. Arthur Finez who supervised my work at ENGIE Green. I can count myself lucky to be part of your team and work under your guidance and management. I will remember fondly discussion over lunch and our various seminars.

What would be a doctoral student without supervisors? I wish to thank so very much Dr. Caroline Braud and Dr. Emmanuel Guilmineau for being there and available throughout those three years. I couldn't have wished for a better supervision team: available, patient, complementary and understanding. Thanks to both of you I manage to learn a lot about the numerical simulation world and how it relates to physical phenomenon.

Thanks also to the PhD defence committee: Dr. Gerard Schpers, Pr. Carlos Simao Ferreira, Pr. Niels Nørmark Sørensen and Pr. Sandrine Aubrun for their availability.

All the 3D CFD computations presented as part of this thesis were performed using HPC resources from GENCI (Grand Equipement National de Calcul Intensif) (Grant-A0112A13014) which is gratefully acknowledged.

A special thanks to: Dr. Sofien Kerkeni, who proves that forwarding email and application can enable great things. Special thanks also to Nicolas Girard and Dr. Philippe Alexandre from ENGIE Green for initially writing the thesis proposal and accepting me as PhD student. Thanks also to Rishabh, my PhD-mate, I will miss our long conversations about science and life in general. Now, it is your turn to start writing.

Je souhaite aussi remercier mes parents qui ont toujours su me pousser à donner le meilleur de moi-même tout en respectant les choix que j'ai pu faire dans la vie. J'espère que je serais capable de transmettre à mon fils les mêmes valeurs morales que vous avez pu m'inculquer. I wish to thanks my sister, Aurélie, it is important for me to know that I can count on you on any matter. Thanks to all my friends here and abroad, I know we don't meet enough and despite that you are always available.

I also have a dear thought for those who left us and couldn't be here today.

Finally, I cannot start to put into words the thanks I wish to express to my wife Caroline. Thank you for following me there and back, thank you for putting up with me, thank you for being there lifting me up when I am down and sharing the positive with me and finally thanks for giving us a wonderful son: Eloan.

Thank you Eloan for being so nice and smiling, it is such a pleasure to come back home and see your, no longer, toothless mouth with a beaming smile.

Abstract

The first objective of the thesis is to characterise the role of the local aerodynamic unsteadiness introduced by thick aerofoils equipped with root aerodynamic add-on. A special focus will be on the aerofoil loads, turbine lifetime and turbine energy production. During routine maintenance, ENGIE Green, a french exploiting party of renewable energy sources, noticed some cracks at the blade root near the spoiler installation. Until this day, all studies performed to assess the effectiveness of the spoiler were inconclusive.
The thesis aims at understanding the aerodynamic causes of the structural failure using state of the art calculation methods. The use of high fidelity tool such as Computational Fluid Dynamics, both in 2D and 3D, allowed for a better understanding of the unsteady phenomenon.
One of the main calculation tool used by the industry is the Blade Element Momentum theory despite the limitations inherent to the model. Among the simplification hypothesis is the assumption of 2D steady flow. Therefore, a novel way of accounting for unsteadiness in the fatigue calculation is proposed as part of the thesis.
In today's available literature, many references exist about aerodynamic add-on. Nevertheless, few are targeting thick aerofoils and/or large wind turbine operating conditions (Reynolds number and angle of attack). The present thesis aims also at bridging the gap in the literature by providing an analysis of simulated thick profiles with and without spoilers.
Finally, the main findings of the thesis are:

- The negative impact of the spoiler upon the turbine lifetime
- The conservativeness of 2D simulated aerodynamic polars used for BEM aeroelastic simulation and fatigue calculation
- The independence of the vortex shedding frequency with the blade rotation and span

A dedicated analysis about the 3D dampening effect on the unsteady behaviour would allow a better correlation between 2D and 3D.

Résumé

L'objectif premier de la thèse est de caractériser le rôle de l'instationnarité aérodynamique générée par des aérofoils épais et équipés d'ajouts passifs aérodynamiques. Une attention particulière sera donnée aux charges locales, la durée de vie de la turbine et la production énergétique.
Au cours d'une maintenance de routine, ENGIE Green, un exploitant français d'énergies renouvelables, a relevé des fissures en pied de pale proche de la zone d'installation du spoiler. Jusqu'à ce jour, les études menées pour vérifier l'efficacité du spoiler n'avaient pas données de résultats concluants.
La thèse cherche à améliorer la compréhension des causes aérodynamiques des casses structurelles en utilisant les plus récentes méthodes de calculs. L'utilisation d'outil de simulation à haute fidélité, tel que la Mécanique des Fluides Numérique, a permis une meilleure compréhension du phénomène instationnaire.
L'un des outils de calcul utilisé dans l'industrie est la théorie de l'élément de pale malgré ses limitations intrinsèques. Parmi les hypothèses simplificatrices est l'écoulement 2D stationnaire. Une nouvelle méthode pour prendre en compte l'instationnarité dans le calcul de fatigue est proposée dans cette thèse.
Dans la littérature disponible aujourd'hui, il existe de nombreuses références à propos d'ajouts passifs. Néanmoins, peu ont pour objectif les aéofoils épais et/ou les conditions d'opérations des éoliennes modernes (nombre de Reynolds ou angle d'attaque). La thèse a aussi pour but de compléter la littérature existante en faisant l'analyse d'aérofoils épais équipés (ou non) de spoilers.
Enfin, les constatations principales de ces travaux sont:

- L'impact négatif du spoiler sur la durée de vie de la turbine
- Le conservatisme des polaires aérodynamiques 2D simulées pour des simulation BEM aéroélastiques et des calculs de fatigue
- L'indépendance de la fréquence de lâcher tourbillonnaire avec la rotation du rotor

Une étude détaillée sur l'atténuation en 3D des effets instationnaires permettrait de mieux corréler simulations 2D et 3D.

Table of Contents

List of Figures

List of Tables

NOMENCLATURE

The next list describes the symbols and letters used within the body of the document organised by chapter.

Chapter 1

$\bar{U_x}$	Mean wind speed following the x-axis	$[m/s]$
κ	Wind shear exponent	$[-]$
θ'	temperature variation across the time period considered	$[^\circ]$
A	Weibull shape factor	$[-]$
C	Weibull scale parameter	$[-]$
$U(z)$	Wind speed distribution along the vertical direction	$[m/s]$
Z	Height distribution along the vertical direction	$[m]$
Z_r	Reference height	$[m]$
AAO	Aerodynamic Add On	
GF	Gurney Flap	
IEC	International Electrotechnical Commission	
VG	Vortex Generator	

Chapter 2

α	Angle of attack	$[^\circ]$
$\bar{\rho}$	Averaged fluid density	$[kg/m^3]$
$\bar{P}$	Mean pressure in the Reynolds equation	$[Pa]$
β	Blade pitch	$[^\circ]$
χ	Wake skew angle	$[^\circ]$
$\ddot{q}$	Acceleration vector	$[m/s^2]$
$\ddot{u}_y$	Blade element acceleration in the y-direction of the blade coordinate system	$[m/s^2]$
$\ddot{u}_z$	Blade element acceleration in the z-direction of the blade coordinate system	$[m/s^2]$
$\dot{m}$	Air mass flow	$[kg/s]$
$\dot{q}$	Velocities vector	$[m/s]$

ϵ	Convergence criteria	
Γ_Φ	Diffusion coefficient of the transported quantity	arbitrary unit
$\mathbf{\Phi}$	Transported quantity	arbitrary unit
$\tilde{\mathbf{U}}$	Favre averaged velocity vector	$[m/s]$
$\mathbf{n}$	Normal vector of A_{cs} pointing outwards	
$\mathbf{V_w}$	Wind inflow measured at several heights by the met mast	$[m/s]$
$\mathbf{V_b}$	Local blade velocity due to deformation	$[m/s]$
$\mathbf{V_{rot}}$	Corrected wind speed to account for yaw, cone angles	$[m/s]$
$\mathbf{V_{w_{ts}}}$	Corrected wind speed to account for the tower shadow effect	$[m/s]$
$\mathbf{W_i}$	Corrected wind speed to account for dynamic wake effect (induced velocity)	$[m/s]$
$\mathbf{W_{int}}$	Intermediate induced velocity	$[m/s]$
$\mathbf{W_{qs}}$	Quasi-steady induced velocity	$[m/s]$
μ	Dynamic viscosity	$[Ns/m^2]$
ω	Rotor rotational speed	$[rad/s]$
ϕ'	Fluctuation around the mean of the transported quantity	arbitrary unit
$\phi_1, \phi_2, A_0, A_1, B_1, k_1, k_2$	Yaw model parameters	$[-]$
ρ	Air density	$[kg/m^3]$
ρ	Measured air density	$[kg/m^3]$
σ	Annular solidity	$[-]$
τ_1, τ_2, k	Dynamic wake model parameters	$[-]$
θ	Local twist angle	$[^\circ]$
$\tilde{U}$, $\tilde{V}$, $\tilde{W}$	Favre averaged velocity vector components	$[m/s]$
φ	Inflow angle	$[^\circ]$
A	Rotor/disk area	$[m^2]$
a	Axial induction	$[-]$
a'	Tangential induction	$[-]$
A_0	Inlet area	$[m^2]$
A_1	Outlet area	$[m^2]$
A_{cs}	Area of the entire control surface	$[m^2]$
a_{yaw}	Yawed axial induction	$[-]$

B	Number of blades	$[-]$
c	Local blade chord	$[m]$
C_D	Drag coefficient	$[-]$
C_L	Lift coefficient	$[-]$
C_n	Normal coefficient projection of C_L and C_D in the rotor rotational plane	$[-]$
C_T	Thrust coefficient	$[-]$
C_t	Tangential coefficient projection of C_L and C_D in the rotor rotational plane	$[-]$
C_{po}	Power coefficient	$[-]$
D	Life damage	$[-]$
dV	Small volume particle.	$[m^3]$
E	Material Young's modulus	$[N/m^2]$
EI_{xx}	Edgewise stiffness	$[Nm^2]$
EI_{yy}	Flapwise stiffness	$[Nm^2]$
F	Prandtl's tip correction factor	$[-]$
f	Forcing vector	
F^{X_i},M^{N_i}	Active forces applied at the mass point centre	$[N]$,$[Nm]$
F_D	Drag force	$[N/m]$
F_L	Lift force	$[N/m]$
F_m	Kane's equation generalised active forces	
F_m^*	Kane's equation inertia forces	
F_X	OpenFast and UiBEM coordinates Normal to the rotor plane force	$[N/m]$
F_X	OpenFast force normal to the rotor plane	$[N/m]$
F_Y	OpenFast and UiBEM coordinates Tangential to rotor the plane force	$[N/m]$
G	Material rigidity modulus	$[N/m^2]$
I_{xx}	In-plane sectional inertia	$[m^4]$
I_{yy}	Out-of-plane sectional inertia	$[m^4]$
L^{ult}	Component material's ultimate design load	arbitrary load unit
L_i^{MF}	Fixed load-mean	arbitrary load unit
L_i^M	Mean load	arbitrary load unit
L_i^{RF}	Cycle range about a load mean	arbitrary load unit

L_i^R	Range about a load mean	arbitrary load unit
M	Acceleration matrix	$[m/s^2]$
m	Wöhler exponent	$[-]$
M_L	Linear mass	$[kg/m]$
$M_L(x)$	Linear mass	$[kg/m]$
M_y	Moment in the y-direction of the blade coordinate system	$[N/m]$
M_z	Moment in the z-direction of the blade coordinate system	$[N/m]$
N	Number of cycles to failure	$[-]$
n	Number of cycles counted	$[-]$
OV	Rotor overhang	$[m]$
P	Power	$[W]$
p	Pressure	$[Pa]$
P^+	Pressure in front of the rotor disk	$[Pa]$
P^-	Pressure behind the rotor disk	$[Pa]$
p_0	Pressure at the inlet	$[Pa]$
p_1	Pressure at the outlet	$[Pa]$
p_y	Distributed load in the y-direction of the blade coordinate system	$[N/m]$
p_z	Distributed load in the z-direction of the blade coordinate system	$[N/m]$
q	Displacement vector	$[m]$
R	Blade length	$[m]$
r	Local radius	$[m]$
R_T	Tower radius	$[m]$
r_{hub}	Hub radius	$[m]$
RBM	Root Bending Moment	$[Nm]$
S	Load range	arbitrary load unit
S_Φ	Source term of the transported quantity	arbitrary unit
$S_{M_X}, S_{M_Y}, S_{M_Z}$	Reynolds's equation source terms	$[-]$
T	Thrust	$[N]$
T^{fail}	Time to failure	$[s]$
T^{life}	Component design life time	$[s]$

T_y	Shear force in the y-direction of the blade coordinate system	$[N/m]$
T_z	Shear force in the z-direction of the blade coordinate system	$[N/m]$
u	Velocity at the disk	$[m/s]$
u', v', w'	Velocity fluctuations around the mean value	$[m/s]$
u_1	Wake velocity	$[m/s]$
V_0	Incoming velocity	$[m/s]$
W_{rb}	Number of rigid bodies in the system	
AEP	Annual Energy Production	$[GWh]$
AGR	Automatic Grid Refinement	
DDES	Delayed Detached Eddy Simulation	
DNS	Direct Numerical Simulation	
DoF	Degree of Freedom	
IDDES	Improved wall modelling Delayed Detached Eddy Simulation	
LES	Large Eddy Simulation	
RANS	Reynolds Averaged Navier Stokes	
URANS	Unsteady Reynolds Averaged Navier Stokes	

Chapter 4

σ	Rotor solidity	$[-]$
a_{crit}	Critical axial induction value	$[-]$
C_T	Rotor thrust coefficient	$[-]$
k_1, k_2, k_3	Madsen induction model polynomial coefficients	$[-]$
Re_c	Aerofoil chord based Reynolds number	$[-]$
V_{rel}	Relative velocity	$[m/s]$
DoE	Design of Experiment	

Chapter 5

$\mathbf{U}$	Velocity vector	$[m/s]$
Φ	Blade azimuthal position with respect of time	$[°]$
ψ	Horizontal angle between the mean wind speed direction and the orientation "mast-turbine"	$[°]$
$a_{r,y}$	Blade local acceleration following the y-axis	$[m/s^2]$

$a_{r,z}$	Blade local acceleration following the z-axis	$[m/s^2]$
F_z	Aerodynamic thrust following the ISIS-CFD coordinates system	$[N/m]$
l	Distance between mast and turbine	[m]
U_x, U_y, U_z	3D CFD velocity vector components	$[m/s]$
PSD	Power Spectral Density	
RMS	Root Mean Square	

Chapter 6

C_p	Local wall pressure coefficient	$[-]$
f	Strouhal number main frequency	$[Hz]$
L	Strouhal number characteristic length	$[m]$
P_{meas}	Measured pressure at the aerofoil's wall	$[N/m^2]$
P_{ref}	Reference pressure	$[N/m^2]$
S_t	Strouhal number	$[-]$

Chapter 7

δE	Weibull weighted average energy variation	$[kWh]$
ΔP_{WS}	Power range over a wind speed	$[kW]$
Δt_{OF}	OpenFAST sampling time step	$[s]$
Pr(WS)	Wind speed occurrence probability	$[-]$
$c_{r/R}^{\mathrm{EG}}$	ENGIE Green turbine local chord	$[m]$
$c_{r/R}^{\mathrm{NREL}}$	NREL's 5MW turbine local chord	$[m]$
I_{xx}^{EG}	ENGIE Green turbine local in-plane inertiae	$[m^4]$
I_{xx}^{NREL}	NREL's 5MW turbine local in-plane inertiae	$[m^4]$
I_{yy}^{EG}	ENGIE Green turbine local out-of-plane inertiae	$[m^4]$
I_{yy}^{NREL}	NREL's 5MW turbine local out-of-plane inertiae	$[m^4]$
M_L^{EG}	ENGIE Green turbine linear mass	$[kg/m]$
M_L^{NREL}	NREL's 5MW turbine linear mass	$[kg/m]$
$P_{\mathrm{WS}}^{\mathrm{max}}$	Maximum power produced for a wind speed	$[kW]$
$P_{\mathrm{WS}}^{\mathrm{min}}$	Minimum power produced for a wind speed	$[kW]$
$Li_j^{nospoiler}$	No spoiler life index	$[-]$
$Li_j^{spoiler}$	Spoiler life index	$[-]$

SCADA	Supervisory Control and Data Acquisition	
VSF	Vortex Shedding Frequency	$[Hz]$
WS	Considered wind speed	$[m/s]$

Chapter 8

$\mathbf{U}$	3D CFD Velocity vector	$[m/s]$
μ	Dynamic viscosity	$[m^2/s]$
τ_x	Wall shear stress following the x-axis	$[N/m^2]$
τ_y	Wall shear stress following the y-axis	$[N/m^2]$
V_z	Dimensionless velocity following the z-axis	$[-]$

Appendix

α_a	Difference between the highest quadrant averaged angle of attack and lowest quadrant averaged angle of attack	$[^\circ]$
α_m	Mean angle of attack	$[^\circ]$
$\bar{\bar{T}}$	Stress tensor	$[N/m^2]$
$\mathbf{F}$	Sum of all applied forces on the considered volume	$[N]$
$\mathbf{g}$	Acceleration due to gravity	$[m/s^2]$
$\mathbf{n}$	Vector normal in each point to the surface	
$\mathbf{U}$	Velocity vector	$[m/s]$
ρ	Fluid density	$[kg/m^3]$
k	Reduced frequency	$[Hz]$
V	Considered volume	$[N]$

INTRODUCTION

The last century showed an increase in the standard of living in most of countries in the world thanks to great technological advances. Such advances come with a drastic increase in energy needs. At first, the energy was produced mainly with fossil fuels, the last decades showed an increase in renewable energy sources such as wind, solar, hydroelectric as pictured in Figure 1. Despite the many power plants installed to produce 160 000 TWh annually in 2019, more than 25 million people cannot afford basic electricity needs. The CO_2 emissions from existing energy infrastructure and power plants under construction would lead to a long-term temperature rise of 1.65°C according to the International Energy Agency [1]. The population increase, expected to reach 8.5 billion in 2050, will further increase this tendency.
A worldwide unexpected pandemic occurred in 2019 due to the SARS-CoV-2 virus (Covid-19), leading to a worldwide lockdown for several months and two more years for the countries to relieve the sanitary restrictions. During this time the CO_2 dropped emission and energy needs decreased, however as of 2021 the energy demands rose up back to pre-Covid levels with an increasing trend.

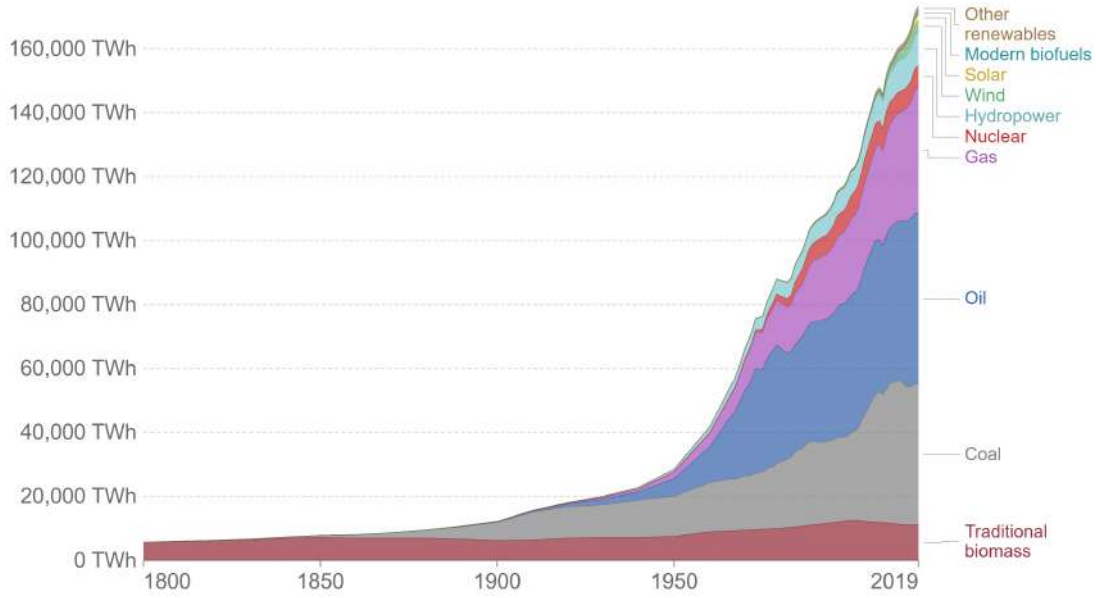

Figure 1 – Global primary energy consumption by source.[132]

In order to give access to commodities and reliable sources of electricity to the majority of people, more energy is needed. However generating more energy as it is produced today will lead to an increase in global warming with disastrous consequences. Over the last 40 years, the average temperature increased by 2.2°C in Europe, with dire consequences for the inhabitants e.g. flood, fire. In December 2019 the European Union (EU) agreed to fight climate change and global warming by becoming "climate-neutral" by 2050. To

achieve this goal several milestones have been set, one of them is "Fit for 55". This program should enable each country to halve its carbon emission (compared to 1990 levels). Several actions including energy efficiency or alternative fuels have been put forward by the EU. The share of renewable energy in the energy mix should also increase to 40% by 2030.

Among the selected possible renewable sources of energy is the wind, both onshore and offshore. The recent developments in turbine design allowed turbine manufacturers to be competitive on the electricity market. The Levelised Cost of Energy (LCoE [1]) of wind (onshore and offshore) is within the production cost of coal since 2010 according to IRENA's report [65].

Motivation and objectives

Wind energy, over the last decades, increased its market share thanks to a steady rotor size increase and a continuous increase in rated power. Nevertheless, to keep lowering the LCoE, onshore turbines need to produce more energy within the same swept area. Indeed, the blade size is restricted to avoid (or limit), among other things: acoustic emission, aeronautical interference, local population rejection... The blade design imposes high blade thickness at the root end of the blade for structural reasons, it leads to significant loss of the aerodynamic performances. Consequently, it is detrimental to the energy extraction. Solutions were developed to improve this blade region, among them, the passive Aerodynamic Add-On (AAO). AAOs add a small Captital Expenditure cost (CAPEX [2]) but increase the overall energy production[58, 160, 2].

With the increased rotor diameter and hub height, turbine manufacturers are now facing aeroelastic challenges where tower and blades can deform over large distances. Larger blades requires more attention to details during the design phase to reduce the cost. The maintenance cost during the turbine lifetime increases too, a good understanding of the turbine ageing is necessary. During routine maintenance, ENGIE Green, an exploiting party, noticed that some turbines equipped with a specific root AAO presented cracks. The AAO is the canoe-spoiler or *spoiler* and is installed between the radial position 3m from the blade root until 7.5m. The material initially chosen to build the spoiler may be too stiff leading to stress concentration and facilitating the cracks appearance. However, some aerodynamic phenomena unaccounted for in the design could be at play and will be investigated here.

The main objective of the thesis is to characterise the role of the local aerodynamic unsteadiness (self generated) on the aerofoil loads, turbine lifetime and turbine energy production. To that end, several state of the art tools and simulation methods will be used throughout the thesis.

1. Measure of the average net present cost of electricity generation for a generating plant over its lifetime

2. Funds used by a company to acquire, upgrade, and maintain physical assets such as property, plants, buildings, technology, or equipment

Thesis outline

The manuscript is split into eight main chapters where the different aspects of the work done will be detailed. The first chapter gives a definition of wind turbine principles: a characterisation of the wind is given followed by a description of the history of wind turbine technology.
The Chapter 2 explains the different theories used as part of the thesis along with a brief description of the associated tools.
Chapter 3 details the database used as part of the thesis. The DANAERO project being the main provider of numerical and experimental (wind tunnel and field) data. The blade acquired by ENGIE Green using 3D scan technology is also presented.
The next chapter, Chapter 4, will present the verification activities performed to ensure the validity of the tools used.
The Chapter 5 will present the analysis of the DANAERO field data highlighting the need of unsteady models in wind turbines. Then, in the Chapter 6 a detailed 2D simulation, using high fidelity tool, of a section equipped (or not) with spoiler will be shown. Both steady and unsteady aerodynamics are presented. The fatigue and energy production impact of spoilers is assessed in the Chapter 7. Finally, a 3D CFD analysis is performed on the ENGIE Green blade with and without spoiler, allowing a direct comparison with the 2D CFD and BEM calculation in the Chapter 8.
A conclusion is closing the thesis summarising the work performed and outlining proposal for future work.

Chapter 1

Wind turbine principles

Contents

The first chapter is dedicated to give a broad overview and understanding of the wind and wind turbines. First a definition of the wind and its characteristics will be given, then a review about wind turbine history is detailed.

1.1 Wind

1.1.1 Origins

To understand the origin of wind, one need to step back all the way to space. Indeed, the wind is the change of air masses location across Earth. Because the Earth is spherical and tilted, all its surface is not exposed similarly to the same amount of solar energy. On top of that, the Earth's surface different composition leads to different absorption and release rates of heat in the air. Those differences are the main reasons for the large scale air masses displacement. At a continental scale, the wind is driven from local high to low pressure regions. The flow is "bend" due to the Coriolis force, it forms the so-called convection cells, as illustrated on Figure 1.1. Within these meso scale cells (kilometres wide) several layers of flow exist, we will focus on the one closest to the ground, where wind turbine operate: the Atmospheric Boundary Layer (ABL).

The ABL depth varies both in time and space i.e. depending on time of the day and the terrain roughness (cities, landscapes, open seas,...). With the sun heating the ground and air, a Convective Boundary Layer (CBL) is developing near the ground growing up to 2000m in height. The CBL then reduces in depth toward the end of the day. A

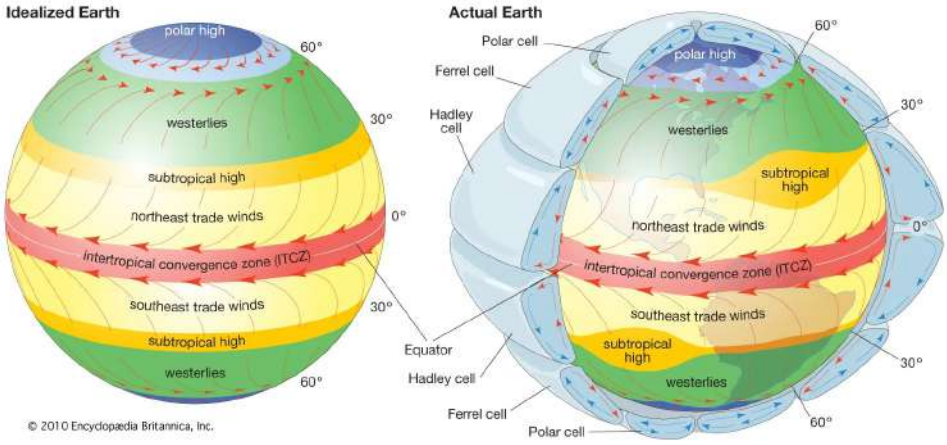

Figure 1.1 – General patterns of atmospheric circulation over an idealised Earth with a uniform surface (left) and the actual Earth (right). Both horizontal and vertical patterns of atmospheric circulation are depicted in the diagram of the actual Earth [5]

surface layer (up to 100m) develops where the wind structure is determined primarily by surface friction and the vertical gradient of temperature throughout the day ([76]). Figure 1.2 illustrates the ABL typical evolution during a 24h period. Above 100 meter and up to few kilometres, Coriolis forces cannot be neglected anymore, an Ekman layer develops [76]. Wind turbines operate in this changing environment where *atmospheric unsteadiness* can be well characterised through analysis of turbulence (from few millimetres up to few kilometres) with a surface roughness homogeneity assumption (see 1.1.2). The macro scale (metres wide) of a wind farm flow evolution is dependent of a micro scale flow down to the Kolmogorov scale (millimetres wide) near the wind turbine blade where *aerodynamic unsteadiness* is developed. The difficulty of wind turbine aerodynamics is to be able to account for all the different scales, be able to accurately solve them and link them correctly.

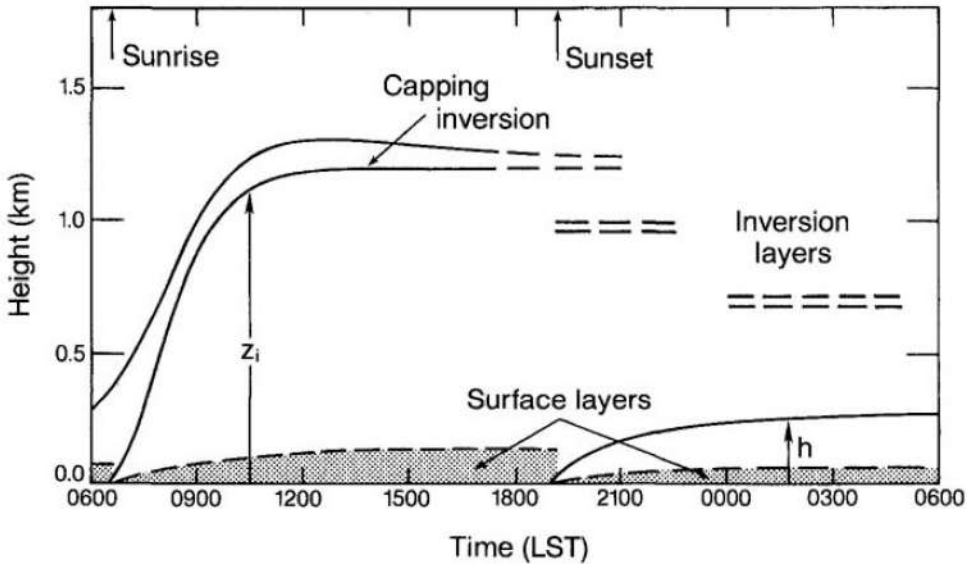

Figure 1.2 – Evolution of the convective and stable boundary layers in response to surface heating and cooling. The time indicated is Local Standard Time (LST). [76]

1.1.2 Characterisation

For most of the wind energy applications, the wind can be characterised by a superposition of a mean and a turbulent organisation that is highly dependent on the surface roughness and thermal stability (see Figure 1.3). More details are available in the following meteorological references [141, 78, 37, 43, 157, 33, 63].

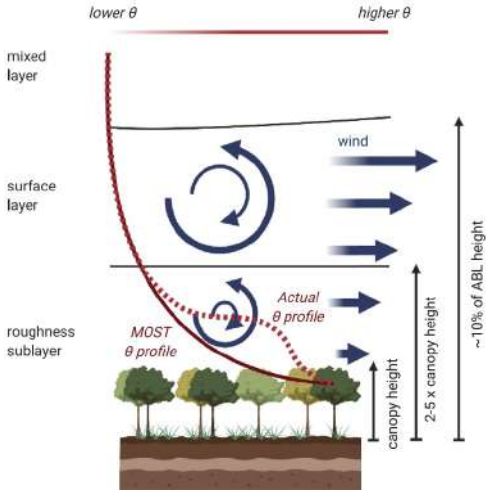

(a) Effect of the terrain on the surface layer measured compared to the calculated using Monin-Obukov [59]

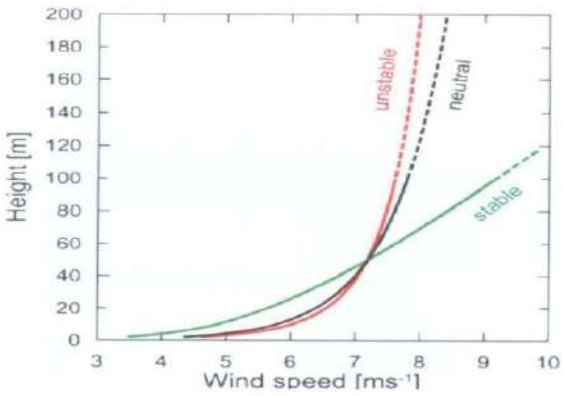

(b) Influence of atmospheric stability on the vertical wind speed profile [142]

Figure 1.3 – Impact of surface roughness and thermal stability on the wind profile

Mean wind

The wind direction is defined based on three vectorial components. In a Cartesian coordinate system, the main direction is usually defined following the x-axis, the lateral component of the wind is defined on the y-axis and the vertical direction is defined by the z-axis. At wind farm level it is mostly defined on a wind rose subdivided into quadrant (or sector) as illustrated in Figure 1.4. The total wind velocity is the vectorial sum of the speed following its three directions. The main wind speed is the speed with the highest value on a direction (usually the x-axis). Due to the ABL, the wind speed experiences a gradient in the vertical direction. At ground level the wind speed is non-existent and grows linearly following a viscous law (within few millimetres). Then, theories were developed to describe the wind speed growth with height such as the surface layer (log profile dominated by the surface roughness and the thermal stability) and the Ekman layer profile (where the impact of Coriolis forces are accounted for [76]). For practical reasons the empirical power-law (see equation 1.1) is most often used within the wind energy community. This law include a coefficient κ which is function of the surface roughness and the thermal stability. The thermal stability can be determined from the Monin-Obukhov similarity theory (see Section 1.1.2).

$$U(Z) = U \times \left(\frac{Z}{Z_r}\right)^{\kappa} \tag{1.1}$$

Where, $U(Z)$ is the wind speed distribution along the vertical direction, U is the reference wind speed, Z is the height varying between the ground and the top of the turbine, Z_r is reference height and κ is the wind shear exponent.

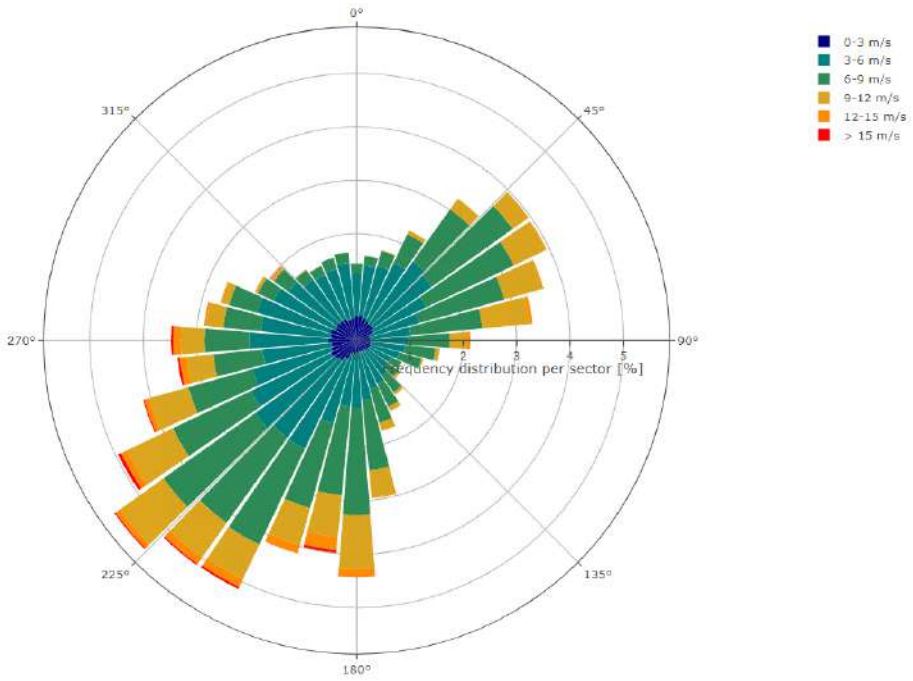

Figure 1.4 – Wind farm Les Hauts Pays (MM92) in Epizon (52230 - France) Wind rose distribution (2020-2021).

The mean wind speed varies with time. The most popular wind distribution used within the community is the Weibull distribution. Thanks to two parameters any wind site can be defined following the International Electrotechnical Commission (IEC) standard: IEC 61400-1.

$$\begin{aligned} W(A, C, x) &= \frac{A}{C}\left(\frac{x}{C}\right)^{(A-1)} e^{-\left(\frac{x}{C}\right)^{A}} \\ A &= \frac{U_{mean}}{e^{\Gamma\left(1+\frac{1}{C}\right)}} \end{aligned} \tag{1.2}$$

Where A is the shape factor, C is the scale parameter, U_{mean} is the site mean wind speed and Γ, the Gamma function defined as: $\Gamma(n) = \int_0^{\infty} e^{-x} x^{n-1} dx$.

The Figure 1.5 shows the Weibull density function for an IEC class II wind site and the Table 1.1 summarises the most common wind classes.

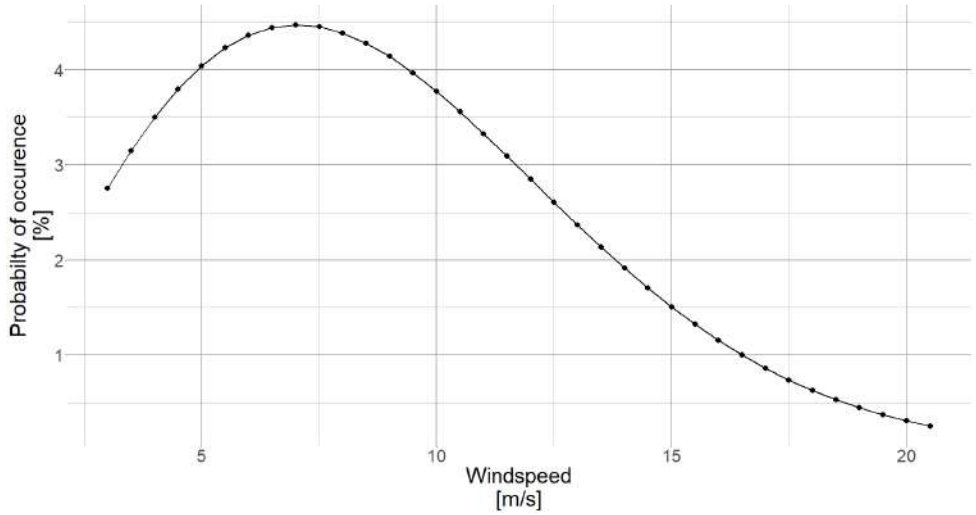

Figure 1.5 – IEC class II wind distribution.

Table 1.1 – IEC wind class definition

Wind class	**Mean wind speed [m/s]**	**Turbulence intensity at 15m/s [%]**	**Extreme 50 years gust [m/s]**
I	10	16 - 18	70
II	8.5	16 - 18	59.5
III	7.5	16 - 18	52.5
IV	6	16 - 18	42

The turbulence intensity is important for the turbine, as it influences the energy production and the perceived load levels. It is defined as the ratio between the fluctuating part of the wind and the mean wind speed in the considered direction. Equation 1.3 shows the turbulence intensity following the x-axis direction.

$$TI = \frac{u'}{\bar{U_x}} \tag{1.3}$$

Where u' is the velocity variation around the mean value following the x-axis and $\bar{U_x}$ is the mean velocity following the x-axis.

Turbulence

For a more detailed description of the wind, more parameters can be analysed such as the stationarity and stability. A test elaborated by Foken [43], is commonly used to assess the atmospheric stationarity, allowing further statistical analysis. According to Foken, the wind is considered stationary when, within a 30min period, the difference between the complete time series average of $\overline{w'\theta'}$ and the average of the sum of 5 minutes-pieces for $w'_i\theta'_i$ is less than 30% (see equation 1.4).

$$\frac{\overline{w'\theta'} - \frac{1}{6}\sum_{i=0}^{i=6}\overline{w'_i\theta'_i}}{\overline{w'\theta'}} \leq 0.3 \tag{1.4}$$

Where w' is the wind speed fluctuation in the vertical direction and θ' is the temperature variation across the time period considered.

Atmospheric stability is defined in terms of the tendency for a small air volume dV to move upward or downward after it has been displaced vertically (up or down) by a small amount. It can be determined using several methods: Richardson number, vertical temperature gradient and solar irradiation or the Monin-Obukov length (see [76, 157, 63, 63]). In the Richardson number and the Monin-Obukov length, the turbulent momentum flux $\overline{u'w'}$ (with $'$ the fluctuating quantity according to the the Reynolds decomposition) and the surface heat flux $\overline{w'\theta'}$ are explicitly formulated and represent the most important turbulent quantities used to classify the atmosphere stability. Regardless of the chosen method, five main stability categories are describing the effect of boundary layer stability on the wind profile as seen in Table 1.2.

Table 1.2 – Atmospheric boundary layer conditions according to stability regime.

Boundary layer class	**Main characteristics**
Very Stable	High wind shear across the rotor disk and low turbulence
Stable	Moderate to high wind shear in rotor disk, low turbulence
Neutral	Strongest wind speeds throughout the rotor disk with moderate level of turbulence expected. Wind speed increases logarithmically with height
Unstable	Lower wind speeds, low wind shear across the rotor disk, moderate to high turbulence.
Very unstable	Lowest wind speeds, very little wind shear across the rotor disk, highly turbulent

Finally, the turbulent part of the wind can be modelled and added to the mean wind profile through wind spectrum. The main spectra used in the wind energy community are the Kaimal spectrum and the Mann spectrum [76, 92]. Both spectra are used as part of the IEC standards for wind turbine certification.

1.2 Wind turbine

1.2.1 History

Taming the wind with any type of devices has been ongoing since the antiquity. The aim is to convert the wind kinetic energy into mechanical energy. Initially it was used to pump water or grind cereals, nowadays another conversion takes place: from mechanical rotation into electrical energy.
The first recorded wind powered machine dates from 1700 BC in Mesopotamia. By the IX^{th} century, in Seistan (current Iran), windmills were used to grind corn, flour and pump water. The same application is found from approximately the 1200s in Northern Europe. In 1887, the first ever electricity producing wind turbine was created by the Scottish professor James Blyth in Scotland. The turbine was vertical axis and relied on the wind "pushing" into half barrels as depicted on Figure 1.6. The turbine is a so-called drag machine, as the wind pushes against the "blades" making it turn around its axis.

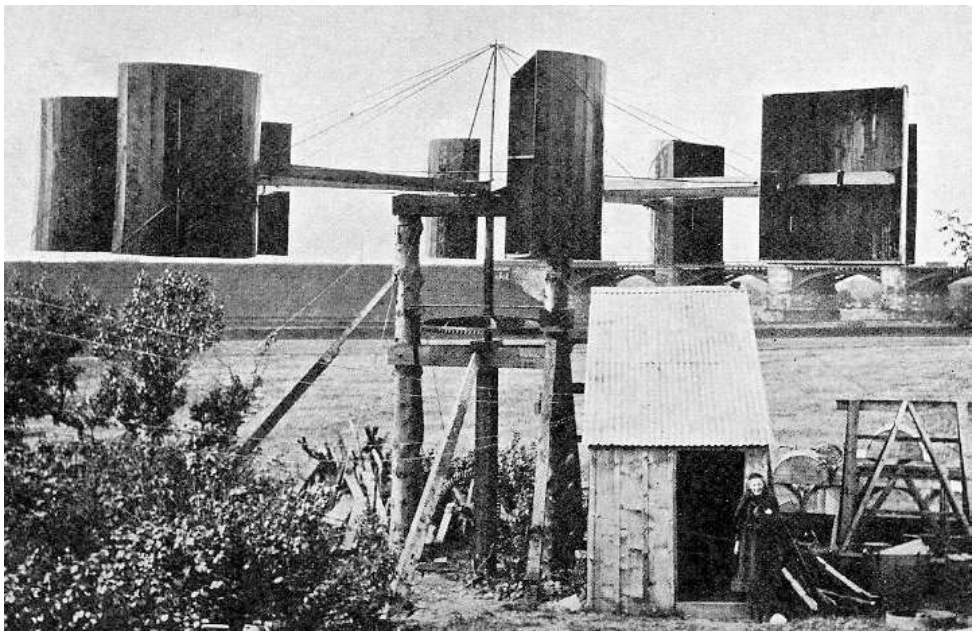

Figure 1.6 – James Blyth's wind turbine at his cottage in Marykirk in 1891.

Later, in 1931, a french engineer Georges Jean Marie Darrieus designed and patented a vertical axis wind turbine relying on aerofoils. Using aerofoils to generate lift rather than relying on the drag was novel at the time. Ever since the first windmills, the drag force was used to generate rotation. In the Darrieus turbine, for the first time the lift was used on purpose. A new class of machine called lift machine is created. Several designs were then created such as the small wind turbines used for irrigation purposes up to the first ever mega watt sized machine in 1941 (Smith–Putnam wind turbine).

In 1978, the design as is still mainly used today was introduced by the teachers and students of the Tvind school, in Denmark. The turbine had three pitch controlled blades and tubular steel tower and was producing 2MW (see Figure 1.8).

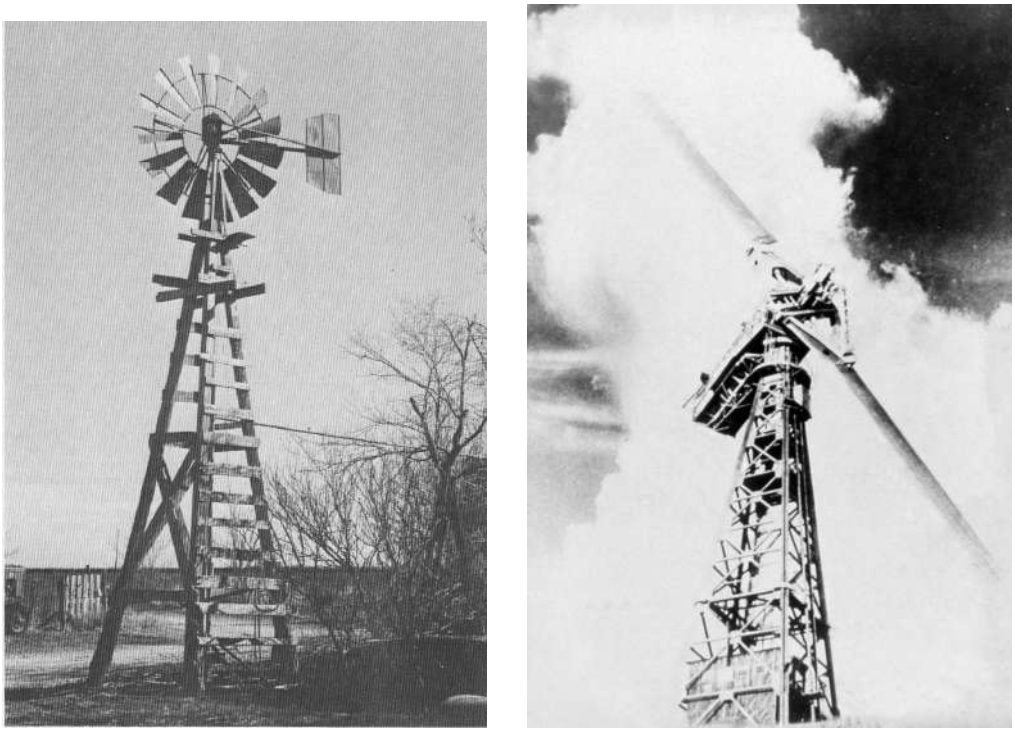

(a) Small wind turbine used for irrigation.

(b) First Megawatt wind turbine (1941).

Figure 1.7 – Different wind turbine designs.

Figure 1.8 – First multi MegaWatt turbine (2MW) build by teachers and students from Tvind school in 1978.

1.2.2 Modern days

Wind turbine design

Following years of development and improvement, all major turbine manufacturers use similar design: horizontal rotarion axis, upwind rotor, clockwise rotation, three bladed, steel tower and nacelle. The Figure 1.9 depicts the majors wind turbine components: the rotor and its three blades, the nacelle with the gearbox and generator and the tower.

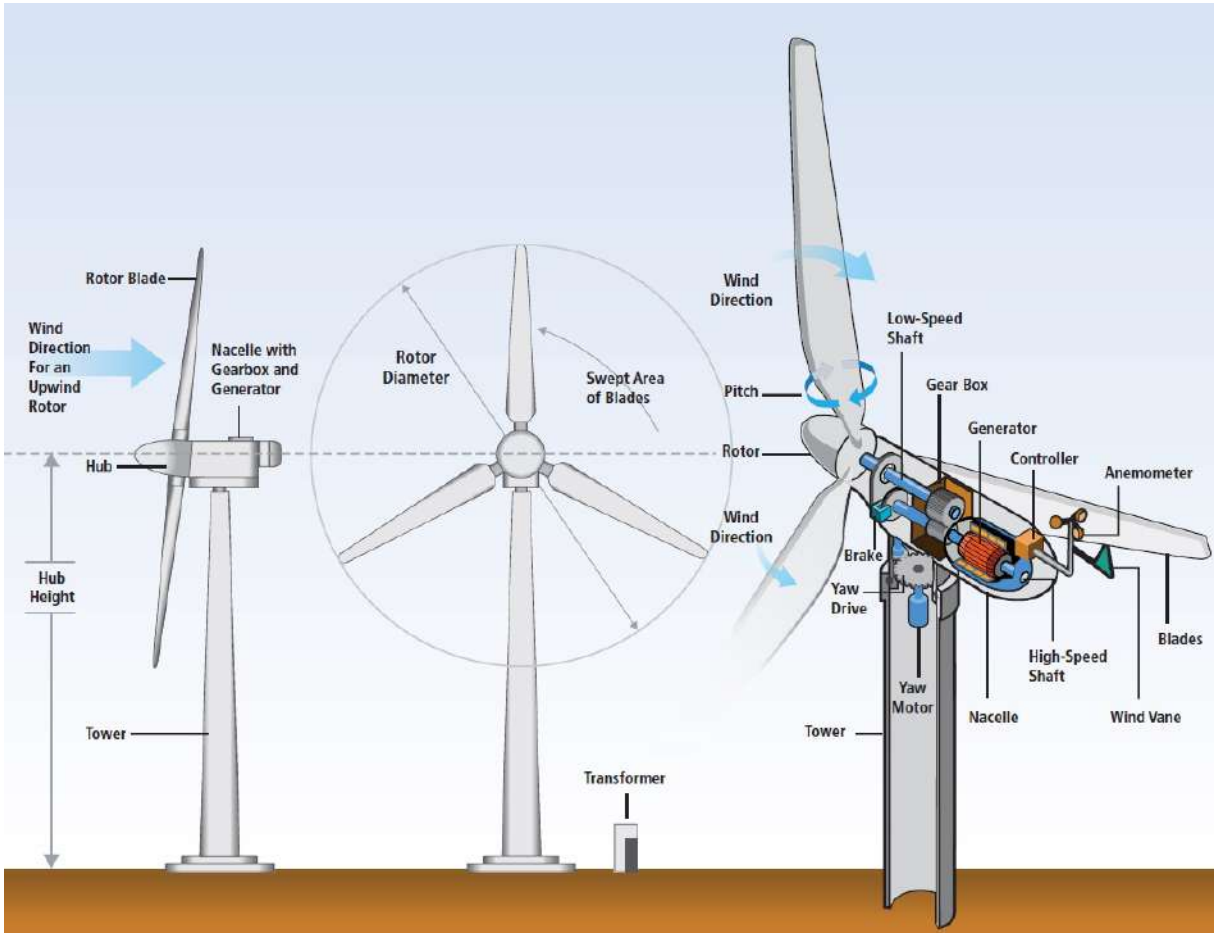

Figure 1.9 – Majors wind turbine components.[116]

A wind turbine blade is a hollow structure made of composite materials (glue with glass fibres and/or carbon fibres mainly). The blade can be split up in three main regions: root, middle and tip regions, each accounting for approximately 1/3 of the total blade length (or radius). The outer shell gives the aerodynamic shape while the loads are carried by the spar and/or webs inside. The aerodynamic shape can be viewed as a succession of 2D cross sections along the blade longitudinal axis. Each cross section is called an *aerofoil* and is comprised of: upper side (suction side, leeward side), lower side (pressure side, windward side), leading edge and trailing edge. The Figure 1.10a shows a typical blade design while the Figure 1.10b illustrates a typical middle region aerofoil.

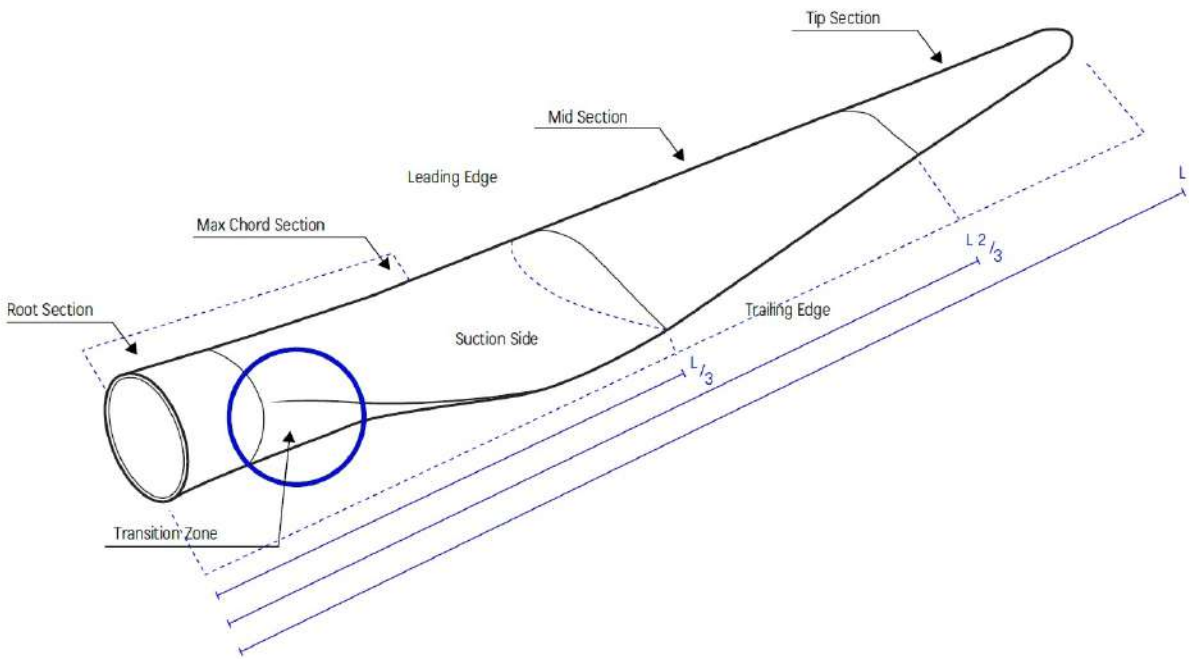

(a) Wind turbine blade illustration

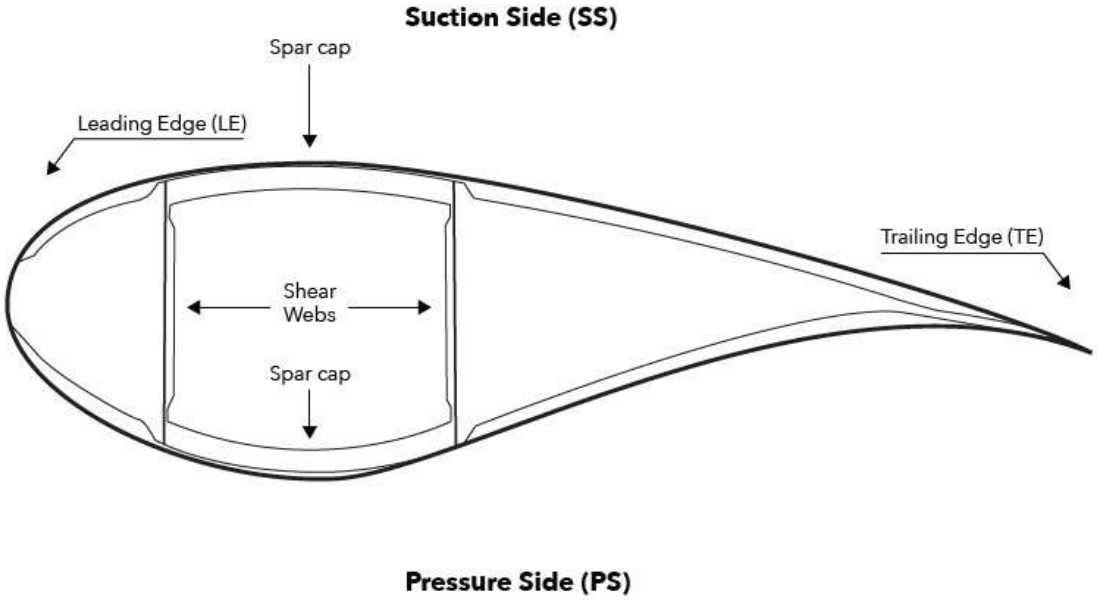

(b) Wind turbine aerofoil illustration.

Figure 1.10 – Wind turbine blade definition [145]

Spoiler and other Aerodynamic Add-Ons

As per Figure 1.10a, it is apparent that the root end of the blade is not very efficient in terms of energy extraction from the wind. The reason lies in its cylindrical form and the low relative speed. For many years, the root end was solely considered by turbine manufacturers as structural. In the recent years however, many add-on devices (Aerodynamic Add-On - AAO) have been developed to increase further the turbines efficiency. AAOs are devices attached to the blade surface to either increase the power extraction locally or reduce the acoustic emission of the turbine and thereby allowing the exploiting party to use the full turbine's capacity. The AAO solution has been explored by many authors before (see [105, 118, 6]). It is to be noted that in opposition to passive devices, some active solutions exist in the research state (such as solutions described in: [69, 16, 94]) but are not yet available to the market. In this thesis the focus will be on the former type: passive AAO installed in the root blade area to improve the aerodynamic performances of the thick aerofoil profile types.
The flow behind two well-known AAO devices, the Vortex Generators (VG) and the Gurney Flaps (GF), has been largely investigated in order to understand its mechanism and control benefit which is summarised hereafter. VG are small fins (thin plates of usually triangular or rectangular shapes attached to a base plate) attached on the aerofoil suction side to delay stall by re-energising the boundary layer (see [144, 47, 22, 30, 45, 82, 131, 106]). The vortices, aligned with the inflow leaving the device, increase the mixing between high speed flow (free stream) and low speed flow (boundary layer) thus delaying the flow separation (see [126]). GF are devices installed at the aerofoil trailing edge on the pressure side. They aim to create an artificial camber seen by the flow, it will decrease the lower pressure on the suction side and therefore increase the pressure difference between both sides of the aerofoil thus increasing the generated lift (see [81, 26, 46, 156, 68, 137, 99, 80, 2, 95]). The main difficulty in AAO design is the correct sizing. For GF, if the height is too small the gain is nonexistent, too large and the drag penalty cannot be compensated by the lift gain. Similarly for VGs, geometrical parameters of the device are affecting the control efficiency. The combined effect of both VG and GF solutions seems to be additive according to [140]. The Figure 1.11 shows in graphical form the VG and GF as designed by Vestas [152].

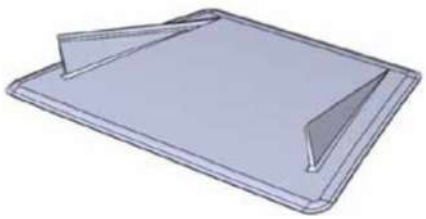

(a) Graphical illustration of a Vortex Generator (VG)

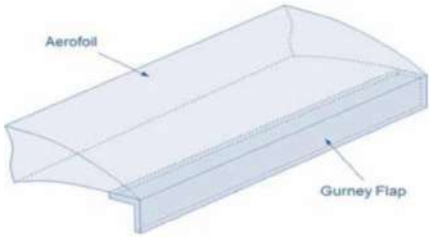

(b) Graphical illustration of a Gurney Flap (GF)

Figure 1.11 – Graphical illustration of the main Aerodynamic Add-Ons used to generate more power

Megawatt size wind turbines are experiencing high Reynolds number ($Re > 10^6$) for high relative aerofoil thicknesses at the blade root (relative thickness $> 36\%$), whereas most of the literature available is either targeting thin aerofoils at generally low to moderate Reynolds number, or small AAO sizes generally within the boundary layer thickness. Interesting outputs from low Reynolds study such as [95]) could be drawn. The detailed characterisation of the vortex shedding types occurring behind aerofoils equipped with different GF heights using Unsteady Reynolds-Averaged Navier-Stokes (URANS) and Large Eddy Simulations. However, the simulations were limited to thin profiles and low Reynolds numbers. Also, there is a gap on the AAO size used by manufacturers (usually $\geq 5\%$ of blade chord) and the one available in the literature (up to 1% of blade chord). The European AVATAR project (see [122]) studied thick sections at realistic Reynolds number ($Re > 10^6$). It is one of the few reference about wind turbine blade root spoilers at realistic operating conditions available. 2D Computational Fluid Dynamics (CFD) simulations were performed on the blade root with and without spoiler using Reynolds Average Navier-Stokes (RANS), thereby smoothing out the possible unsteady effects.
The AAO solution presented in this thesis is the spoiler, it is a passive obstacle installed on the aerofoil pressure side to increase the aerofoil camber perceived by the flow. Despite a lift enhancing mechanism similar to the large GF one, there is a main difference which lies in its position. The spoiler is installed between 60% and 80% of the local chord and is a long single aerodynamically designed part while the GF is installed perpendicularly to the local chord at the trailing edge and is usually comprised of several smaller parts butted up against one another.

AAOs are only useful below the turbine's rated power. The Figure 1.12 illustrates a typical wind turbine power curve with its associated regions: low energy production (I), high energy production (*knee of power curve* - II), rated power (III). The green shaded area shows the wind speeds where having any type of root AAO is producing higher power. It represents a possible power gain which, when integrated produces more energy.

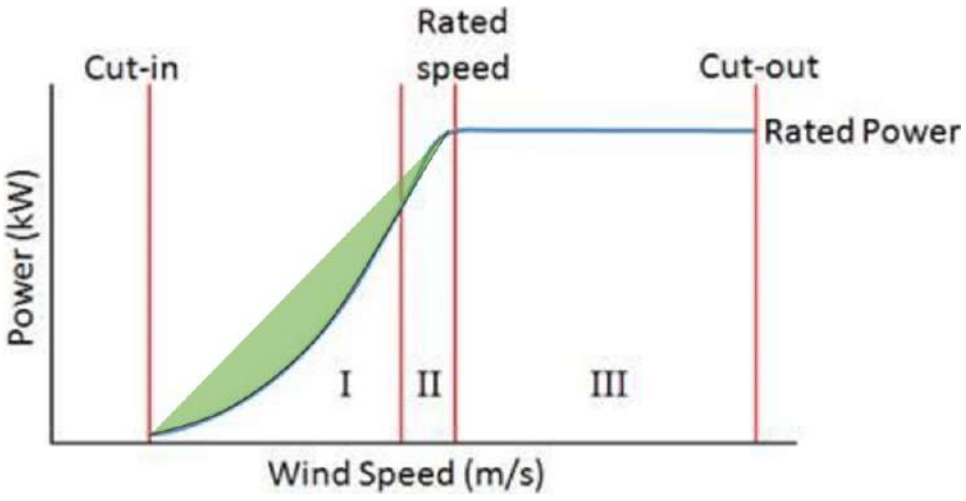

Figure 1.12 – Typical wind turbine power curve.

ENGIE Green is a french exploiting party of renewable energy sources. During routine maintenance, some cracks have been noticed at the blade root near the spoiler installation. As part of the business case to repair or replace the spoilers several projects to measure in the field the AEP increase thanks to spoilers were launched. Until this day the results were inconclusive because of the high measurement uncertainties coupled to the supposed low gain. The thesis aims at understanding the aerodynamic causes of the structural failure using state of the art calculation methods and proposing a novel way of predicting the lifetime impact of AAO onto the blade structure, the AEP gain will also be evaluated. Particular attention will be given to the aerodynamic unsteadiness generated by the spoiler.

(a) Spoiler installed at the blade root

(b) Repair patch near the spoiler location

Figure 1.13 – Parked blade with root spoiler installed

1.3 Summary

The wind characterisation occurs over large range of scales: from mesoscale with the atmospheric classification lasting days, to microscale at the aerodynamic unsteadiness level where the time scale is in order of the second or less. Regarding the turbine design it has evolved from drag power machine used to grind cereal or pump water for irrigation purposes, to highly efficient lift machine with a generator size up to 15MW available in the near future. The field is still evolving, wind turbine manufacturers are still developing solution to increase the robustness, the energy production while reducing the levelised cost of energy.

Chapter 2

Description of modelling tools

Contents

The following chapter will show the state of art in term of modelling tools: engineering codes and high fidelity solvers. Before each tool description a brief overview of the theory underlying each concept is proposed. The existing literature about each topic is already vast and therefore only the necessary basics are detailed. References are given in each section for a deep dive into the equations and models.

2.1 Blade Element Momentum

2.1.1 Aerodynamic modelling theory

Blade Element Momentum theory (BEM) first derives from ideal 1D momentum theory, where the rotor is represented by a porous, non-rotating, frictionless disk. Thanks to the ideal rotor assumption, the thrust can be derived simply as the pressure drop at the rotor plane (equation 2.1) thereby reducing the inflow.

$$T = \Delta p A \tag{2.1}$$

Where T is the thrust, Δp is the pressure drop and A is the disk area.

By assuming flux conservation and applying Bernoulli equations to the ideal disk control volume, as per Figure 2.1, (upstream, downstream and at the rotor disk) and assuming a stationary, frictionless and incompressible flow without any external forces, it is possible to find the velocity and pressure behaviour in the disk vicinity (equations 2.2 to 2.6).

$$V_0 A_0 = uA = u_1 A_1 \tag{2.2}$$

$$p_0 + \frac{1}{2}\rho V_0^2 = P^+ + \frac{1}{2}\rho u^2 \tag{2.3}$$

$$P^- + \frac{1}{2}\rho u^2 = p_1 + \frac{1}{2}\rho u_1^2 \tag{2.4}$$

$$\Delta P = P^+ - P^- = p_0 + \frac{1}{2}\rho(V_0^2 - u^2) - p_1 - \frac{1}{2}\rho(u_1^2 - u^2) \tag{2.5}$$

$$\Delta p = \frac{1}{2}\rho(V_0^2 - u_1^2) \tag{2.6}$$

Where p_0 and p_1 are equal since they are the pressure at the inlet and outlet of the control volume, V_0 is the velocity at the inlet of the control volume, P^+ is the pressure just in front of the rotor and P^- is the pressure just behind the rotor, u_1 is the velocity at the outlet of the control volume and u is the velocity at the rotor disk, A_0 is the inlet area and A_1 the outlet area.

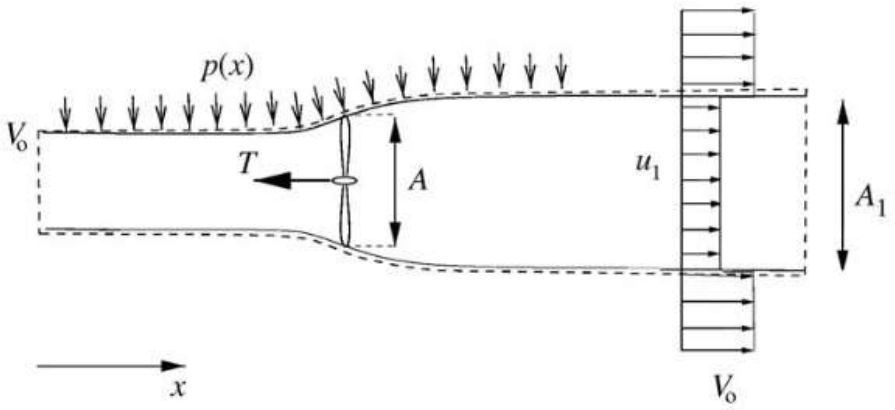

Figure 2.1 – Control volume around a rotor disk [53]

Through the conservation of mass and accounting for the external pressure along the control volume walls, the internal energy from inlet to outlet cannot change. It yields a relationship allowing to find the power and updated thrust definition (equation 2.7).

$$\begin{aligned} P &= \dot{m}\left(\frac{1}{2}V_0^2 + \frac{p_0}{\rho} - \frac{1}{2}u_1^2 - \frac{p_0}{\rho}\right) \\ \text{knowing that} \quad \dot{m} &= \rho u A \quad \text{then} \\ P &= \frac{1}{2}\rho u A(V_0^2 - u_1^2) \\ T &= \rho u A(V_0 - u_1) = \dot{m}(V_0 - u_1) \end{aligned} \tag{2.7}$$

Where P is the power, T is the thrust, $\dot{m}$ is the air mass flow, p_0 is the atmospheric pressure, V_0 is the inflow, u is the velocity at the disk and u_1 is the wake velocity

The axial induction, noted a, is then introduced as a fraction of the incoming velocity:

$$u = V_0(1 - a) \tag{2.8}$$

The power P and thrust T produced can be rewritten as function of the axial induction (equation 2.9 and 2.10).

$$P = 2\rho V_0^3 a(1 - a)A \tag{2.9}$$

$$T = 2\rho V_0^2 a(1 - a)A \tag{2.10}$$

The total available power in the wind is defined by $P_{avail} = \frac{1}{2}\rho V_0^3 A$. Making a ratio of the available power to the actual produced power is the so-called *power coefficient* as described in equation 2.11:

$$C_{po} = \frac{P}{P_{avail}} = \frac{2\rho V_0^3 a(1 - a)A}{\frac{1}{2}\rho V_0^3 A} \tag{2.11}$$

The highest ratio of energy extraction is found by deriving the power coefficient with respect to the axial induction :

$$\begin{aligned} \frac{dC_{po}}{da} &= 4a(1 - a)(1 - 3a) \\ C_{po_{max}} &= \frac{16}{23} \quad \text{for} \quad a = \frac{1}{3} \end{aligned} \tag{2.12}$$

A similar derivation is possible for the thrust coefficient, yielding the well-known C_{po} and C_T versus a plot as seen on Figure 2.2.

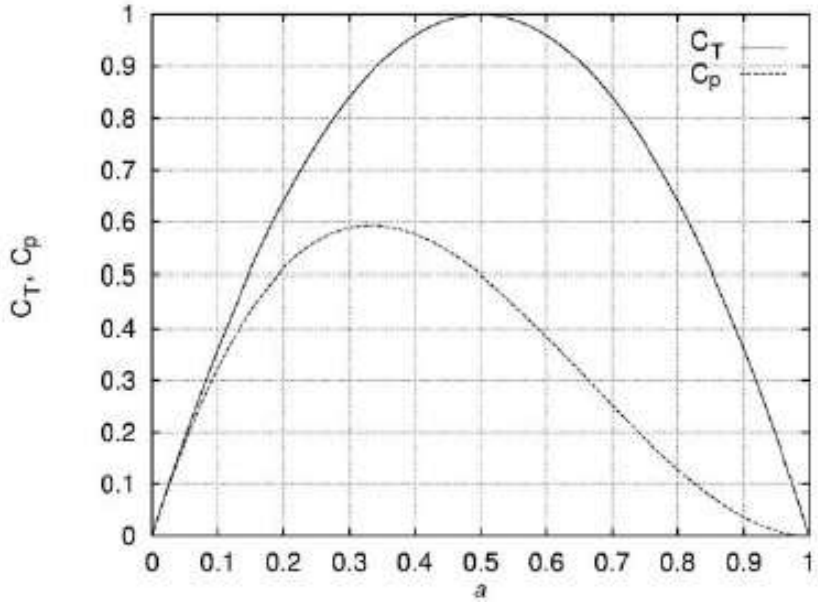

Figure 2.2 – Evolution of the power coefficient (C_{po}) and thrust coefficient (C_T) with respect to the axial induction a. [53]

Building on the fundamentals of momentum theory, Blade Element Theory introduces the rotor geometry, the blade discretisation and blade rotation. BEM combines the streamtube and control volume introduced by the 1D momentum theory with the geometric aspect of the rotor (discretised into a finite number of blades with independent aerofoils). The Figure 2.3 summarises the aerofoil forces and velocities introduced by the BEM.

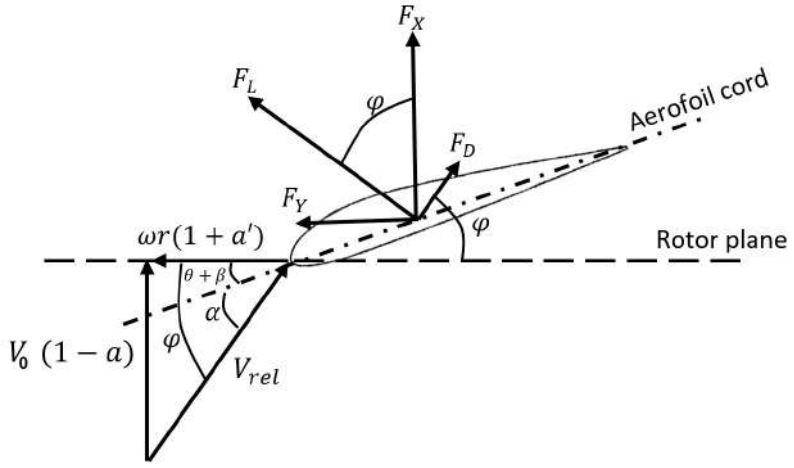

Figure 2.3 – BEM velocity triangle showing the inflow angle φ , twist and pitch angle $\theta + \beta$ and angle of attack α. The normal force (F_X), tangential force (F_Y), lift force (F_L) and drag force (F_D) are also represented showing the relationship between rotor and local coordinates.

The BEM is widely used by turbine manufacturers to design wind turbines, calculate associated loads and compute the turbine Annual Energy Production (AEP). The BEM

model has the advantage of being very fast, but does not account for real-life conditions since it assumes stationary and uniform inflow conditions, no misalignment of the rotor with the wind direction, independence of the flow between blade sections, 2D flow on the blade sections. Since the introduction of the BEM method in the 1900s, many authors have developed and implemented engineering correction models to overcome the BEM limitations thanks to several extensive measurement campaigns of scale models in large wind tunnels or in the field (see [51, 130, 133, 17, 91, 148]). Several correction models such as three dimensional effects of the flow at the tip [113], at the root [62, 84, 24], dynamic stall effects [79, 52], yaw corrections [15, 90, 100], dynamic inflow [134], are common knowledge rendering the steady BEM solver into an unsteady model. The physical phenomena of wind loading unsteadiness are now better understood thus the safety factors used to ensure the turbine robustness and design lifetime can be reduced. It is also possible to couple to the aforementioned corrections models, structural solvers and/or controllers in order to simulate the wind turbines in a so-called aero-servo-elastic tool. Consequently, this coupling enhances even more the model accuracy along with the computational power needed. A thorough explanation of the BEM theory is available in textbooks such as [53] or [19]. The following brief step-by-step approach summarises the iterative BEM procedure:

1. The axial induction factor a and the tangential induction factor a' are first estimated (typically $a = a' = 0$) only during the first loop. For the following loops the induction values used are those from the previous iteration (see step 7).
2. Then, the inflow angle φ is estimated from the instantaneous velocity inflow V_0, the rotor rotational speed ω and the local radius r.
3. The angle of attack, α, is computed with θ the local twist angle and β the blade pitch angle.
4. The C_{L} (lift coefficient) , C_{D} (drag coefficient) and C_{M} (moment coefficient around the quarter chord position) are read from the polar associated with the analysed radius.
5. Calculate the loads in the rotor plane using C_{L}, C_{D}, C_{M} and φ.
6. To account for the finite blade span, the Prandtl tip correction factor is calculated.
7. The initial induction coefficients, a and a', are updated accounting for highly loaded rotors induction model.
8. The unsteady BEM equations can be applied: rotational effects, yaw models, dynamic wake model, dynamic stall, blade acceleration due to its deflection and tower shadow effect.
9. A convergence criterion, ϵ, is defined, and the iteration process restarts from step 2, using the updated induction values, until the convergence criterion is reached.
10. After convergence, the local loads (aerofoil level) can be calculated.
11. Once all blade elements are converged, the integrated loads (rotor and turbine level) can be computed.

2.1.2 OpenFAST

OpenFAST is a framework developed by NREL [1] which aims to employ multi-physics, multi-fidelity tool for simulating the coupled dynamic response of wind turbines. To that end, several independent modules (see Figure 2.4) have been developed to address the needs in: aerodynamics, hydrodynamics for offshore structures, control and electrical system (servo) dynamics, and structural dynamics thereby enabling coupled nonlinear aero-hydro-servo-elastic simulation in the time domain. As part of the thesis the modules AeroDyn (section 2.1.3), ElastoDyn (2.3.3) and InflowWind (not detailed in this thesis) have been used to calculate the power production and loads of turbines with or without spoilers.

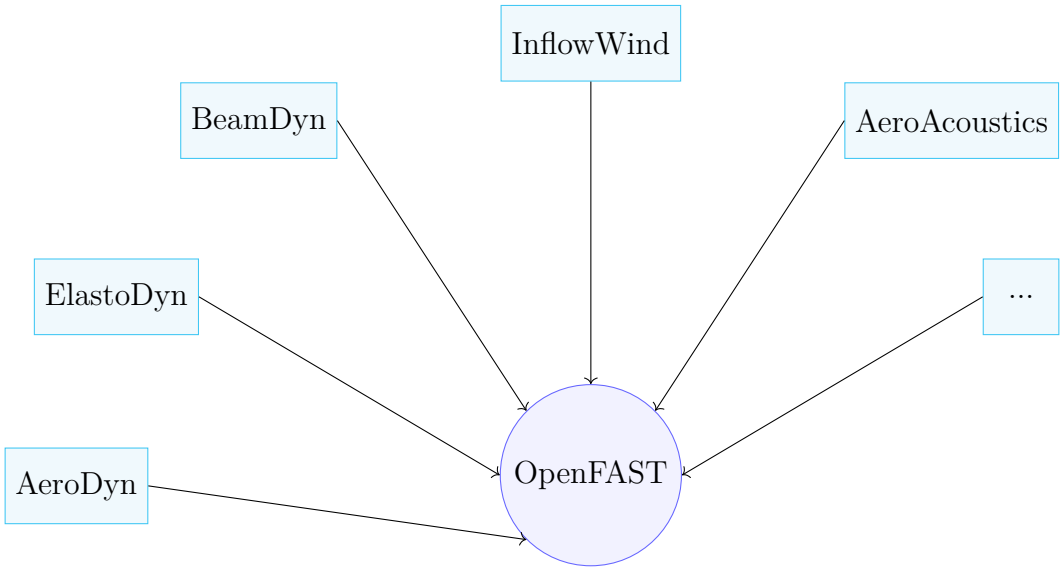

Figure 2.4 – OpenFAST modules overview

2.1.3 AeroDyn

AeroDyn was initially developed by Craig Hansen and researchers at the University of Utah and Windward Engineering for wind turbine aeroelastic simulations [100]. AeroDyn can now be used as a standalone module or part of OpenFAST, running the BEM theory. Because of its ability to run in batch mode, the AeroDyn standalone driver was preferred, in this thesis, over the OpenFAST integrated version. The necessary inputs are text files based and can be summarised as:

- Simulation set-up file
- Blade geometric definition
- Aerofoil data: coordinates, polar, operational Reynolds number and unsteady model parameters (if needed)
- Driver file: turbine operating conditions

1. https://openfast.readthedocs.io/en/main/ - website accessed on 08/11/2021

Most of the state of the art correction models are included: hub, tip and root loss, highly loaded rotor correction, yaw misalignment correction model and rotational correction model. The user has full control over the use or not of the implemented correction models. The outputs of AeroDyn are then used for load and deformation calculation as explained in Section 2.3.1 and Section 2.3.2.

2.1.4 Unsteady inverse BEM

The Unsteady inverse Blade Element Momentum (UiBEM) method is the application in reverse of the classical unsteady BEM theory described in Section 2.1.1. UiBEM allows conversely to back-calculate from the aerodynamic loads the aerodynamic coefficients for a given inflow time series. The UiBEM solver was developed as part of the thesis. Its verification is detailed in Section 4.1.2.
By adapting the unsteady BEM procedure, it is possible to calculate for a given turbine operating condition: the local velocity, the lift coefficient (C_L) and drag coefficient (C_D) as well as the induction and the angle of attack from the normal F_X and tangential forces F_Y (here from integrated local pressure measurements). A graphical format of the code developed during the thesis, with detailed equations is shown in Figure 2.5. The process is repeated until convergence is reached for each time step of the acquired inflow velocity and for each blade section. The axial and tangential induction in the convergence loop are marked with subscript j. The black path shows the use of steady BEM equations, the blue path shows the use of unsteady BEM equations, the red path shows outputs of the present solver, which comprises of the measured forces projected in the aerofoil coordinates, C_L and C_D, the angle of attack α and the converged axial and tangential induction.

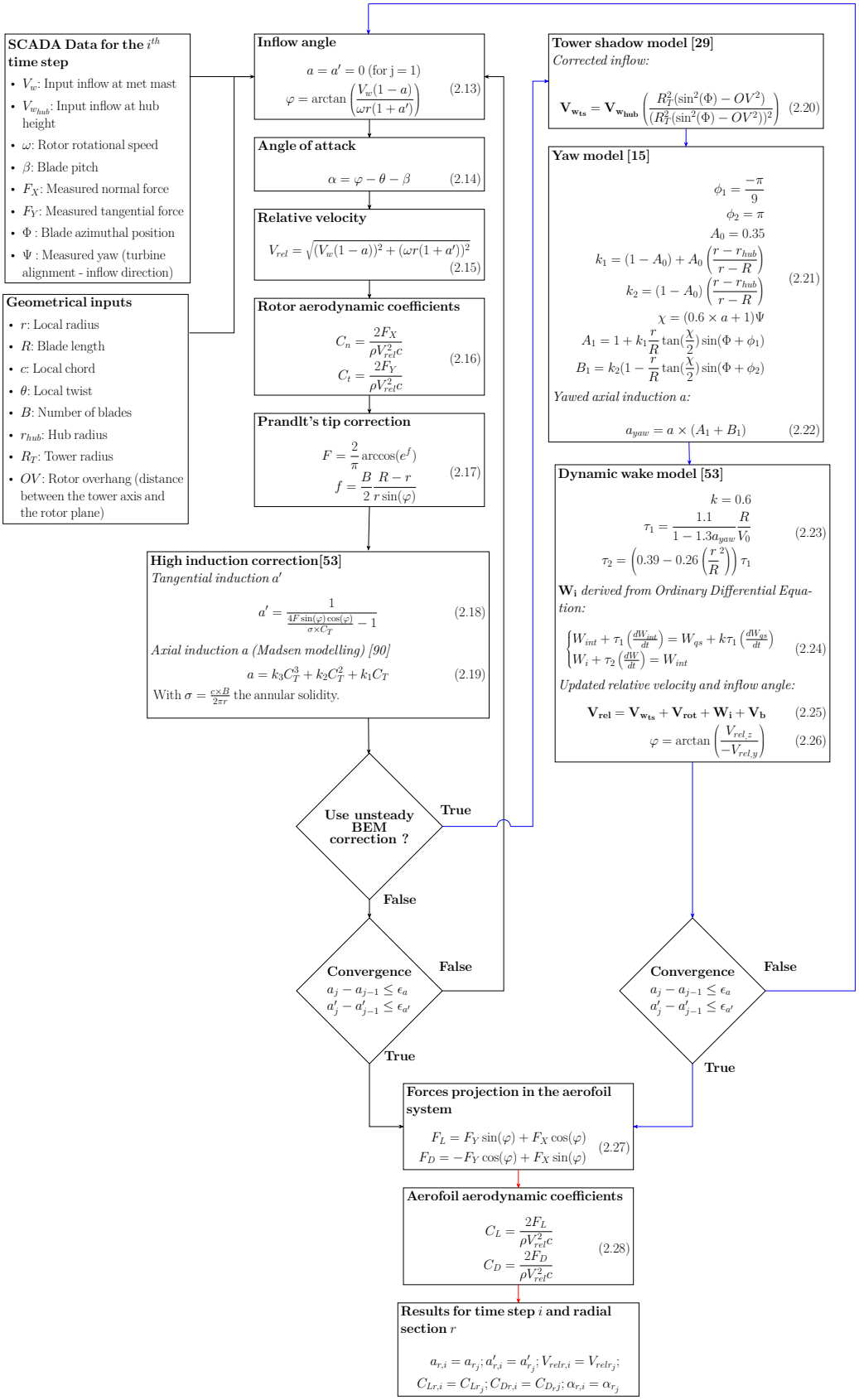

Figure 2.5 – Diagram of the inverse Blade Element Momentum (iBEM) and Unsteady inverse Blade Element Momentum (UiBEM) method algorithm.

2.2 Computational Fluid Dynamics

Computational Fluid Dynamics (CFD) is a broad subject, even when only referring to external aerodynamics. It encompasses calculation methods using the fast 2D aerofoil solvers, such as Xfoil [36], which use inviscid formulation up to Direct Numerical Simulation (DNS), where the turbulence is solved at all scales without turbulence modelling. To some extent, BEM or other computational method such as Lifting Line or Actuator Disk can be considered CFD. To avoid confusion, in this chapter and for the rest of the manuscript, *CFD*, will refer to the computational means of solving the Navier-Stokes equations using grid (also called mesh). It is to be noted that the present thesis did not aim at improving CFD modelling. The work presented uses an existing solver detailed in Section 2.2.2 (ISIS-CFD) which includes state of the art Navier-Stokes formulations (RANS, URANS, coupling LES/RANS) as well as state of the art turbulence models near the wall.

The governing equations of CFD methods represent, in mathematical form, the different physics conservation laws:

- The mass of a fluid is conserved
- The rate of change of momentum equals the sum of the forces on a fluid particle (Newton's second law)
- The rate of change of energy is equal to the sum of the rate of heat addition to and the rate of work done on a fluid particle (first law of thermodynamics)

Extensive literature exists and the reader is advised to peruse the following references [3, 4, 151, 39]
The Navier–Stokes equations describe turbulent flows, but, due to the properties of the flow, it is rarely possible to solve the equations for real engineering applications even with supercomputers. Direct solution of the Navier–Stokes equations (DNS) for wind turbine applications are getting more accessible but remains computationally expensive because of the different length scales solved by this approach. The time needed to solve a problem simulated with the DNS method is proportional to Re^3, making the application to wind turbine, where the Reynolds number is $Re > 10^6$, impracticable for industrial application. A more cost-effective method is to resolve only the large-scale turbulence, by filtering out the fine-scale turbulence, and model these small scales as flow-dependent effective viscosity. This method, Large Eddy Simulations (LES) are faster than DNS but still require supercomputers running for days before converging to a solution.
The lowest level of complexity and fastest means to achieve a sensible result is to use Reynolds Averaged Navier Stokes (RANS) formulation. In these models the turbulent fluctuations are time averaged creating an open problem, i.e. there are more unknowns than equations. For this reason turbulence models were developed so as to close the RANS set of equations. A focus about the unsteady formulation of the RANS is shortly detailed in Section 2.2.1. Hybrid solution of RANS/LES models are now available and bring the best of the two numerical approaches: the high energy vortices are resolved using the LES

method while near the wall the RANS technique is applied. This approach is called Delayed Detached Eddy Simulation (DDES) or Improved wall modelling Delayed Detached Eddy Simulation (IDDES). DDES or IDDES are well suitable simulation methods because of the large eddies created due to the massive flow separation near the blade root. Nevertheless, the mesh required is finer and the time step needed is smaller than in RANS, thus increasing the calculation time. Detailed explanations about RANS/LES are out of the scope of this thesis, instead the reader is advised to read [23].

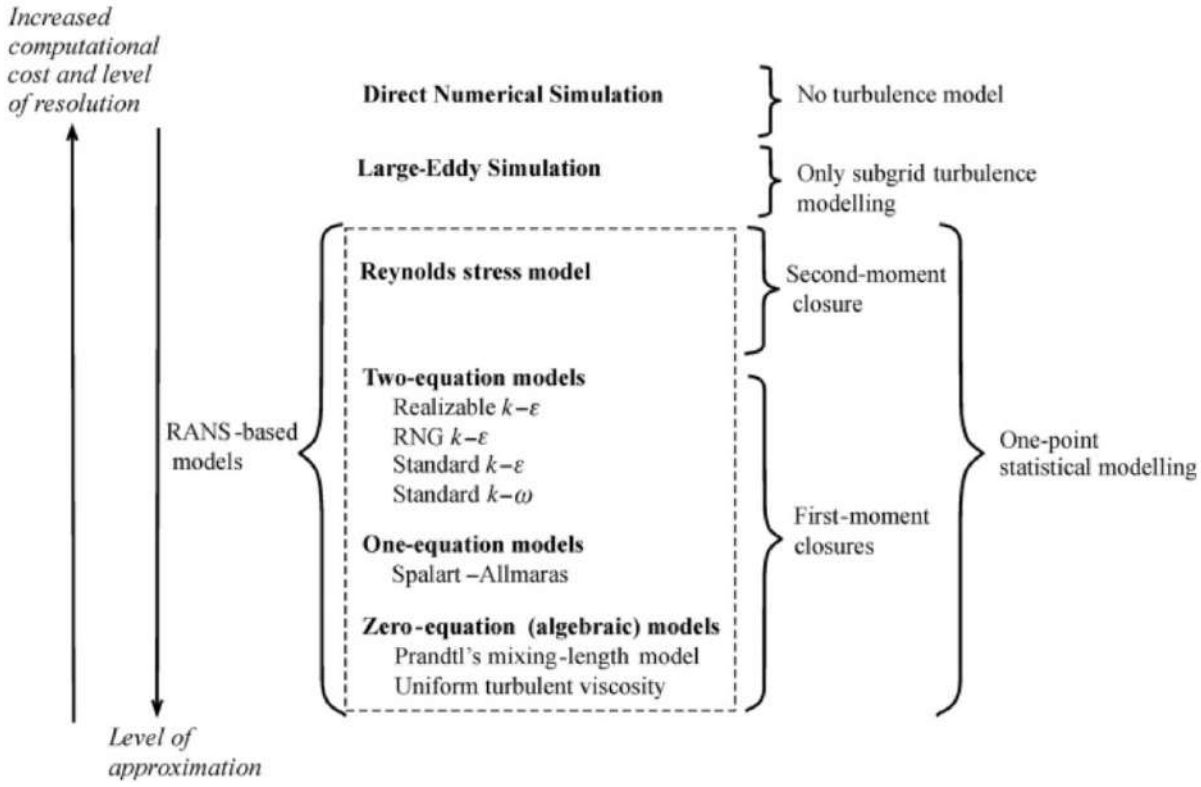

Figure 2.6 – The different modellings available in CFD [4]

2.2.1 URANS

The following section is dedicated to the RANS-based model, more specifically the URANS formulation as it will be used throughout the thesis. There are three main methods of numerical solution techniques: finite difference, finite element and spectral methods. The following explanations will focus on the finite volume method, as it is the solution used by ISIS-CFD. ISIS-CFD is a CFD solver developed by Centrale Nantes and CNRS and used as part of the thesis, a dedicated section will present its features (see Section 2.2.2).

Navier-Stokes equations

After deriving the mathematical statements for conservation of mass, the conservation of momentum, the energy rate of change for a fluid particle and defining the equations of state, it is possible to write a closed form of the Navier-Stokes equations. It is to be noted that the equations presented in equations 2.29 to equation 2.31 are written following the Reynold's decomposition, i.e. the velocity quantity is decomposed into a mean and fluctuating part (e.g. $\Phi = \bar{\Phi} + \Phi'$) and the Favre's density-weighted averaged is used (e.g. for the mean velocity $\tilde{u} = \frac{\overline{\rho u}}{\bar{\rho}}$).

Continuity equation:

$$\frac{\partial \bar{\rho}}{\partial t} + \text{div}(\bar{\rho}\tilde{\mathbf{U}}) = 0 \tag{2.29}$$

Where $\tilde{\mathbf{U}}$ is the Favre averaged velocity vector and $\bar{\rho}$ is the averaged fluid density.

Reynolds equations:

$$\begin{aligned}
\frac{\partial \bar{\rho}\tilde{U}}{\partial t} + \text{div}(\bar{\rho}\tilde{U}\tilde{\mathbf{U}}) &= -\frac{\partial \bar{P}}{\partial x} + \text{div}(\mu \ \text{grad} \ \tilde{U}) + \\
&\left[-\frac{\partial \overline{(\bar{\rho}u'^2)}}{\partial x} - \frac{\partial \overline{(\bar{\rho}u'v')}}{\partial y} - \frac{\partial \overline{(\bar{\rho}u'w')}}{\partial z} \right] + S_{M_X} \\
\frac{\partial \bar{\rho}\tilde{V}}{\partial t} + \text{div}(\bar{\rho}\tilde{V}\tilde{\mathbf{U}}) &= -\frac{\partial \bar{P}}{\partial y} + \text{div}(\mu \ \text{grad} \ \tilde{V}) + \\
&\left[-\frac{\partial \overline{(\bar{\rho}u'v')}}{\partial x} - \frac{\partial \overline{(\bar{\rho}v'^2)}}{\partial y} - \frac{\partial \overline{(\bar{\rho}v'w')}}{\partial z} \right] + S_{M_Y} \\
\frac{\partial \bar{\rho}\tilde{W}}{\partial t} + \text{div}(\bar{\rho}\tilde{W}\tilde{\mathbf{U}}) &= -\frac{\partial \bar{P}}{\partial z} + \text{div}(\mu \ \text{grad} \ \tilde{W}) + \\
&\left[-\frac{\partial \overline{(\bar{\rho}u'w')}}{\partial x} - \frac{\partial \overline{(\bar{\rho}v'w')}}{\partial y} - \frac{\partial \overline{(\bar{\rho}w'^2)}}{\partial z} \right] + S_{M_Z}
\end{aligned} \tag{2.30}$$

Where $\tilde{U}$, $\tilde{V}$, $\tilde{W}$ are the Favre averaged velocity vector components, μ is the fluid's dynamic viscosity, u', v', w' are the velocity fluctuations around the mean value in each direction, $S_{M_X}, S_{M_Y}, S_{M_Z}$ are the source terms in each direction and $\bar{P}$ is the mean pressure.

Scalar transport equation of Φ:

$$\begin{aligned}
\frac{\partial \bar{\rho}\tilde{\Phi}}{\partial t} + \text{div}(\bar{\rho}\tilde{\mathbf{\Phi}}\tilde{\mathbf{U}}) &= \text{div}(\Gamma_\Phi \ \text{grad} \ \tilde{\Phi}) + \\
&\left[-\frac{\partial \overline{(\bar{\rho}u'\phi')}}{\partial x} - \frac{\partial \overline{(\bar{\rho}v'\phi')}}{\partial y} - \frac{\partial \overline{(\bar{\rho}w'\phi')}}{\partial z} \right] + S_\Phi
\end{aligned} \tag{2.31}$$

Where $\mathbf{\Phi}$ is the considered quantity, ϕ' fluctuation around the mean of the transported quantity, S_Φ is the source term and Γ_Φ is the diffusion coefficient of the quantity Φ.

The previous equations describe the RANS modelling, the following development will show the integration of the time step into the averaging process. The transport equation (equation 2.31), can be rewritten in general form for unsteady flows as:

$$\frac{\partial \bar{\rho}\phi}{\partial t} + \mathrm{div}(\rho\tilde{\mathbf{U}}\phi) = \mathrm{div}(\Gamma_\Phi \ \mathrm{grad} \ \tilde{\phi}) + S_\Phi \tag{2.32}$$

This equation is used as the starting point for computational procedures in the finite volume method. By setting Φ equal to the appropriate quantity and selecting appropriate values for diffusion coefficient Γ and source terms, special forms the partial differential equations for mass, momentum and energy conservation are obtained (equation 2.29 to equation 2.31). The key step of the finite volume method is the integration of equation 2.32 over a three-dimensional control volume (CV):

$$\int_{CV}\left(\frac{\partial \bar{\rho}\phi}{\partial t}dV\right) + \int_{CV}\left(\mathrm{div}(\rho\tilde{\mathbf{U}}\phi)dV\right) = \int_{CV}\left(\mathrm{div}(\Gamma_\Phi \ \mathrm{grad} \ \phi)dV\right) + \int_{CV}\left(S_\Phi dV\right) \tag{2.33}$$

Using Gauss's divergence theorem, the volume integrals from equation 2.33 are rewritten in terms of surface integrals as seen in equation 2.34.

$$\frac{\partial}{\partial t}\int_{CV}\left(\bar{\rho}\phi dV\right) + \int_{A_{cs}}\mathbf{n}\left(\rho\tilde{\mathbf{U}}\phi dA_{cs}\right) = \int_{A_{cs}}\mathbf{n}\left(\Gamma_\Phi \ \mathrm{grad} \ \phi dA_{cs}\right) + \int_{CV}\left(S_\Phi dV\right) \tag{2.34}$$

Where A_{cs} is the area of the entire control surface, $\mathbf{n}$ is the normal vector of A_{cs} pointing outwards and dV a small volume particle.

To predict unsteady solutions the rate of change ($\frac{\partial}{\partial t}\int_{CV}\left(\bar{\rho}\phi dV\right)$) must be included into the discretisation problem. Therefore in addition to the control volume integration due to the finite volume method, a time integration over Δt is necessary:

$$\int_{\Delta t}\left(\frac{\partial}{\partial t}\int_{CV}\bar{\rho}\phi dV\right)dt + \int_{\Delta t}\int_{A_{cs}}\mathbf{n}\rho\tilde{\mathbf{U}}\phi dA_{cs}dt = \int_{\Delta t}\int_{A_{cs}}\mathbf{n}\Gamma_\Phi \ \mathrm{grad} \ \phi dA_{cs}dt + \int_{\Delta t}\int_{CV}S_\Phi dV dt \tag{2.35}$$

Discretisation scheme

The results from equation 2.35 are calculated on the faces of the control volume whereas the outcome is needed at the nodal points of the mesh. The discretisation scheme is the method to interpolate data from the faces to the nodes. A straightforward method is the linear interpolation between two points (assuming a uniform grid): it is the central differencing scheme. The limitation of central differencing is that the flux direction is unknown. Another scheme widely used is the upwind differencing scheme. It compensates for this limitation, the convected value at a cell face is set equal to the value at the upstream node. Both schemes can be used in conjunction by ways of piecewise functions to be used based on local parameter (Peclet number).

Various mathematical and algebraic manipulations are necessary to transform the equations 2.35 into their discretised forms, which are out of the scope of the thesis, instead good worked examples are detailed in [151].

Turbulence model

Because of the averaging process taking place in the RANS formulation, extra terms appear: the Reynolds stresses and the transport equation time average terms. The use of turbulence modelling is necessary in order to have a closed problem. It exists many different types of model adding (or not) extra equations to ensure the closure: mixing length model, Spalart–Allmaras, $k-\epsilon$, $k-\omega$, SST $k-\omega$, Reynolds stress model.
The turbulence model developed by Menter (SST $k-\omega$) [96], is a combination of the best features of the $k-\epsilon$ and $k-\omega$ turbulence models. Near the wall, the $k-\omega$ model is used and far from the wall, where the turbulence is fully developed, the $k-\epsilon$ is used. It relies on empirical constants which have been tuned since the first paper published in 1993. Only the SST $k-\omega$ model has been used as part of this thesis.

2.2.2 ISIS-CFD

ISIS-CFD, developed by Centrale Nantes and CNRS and available as a part of the FINE™/Marine computing suite, is used in the present thesis to solve the incompressible Unsteady Reynolds-Averaged Navier-Stokes (URANS) equations. It is based on the finite volume method to build the spatial discretization of the transport equations (see Section 2.2.1). The unstructured discretisation is face-based, which means that cells with an arbitrary number of arbitrarily shaped faces are accepted (producing thus an *unstructured mesh*), as illustrated in Figure 2.7. A second order backward difference scheme is used to discretise time. The solver can simulate both steady and unsteady flows. In the case of turbulent flows, transport equations for the variables in the turbulence model are added to the discretisation.

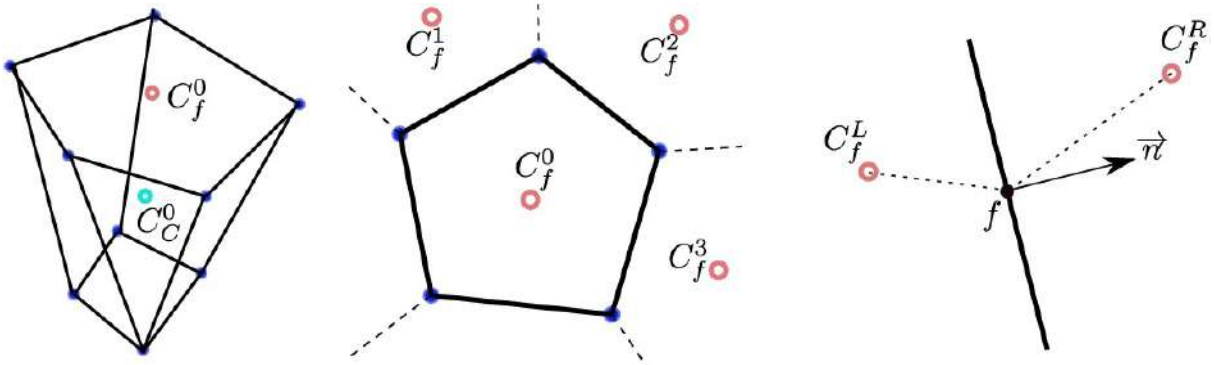

Figure 2.7 – Generic unstructured mesh. Left: Typical unstructured control volume. Middle: Cell C^0 and its neighbour cells. Right: Centred face reconstruction notations.

All flow variables are stored at the cells geometric centre. Volume and surface integrals are evaluated with second-order accurate approximations. The method is face-based, which means that the net fluxes in the cells are computed face by face. Numerical fluxes are reconstructed on the mesh faces by linear extrapolation of the integrand from the neighbouring cell centres. A centred scheme is used for the diffusion terms, whereas for the convective fluxes, a blended scheme with 80% central and 20% upwind is used. The velocity field is obtained from the momentum conservation equations and the pressure field is extracted from the mass equation constraint, or continuity equation, transformed into a pressure equation. The pressure equation is obtained by the Rhie and Chow interpolation [117]. The momentum and pressure equations are solved in a segregated manner as in the SIMPLE coupling procedure [67]. A detailed description of the discretisation is given in [114]. ISIS-CFD refinement routine Automatic Grid Refinement (AGR) allows for cell count reduction in the mesh by refining only where necessary based on the several user defined criteria (see [155, 154]).

2.3 Loads and Structure

2.3.1 Loads modelling

The following section will focus on the blade loads. Because of its manufacturing process and shape, a turbine blade can be approximated like a beam with varying stiffness properties [146]. For an OpenFAST aeroelastic simulation, the blade structural properties needed are the edgewise and flapwise local stiffnesses along the radius: EI_{xx} and EI_{yy}, as well as the linear mass M_L. E is the Young's modulus while I_{xx} and I_{yy} are respectively the in-plane and out-of-plane the sectional moment of inertia. Because of the small perturbation assumption, OpenFAST (using the ElastoDyn module) does not require torsional stiffness. Otherwise similar to the bending stiffness, the local torsional stiffness GI must be defined. The HAWC2[2] solver developed by DTU uses it for instance..
The following equations are the basis to any load calculation, they treat the blade as a cantilevered beam as presented in Figure 2.8 and detailed in [53]. In the next example an arbitrary blade coordinate system is defined as: x-axis the longitudinal direction, y-axis as the edgewise (in-plane deflection) direction and the z-axis as the out-of-plane direction. The blade is subdivided into elements labelled i and a distributed aerodynamic load $p_z(r)$ is represented in blue. The transversal loading $p_y(r)$ is not shown here.

2. https://https://www.hawc2.dk/ - website accessed on 16/09/2022

$$\frac{dT_z}{dx} = -p_z(x) + M_L(x)\ddot{u}_z(x) \qquad \frac{d\theta_y}{dx} = \kappa_y \tag{2.36}$$

$$\frac{dT_y}{dx} = -p_y(x) + M_L(x)\ddot{u}_z(x) \qquad \frac{d\theta_z}{dx} = \kappa_z \tag{2.37}$$

$$\frac{dM_z}{dx} = -T_y\ddot{u}_y(x) \qquad \frac{du_z}{dx} = -\theta_y \tag{2.38}$$

$$\frac{dM_y}{dx} = T_z \qquad \frac{du_y}{dx} = \theta_z \tag{2.39}$$

Where T_z and T_y are the shear force in the z-direction and y-direction of the blade coordinate system, M_z and M_y are the moment in the z-direction and y-direction of the blade coordinate system, p_z and p_y are the distributed load in the z-direction and y-direction of the blade coordinate system, $M_L(x)$ is the blade linear mass, $\ddot{u}_z$ and $\ddot{u}_y$ are the blade element acceleration in the z-direction and y-direction of the blade coordinate system.

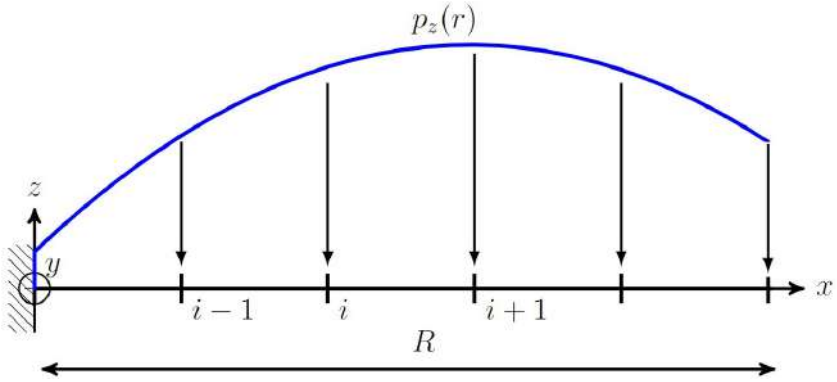

Figure 2.8 – Distributed normal load in the local blade coordinate system

Because the deformation relies on the aerodynamic loads and in turn the loads depends on the blade shape, the problem to solve is highly coupled. Solving and integrating over all blade elements the equations 2.36 to 2.39 allows the user to calculate the different local loads and blade deflection. Similar sets of equations can be derived for any component of the turbine. The presented set of equations define the loads and deformation assuming an equilibrium state, however because of the aeroelastic problem a dynamic structural model is needed. It will be briefly introduced in 2.3.2

2.3.2 Structure modelling

There exists many ways of tackling the coupling between load and structure in an aeroelastic simulations. The Finite Element Method approach, as presented in Section 2.3.1, divides the blade into a discrete number of linear beam elements. Each beam element has six degrees of freedom (DoF) (3 translations and 3 rotations) per end (node) and can be modelled as either 3D Euler-Bernoulli beam elements or Timoshenko beam elements. Thanks to this modelling, the non-linear effects of body motion are accounted

for provided a sufficient number of discrete elements are used along the beam. However, because of the large matrices involved in the problem, the computational resources needed are heavy. Another approach, used by OpenFAST (ElastoDyn), is the combined modal and multibody dynamics formulation.
The following section will give some details about the blade structural dynamic used as part of this thesis. A complete derivation of the complex equations is out of the scope of this thesis, instead the reader is advised to read the following references: [72, 75, 119, 104].
The problem is analogous to solving Newton's second law of motion: $\mathbf{F} = m\mathbf{a}$. The structural model considers the body (in this example, a blade) as a flexible cantilever beam with continuously distributed mass and stiffness. In theory, such bodies possess an infinite number of DoF, since an infinite number of coordinates are needed to specify the position of every point on the body. However, through the normal mode summation method it is possible to reduce the DoF to only a few relevant ones without much of information loss. In this case, the blade is described by 3 DoF, the first two flapwise modes and the first edge wise mode. Thanks to the Kane's structural dynamic model [77] the equation of motion can be re-written into:

$$F_m + F_m^* = 0 \tag{2.40}$$

$$F_m = \sum_{i=1}^{W_{rb}} {}^{E}\nu_m{}^{X_i}.\mathbf{F}^{X_i} + {}^{E}\omega_m{}^{N_i}.\mathbf{M}^{N_i} \tag{2.41}$$

$$F_m^* = \sum_{i=1}^{Wrb} {}^{E}\nu_m{}^{X_i}.(-m_i\ {}^{E}\mathbf{a}^{X_i}) + {}^{E}\omega_m{}^{N_i}.\mathbf{M}^{N_i}.(-{}^{E}\dot{\mathbf{H}}^{X_i}) \tag{2.42}$$

In these equations, W_{rb} is the number of rigid bodies considered, F_m are the generalised active forces and F_m^* are the generalised inertia forces. It is assumed that for each rigid body N_i, the active forces $\mathbf{F}^{X_i}$ and $\mathbf{M}^{N_i}$ are applied at the centre of mass point X_i. The acceleration of the centre of mass point X_i is given by ${}^{E}\mathbf{a}^{X_i}$, and the time derivative of the angular momentum of rigid body N_i about X_i in the inertial frame E is given by ${}^{E}\dot{\mathbf{H}}^{X_i}$. The quantities ${}^{E}\nu_m{}^{X_i}$ and ${}^{E}\omega_m{}^{N_i}$ represent the partial linear and partial angular velocities of the considered body, respectively.

Kane's equation can be written in matrix form so as to be solved by a numerical time integration scheme (see equation 2.44). ElastoDyn uses the Adams-Bashforth-Moulton 4^{th} order predictor–corrector method.

$$\mathbf{C(q},t)\ddot{\mathbf{q}} + \mathbf{f}(\dot{\mathbf{q}}, \mathbf{q}, t) = 0 \Rightarrow \mathbf{C(q},t)\ddot{\mathbf{q}} = -\mathbf{f}(\dot{\mathbf{q}}, \mathbf{q}, t) \tag{2.43}$$

$$\begin{bmatrix} C_{11} & C_{12} & \cdots & C_{1n} \\ C_{21} & C_{22} & \cdots & C_{2n} \\ \vdots & \vdots & \ddots & \vdots \\ C_{m1} & C_{m2} & \cdots & C_{mn} \end{bmatrix} \begin{Bmatrix} \ddot{q_1} \\ \ddot{q_2} \\ \cdots \\ \ddot{q_n} \end{Bmatrix} = \begin{Bmatrix} -f(\dot{q_1}, q1) \\ -f(\dot{q_2}, q2) \\ \cdots \\ -f(\dot{q_n}, qn) \end{Bmatrix} \tag{2.44}$$

Where $\mathbf{C}$ is the acceleration matrix and its components are the accelerations of each DoF variable, f is a forcing vector depending on a nonlinear combination of displacements (q), velocities ($\dot{q}$), and time (t). The equations of motion above represent the standard multibody dynamics form (with no constraints). The previously calculated modes play a role through the DoF definition for the flexible blades (and tower). The Figure 2.9 shows the different degrees of freedom associated to the wind turbine, for instance: q_1 refers to q_{B1E1}.

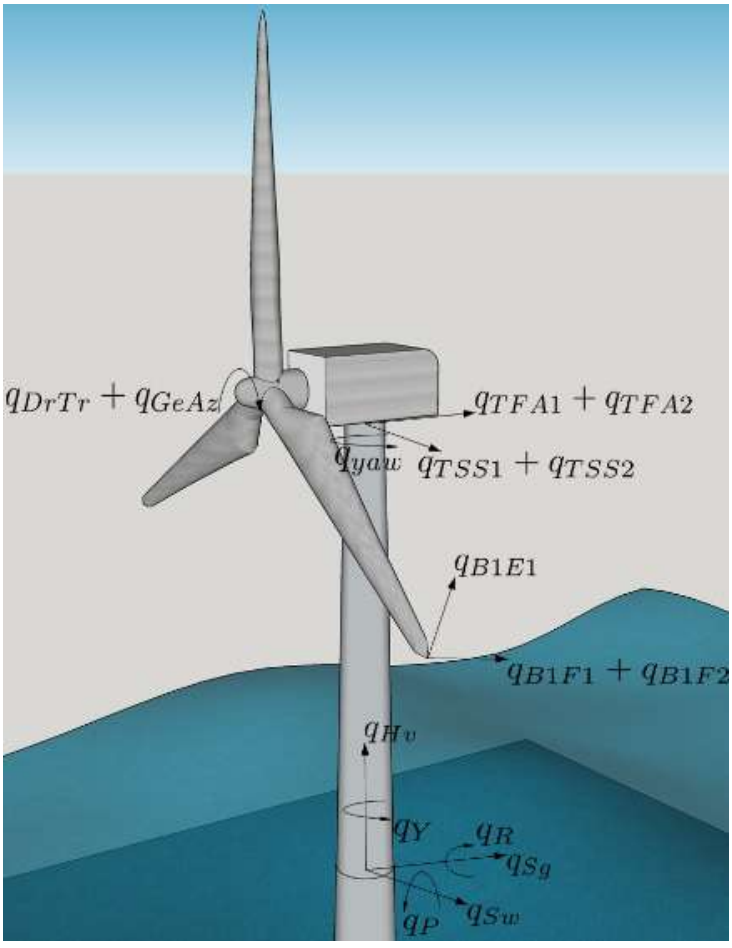

Figure 2.9 – Wind turbine degrees of freedom illustration from [119].

2.3.3 ElastoDyn

As briefly explained in Section 2.3.2, ElastoDyn is a nonlinear time-domain model, which solves equations of motion (see equation 2.43), it combines modal and multibody dynamics formulation. Through OpenFAST it uses the AeroDyn module outputs to calculate the turbine's acceleration, velocities, displacements and reaction loads. The necessary inputs to ElastoDyn are the turbine mechanical properties, the degrees of freedom allowed (turbine flexibility), the initial controller conditions (pitch and RPM).
A representative loading case is the root bending moment (RBM, see equation 2.45) as illustrated in Figure 2.10. The Figure 2.10 shows that aeroelastic simulations yield large variation for the calculated loads. The alternation of loads over a long period of time, typically 25 years, can give rise to fatigue problems. The following section will show the usual steps to follow in order to perform fatigue calculation.

$$RBM = \int_{R=root}^{R=tip} rF_X(r)dr \tag{2.45}$$

Where r is the considered radial section, F_X is the force normal to the rotor plane acting on the considered section.

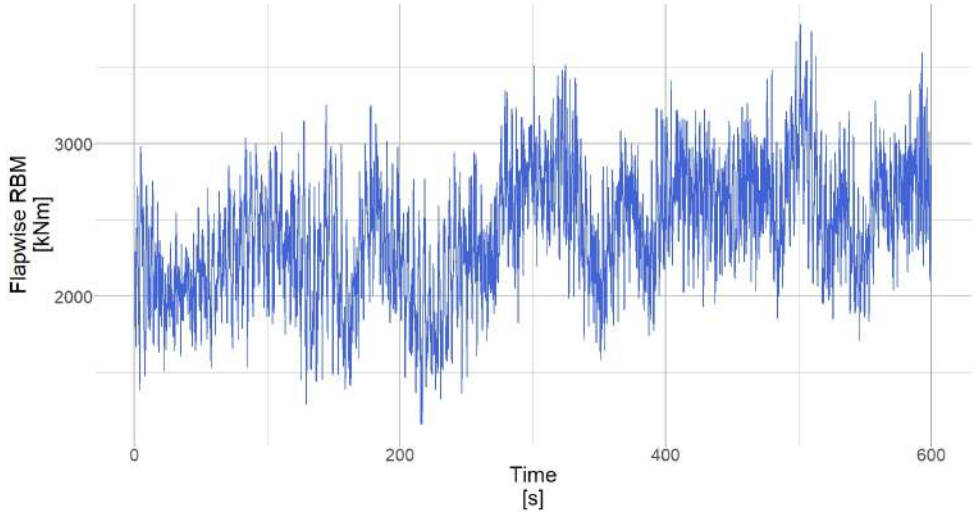

Figure 2.10 – Root Bending Moment simulated for 600s using OpenFAST for a fully flexible turbine at 8m/s.

2.4 Fatigue

The intent here is to give the basics to understand the concept behind fatigue simulations. The reader is advised to read the following references for an exhaustive review [34, 143, 57].

2.4.1 Lifetime calculation

Over the years fatigue in wind turbine became more and more important thanks to the better understanding of the physics involved. The number of publications has increased steadily over the years according to `sciencedirect` [3]. The larger turbines induce more expensive blades, tower and other components. Being able to predict the loads and the lifetime of the turbine more accurately helps defining business cases and reducing manufacturing costs. The Figure 2.11 illustrates the interest in fatigue applied to wind turbine problem. The year 2009 being a turning point where the number of publications related to fatigue in wind turbine increased drastically. Around this time, the scientific community had post-processed some of the novel unsteady experimental results both in the wind tunnel or in the field (see [51, 130, 133, 91]), enabling the improvement of existing aerodynamic models.

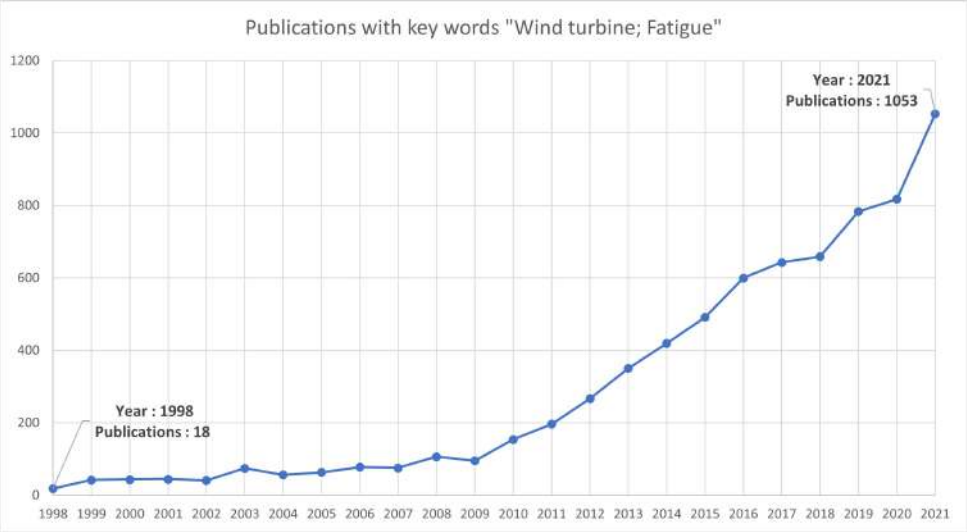

Figure 2.11 – Wind turbine fatigue related publications chart over the years.

The Miner's rule (or Palmgren-Miner rule) [103, 97] despite its simplicity is the accepted method to calculate the fatigue damage in wind turbine following the standard IEC 61400-1 Annex G (edition 3) (see equation 2.46).

$$D = \sum_{i=1}^{i=N} \frac{n_i}{N_i} \tag{2.46}$$

Where D is the life damage (when $D = 1$ the component fails), n_i is the cycle count and N_i is the number of cycles to failure.

To address the initial discrepancies, noted by several authors [127, 38, 125], when using the Miner's rule, several corrections were implemented such as the rain flow counting. Because wind turbine loads are seemingly random, defining patterns to apply the Miner's

3. https://www.sciencedirect.com/search?qs=fatigue%20wind%20turbine - website accessed on 25/01/2022

rule is difficult. Rainflow counting method was developed to identify alternating stress cycles and mean stresses for such applications. Once the rainflow counting has been applied, the data is converted into a zero mean time series and then the Miner's rule is applied. More details about the rainflow counting method can be found in the original paper from Downing and Socie [35]. Because the loading in a real case will occur over a range of fixed means rather than a single value, a correction model can be used: the Goodman correction (see equation 2.47).

$$L_i^{RF} = L_i^R \times \left(\frac{L^{ult} - |L^{MF}|}{L^{ult} - |L_i^M|} \right) \tag{2.47}$$

Where L_i^{RF} the i^{th} cycle's range about a load mean of L_i^M, L^{ult} is the material ultimate design load, L_i^R is the range about a load mean of L_i^M and L_i^{MF} is the fixed load-mean. The relationship between load range and cycles to failure yields the well known S-N curve. The curve links the load range (S) with the number of cycles (N) and the material property via the Wöhler exponent (m). A generic S-N curve is displayed in Figure 2.12.

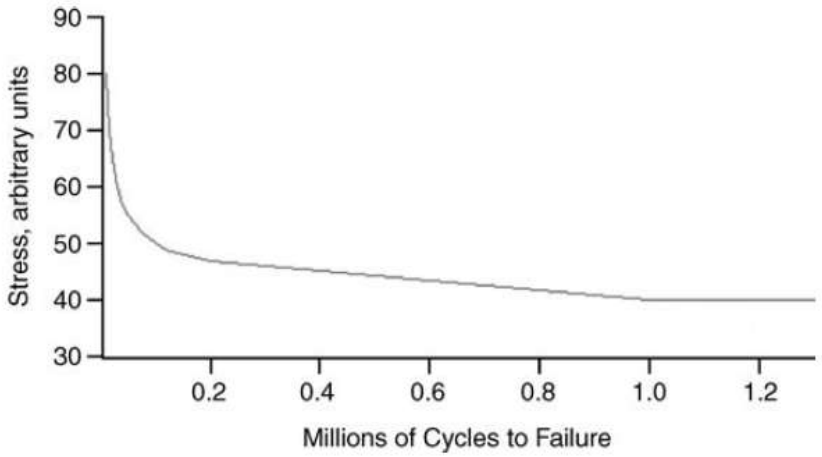

Figure 2.12 – Generic S-N curve from [93].

Based on equations 2.46 and 2.47 the damage perceived for a single wind speed is known. To account for all wind speeds and calculate the total damage perceived by the turbine during operation mode the sum of all wind speed weighted by the Weibull distribution is applied. Similarly, other operation modes such as idling or parking, need to be accounted for in the damage life calculation. Also, because the number of cycles is high ($N >> 10^6$), converting the cycles to failure to *time* to failure will facilitate the interpretation of fatigue calculations. It can easily be done since a component fails when $D = 1$, so using the ratio between the accumulated damage and the design life time T_{life} one can deduce the estimated time to failure using equation 2.48.

$$T^{fail} = \frac{T_{life}}{D} \tag{2.48}$$

Where T^{fail} is the time to failure and T^{life} is the design life time.

2.4.2 Mlife

Mlife is a tool developed by NREL (see [56]) allowing the user to calculate fatigue lifetime based on numerical simulations or from test benches. Mlife follows the requirements of the standard IEC 61400-1 Annex G (edition 3). If several wind speeds are used (for turbine lifetime calculation for instance), Mlife will require that all time series have the same sampling rate, as it is used in the time to failure conversion. This limitation was accounted for in Chapter 7.

2.5 Summary

Throughout the years the atmospheric boundary layer unsteadiness is better understood and engineering models are available for industrial and research applications. However, the aerodynamic unsteadiness is not yet accounted for into the low fidelity models such as BEM. On the other hand, CFD thanks to the turbulence modelling, can simulate several unsteadiness length scales at a high computational cost. The aim of the thesis is to help bridge the gap using the strengths of both numerical methods and then assess the spoiler impact on the turbine lifetime and AEP.

Chapter 3

Databases

Contents

The DANAERO project is one of the few, full-scale field test campaign ever been performed. It spanned over three months, between July and September 2009 including many different operating conditions (wind direction and intensity, misalignment, wake effects from neighbouring turbines)[91, 148]. Alongside with these field tests, wind tunnel tests of blade sections (aerofoils) were performed. Also, 2D and 3D CFD simulations of the identical aerofoils and rotor were performed. This important database was available through the IEA group Task 29 Phase IV led by G. Schepers since 2010 and used in many studies [91, 148, 8, 7, 88, 41, 40, 89, 42, 14, 13, 102, 90]. The focus of IEA Task 29 Phase IV Work Package 3 was the validation, improvement and understanding of aerodynamic models as implemented in wind turbine design codes by analysing detailed aerodynamic measurements from the DANAERO experiment. Different phenomena were targeted: the impact of the turbulent inflow, the yawed conditions, the wake inflow, 2D/3D aerofoil characteristics, aeroelastic effects, the transition and acoustics. For the complete report about the DANAERO project see [123]. The Section 3.1 and Section 3.2 will describe the available DANAERO database.
The industrial partner of this thesis, ENGIE Green, has 3D scanned the outer shell of a blade equipped with root spoiler. The available data will be detailed in the Section 3.3.

3.1 DANAERO turbine data

3.1.1 Experimental data

Field tests of the DANAERO project took place in the Tjaereborg wind farm located in Western Denmark (see Figure 3.1).

Figure 3.1 – Tjaereborg wind farm, the instrumented wind turbine is shown along with the other wind turbines. The met mast is also shown south-west to the instrumented turbine [148]. The wind turbines are circled in blue and the met mast in green.

The turbine instrumented within the wind farm is a NM80 2MW (80m rotor diameter). The blade tip height ranges between 17m and 96m. One of the LM38.8 blades (38.8m long blade with a hub radius 1.24m) of the reference turbine is equipped with 256 pressure taps at different radial stations starting from the blade root as summarised in Table 3.1. It allows in particular the normal and tangential forces computation at each radial position. The pressure outputs were acquired simultaneously with the reference turbine operating information, including the electrical power production, the blade azimuthal position, the rotor speed and the blade pitch. A meteorological mast was also installed South West (main wind direction) of the reference turbine to record the rotor inflow. For that purpose, met mast sensors (see Table 3.2) acquired atmospheric data simultaneously with the reference turbine operating information and blade instruments. The met mast anemometers were installed at several heights to capture the wind speed across the rotor. Finally, the wind farm altitude is at sea level and does not vary significantly throughout the wind farm.

Table 3.1 – Pressure sensors installed on one of the LM38.8 blade of the reference turbine and used in the present study from [148].

Sensor type	**Physical quantity extracted**	$^{r}/_{R}$**(from the blade root)** [-]	**Sampling rate** [**Hz**]
Pressure taps	Surface pressure (Normal and tangential forces from pressure integration)	0.34, 0.49, 0.77, 0.95	35
Accelerometers	Acceleration in all three axes	0.34, 0.49, 0.77, 0.95	35

Table 3.2 – List of instruments installed on the Tjaereborg wind farm met mast with the signal acquired at 35Hz and synchronised with the other measurements from [148]. H is the distance from the ground.

Sensor type	**Physical quantities extracted**	**H** [**m**]
Cup anemometers	Wind speed	17.0, 28.5, 41.0, 57.0,19.0, 77.0, 93.0
Sonic anemometers	Velocity, wind direction	17.0, 57.0, 93.0
Wind vanes	Wind direction	17.0, 57.0, 93.0
Thermometer	Temperature	5.7, 57.0, 93.0
Barometer	Pressure	5.7

3.1.2 Numerical data

Several simulation rounds involving different operating conditions and many contestants were carried out over the years of the project, e.g.:

- Axial flow
- Sheared flow
- Yawed flow
- Turbulent flow

Also, a variety of codes have been blind tested against the field database presented in Section 3.1.1: engineering codes (BEM and lifting line) and CFD. Some of the cases also included a fully flexible turbine. The Table 3.3 shows the axial simulation cases.

Table 3.3 – DANAERO axial flow comparison cases

Case	**Model**	**Inflow** [**m/s**]	**Pitch angle** [°]	**Rotational speed** [**RPM**]
IV.1.1	Rigid	6.1	0.15	12.3
IV.1.2	Flexible	6.1	0.15	12.3

All those trials gave rise to a large numerical database where many metrics such as the local forces, pressure distribution and integrated load are available.

3.2 DANAERO aerofoil data

3.2.1 Experimental data

As part of the DANAERO project, wind tunnel experiments at high Reynolds number were performed. Several aerofoils in several wind tunnels were assessed [10, 8] and summarised in Table 3.4.

Table 3.4 – DANAERO wind tunnel tests.

Wind tunnel	Aerofoils tested	Test configurations
LM	DU96-W-180, NACA63-418, Risø-B1-18, **Section03, Section05, Section08, Section10**	clean, tripped, $1.5 \times 10^6 < Re_c < 6.0 \times 10^6$
Velux	DU96-W-180, NACA63-418, Risø-B1-18	clean, tripped, $1.5 \times 10^6 < Re_c < 3.0 \times 10^6$
Delft	NACA63-418, Risø-B1-18	tripped, $Re_c = 1.5 \times 10^6$

The aerofoils forming the LM38 are in bold in Table 3.4, detailed in Table 3.5 and illustrated in Figure 3.2. The Section03 illustrates a typical thick profile tested in wind tunnel. Above the relative thickness of 36% the blockage due to the aerofoil thickness is too important for aerodynamic wind tunnels leading to possibly misleading results. Upscaling to atmospheric wind tunnel will yield a turbulence intensity too large and therefore not comparable with smaller wind tunnel. For this reason, experimental data for thick aerofoils are rare and should be treated with care.

Section ID	Aerofoil thickness [%]
Section03	33
Section05	24
Section08	19.6
Section10	18.6

Table 3.5 – DANAERO aerofoils tested in the LM wind tunnel

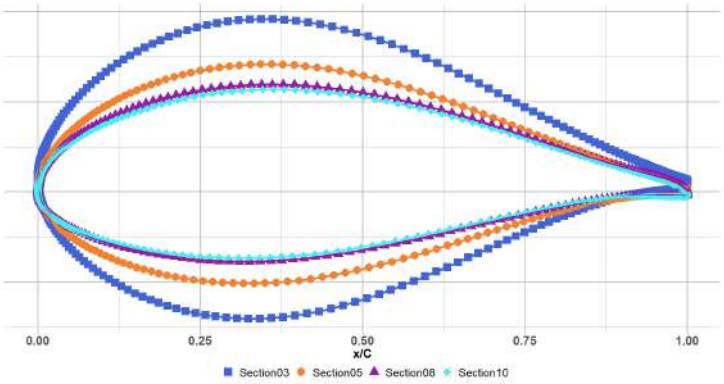

Figure 3.2 – DANAERO aerofoils used for validation: the blue square (■) shows the Section03, the orange dot (●) shows the Section05, the purple triangle (▲) shows the Section08 and the cyan diamond (◆) shows the Section10.

3.2.2 Numerical data

All the presented aerofoils in Section 3.2.1 were also simulated using a variety of 2D CFD tools forming a large polar database used by BEM code users. The Figure 3.3 shows that 2D simulations using EllipSys [138] is matching well the wind tunnel experiment. More details about the wind tunnel experiments can be found in [150, 7, 8]

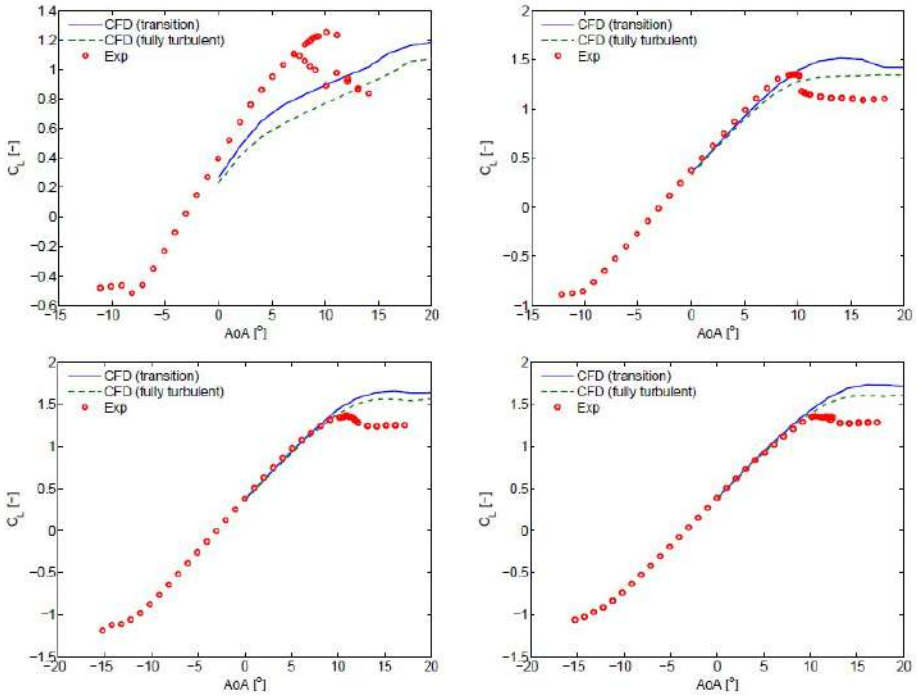

Figure 3.3 – DANAERO numerical comparison with wind tunnel data for Reynolds number of $Re_c = 5 \times 10^6$ [150]. Top left: Section03, top right: Section05, bottom left: Section08, bottom right: Section10.

3.3 ENGIE Green blade data

The wind turbine geometry used in the present thesis was acquired during a scanning campaign organised by Maïa Eolis (former ENGIE Green) as part of a master thesis project [28]. Because the scan is not recent (2010), the technology was not at today's accuracy level, resulting in some gaps in the geometry (Figure 3.4). The Figure 3.4 shows the scanned section in its original coordinate system. Several steps are taken to ensure that the smoothing of the cloud point does not distort the geometry and four different high order Bezier splines are used to fit through the cloud of point.

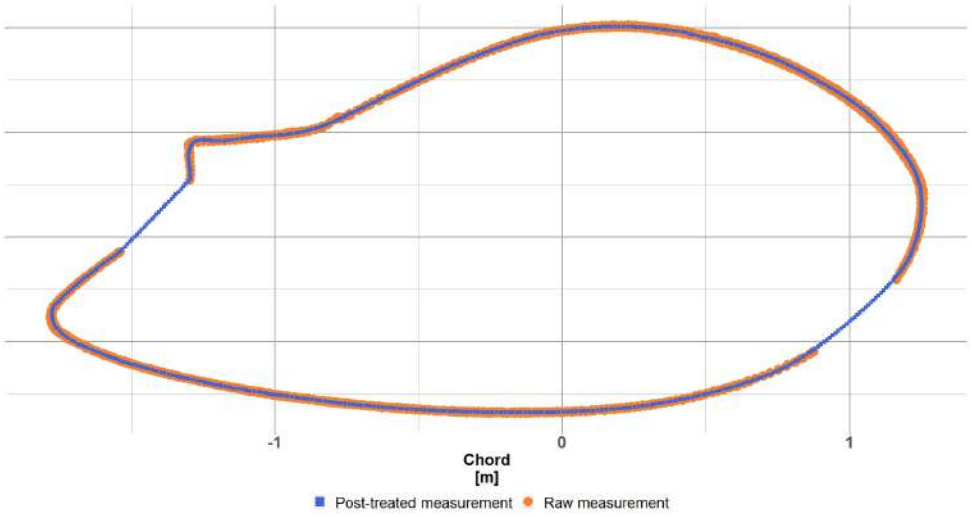

Figure 3.4 – Radius $r/R = 0.13$ for the scanned ENGIE Green blade: the blue square (■) shows the rebuilt section, the orange dot (●) shows the raw measurement data.

Thanks to the scan post-process, the blade geometry was extracted as presented in Figure 3.5. The turbine radius is 45m long and is equipped with a root spoiler from the radial position $r/R = 0.07$ until $r/R = 0.17$.

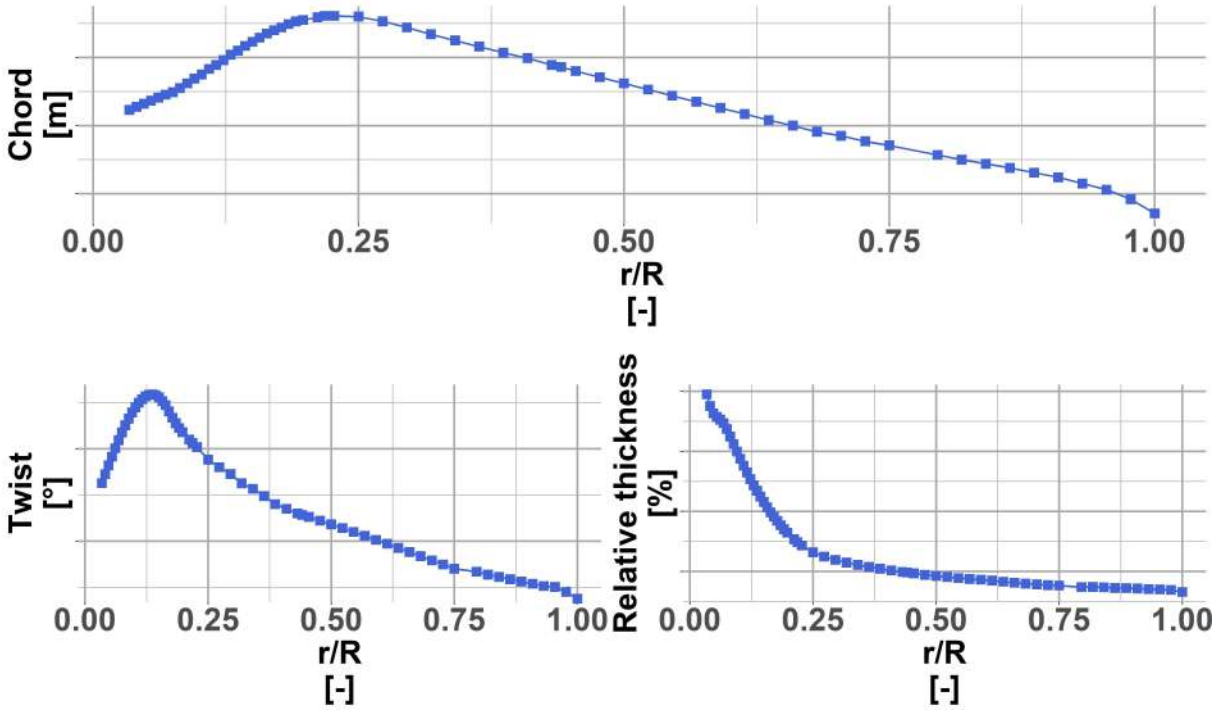

Figure 3.5 – The scanned blade geometry: chord, twist and relative thickness distribution against the normalised radius.

Unfortunately, the last 2m of of the blade were not properly scanned due to the blade vibrations happening during the scan. Consequently, the last two meters have been extrapolated both for the BEM and 3F CFD solver as illustrated in Figure 3.6. The extrapolated

geometry may not represent the original design intent, but it allows to produce a closed blade with the right length.

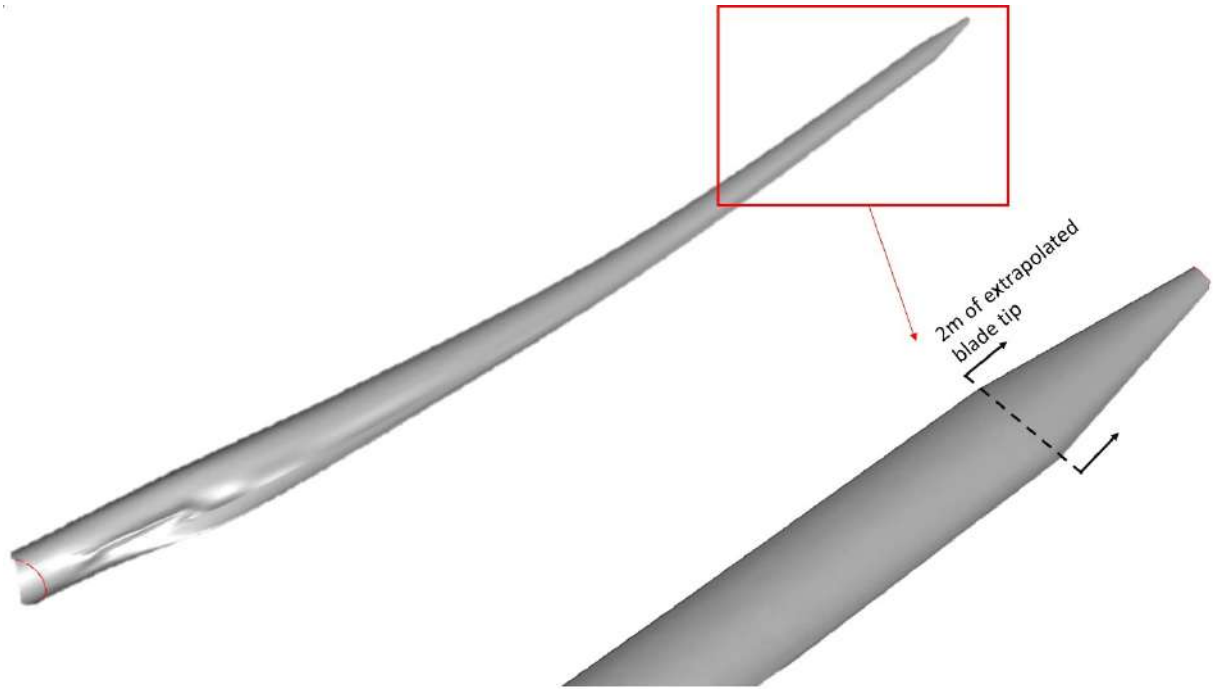

Figure 3.6 – The extrapolated scanned blade geometry reconstructed using CAD software for 3D CFD simulations.

3.4 Summary

The large database available during this thesis was used to verify several tools, namely the developed UiBEM solver as well as the commercially available ISIS-CFD. ISIS-CFD has already been verified for naval and automotive applications but never for wind turbine. The verification activities will be explained in the following chapter.

Chapter 4

Simulation validation against databases and post-processing methodology

Contents

The following sections will detail the tools validation against the DANAERO database (see Chapter 3). First the developed inverse BEM tool used to analyse the field measurements is verified against CFD simulations, then ISIS-CFD will be validated both in 2D and 3D against aerofoil sections and rotor case.

4.1 UiBEM

4.1.1 Induction models

The UiBEM method developed during the thesis compares several existing formulations to model the induction (axial and tangential): the BEM method as documented by Hansen [53] and the one from Madsen [90]. After comparing both methods, it was decided to merge both implementations to create a third modelling. Thereafter the results will be named as follow and detailed below:

- Hansen
- Madsen
- Hybrid

Hansen modelling

In the reference book from Hansen [53], the axial induction and tangential induction are derived following the BEM theory associated to the highly loaded rotor correction.

$$\begin{cases} a > a_{crit} & a = \frac{1}{2}[2 + K(1 - 2a_{crit}) - \sqrt{(K(1 - 2a_{crit}) + 2)^2 + 4(K \times a_{crit}^2 - 1)}] \\ a < a_{crit} & a = \frac{1}{\frac{4F\sin(\varphi)^2}{\sigma_n} + 1} \end{cases} \tag{4.1}$$

Where the constant K and local solidity σ are calculated as follow:

$$K = \frac{4F\sin^2(\varphi)}{\sigma C_n} \tag{4.2}$$

$$\sigma = \frac{c(r)B}{2\pi r} \tag{4.3}$$

$$a' = \frac{1}{\frac{4F\sin(\varphi)\cos(\varphi)}{\sigma C_t} - 1} \tag{4.4}$$

Here, a and a' are the local axial and tangential induction, a_{crit} is the critical axial induction value (typically $a_{crit} = 0.2$), F is the Prandtl's tip loss factor, C_n and C_t are the force coefficients normal and tangential to the rotor plane, φ is the inflow angle and r the considered radius.

Madsen modelling

In Madsen et al. [90] the authors defined an alternative approach to the axial induction modelling for highly loaded rotors. Rather than using the conditional approach as in equation 4.1, they have fitted a polynomial curve following the curve shape for low induction values and the highly loaded correction (see Figure 4.1). The fitted polynomial equation for axial induction is:

$$a = k_3 C_T^3 + k_2 C_T^2 + k_1 C_T \tag{4.5}$$

Where k_1, k_2, k_3 are polynomial coefficients. The tangential induction is derived with respect to the axial induction through:

$$a' = \frac{B V_{rel}^2 C_n(\alpha) c}{8\pi r^2 (1-a)\omega V_0} \tag{4.6}$$

Where V_{rel} is the relative velocity, C_T is the rotor thrust coefficient, ω is the rotor speed and V_0 the inflow.

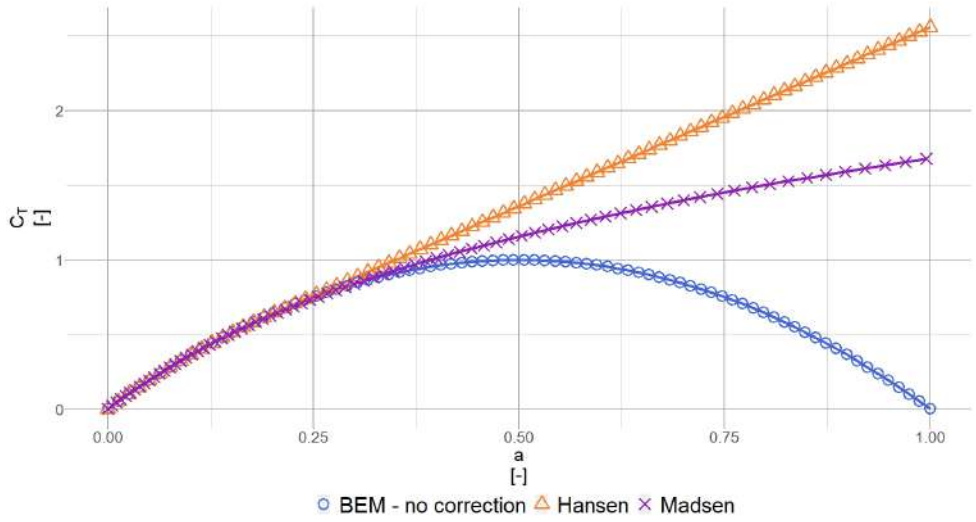

Figure 4.1 – Different induction modellings assuming the Prandtl's tip correction factor $F = 1$ and the critical induction factor $a_{crit} = 0.2$. The blue circles (○) represent the evolution of the induction following the BEM equation: $C_T = 4a(1-a)$, the orange triangles (△) are the Hansen induction modelling (Spera equation) presented in equation 4.1 and the purple crosses (×) represent Madsen's polynomial curve fitting from equation 4.5.

Hybrid modelling

The Hybrid model combines the axial induction model derived by Madsen et al[90] (see equation 4.5) and the tangential induction described by Hansen (equation 4.4). The tangential induction is therefore described independently from the axial induction. It is possible to merge those two modellings because both are build on independent formulations.

4.1.2 iBEM verification

To verify the iBEM solver, benchmark cases in the form of CFD outputs of a wind turbine immersed in a constant and uniform flow for several wind speeds are used. The CFD cases were performed in RANS (Reynolds Averaged Navier-Stokes) with a Shear Stress Tensor (SST) $k-\omega$ turbulence model. The IEA Tasks 29 members extracted aerodynamic results using the AAT (Average Azimuthal Technique) as described in Section 4.3.3. The results are presented in Table 4.1. The blade is rigid, the inflow is uniform and constant (without shear or yaw), and the rotor operating conditions are constants (RPM, pitch). The numerical environment is therefore controlled and within the limits of the BEM theory. The local velocity (V_{rel}), lift force (F_L) and drag force (F_D) are calculated thanks to the other given inputs using the equation 2.15 and equation 2.28 seen in Figure 2.5. The axial induction modelling differences from BEM solvers (visible in Figure 4.1) and CFD computations can then be evaluated similar to the work of Rahimi et al.[115].

Table 4.1 – DANAERO CFD results used as benchmark.

Inputs	**Symbol**	**Value**	**Units**
Wind speed	V_w	3, 6.1, 10, 20	$[m/s]$
Rotor rotational speed	ω	12.3	$[RPM]$
Air density	ρ	1.231	$[kg/m^3]$
Pitch	β	-0.15	$[^\circ]$
Radius	r	Radial distribution	$[m]$
Chord	c	Radial distribution	$[m]$
Twist	θ	Radial distribution	$[^\circ]$
Normal Force	F_n	Radial distribution	$[N/m]$
Tangential Force	F_t	Radial distribution	$[N/m]$
Normal Force coefficient	C_n	Radial distribution	$[-]$
Tangential Force coefficient	C_t	Radial distribution	$[-]$
Lift coefficient	C_L	Radial distribution	$[-]$
Drag coefficient	C_D	Radial distribution	$[-]$
Angle of attack	α	Radial distribution	$[^\circ]$
Axial induction	a	Radial distribution	$[-]$
Tangential induction	a'	Radial distribution	$[-]$

Verification results

The iBEM model verification is first analysed by comparing the outcome between the iBEM model output and the steady CFD computations at section $r/R = 0.49$, for $V_0 = 6.1$m/s. The forces (F_L and F_D), the aerodynamic coefficients (C_L, C_D), the relative velocity (V_{rel}), the axial induction (a), the tangential induction (a') and the angle of attack (α) are analysed and plotted.
Figure 4.2 shows that the lift and drag force calculations are well predicted for all three induction modellings (i.e. Hansen, Madsen and Hybrid). The aerodynamic coefficients (C_L, C_D), the relative velocity (V_{rel}) are within $\pm 0.1\%$ of the reference, depending on the

induction model. The Hansen model seems to slightly underpredict the relative velocity leading to a marginally higher lift coefficient. However, the axial induction (a), tangential induction (a') and the angle of attack (α) results show large differences between the models. Madsen and Hybrid results show an axial induction error less than 1%, while Hansen model is closer to 10% error. The tangential induction results are similar (6% error across all models) despite the slightly better prediction from Hansen. Finally, the angle of attack prediction shows 10% error when using Hansen model and less than 1% when using either Madsen or Hybrid.

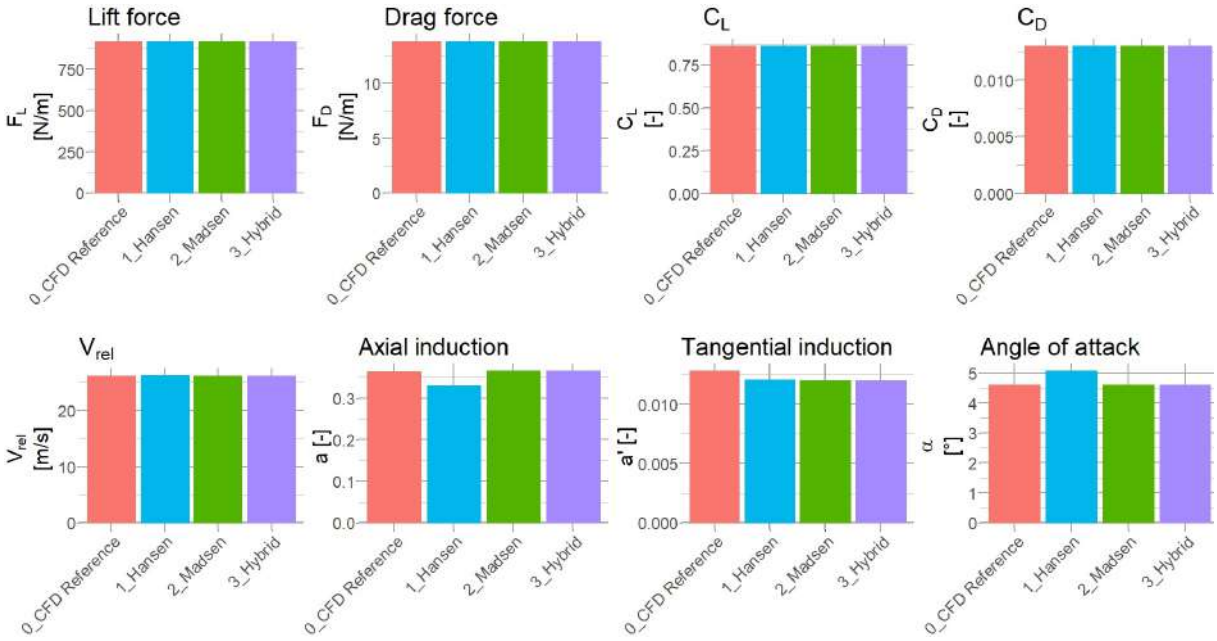

Figure 4.2 – UiBEM Verification for different induction models at 6.1m/s for $r/R = 49\%$.

Along the blade span, results from the Madsen modelling and Hybrid modelling are overlapping each other (see Figure 4.3a left) and close to the reference case (within 1%). The worse results for the Hansen model highlighted in Figure 4.2 are confirmed for the entire blade span. The axial induction starts to deviate from the other models as early as $r/R = 0.35$. It is to be noted that all models fail to capture the axial induction behaviour calculated by CFD between $r/R = 0.7$ and $r/R = 0.9$ (see Figure 4.3a left), similarly found in Rahimi et al [115].

The tangential induction modellings show differences with the CFD reference up to $r/R = 0.45$, after this radial position the agreement is better. The independence of the tangential modelling used in Hansen and Hybrid is captured and is beneficial towards the tip of the blade (see Figure 4.3a right). Madsen modelling for tangential induction is underpredicting compared to the CFD reference from $r/R = 0.82$ until the tip of the blade (see Figure 4.3a right). The calculated aerodynamic coefficients, presented in Figure 4.3b show very good agreement between the CFD and all BEM models, albeit the Hansen results are slightly underpredicted.

By combining the tangential induction model from Hansen and the more accurate axial induction from Madsen, the Hybrid model yields results marginally better than the other

two models. The C_L and C_D calculated by the Hybrid and Madsen modelling yield almost identical results. The verification is repeated for all wind speeds listed in Table 4.1 (see Figure C.1 to Figure C.3). Following the presented results and the previous outcomes from Rahimi et al.[115], the iBEM method is considered verified. For the rest of the analysis the Hybrid model will be used.

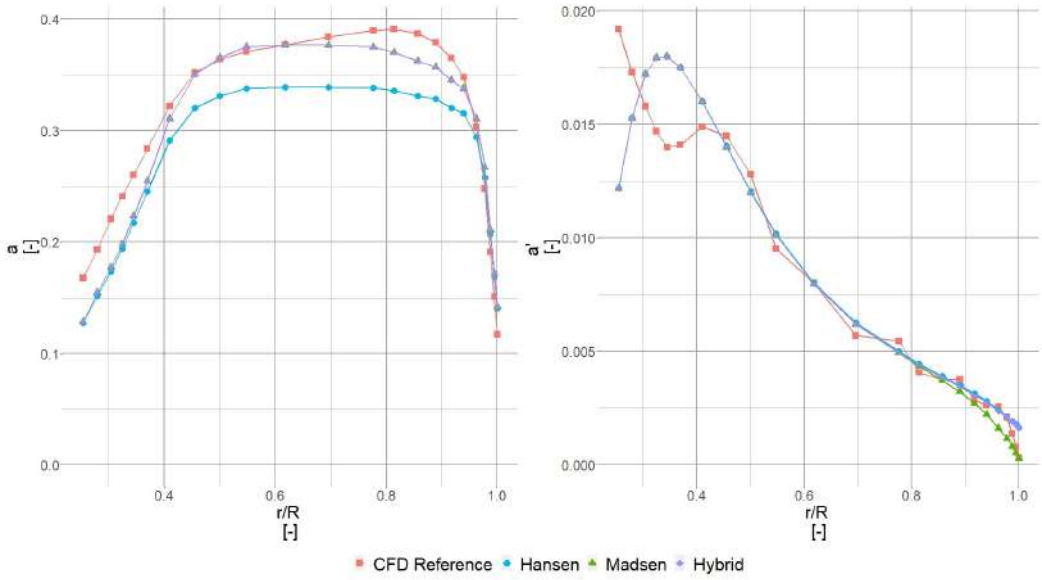

(a) UiBEM Verification: a and a'

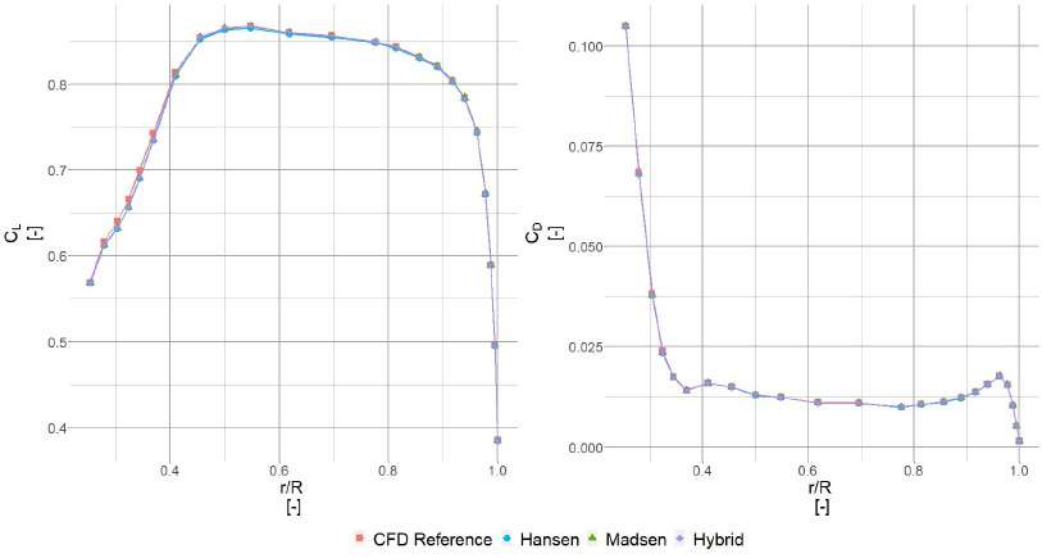

(b) UiBEM Verification: C_L and C_D

Figure 4.3 – Full blade comparison between the reference data and the different axial induction modellings at 6.1m/s. The red square (■) represents the reference data, the blue circle (●) the Hansen modelling, the green triangle (▲) the Madsen modelling and the purple diamond (♦) the Hybrid modelling.

4.2 ISIS-CFD 2D

4.2.1 Domain size verification

In order to verify ISIS-CFD in the context of wind turbine aerodynamics, a Design of Experiment (DoE) approach will be employed to help define the CFD domain boundaries. ISIS-CFD has already been extensively validated in 2D and 3D marine hydrodynamics applications [32, 31, 50, 49]. However, it has not been used for 2D aerofoil aerodynamics. By applying a DoE approach, a robust test matrix is built, it will provide the means to study the effects and interactions between the selected factors. To verify ISIS-CFD, a goal of 2% difference with the wind tunnel results for the C_L in the linear region is set. This threshold has been chosen following a previous codes comparison where seven CFD software were benchmarked against each other [139]. Four of the the codes tested were within a 2% accuracy margin. Several sections tested in the wind tunnel and numerically as part of the DANAERO project (see Section 3.2.1 and Section 3.2.2) will serve as benchmark.

Six Sigma - Design of Experiments

The Six Sigma purpose is to understand the relationship between factors and their possible interactions in order to reduce variation in the outcome. The Design of Experiments (DoE) is a standardised way of ordering possible combinations of several factors (parameters) and levels (values they can take) to compare the outcome with a validation criteria. The validation criteria will be the calculated lift coefficient (C_L). Extrapolating on the DoE results will allow to decide on the appropriate calculation domain size.
Several factors related to the flow model and turbulence model were already fixed and will not be taken into account here. However, the domain boundaries for an infinite simulation remain unknown and the test matrix will help us decide which domain size is the most appropriate. The term "infinite simulation" here, means free from any interaction with external boundaries, e.g. the wind tunnel walls are not simulated, therefore the aerofoil is considered at rest in a moving fluid.
The aerofoil leading edge is positioned at the domain origin (0,0) with the trailing edge pointing towards the Outlet. Consequently the Inlet is positioned in front of the leading edge and the Outlet behind the trailing edge while the aerofoil chord is parallel to the Top/Bottom boundaries. The vertical dimension is symmetrical around the aerofoil chord. Since all the tested DANAERO aerofoils are relatively thin, it is assumed that using the outcome of the DoE will be valid for all sections. The section ran through the DoE is the Section05 whose relative thickness is 24%.

The factors chosen in this experiment are the Inlet position, the Outlet position (both together defining the domain length) and the Top/Bottom position (constituting the domain vertical dimension). All factors are expressed in aerofoil chord length, defined between 0 and 1. By using three factors with two levels each, the total number of possible combinations is $2^3 = 8$. The total number of cases possible are proportional to the power of the number of levels, i.e. if three levels are utilised for the same three factors, the DoE will yield more detailed results but the numbers of cases will increase drastically ($3^3 = 27$). To avoid running many unnecessary test cases, a centre point will be added to the 8 cases. It will assess the non-linearity in the results for a lower cost. The Table 4.2, shows how the parameters must be set to run the DoE. The values 1 and -1 represent the low (Level 1) and high (Level 2) levels for each parameters while the 0 represents the centre point case between the chosen levels (see Table 4.3). In order to asses the independence of the domain with the angle of attack, a DoE for three angles of attack ($\alpha_1 = 0°$, $\alpha_2 = 7°$, $\alpha_3 = 12°$) will be calculated. The test matrix will be run once for each angle of attack. For conciseness, only the results for $\alpha = 0°$ will be presented.

Table 4.2 – Design of Experiments test matrix

Test ID	**Inlet position**	**Outlet position**	**Top/Bottom position**
1	-1	-1	-1
2	1	-1	-1
3	-1	1	-1
4	1	1	-1
5	-1	-1	1
6	1	-1	1
7	-1	1	1
8	1	1	1
9	0	0	0

Table 4.3 – Factors levels

Factor	**Level 1**	**Level 2**	**Centre point**
Inlet position	-20	-40	-30
Outlet position	20	40	30
Top/bottom position	-20/20	-40/40	-30/30

DoE results analysis

The Figure 4.4 shows the main effects for each factor. The x-axis shows the different levels, centre point included (∗) for each parameter, while the y-axis shows the averaged C_L response. The dotted line is the average C_L for all 9 cases. Each data point on any subplot is calculated by taking the average C_L corresponding to this factor level. For instance, the data point when the Outlet is at Level 2 is calculated by averaging all the C_L values for the test ID: 3, 4, 7 and 8.
The Figure 4.4 is read as follow: for the first subplot, the further from the origin the inlet position is the more the average C_L tends to increase. For the second subplot the line is almost flat, which means that the position of the Outlet doesn't influence the average C_L. Lastly, the third subplot shows that the vertical dimension tends to reduce slightly the C_L with increasing size. The maximum effect from a factor upon the C_L is seen for the Inlet position: $\Delta C_L = 0.360 - 0.338 = 0.021$, which is equivalent to a variation of 6%. Analysing those plots alone is not enough, since we are averaging the test cases based on the factor, it may be possible that interactions between factors play a more significant role than a factor alone. Moreover, the centre point (∗) is far from the linear model, which indicates that some non-linearity exists. Again the analysis of interaction between factors will help us define the non-linearity.

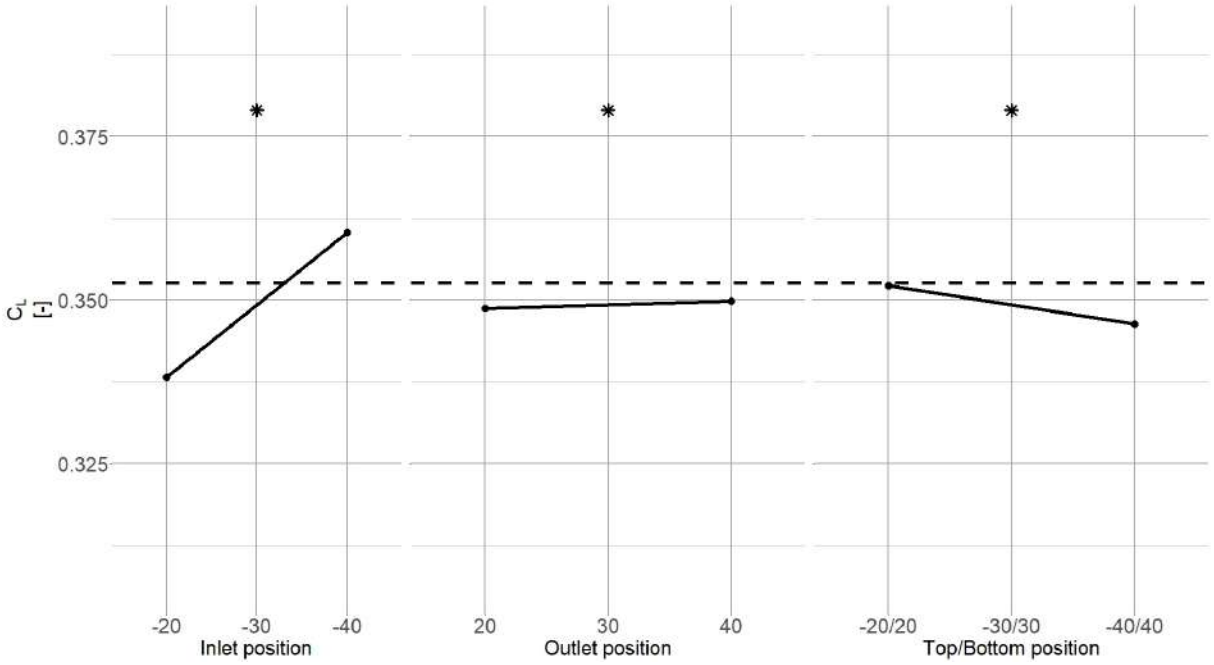

Figure 4.4 – Main effects plot for all factors for $\alpha = 0°$. The dashed line represents the average C_L across the test matrix. The black star (∗) represents the centre point case.

The Figure 4.5 shows the interactions between factors. The x-axis shows the different levels (centre point included) for each parameter. The y-axis shows the averaged C_L response for this factor when only a single other factor is considered.

Looking at the first subplot, the interaction between the Inlet (marker shapes ● and ▲) and Outlet position (line types and colours) is assessed. The lines are intersecting, it indicates a strong interaction between the two factors, as it should be expected since they both define the domain length where the wake is calculated. However, the two lines for the second subplot are parallel, meaning there is no interaction between the Inlet position and the Top/Bottom position. The third subplot shows also an intersection but not at the centre, closer to the Level 1 results; indicating that there is also an interaction between the Outlet position and the Top/Bottom position. Analysing those plots is not trivial: while looking more carefully at the results it is found that the interaction between factors and the non-linearity seen in the main effect is explained by the non-symmetrical chordwise dimension of the domain. Indeed, the test cases 2, 3, 6 and 7 are responsible for the behaviour seen in Figure 4.5. This is an important conclusion: the unstructured mesh from ISIS-CFD can behave unexpectedly if the domain is not symmetric. In particular, the automatic refinement process may not refine properly small surfaces e.g.: trailing edge. The first cell would be skewed and too small for a proper viscous cells insertion. Moreover, in the first subplot, the centre point and Outlet position Level 2 are presenting similar C_L values. It indicates that the non linearity is more important for lower values. Therefore, acknowledging this new information and analysing the rest of the plots, the domain dimensions for an aerofoil with chord $c = 1$ are:

- Inlet position: -40
- Outlet position: 40
- Top/bottom position: -40/40

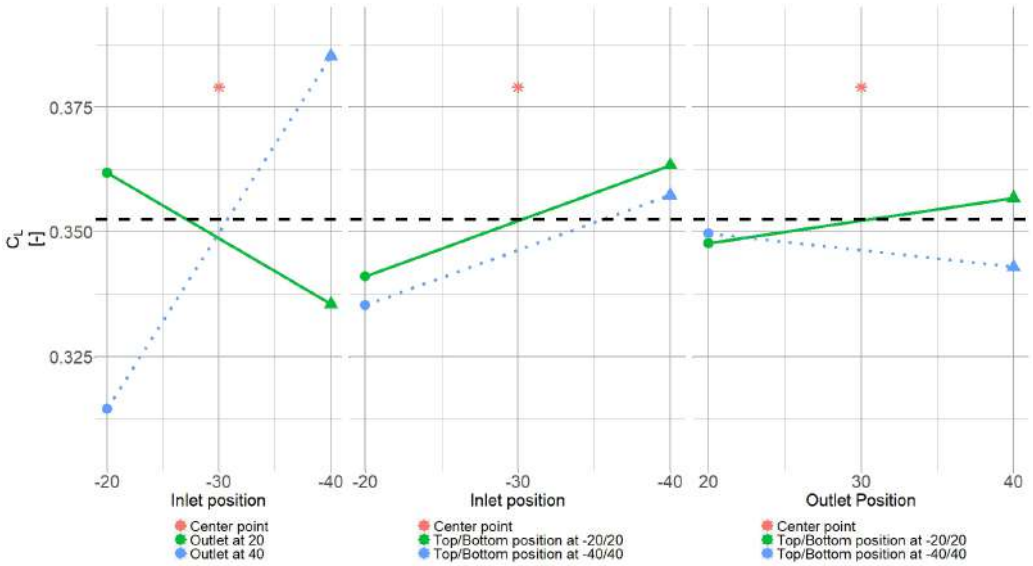

Figure 4.5 – Interaction diagram for $\alpha = 0°$. The dashed line represents the average C_L across the test matrix. The red star (*) represents the centre point case. The green dot (●) represent the considered factor at Level 1. The blue triangle (▲) represents the analysed factor at Level 2. The solid and dotted line represent the Level 1 and Level 2 of the other factor analysed.

Finally the polar for the selected sections were all calculated and compared against wind tunnel and numerical data [150] for a Reynolds number of $Re_c = 5 \times 10^6$. The results are illustrated in the following figures (Figure 4.6 to Figure 4.9) and summarised in the Table 4.4. For all analysed sections, the numerical results follow the lift coefficient perfectly in the linear region. Approaching stall (near the maximum C_L), both numerical methods deviate from the measurement. Also both CFD methods tend to slightly overpredict the drag coefficient in the linear region and underpredict it after the stall point. The thickest section (Section03), is the most challenging one. ISIS-CFD manages to capture the trend correctly between -8° and 8° but the absolute values are underestimated for the lift and overpredicted for the drag.

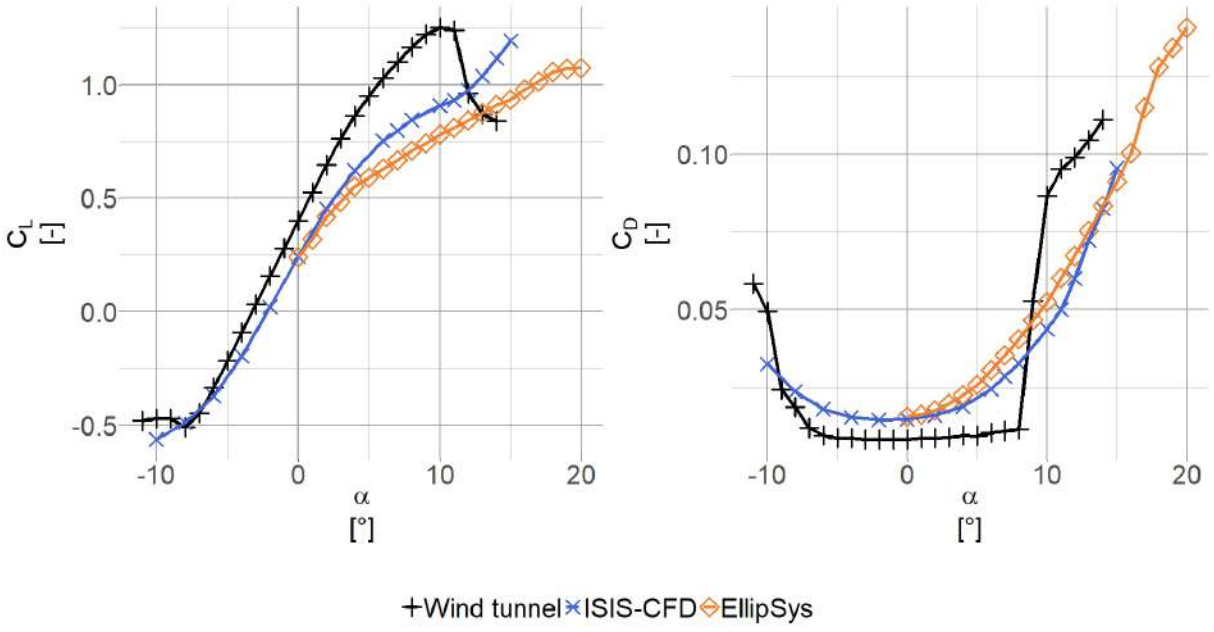

Figure 4.6 – DANAERO Section03: the blue cross (×) represents the ISIS-CFD results, the orange diamond (◇) the DANAERO CFD reference and the black plus (+) are the DANAERO wind tunnel data results. Left: C_L, right: C_D curve.

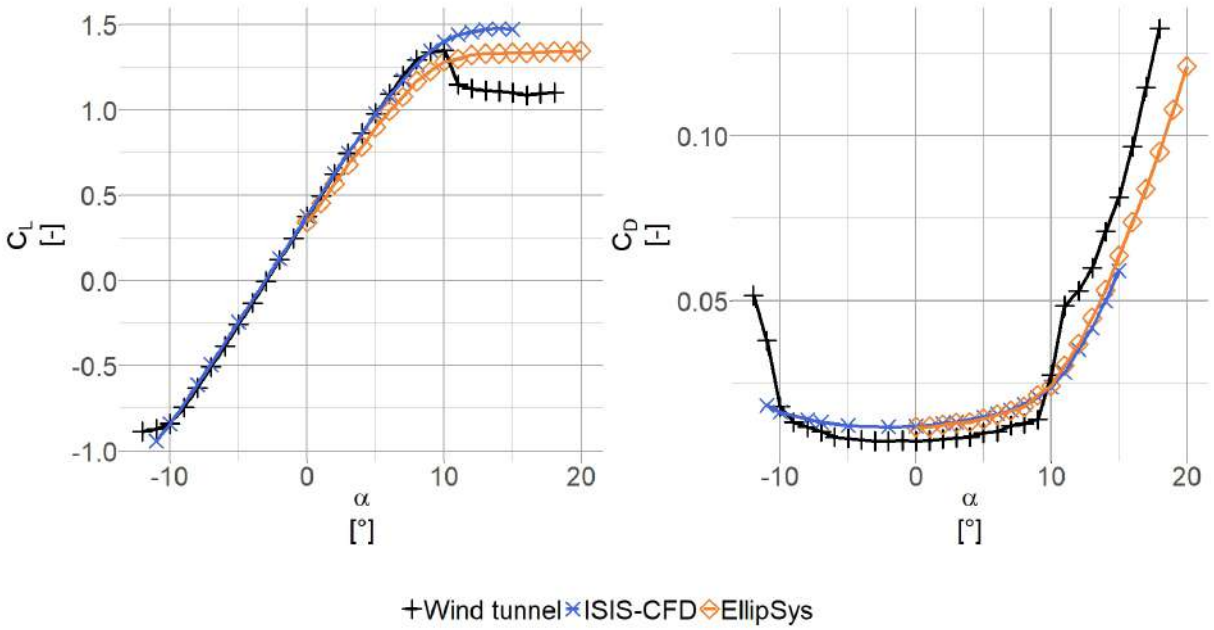

Figure 4.7 – DANAERO Section05: the blue cross (×) represents the ISIS-CFD results, the orange diamond (◇) the DANAERO CFD reference and the black plus (+) are the DANAERO wind tunnel data results. Left: C_L, right: C_D curve.

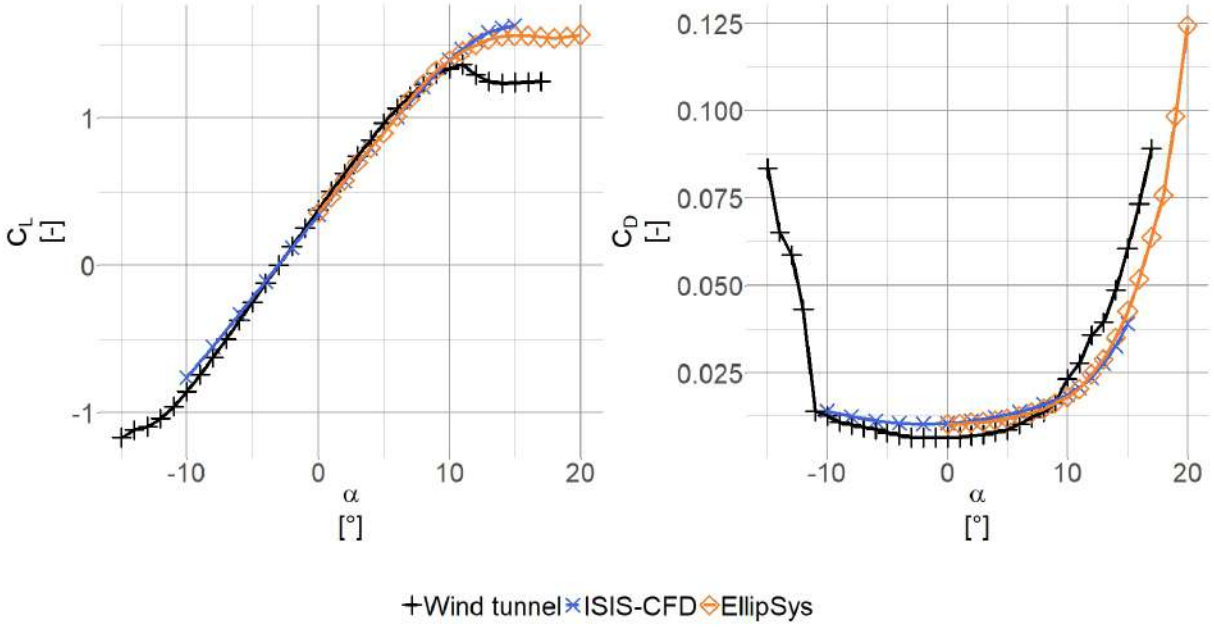

Figure 4.8 – DANAERO Section08: the blue cross (×) represents the ISIS-CFD results, the orange diamond (◇) the DANAERO CFD reference and the black plus (+) are the DANAERO wind tunnel data results. Left: C_L, right: C_D curve.

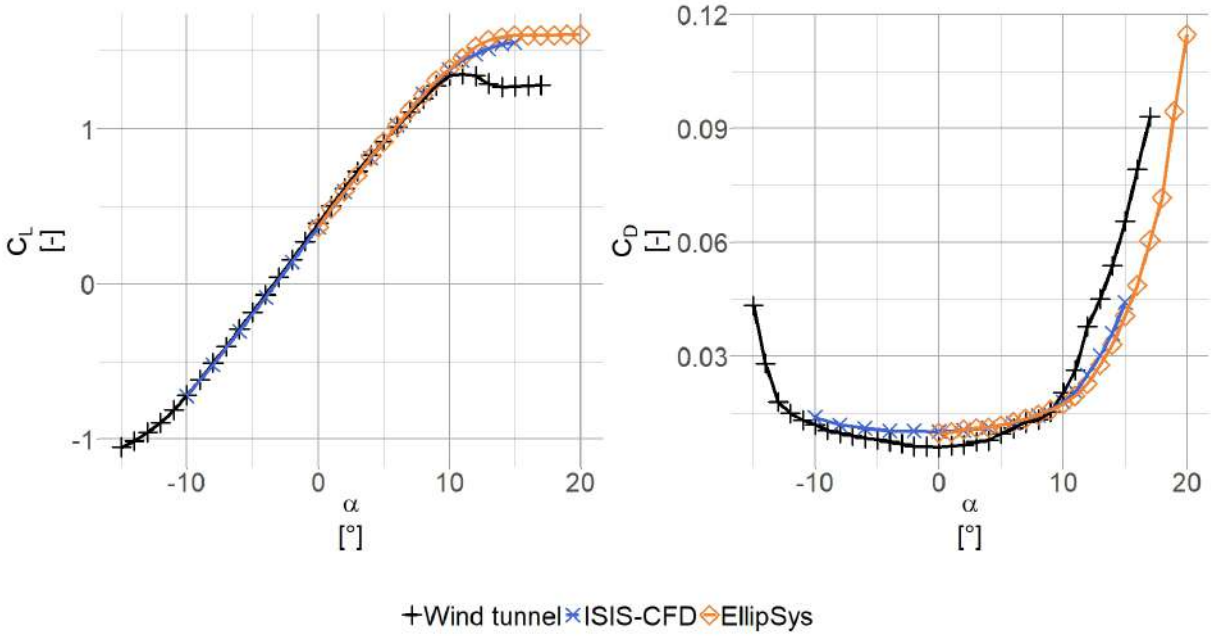

Figure 4.9 – DANAERO Section10: the blue cross (×) represents the ISIS-CFD results, the orange diamond (◇) the DANAERO CFD reference and the black plus (+) are the DANAERO wind tunnel data results. Left: C_L, right: C_D curve.

The Table 4.4 shows the average deviation between the different sections analysed and the wind tunnel in the linear region ($-10° < \alpha < 9°$). The Section05, which was used in the DoE, shows the best agreement. However, the results from the Section03 and Section08 are outside the set tolerance of 2% defined. It is to be noted that the differences calculated for ISIS-CFD are of the same order of magnitude than the ones calculated for EllipSys. The difference between the Section03 and the wind tunnel data is a well known issue where relatively thick profile simulations fail to follow accurately the wind tunnel measurements. Investigating whether the wind tunnel blockage effect or the simulations are the closest to reality is out of the scope of the current thesis. The slightly larger offset with wind tunnel results for the Section08 is explained by a poor trailing edge capture by the mesh at the time of the DoE and polar calculations. Since then, particular care has been taken with a new methodology for thin trailing edges and the offset is now corrected (not shown here).

Table 4.4 – Average C_L deviation with wind tunnel reference in the linear region

Sections	**ISIS-CFD difference with WT**		**EllipSys difference with WT**
	$-10° < \alpha < 9°$	$0° < \alpha < 9°$	$0° < \alpha < 9°$
Section03	-11%	-29%	-38%
Section05	-0.6%	-0.3%	-9%
Section08	-8%	-6%	-5%
Section10	-0.8%	-0.7%	-1%

4.2.2 Grid independence study

Using a thick section with and without spoiler from the scanned blade as benchmark and building upon the results from the Section 4.2.1 a grid independent study was carried out.

The aerofoil related surfaces boundary conditions were described as "no slip wall". The free stream velocity condition was imposed on the inlet, upper and lower boundaries and the outlet boundaries were using the "prescribed pressure" condition. Finally, $y^+ = 0.15$ was imposed on the aerofoil surfaces and the automatic grid refinement feature was activated so as to track more accurately the wake vortices (see [155, 154]). The no spoiler aerofoil is originally described with 362 pairs of [X;Y] coordinates and the spoiler case with 503. The leading edges are both positioned at [0;0]. A convergence study was carried out using the lift and drag coefficients. During the mesh refinement the number of faces defining the aerofoil geometry changed as described in Table 4.5 and Table 4.6. ISIS-CFD provides the time series for the lift (L) and drag (D) evolution, the respective coefficients are calculated by the equation 4.7.

$$C_L = \frac{2 \times L}{\rho c V_{rel}^2} \qquad C_D = \frac{2 \times D}{\rho c V_{rel}^2} \tag{4.7}$$

Where V_{rel} is the relative velocity of 45m/s,$\rho = 1.225$ is the air density and $c = 1$ the aerofoil chord, corresponding to $Re_c = 3 \times 10^6$. Four meshes were tested to assess the grid independence: Coarse, Medium, Fine and Very fine. Both cases used the same input conditions for the viscous layers insertion for each mesh. Because the calculations were performed using the automatic grid refinement, the Richardson extrapolation is calculated using the final mesh configuration. The cell size threshold followed a variation of $\sqrt{2}$, with the first value defined for the Medium mesh Threshold = 0.2.

The results in Table 4.5 and Table 4.6 show that the grid is independent both in C_L and C_D. The error between the "Very fine" and "Fine" mesh is small enough to be acceptable. For the rest of the study, the "Fine" mesh will be used.

Table 4.5 – Grid independence study for the scanned blade without spoiler at $\alpha = 0°$ and $Re_c = 3 \times 10^6$.

Mesh type	**Domain cell count**	**Aerofoil faces count**	**C_L** [-]	**C_L error** [%]	**C_D** [-]	**C_D error** [%]
Coarse	44 298	459	0.319	-10.28	0.07697	4.05
Medium	71 205	675	0.342	-3.97	0.07622	3.04
Fine	104 907	1048	0.346	-2.70	0.07488	1.23
Very fine	176 921	1535	0.355	-0.41	0.07486	1.19
Richardson extrapolation	∞	NA	0.356		0.07397	

Table 4.6 – Grid independence study for the scanned blade with spoiler at $\alpha = 0°$ and $Re_c = 3 \times 10^6$.

Mesh type	**Domain cell count**	**Aerofoil faces count**	**C_L** [-]	**C_L error** [%]	**C_D** [-]	**C_D error** [%]
Coarse	54 543	527	0.658	6.04	0.09015	5.62
Medium	82 543	733	0.630	1.63	0.08740	2.39
Fine	137 122	1085	0.619	-0.18	0.08705	1.98
Very fine	227 686	1591	0.620	-0.03	0.08584	0.57
Richardson extrapolation	∞	NA	0.620		0.08536	

4.2.3 Time step independence study

A time step convergence study using the "Fine" mesh has also been performed and summarised in Table 4.7. The initial time step was chosen to be $\Delta t = \frac{T_{chord}}{100}$, where T_{chord} is the time for an air particle to travel across the aerofoil chord. Then time step was varied successively until reaching $\Delta t = \frac{T_{chord}}{1000}$.
The chosen time step for the rest of the study is $\Delta t = \frac{T_{chord}}{500} \Leftrightarrow 4.44 \times 10^{-5} s$ because of the good balance between result accuracy and rapidity to achieve convergence.

Table 4.7 – Time step independence study for the scanned blade with spoiler at $\alpha = 0°$ and $Re_c = 3 \times 10^6$.

Time step	**Time step** [s]	**C_L** [-]	**C_L error** [%]	**C_D** [-]	**C_D error** [%]	**Time before convergence** [min]
$T_{chord}/100$	2.22×10^{-4}	0.596	-5.70	0.0828	-6.18	2719
$T_{chord}/250$	8.89×10^{-5}	0.599	-5.17	0.0829	-6.08	3028
$T_{chord}/500$	4.44×10^{-5}	0.619	-1.99	0.0871	-1.36	3709
$T_{chord}/1000$	2.22×10^{-5}	0.628	-0.54	0.0881	-0.17	11118
	Richardson extrapolation	0.632		0.0883		NA

4.3 ISIS-CFD 3D

The verification analysis is first focused on the DANAERO rotor, then a similar mesh independence study will be performed for the ENGIE Green blade.
Firstly the influence of the domain size is assessed. Then, once the results are domain size independent, the impact of the blade discretisation will be analysed. The force normal to the local chord, here called F_z, as defined in the final IEA report [123], is the metric used to define the correctness of the results.

The DANAERO results used as benchmark are numerised from [123] and summarised in the Figure 4.10. Each coloured line represents a participant and the thick black line the average F_z of all participants. For the rest of the study only the DANAERO mean force will be used. The error bars represent the participants' standard deviation.

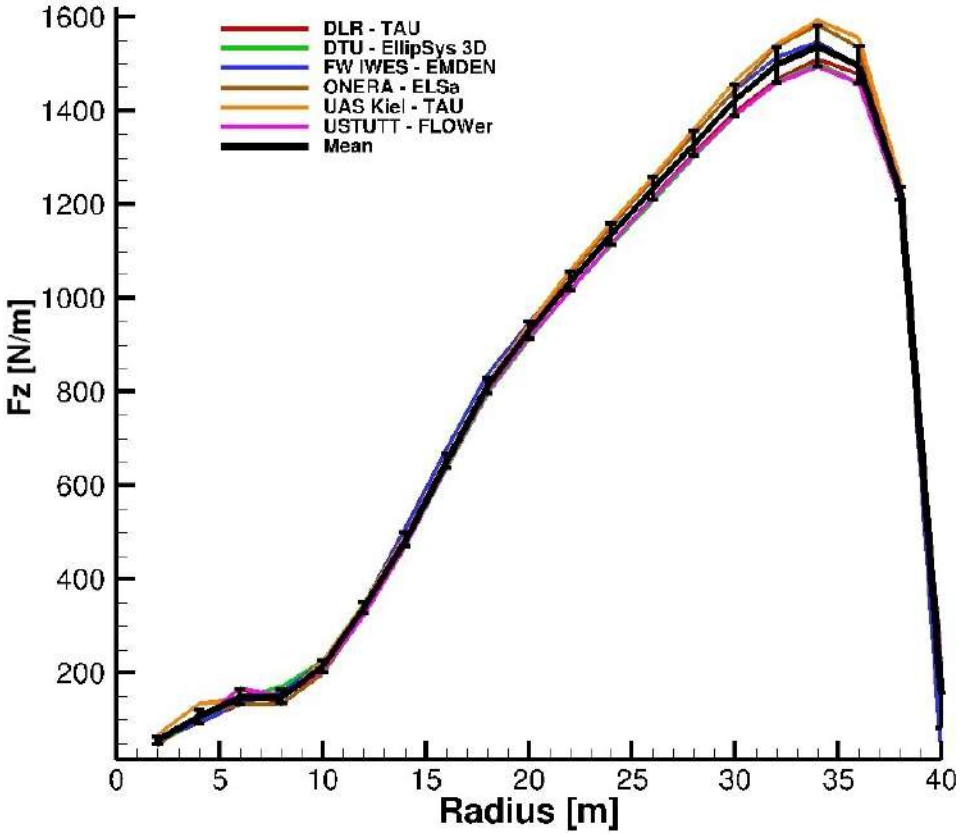

Figure 4.10 – DANAERO participants numerised results (F_z) along with the mean and standard deviation (from [123])

As illustrated in Figure 4.11, the computational domain is positioned vertically, the inflow aligned with the vertical axis (z-axis). Further details about the domain and blade discretisation are given in Section 4.3.1.

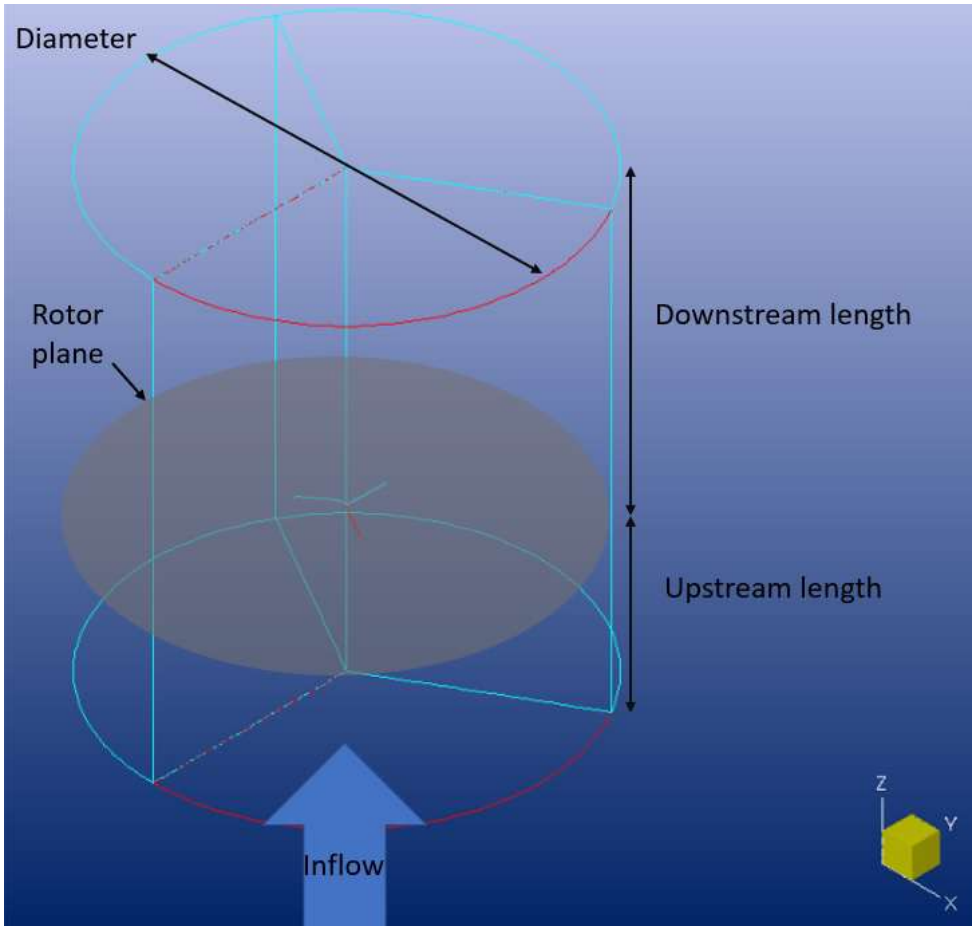

Figure 4.11 – ISIS CFD set-up and coordinate system

4.3.1 DANAERO rotor

Domain size sensitivity

Four different domains are first simulated in order to assess the results dependency to the domain size. The domains are referred later as *single blade*, *small*, *medium* and *large*. The Table 4.8 shows the different configurations initially simulated.

Table 4.8 – Domain size in the grid independence study

Case	Diameter [m]	Upstream length [m]	Downstream length [m]	Number of cells	Comment
Single blade domain	400	150	300	45M	Single blade
Small domain	400	150	300	118M	Full rotor
Medium domain	1000	150	300	147M	Full rotor
Large domain	1600	800	800	150M	Full rotor

Figure 4.12 and Table 4.9 show that larger domains bring the output closer to the literature with diminishing return. The single domain exhibits non-smooth behaviour due to the blade geometry being poorly captured at the trailing edge toward the tip. The force evolution on the larger two domains is smoother despite being higher than the reference (Mean). The integrated loads show the same trend. Based on those results, the large domain is chosen for the rest of the study. It is to be noted that it is the same domain dimensions as used by some of the DANAERO project participants. The blade is discretised in the same fashion for all full rotor domains and the immediate wake is coarsely meshed knowingly. This first sensitivity study aims at defining the ideal domain size and not matching the DANAERO baseline.

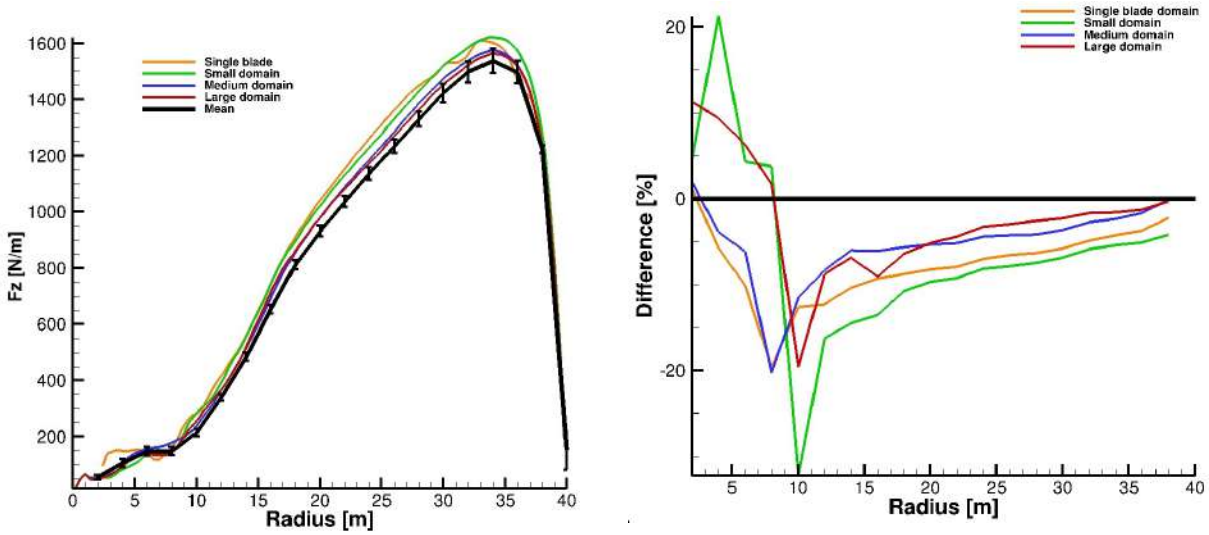

(a) F_z comparison of the different domain sizes

(b) F_z difference of the different domain sizes with respect to the DANAERO mean

Figure 4.12 – Radial evolution of the force normal to the rotor plane based on the different domain sizes

Table 4.9 – Integrated loads

Case	**Integrated rotor load [N]**	**Difference [%]**
DANAERO Mean	3.17×10^4	N/A
Single blade domain	3.45×10^4	8.8
Small domain	3.44×10^4	8.5
Medium domain	3.32×10^4	4.7
Large domain	3.26×10^4	2.8

Blade discretisation sensitivity

In all full rotor configurations the blade was highly discretised in order to accurately capture the trailing edge and other small surfaces. However, the wake is left unrefined leading to discrepancies with the literature results. The following section aims at approaching the DANAERO baseline while keeping the cell count below 100M.
Hexpress™/Hybrid is the mesh generator used during this study, it produces an unstructured mesh which contains only hexahedral cells (in our case). The level of refinement is user defined through two main parameters: baseH and iteration. The baseH is the largest cell in the mesh and iteration is the number of times the cells are divided to reduce the cell size and thus capture the geometry. A simple relationship $cell_{size} = baseH \times 0.5^{iteration}$ gives the smallest cell size achieved based on the user inputs. The DANAERO blade possesses its smallest dimension at the trailing edge (TE), where $min(TE) = 0.001m$. The number of cells of the chosen domain (*large*), in Table 4.8 will increase significantly once the wake is more densely meshed thereby increasing the computational cost and difficulty of post-processing.
Using the large domain as baseline, three blade discretisations are tested: fine, medium, coarse. Reducing further the number of blade discretisation iterations would risk of not capturing accurately the trailing edge. The Table 4.10 shows that the coarse discretisation will produce a cell at most twice as small as the smallest dimension from the DANAERO blade, while the fine mesh has a safety factor of 52.

Table 4.10 – Different minimum cell sizes based on the discretisation chosen

Case	baseH [m]	Iteration	Minimum cell size [m]	Safety margin
Fine	20	20	1.9×10^{-5}	52.4
Medium	8	16	1.2×10^{-4}	8.2
Coarse	8	14	4.9×10^{-4}	2.0

Each discretisation configuration is now simulated following two Automatic Grid Refinement (AGR) refinements, where the refinement criterion thresholds are 8m and 4m, corresponding to the reference length (blade radius) divided by 5 and 10 respectively, and the minimum cell size is 0.1m. The cases will be called *Ref 1* and *Ref 2*. The criterion threshold mean that any cell larger than the threshold can be refined. The AGR will dynamically refine and coarsen the mesh based on the vortices present in the wake. For this reason only the number of cells of the last iteration will be presented.
The outcome of the sensitivity study shows that the "no refinement" configuration can be improved by activating the AGR option as seen by the results in Table 4.11. The blade discretisation does not have an influence on the simulated convergence time, i.e. the coarse and fine blade discretisation converge to a steady solution in the same length of simulated time (approx. 300s). However, the computational time is reduced by 20% when using less cells. Using a coarse blade discretisation is enough for ISIS-CFD to provide accurate results compared to the DANAERO baseline. Also, the Ref 2 cases, despite its

smaller cells does not seem to add extra accuracy compared to Ref 1 regardless of the initial mesh settings. More details about the validation and deeper analysis are available in [107].

Table 4.11 – Impact of the blade discretisation and refinement procedure

Case	**Integrated load [N]**	**Difference [%]**	**Number of cells**
DANAERO Mean	3.17×10^4	N/A	N/A
Fine No refinement	3.26×10^5	2.8	150M
Medium No refinement	3.25×10^5	2.5	98M
Coarse No refinement	3.26×10^5	2.9	71M
Fine Ref 1	3.16×10^5	-0.4	167M
Medium Ref 1	3.17×10^5	0.1	112M
Coarse Ref 1	3.17×10^5	-0.1	86M
Fine Ref 2	3.14×10^5	-1	244M
Medium Ref 2	3.14×10^5	-0.9	174M
Coarse Ref 2	3.16×10^5	-0.5	147M

The coarse blade discretisation cell number evolution is presented in Figure 4.13. After a rapid increase, the cell count stabilises for Ref 1 and Ref 2. The Figure 4.14 shows the blade discretisation impact when coupled with the AGR Ref1. It is clearly seen that increasing the blade discretisation doesn't increase the overall accuracy. The blade geometry needs to be captured properly using the coarser discretisation possible, then the AGR refines the wake to improve the overall results accuracy.

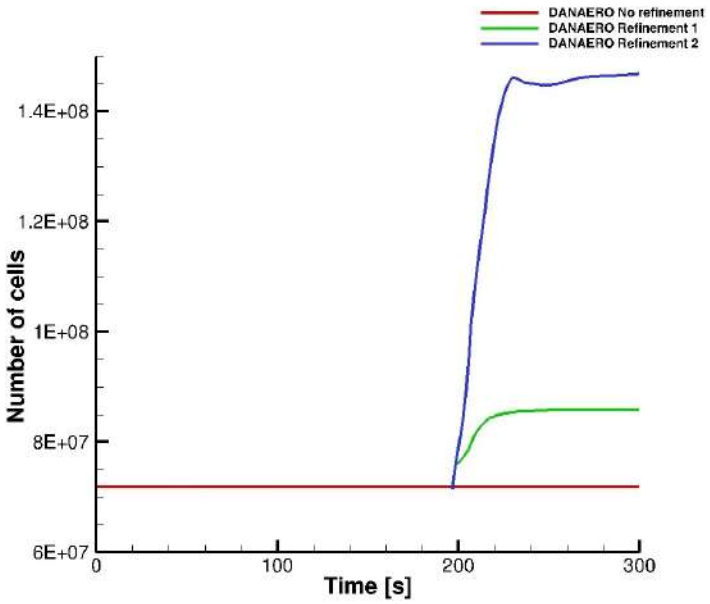

Figure 4.13 – DANAERO number of cells for the coarse blade discretisation

The Figure 4.15 illustrates the impact on the mesh of the AGR. The Figure 4.15a shows that the mesh is quite coarse behind the rotor leading to a rapid dissipation of the wake. Whereas, in the Figure 4.15b the tip vortices are well captured along with the vortex near the centre of rotation.

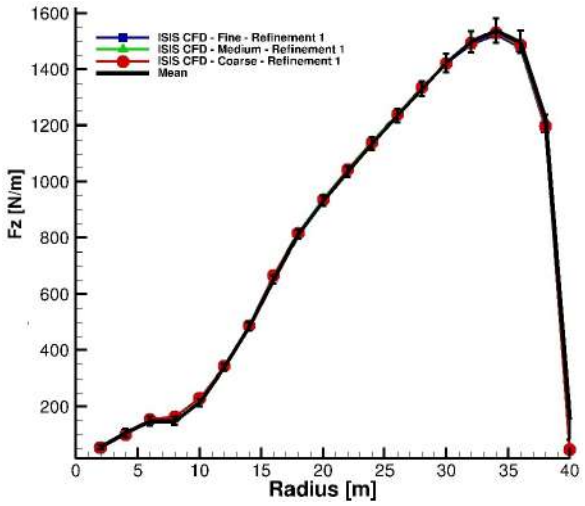

(a) F_z comparison for different blade discretisations with Ref1

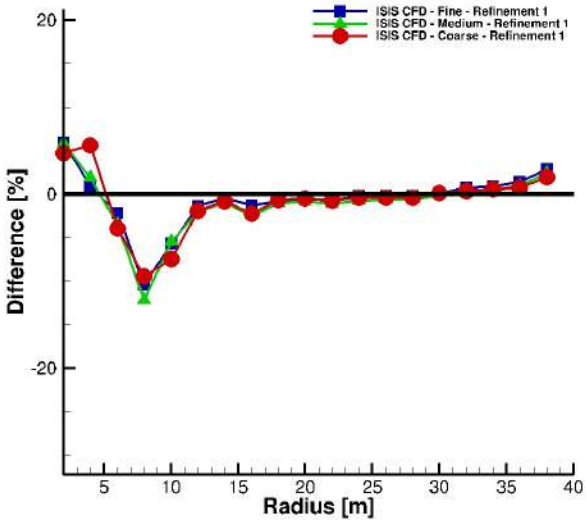

(b) F_z with Ref1 difference for different blade discretisation with respect to the DANAERO mean

Figure 4.14 – Radial evolution of the force normal to the rotor plane based on different blade discretisations with Ref 1

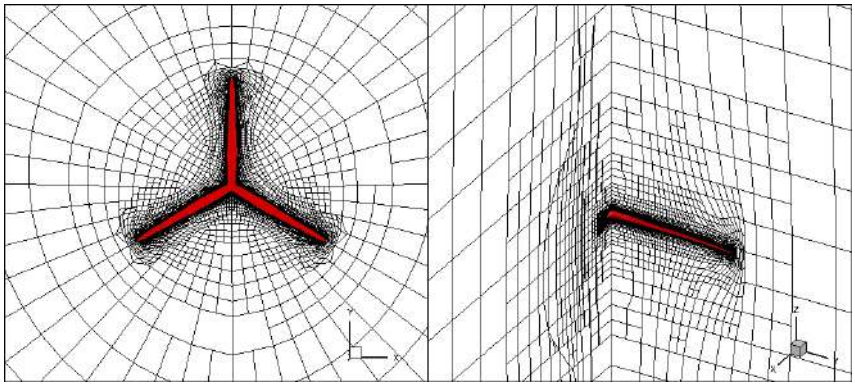

(a) DANAERO blade without refinement: mesh in the vicinity of the rotor

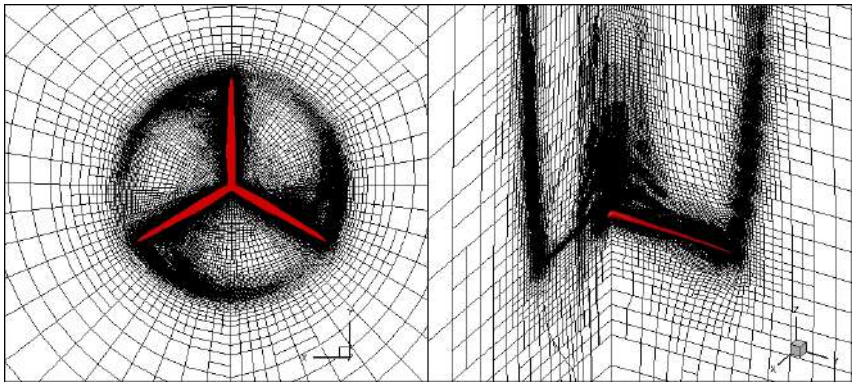

(b) DANAERO blade with Ref 1: mesh in the vicinity of the rotor

Figure 4.15 – AGR method effect on the mesh.

4.3.2 ENGIE Green rotor

Following the methodology presented in Section 4.3.1, a similar approach was taken for the scanned blade to ensure the mesh independence.

Domain definition

In the previously presented verification, using the DANAERO blade, the domain is proportional to the blade size. The scanned blade possesses a larger radius and because of the extrapolated tip a safety margin was taken to ensure no interference between the tip vortices and the domain boundaries. The total domain length from the inlet to the outlet remains however unchanged.

Table 4.12 – Domain size

Case	Diameter [m]	Upstream length [m]	Downstream length [m]	Blade length [m]
No spoiler	4000	800	800	45
Spoiler	4000	800	800	45

The Figure 4.16a shows the total calculation domain. Figure 4.16b to Figure 4.16d show a zoomed-in view of the mesh around a single blade and the rotor.

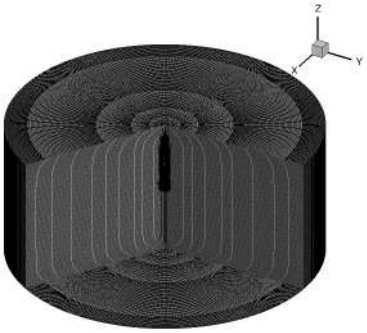

(a) Total calculation domain of the scanned blade.

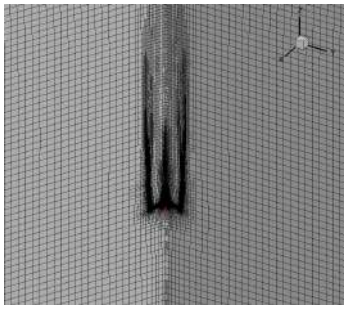

(b) Close-up view of the domain

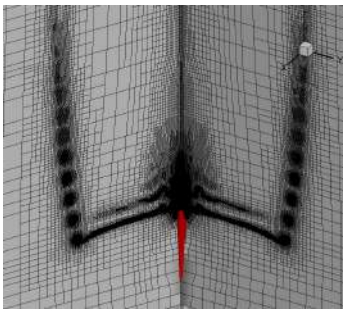

(c) Close-up view of a single blade in the calculation domain.

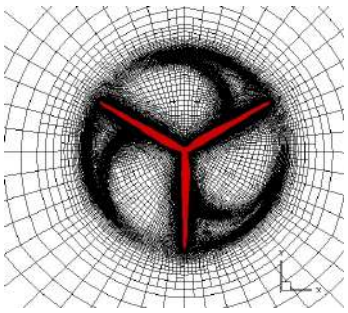

(d) Close-up view of the rotor.

Figure 4.16 – Different views of the scanned blade in its calculation domain.

Mesh independence results

Each case is following two Automatic Grid Refinement (AGR) configurations. The refinement criterion thresholds are 9m and 4.5m, corresponding to the reference length (blade radius) divided by 5 and 10 respectively, and the minimum cell size is 0.1m. The time step is kept constant during the simulations and taken to be $\Delta t = 0.01s$, which is equivalent to a rotation of 2° per time step.
Due to time constraints, the rotor simulations were limited, and in particular it does not include the nacelle and the tower. Also, the wind inflow was considered uniform and steady in the overall 3D simulation. At last, only one operational condition was performed with and without spoiler. The presented results show the simulations outcome for an operating wind speed of 8m/s and a pitch settings of -1.568° following the pitch setting optimisation presented in Section 7.1.5. Indeed, the difference between the optimal pitch settings between the two cases is $\Delta\text{Pitch}_{\text{optim}} = 0.051°$ which is negligible. Therefore a common pitch setting of -1.568° was chosen for both cases. The chosen wind speed is in the part II of the power curve (see Figure 1.12), i.e. the turbine is operating at its optimal power coefficient (here the power coefficient is approximately 0.42).

The Table 4.13 and Table 4.14 show the impact of the AGR on the aerodynamic thrust. The load is almost equal both for the "Refinement 1" and "Refinement 2", while the cell count and calculation time are drastically increased with the highest refinement. Therefore, for the rest of the manuscript only the "Refinement 1" results will be used.

Table 4.13 – Comparison of the aerodynamic thrust, in the no spoiler case, with respect to the applied refinement.

Case	**Thrust** [N]	**Difference** [%]	**Number of cells**	**Calculation time** [h]
No refinement	66167.78	-2.24	28M	40
Refinement 1	64848.53	0.2	43M	60
Refinement 2	64783.68	0.1	117M	100
Richardson extrapolation	64715.88	N/A	N/A	N/A

Table 4.14 – Comparison of the aerodynamic thrust, in the spoiler case, with respect to the applied refinement.

Case	**Thrust** [N]	**Difference** [%]	**Number of cells**	**Calculation time** [h]
No refinement	66436.86	-1.53	29M	40
Refinement 1	65417.63	0.03	45M	60
Refinement 2	65427.46	0.02	115M	120
Richardson extrapolation	65438.81	N/A	N/A	N/A

4.3.3 3D CFD post-processing

The following sections detail the metrics and method used in the 3D CFD analysis (see Chapter 8). First, the definition of the Q-criteria and vorticity are given, then a description of the Azimuthal Averaging Technique (AAT), is shown. The AAT is a necessary step to extract in the rotor plane the velocities.

Q-criteria and isosurface

The most visual method to compare the impact of the refinement method on the wake is through isosurface. The Q-criteria is a metric used to determine the presence of vortices, it is derived from the velocity gradient tensor as depicted in equation 4.8.

$$\frac{\partial u_i}{\partial x_j} = \underbrace{\frac{1}{2}\left(\frac{\partial u_i}{\partial x_j} + \frac{\partial u_j}{\partial x_i}\right)}_{\text{Strain rate tensor: S}} + \underbrace{\frac{1}{2}\left(\frac{\partial u_i}{\partial x_j} - \frac{\partial u_j}{\partial x_i}\right)}_{\text{Vorticity tensor: } \Omega} \tag{4.8}$$

The Q-criteria is defined as the second invariant of the velocity gradient (see equation 4.9).

$$Q = \frac{1}{2}\left(\|\Omega\|^2 - \|S\|^2\right) \tag{4.9}$$

The Figure 4.17 shows isosurfaces of the Q-criteria overimerposed with the axial velocity. This emphasises that small vortices are present throughout the rotor plane and are carried in the far wake. The large ones are concentrated in the blade root vicinity and dissipate within two rotations, in the case of no refinement. While in both refinement cases the tip and root vortices are well formed and propagate far downstream, the vortices for Refinement 2 trails slightly further downstream. This has however no impact on the thrust as seen in Table 4.14.

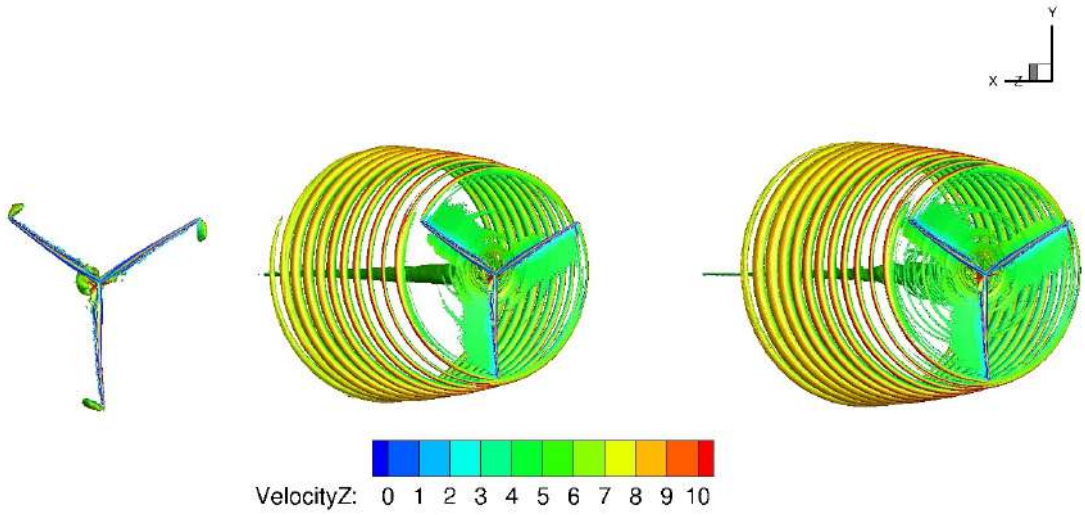

Figure 4.17 – Impact of AGR refinement criteria on the wake using the Q-criteria (Q-crit = 0.1), coloured by the axial velocity, for the spoiler case: Left - No refinement, Middle - Ref 1, Right - Ref 2.

Vorticity

The vorticity is a measure of the fluid local rotation in $[1/s]$. In a 3D field, the vorticity is a vector and by definition in a 2D plane, the vorticity is a scalar as seen in equation 4.10:

$$\vec{rot}\ \mathbf{U} = \nabla \times \mathbf{U} = \begin{Bmatrix} \frac{\partial U_z}{\partial y} - \frac{\partial U_y}{\partial z} \\ \frac{\partial U_x}{\partial z} - \frac{\partial U_z}{\partial x} \\ \frac{\partial U_y}{\partial x} - \frac{\partial U_x}{\partial y} \end{Bmatrix} \tag{4.10}$$

Where $\mathbf{U}$ is the velocity vector and U_x, U_y and U_z are its components. The sectional plane in the Figure 4.18 is through the Y-axis, therefore the Y component of the vorticity is required. The vorticity field varies between -1 and 1. Positive values (blue) show a clockwise rotating fluid particle while negative values (red) show counter-clockwise rotating fluid particle. The black isolines represent the Q-criteria values between 0 and 1000 with logarithmic increment. Despite the lower operating angle of attack, the spoiler case exhibits a wider wake and more vortices activity (Figure 4.18b) than in the no spoiler case (Figure 4.18a).

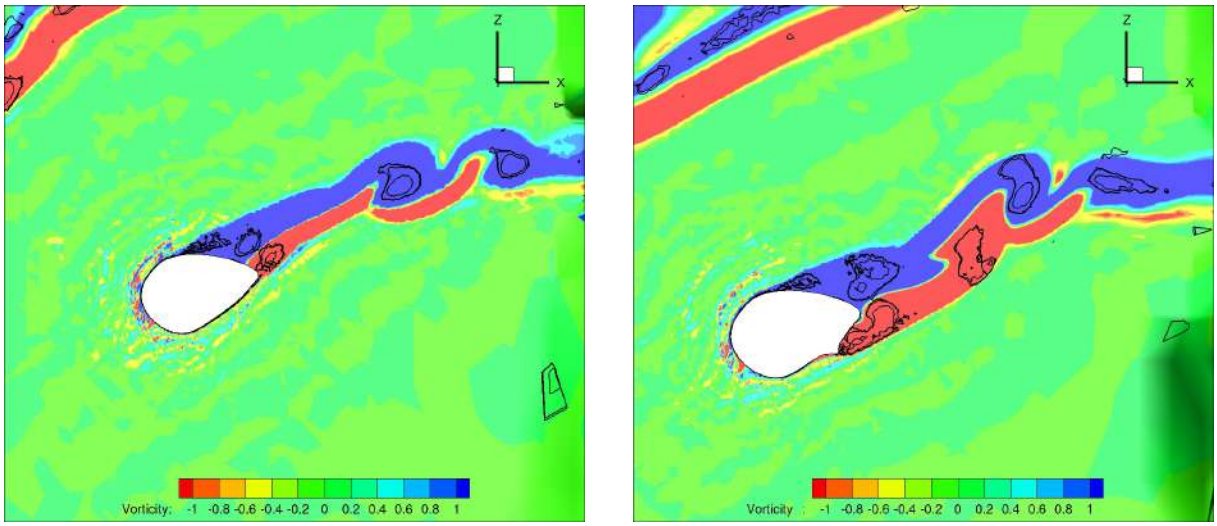

(a) No spoiler R6 - Vorticity and Q-criteria

(b) Spoiler R6 - Vorticity and Q-criteria

Figure 4.18 – Vorticity and Q-criteria in the wake of the rotor.

Azimuthal Averaging Technique

In order to extract the local information, the Azimuthal Averaging Technique (AAT) is used. The AAT is described in [54, 115] and the procedure can be summarised as follow:

- Extract velocity planes upstream and downstream of the rotor ($\pm$ 3 maximum chord)
- Interpolate the data onto the rotor plane, here defined at $Z = 0$ (see Figure 4.19a)
- Average the interpolated data over a quadrant for every radial position desired (see Figure 4.19b)

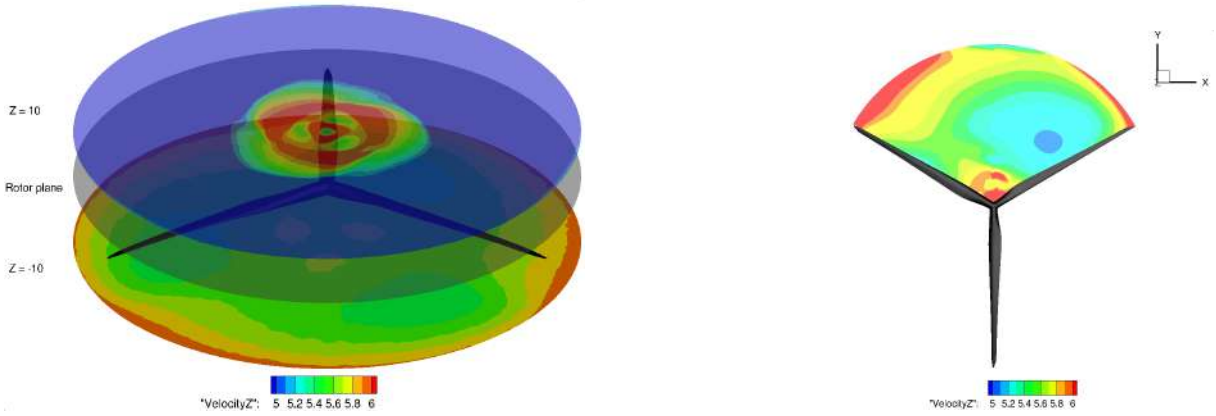

(a) Planes upstream and downstream of the rotor. The rotor plane is displayed for convenience.

(b) Quadrant in which the data is average radially.

Figure 4.19 – Azimuthal Averaging Technique illustration.

4.4 Summary

The UiBEM tool developed as part of the thesis has been verified and validated using the DANAERO database enabling the analysis of unsteady field data. ISIS-CFD is well recognised in the CFD field for its marine application, the present thesis allowed to show that ISIS-CFD performs at least as well as the rest of the available codes used in the DANAERO project for 2D and 3D external aerodynamic applications.

Chapter 5

Evidence of BEM limitations for blade life time estimation

Contents

The DANAERO database presented in Chapter 3 is used here to highlight the BEM limitations to determine blade loads in a real environment. The unsteady aerodynamic loads, responsible of fatigue loads and thus decrease of the blade lifetime, are of particular interest. The following sections relies on the work published in [111].

5.1 Test cases choice

For this field analysis, the normal operating conditions described in [9] were preferred, i.e. the turbine facing the incoming wind, with limited wake effects from neighbouring turbines. The pitch and RPM settings are driven by the turbine controller according to the normal operating conditions. The chosen window of analysis is the measurement campaign done on the 16^{th} of July 2009 between 12h30 and 13h as it reaches the normal operating conditions.
Figure 5.1 shows the wind rose of the times series selected measured by the met mast, with superimposition of the Tjaereborg wind farm turbines. Highlighted in blue, the reference turbine is located downstream of the met mast (in red) recording the rotor inflow.
The wind passed the Foken test and is considered stationary (see Section 1.1.2). The atmospheric stability was computed using the Monin-Obukhov similarity theory [157, 63] and none of the time series analysed show neutral conditions [63]. A high level of turbulence due to the thermal exchanges is expected. This atmospheric condition is obviously

far from the wind tunnel conditions for measuring 2D aerofoil polars used by the BEM method.

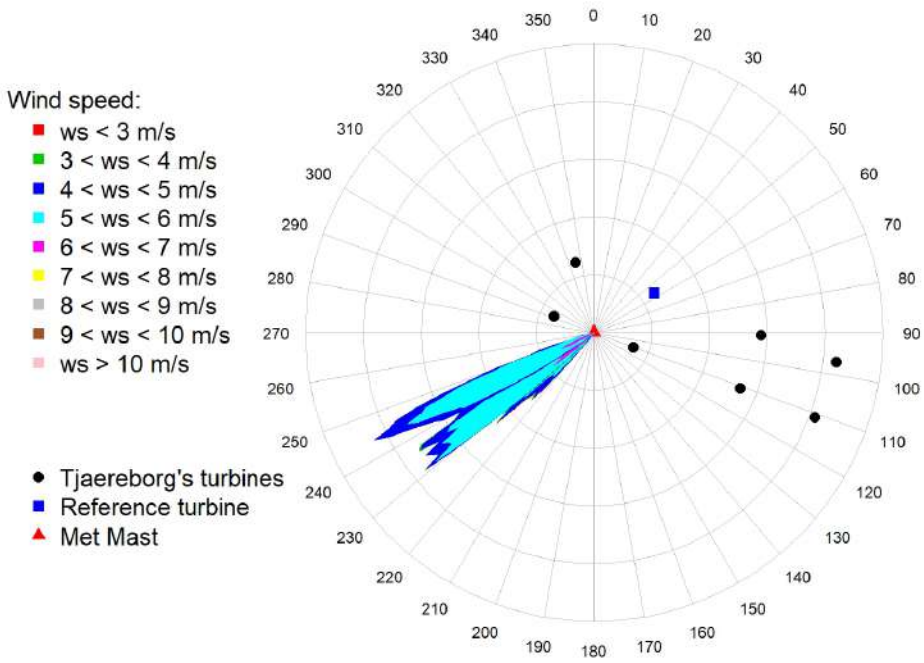

Figure 5.1 – Wind rose distribution in the wind farm for the selected period.

The data in Table 5.1 shows the mean environmental values (wind speed, wind direction and turbulence intensity) for each of the three 10min time series files analysed. The mean wind speed is rather low (6.5m/s) and the turbulence intensity around 9%. With a low wind speed one can expect high induction levels which will lead the turbine to operate in the so-called *turbulent wake state* ($a > 0.5$). The range of wind direction over the 30 minutes analysed is contained within 20°, its standard deviation is 5°.

Table 5.1 – Mean values for the analysed time series at hub height (H = 57m)

	12h30-12h40	**12h40-12h50**	**12h50-13h**
Mean wind speed [m/s]	6.57	6.47	6.31
Mean wind direction [°]	231.1	234.87	233.06
Mean turbulence intensity [%]	7.6	8.7	9.2
Turbulence intensity X-axis [%]	7.1	7.9	9.5
Turbulence intensity Y-axis [%]	8.1	9.5	8.8
Turbulence intensity Z-axis [%]	7.1	8.0	8.0

The normal and tangential forces are measured in different radial positions along the blade. When applying the verified iBEM method to the selected time series it is possible to calculate the lift and drag, thus evaluating the phenomena modelled by the BEM theory for each blade section and each time step. First the comparison with the raw data is presented (Section 5.2.1), then a presentation of different filtering and correction models developed will be shown. Only the lift coefficient will be presented as the pressure sensors cannot measure the complete drag force. As the turbine is operating at high induction

level ($a \geq 1/3$), the calculations are dependent on the highly loaded correction model.
In their work, Ozçakmak et al. [102, 101] performed the analysis of field transition measurements for the tip section, focusing on the boundary layer transition laminar to turbulent. They showed that the turbulent inflow and surface roughness were the main contributors in the boundary layer transition. Transition on the suction side occurs, in the field, at approximately 5% of the aerofoil chord from the leading edge with little to no fluctuation of the mean location. The measurement is very well correlated to 3D CFD results where the transition is also predicted to occur at this location (i.e. 5% from the leading edge at the tip section). The mid-span section, $r/R = 49\%$, showed that the transition on the suction side was at approximately 10% from the leading edge. It is close to the wind tunnel tripped position and rather far away from the predicted 2D natural transition which varies between 50% and 30% (XFOIL, $Re_c = 5 \times 10^6$). The wind tunnel clean conditions are therefore non-realistic operating conditions. It was an expected outcome, as the experiments performed in the wind tunnel are done at very low levels of the turbulent intensity (0.1%) while the turbulent intensity in field measurements is around 9% (see Table 5.1). Also, as already known, the inboard area of the wind turbine blade is sensitive to rotational effects where the lift characteristics tends to be enhanced by the Coriolis forces [62, 11, 61, 83, 121]. Therefore, for a fairer comparison with field data, different corrected values of the 2D wind tunnel tests are included in the C_L plots including:

- Wind tunnel tests with tripped conditions at the blade surface, available from IEA Task 29.
- Rotational effect, also called "3D corrections", of the 2D wind tunnel tests using the model derived by Chaviaropoulos et al.[24]

5.2 BEM data filters and correction models

5.2.1 Raw comparison

The expected dispersion between 2D wind tunnel measurements, 2D CFD simulation (EllipSys [138] data) and field instantaneous C_L using a steady iBEM method without correction or filter, is shown in Figure 5.2. When selecting appropriate wind direction/speed and normal rotor operation, it is still not suitable to compute the aerodynamic coefficients using steady iBEM directly from field measurements.

The next sub-sections will show the different steps taken in order to improve the iBEM results accuracy and assess the importance of each phenomena in the BEM formulation. It is performed by the evaluation of the wind tunnel measurements and the back computed C_L using iBEM for the radial section $r/R = 0.49$. Only one section is presented because this mid-span section is less likely to be affected by the flow three dimensionality: root and tip effects, thus ensuring the most appropriate comparison.
The different steps can be classified in two main categories: filtering applied to the time series and correction of inputs for the iBEM method. The filters and correction methods

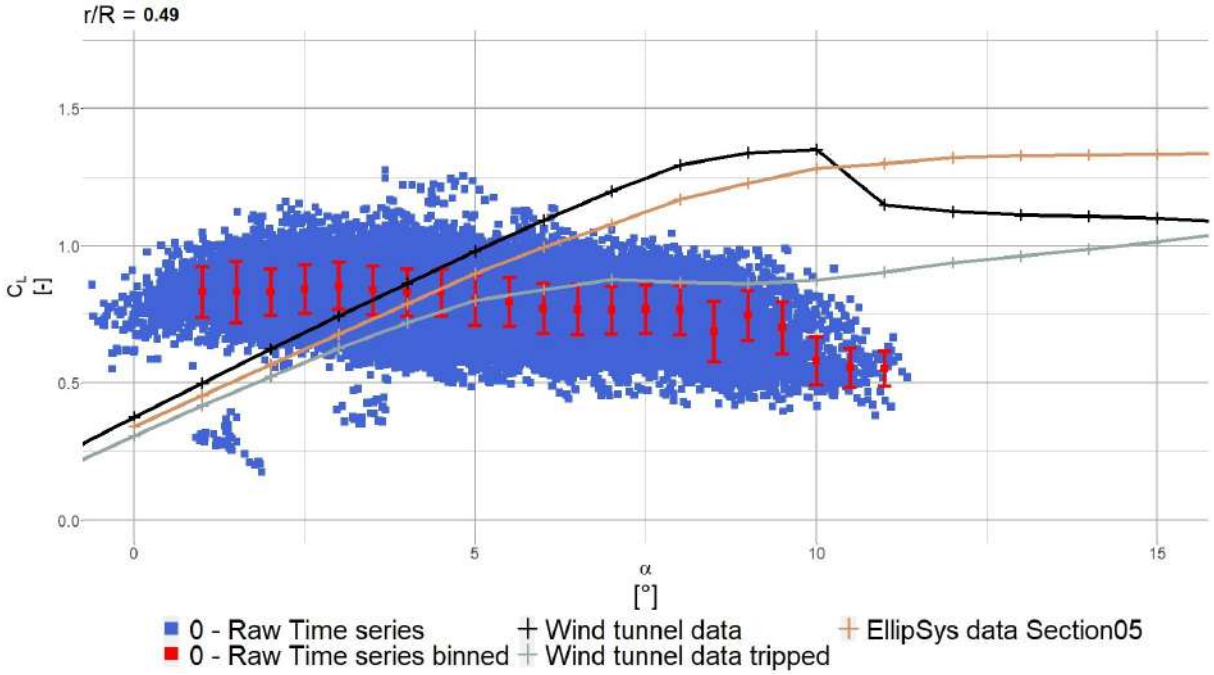

Figure 5.2 – C_L instantaneous data and binned averaged per angle of attack, for the radial location $^r/_R = 0.49$.

developed are cumulative, i.e. the results presented in each sub-section will also account for any previously correction introduced. For instance the neighbouring wake filter presented in Section 5.2.3 will also include the mean vertical gradient filter presented in Section 5.2.2. The unsteady BEM results, will only use the wake filter and the vertical gradient correction as the other filters are addressed in the equations themselves. Each analysed case is numbered from 0 to 6, for conciseness, all the relevant C_L plots for each correction and filter are listed in Appendix C.

5.2.2 Vertical gradient filter

The mean vertical gradient from the atmospheric boundary layer flow is not taken into account by the BEM theory. By analysing the vertical gradient of the mean wind speed, it has been decided to remove from the dataset any time-step whose inflow gradient, measured by the mast, is above a threshold. The limit has been imposed based on the average value of the steepest part of the vertical mean gradient of several time series analysed. Its value is 0.0025 s^{-1}, which corresponds to 50m height, close to the hub height, a region where the speed gradient is the most pronounced. A filter is therefore applied to exclude the data when the blade is passing below the hub. Analysing only the upper part of the rotor reduces the influence of the mean vertical gradient and its associated turbulence and uncertainties due to the tower shadow effects (i.e. when blades are passing in front of the wind turbine tower). It should be pointed out that, obviously, this operation removes approximately 50% of the available data points.

5.2.3 Neighbouring wake filter

Figure 5.3 shows that there is an overlap between the reference wind turbine and the wake from its neighbours during the 30min analysed.

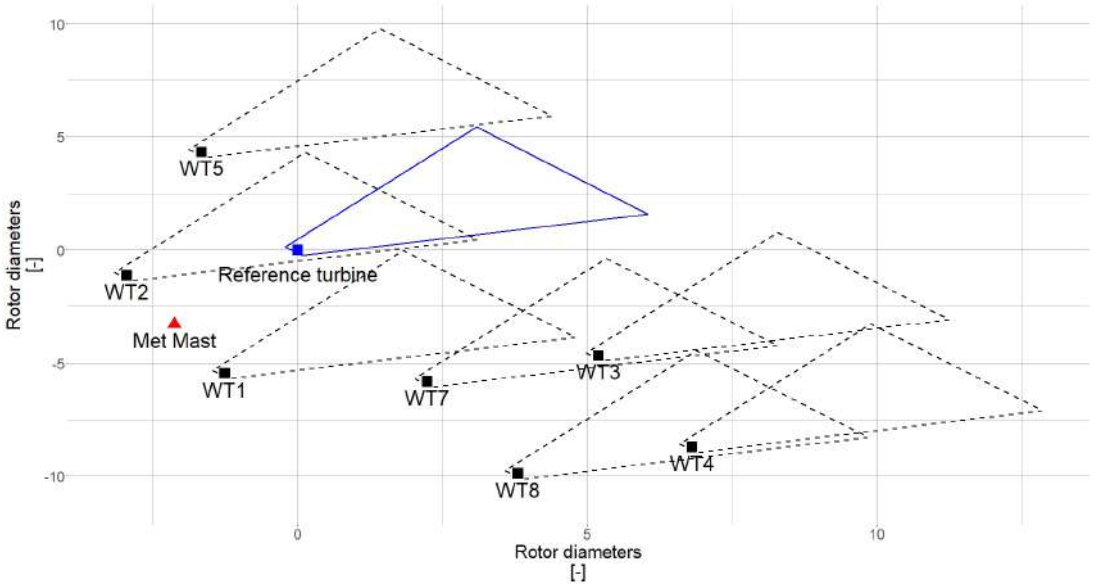

Figure 5.3 – Wake calculated for the extreme wind directions measured by the met mast (in red) in the selected period. The reference wind turbine (in blue) is partially subjected to a wake from WT2

To ensure that the met mast is not reading any wake data and the reference wind turbine is not in the wake of a neighbouring one, a dedicated filter was developed. Figure 5.4 shows the wind rose changes when the wake is accounted for. The wind farm layout is over imposed with the wind direction and intensity. The length of each coloured line represents the probability of occurrence during the time series. Also, to ensure that the wake is well-developed, the Frandsen wake development model [44] is used and represented by black dotted line circles. The wind farm turbines are outside the black dotted circle, meaning the wake is well developed when it reaches the next turbine in the wind farm. The Jensen model is therefore a valid assumption. Using the Jensen wake model [70], it is possible to calculate the wind speed deficit contribution of each wind turbine at any position in the wind farm. The circular red curve shows the wake contribution of all the wind turbines seen by the met mast and the circular blue curve shows the same wake contribution seen by reference wind turbine, but graphically centred on the mast to allow for a visual comparison. Having both curves tangent would mean that there is no wind speed deficit due to the wake of neighbouring wind turbines. For instance, it can be seen in Figure 5.4 left, in the sector between 240° and 250° that both curves are not tangent. The reference turbine is operating in the wake of another turbine. After application of the method, the inflow data is updated and only the wind direction where both circular curves are tangent is plotted in Figure 5.4 right. After filtering out the selected data samples, the inflow data is clean of any wake effect.

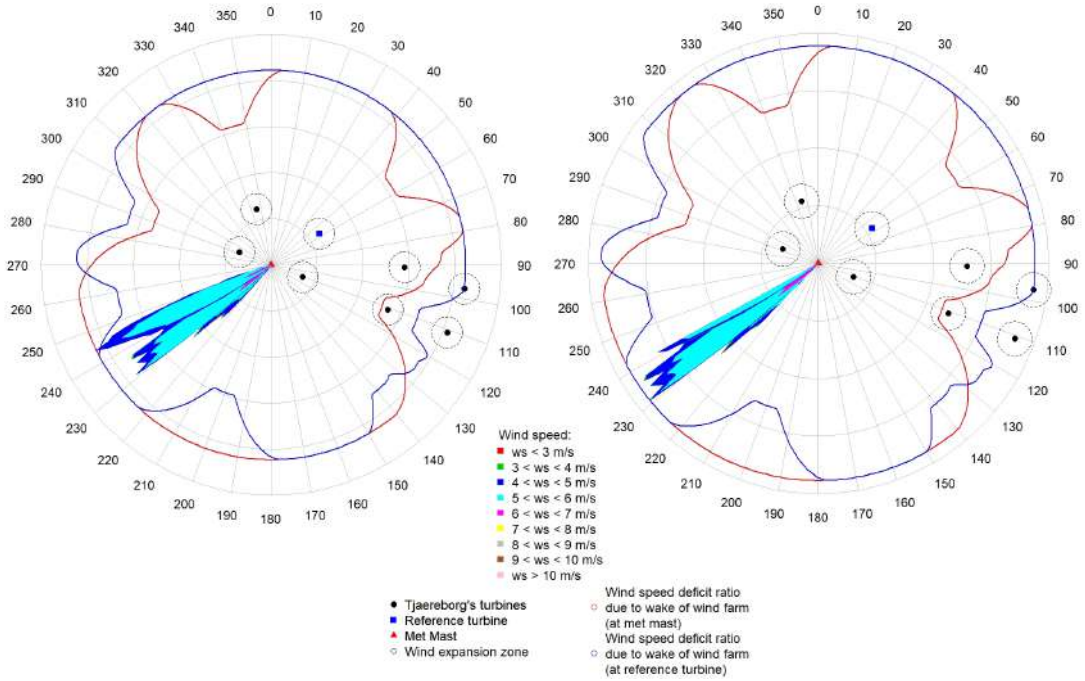

Figure 5.4 – Wake interaction in the wind farm for the chosen time series.

5.2.4 Yaw misalignment filter

An important limitation of the BEM theory is the assumption of rotor alignment with the inflow. In reality large deviations can occur within 30 minutes (see Figure 5.5). The blue curve represents the turbine yaw position and the orange curve the wind direction measured by the met mast. It can be seen that the turbine orientation does not change throughout the 30min time series. The horizontal black dotted lines represent the yaw error allowed, in this example set to be ±5°, around the turbine position. The choice of ±5° allows to deviate slightly from the BEM theory while keeping enough data points for the analysis. The allowed yaw error removes 50% of the entire dataset.

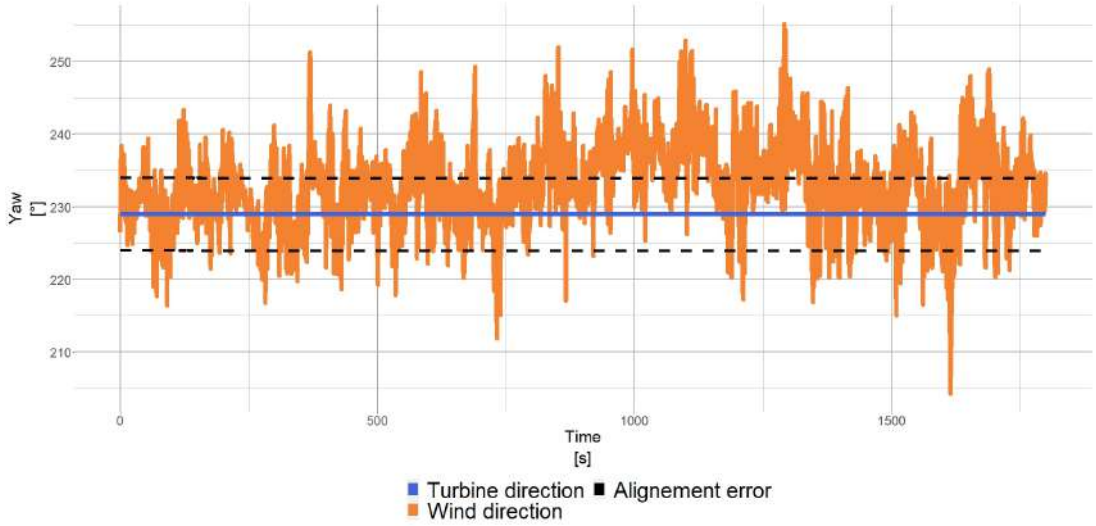

Figure 5.5 – Nacelle alignment discrepancy.

5.2.5 Vertical gradient correction

Rather than filtering out data within the vertical gradient from the atmospheric boundary layer flow (see section 5.2.2) and using a single height measurement as inflow, the present section corrects the wind inflow using known laws describing the vertical gradient velocity profile from atmospheric boundary layer flows (e.g. Monin-Obukhov, power-law). It associates to the analysed section, the calculated inflow based on the azimuthal position. While the Monin-Obukhov method is more accurate than the power-law method to rebuild the wind profile, it requires 10 minutes averaged values to build a velocity profile. It is not fast enough for the correction applied here, since the wind profile is rebuilt for every time-step measured at a sampling frequency of 35Hz. Thus the power-law approach is preferred. The power law exponent, κ, is derived for each time-step i based on the mast anemometer measurement, available at 90m and 57 m above ground:

$$\kappa_i = \frac{\ln(V_{w90_i}) - \ln(V_{w57_i})}{\ln(90) - \ln(57)} \tag{5.1}$$

The blade position, Φ, is discretised per time-step in a Cartesian coordinate system whose origin is centred at the bottom of the tower (x is parallel to the ground and y is parallel to the tower):

$$\begin{cases} x_i = hub_{height} + (r \times \sin(\Phi_i)) \\ y_i = hub_{height} + (r \times \cos(\Phi_i)) \end{cases} \tag{5.2}$$

Finally the wind inflow is reconstructed for each time step using the y_i position of the blade along with the κ_i exponent.

$$V_{w_i} = V_{w57_i} \times \left(\frac{y_i}{57}\right)^{\kappa_i} \tag{5.3}$$

Thanks to equation 5.3, the wind inflow seen by each section is now dependent of the blade azimuthal position. The inflow velocity is assumed homogeneous in the x direction, so that the power law applies across the rotor width. A similar solution was implemented in a BEM codes comparison [87].

5.2.6 Wind inflow location correction

As seen in Figure 3.1, the met mast is far from the turbine, it is installed approximately 300m away. It leads to a discrepancy between the data measured by the mast at t_0 and the data measured by the turbine at t_0. The wind measured by the met mast reaches the turbine after a convective time which depends on the atmosphere state. However, a simple model [158] was found to significantly improve results. Based on a time shift, δt, calculated using the distance between the mast and the turbine accounting for the angle between the mean wind direction and the direction formed by the segment "mast-turbine".

The following time shift is then applied to the met mast data as well as the turbine data:

$$\delta t = \frac{l\cos(\psi)}{V_{w_{mean}}} \tag{5.4}$$

Where l is the distance between the mast and the turbine, ψ is the horizontal angle difference between the mean wind speed direction and the orientation "mast-turbine". In order to assess the pertinence of the convective time correction, the measured electrical power is analysed. At low wind speed the expected power curve evolution is to increase with an increasing wind speed. However, the raw data outcome (blue curve) in Figure 5.6 shows the opposite: the measured power is decreasing with wind speed. When including the convective time correction, the slope is reversed and thus closer to an expected evolution. This clearly demonstrates the importance of the time lag correction.

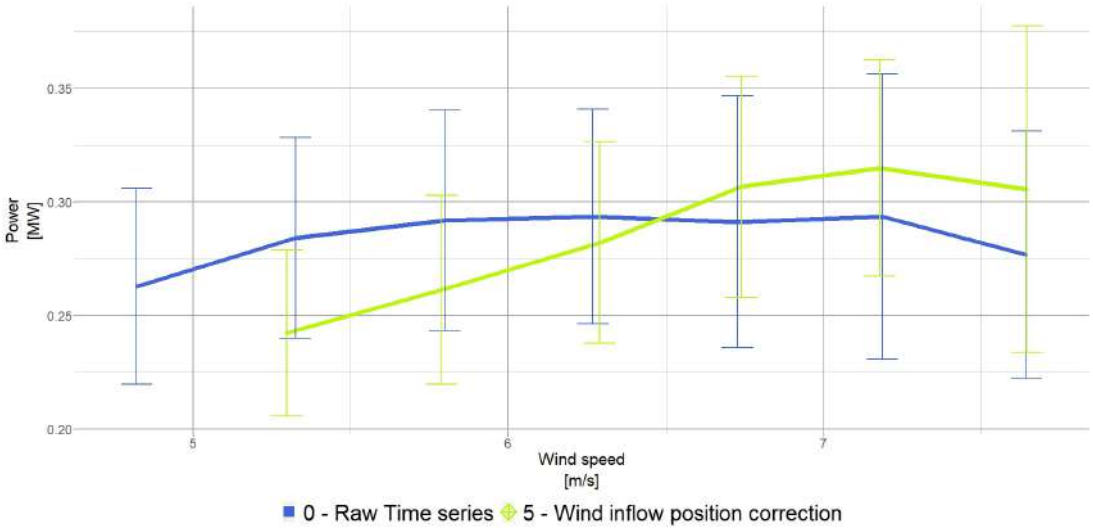

Figure 5.6 – Measured power curve with and without convection time correction.

5.2.7 Unsteady Inverse Blade Element Momentum (UiBEM)

The application of steady BEM method did not yield satisfactory results (see detailed plots from Figure C.4 to Figure C.10). The C_L trend remains opposite to the expected behaviour regardless of the filter or correction applied. In the linear region the lift coefficient decreases while the angle of attack increases, all the while reducing the number of samples available (see Figure 5.9).

The filters and corrections developed, despite ensuring the validity of the BEM equations, do not account for the turbulent conditions and stochastic nature of the environment. For these reasons, the use of the unsteady formulation seems evident. As shown in Figure 2.5, the UiBEM relies initially on steady iBEM computations. The essence of the Unsteady Inverse Blade Element Momentum (UiBEM) doesn't differ from the steady BEM: the aim is to determine the local velocity accounting for atmospheric unsteadiness. The instantaneous local velocity is now considered as a two coordinates vector rather than a scalar as

seen in equation 2.26 and equation 5.5.
The formulation now includes: aeroelastic deformation ($\mathbf{V_b}$), tower shadow effect ($\mathbf{V_{wts}}$), yaw and cone angles ($\mathbf{V_{rot}}$) and dynamic wake ($\mathbf{W}$) [53]. The tilt angle has been ignored as deemed insignificant [124]. This new formulation for the velocity yields an updated velocity triangle (see Figure 5.7).

$$\begin{Bmatrix} V_{rel,y} \\ V_{rel,z} \end{Bmatrix} = \begin{Bmatrix} V_{w_{ts},y} \\ V_{w_{ts},z} \end{Bmatrix} + \begin{Bmatrix} V_{rot,y} \\ V_{rot,z} \end{Bmatrix} + \begin{Bmatrix} W_y \\ W_z \end{Bmatrix} - \begin{Bmatrix} V_{b,y} \\ V_{b,z} \end{Bmatrix} \tag{5.5}$$

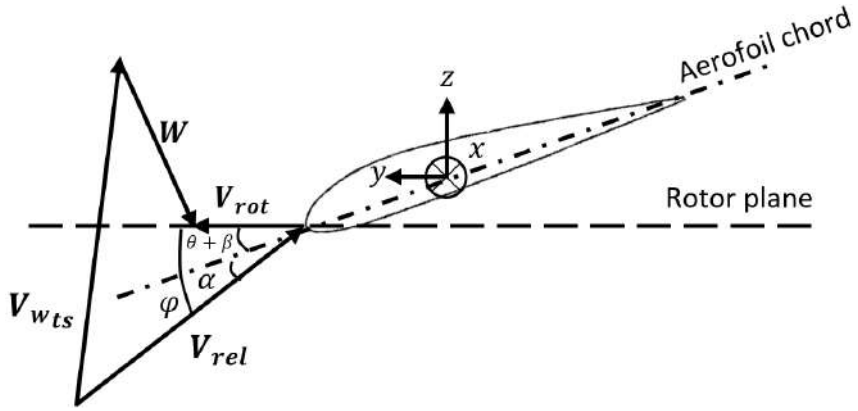

Figure 5.7 – Updated velocity triangle showing the new local velocity formulation. The blade deflection velocity is not pictured.

The DANAERO blade was equipped with tri-dimensional accelerometers (see Table 3.1) positioned along the radius. By applying the equation 5.6 it is possible to use a first approximation of the relative blade velocity based on its local acceleration.

$$V_{b,y} = a_{r,y} \times \frac{1}{f} \qquad V_{b,z} = a_{r,z} \times \frac{1}{f} \tag{5.6}$$

Where $V_{b,y}$ and $V_{b,z}$ are the blade local velocity, $a_{r,y}$ and $a_{r,z}$ are the blade local accelerations and f is the sampling frequency.

Tower shadow effect is the alteration of the uniform inflow due to the tower presence, using potential flow theory Das et al. [29] modelled the tower impact as function of the blade azimuthal position and the blade radius analysed (see equation 2.20).
Many different yaw models exist [64] with various level of complexity and agreement based on the chosen dataset. After benchmarking three different models [15, 100, 90] against a dedicated test case in the DANAERO database, the yaw model from Blondel et al. [15] is chosen (see equation 2.22) because of its better fit on the test case.
The dynamic wake modelling has been developed by Glauert, to account for the time delay before reaching wake equilibrium introduced by the wake deflection behind the rotor in the local velocity definition [135].

Figure 5.8 shows the comparison of all different cases with the corrections and filters developed in Section 5.2.2 to Section 5.2.6 and the reference wind tunnel data. It is apparent that the steady BEM equations are not sufficient to model accurately the expected behaviour of a wind turbine operating in the field. Nevertheless, to ensure remaining within the BEM theory limits, the application of the neighbouring wake filter (Section 5.2.3) is necessary. To account for more realistic inflow conditions the mean vertical gradient velocity correction (Section 5.2.5) and the wind inflow location correction (Section 5.2.6) should be used.

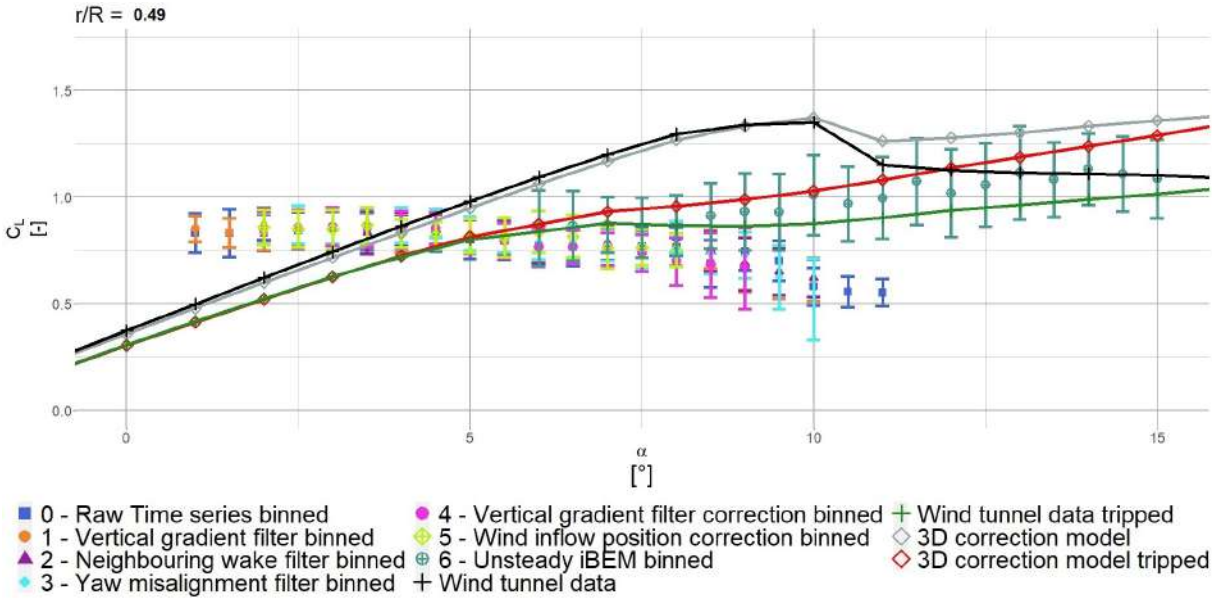

Figure 5.8 – Binned averaged C_L comparison for the radial location $r/R = 0.49$. All the previously filters, corrections and BEM methods are overimposed.

The use of the UiBEM method highlights the importance of the unsteady part in a field data analysis. Firstly, in a physical analysis point of view, the addition of dynamic wake changes the C_L trend outcome thanks to the more accurate description of the inflow velocity. The lift coefficient evolution follows now the trend measured in a wind tunnel rather than the flat or even decreasing $C_L(\alpha)$ relationship seen when using the steady BEM equations. We can also see that some rotational effects are present since the mean results hover between the 2D and 3D corrected lift curves. The error bars show the dispersion in the results and most probably show the effect of transition location displacement, or the intermittent apparition of the flow separation, both phenomena missing in the state-of-art of BEM models. However, available measurements are limited to explain further this dispersion, as instantaneous angles of attack and wind inflow conditions must be known locally in front of the studied aerofoil for that purpose. Secondly, in a statistical point of view, including the unsteady equations improves the confidence in the results. Thanks to the tower shadow model and the yaw model a larger set of samples can be kept compared to the steady BEM equations. Figure 5.9 shows the number of samples converged using iBEM solver with the progressive application of filters and different corrections (from case 0 to case 5) at two radial locations. The addition of the transparent and opaque shaded

area represents the total available number of samples to be analysed after the cumulative application of filters and correction models. The transparent shaded area is the non-converged part of the total number of samples. The converged number of samples decreases with the application of correction and filters (down to 10000 samples for $r/R = 0.49$). It also highlights that the number of input samples and converged samples after the application of the unsteady BEM equations increase drastically. For the tip section the number of converged samples, when using the UiBEM method, is even greater than the raw analysis (see Figure 5.9b). For both sections, when using UiBEM, a maximum of 72% of the available dataset is analysed because of wake effect between neighbouring turbines; out of which 85% have achieved convergence.

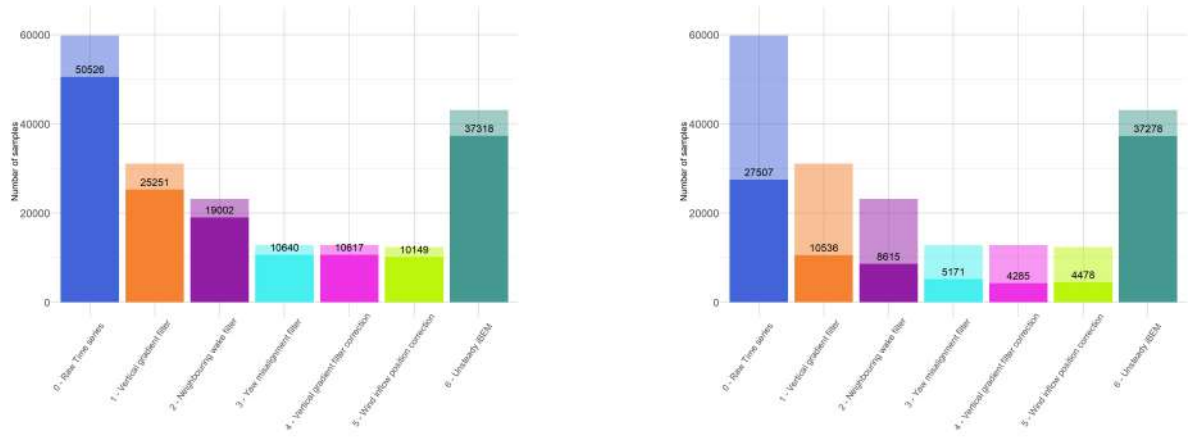

(a) Radial location $r/R = 0.49$.

(b) Radial location $r/R = 0.95$.

Figure 5.9 – Effect on the data points converged of the filters, the corrections and unsteady BEM equations for different radial locations. The transparent shaded area represents the available data points after application of the filters, the opaque area represents the converged number of samples through the iterative iBEM procedure.

5.3 Summary

Using an in-house developed Unsteady inverse BEM solver, the limitations of engineering models were assessed. The aim was to twofold: analyse the rotational effect on aerodynamic coefficient in the field and identify clearly the BEM limits regarding unsteady phenomena. Several filters and correction models were implemented, whose effects on the BEM hypotheses were analysed. The main outcome is that applying only the steady BEM formulation does not prove sufficient enough to capture the dynamic behaviour of the turbine in the field despite the filters developed. In order to better calculate the mean C_L from field measurements, the use of UiBEM is mandatory, since it models the dynamic nature of the inflow and turbine response. However, as hinted in Appendix C.3, more local phenomena involving the flow around the aerofoil are at play, which the state of the art BEM models cannot yet capture. Building upon that knowledge, the following chapters are dedicated to use higher fidelity models to account for aerodynamic unsteadiness and include it into lifetime calculations.

Chapter 6

Impact of blade root spoilers using 2D unsteady simulations

Contents

The flow at the blade root area is highly 3D and unsteady, especially if a spoiler is added. As a first approach and to develop a simplified methodology to estimate fatigue loading during the blade design phase, 2D unsteady simulations are performed. After performing a validation of ISIS-CFD for 2D external aerodynamic cases (see Section 4.2), simulations of the ENGIE-Green blade shape with and without add-on are performed and results are detailed below.
The impact of the spoiler is analysed at the blade location, $r/R = 0.13$. It will be done using URANS simulations from the ISIS-CFD solver (described in Section 2.2.2 and Section 4.2). The steady and unsteady simulation outcomes with and without spoiler are compared in term of aerodynamic forces, local pressure, velocity distribution, Power Spectral Density and instantaneous spatial vortex organisation in Section 6.1 and Section 6.2. All calculations presented are assuming a non-dimensional aerofoil chord. Note that this work has been published in [112].

6.1 Steady aerodynamics

A comprehension of averaged phenomena is necessary before analysing the unsteady behaviour. The first focus will be on the angle of attack $\alpha = 6°$, in the linear part of the lift curve, as it illustrates the first noticeable unsteadiness in the flow, which will be detailed later.

6.1.1 Mean flow reorganisation

The high-velocity region on the upper side (Figure 6.1), associated with a low field pressure level (Figure 6.2), exhibits a longer overspeed area over the upper side for the spoiler case than for the no spoiler case. It induces a longer and stronger negative pressure, in good qualitative agreement with the steady results from [48]. The pressure coefficient C_p, is defined as $C_p = \frac{P_{meas} - P_{ref}}{0.5 \times \rho \times V_{rel}^2}$, where P_{meas} is the measured pressure at the aerofoil's wall, P_{ref} is the reference pressure, ρ is the air density and V_{rel} is the relative wind speed. On the lower side, the high velocity region (Figure 6.1) is more important for the no spoiler case than for the spoiler case, inducing a larger negative pressure region on the lower side of the aerofoil.

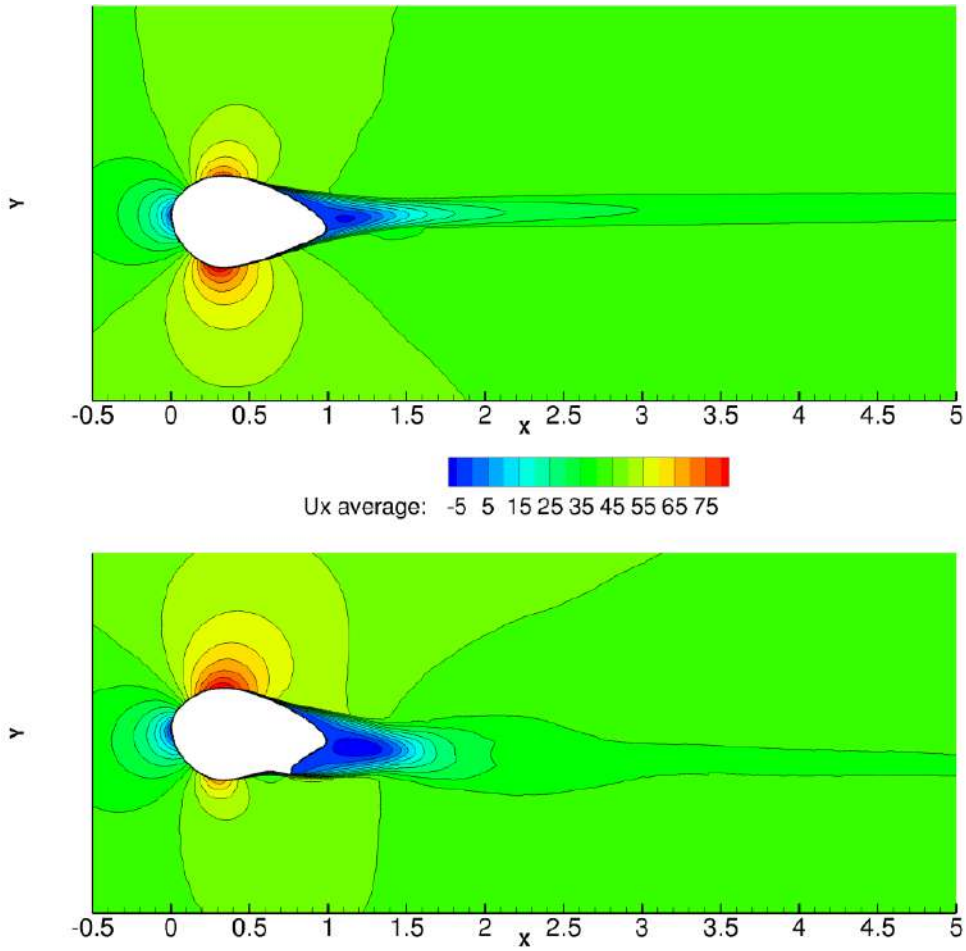

Figure 6.1 – Average horizontal wind speed contour plot for $\alpha = 6°$ and $Re_c = 3 \times 10^6$: top - no spoiler case, bottom - spoiler case.

At the wall, the associated pressure coefficient (C_{p}) clearly shows that the aerofoil with spoiler has a distribution closer to thinner aerofoils, with a much larger net area between the upper and lower curves and thus a much larger lift than the reference case (see Figure 6.3b).

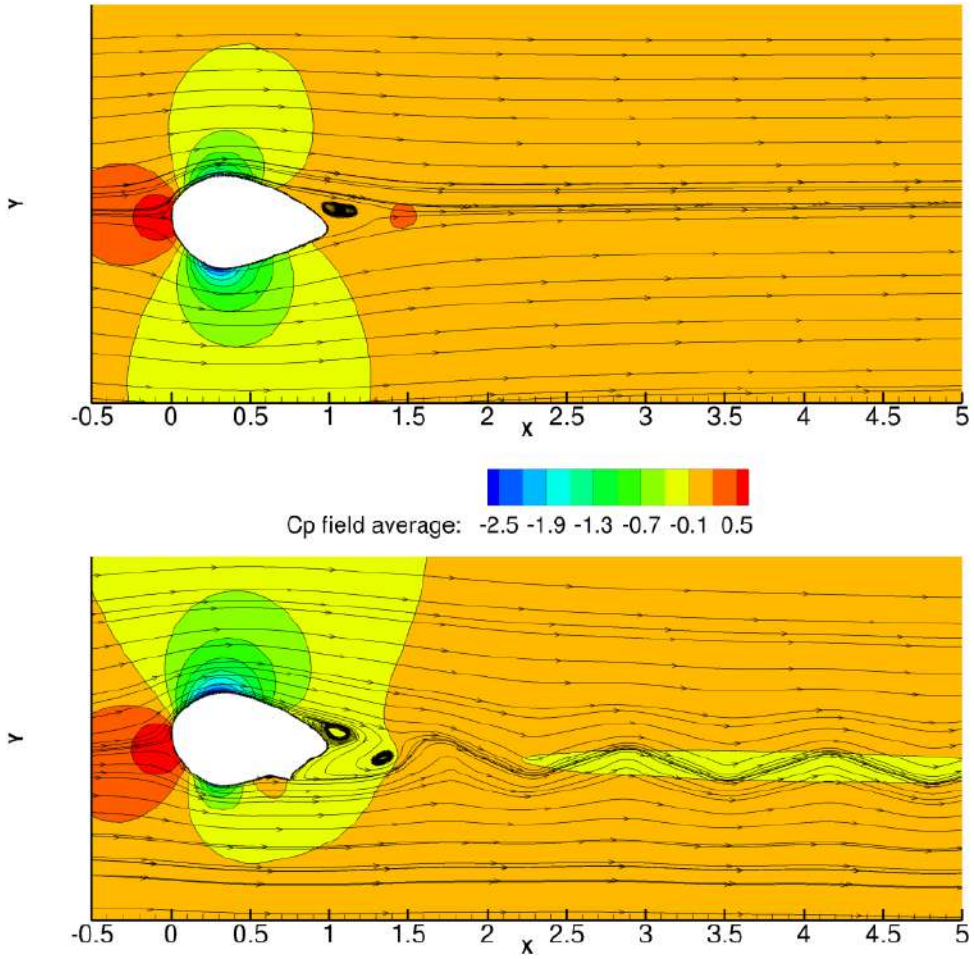

Figure 6.2 – Average pressure field contour plot and instantaneous velocity streamlines for $\alpha = 6°$ and $Re_c = 3 \times 10^6$: top - no spoiler case, bottom - spoiler case.

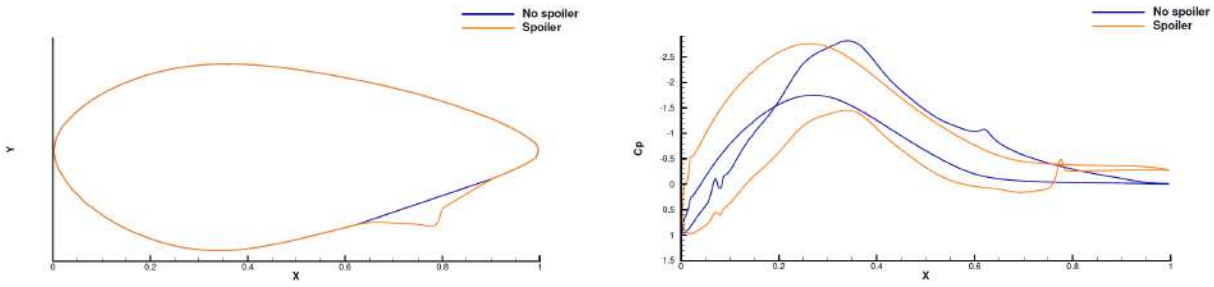

(a) Comparison of the aerofoil shape with and without spoiler.

(b) Average wall pressure coefficient plot for $\alpha = 6°$ and $Re_c = 3 \times 10^6$.

Figure 6.3 – Illustration of the aerofoils shapes along with the mean wall pressure coefficient.

6.1.2 Steady aerodynamic polar

For $\alpha = 6°$, the lift gain when adding a spoiler is $\Delta C_{\mathrm{L}} = 1.34$. This gain however varies with the angle of attack, as can be seen in Figure 6.4. For the no spoiler case, between $-4°$ and $10°$, the C_{L} is decreasing in the linear region to reach negative values. This phenomena has been reported by Schaffarczyk et al. [120]. The authors analysed a symmetrical thick profile without spoiler at a higher Reynolds number ($Re > 6 \times 10^6$). Between $10°$ the C_{L} increases along with the C_{D}. Beyond $14°$ both aerodynamic coefficients exhibit a bluff-body behaviour. Whereas, for the spoiler case, the lift behaviour is more usual for such Reynolds numbers, a clear negative stall in the vicinity of $-4°$ can be seen and a positive stall around $8°$ can be seen despite the constant C_{L} increase.

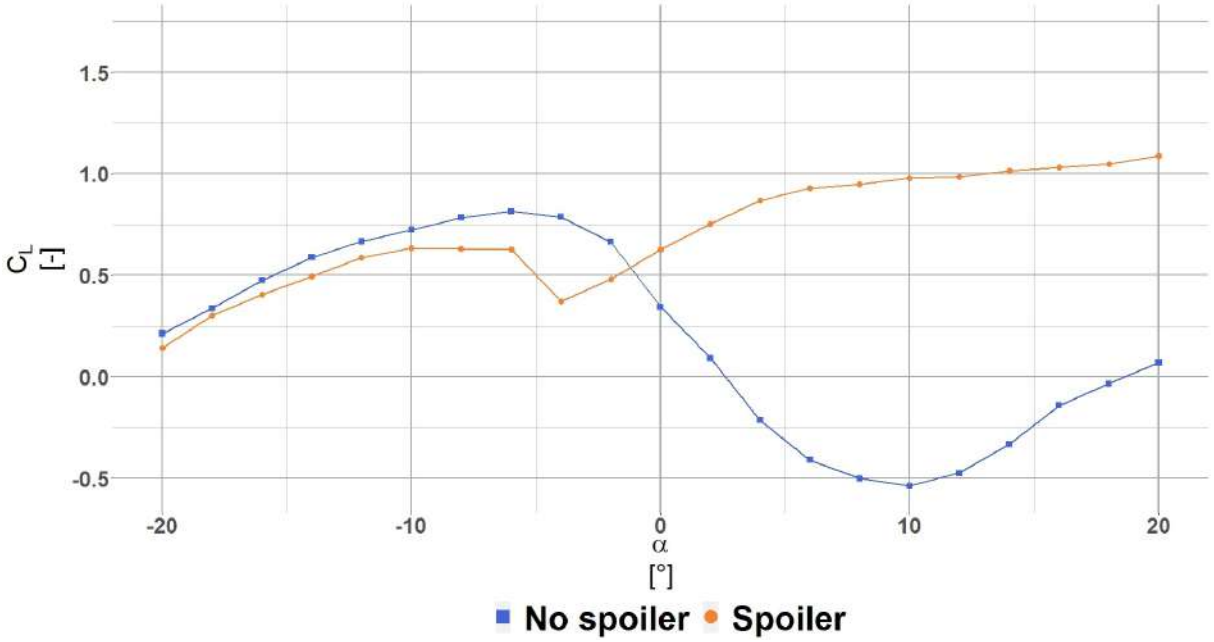

Figure 6.4 – Lift coefficient polar for the radial position R6 ($r/R = 0.13$). The blue square (■) shows the C_L for the no spoiler case and the orange dot (●) shows the C_L for the spoiler case.

In the wake region, the mean streamwise velocity component, U_x, shows that the mean recirculating area (negative streamwise velocity) behind the aerofoil with spoiler is wider and extends further downstream (see Figure 6.1) compared to the no spoiler case. This larger wake reflects a drag penalty generated by the spoiler addition that is found to be of the order of $\Delta C_{\mathrm{D}} = 0.0825$ for $\alpha = 6°$. Again, the penalty is highly dependent on the angle of attack (see Figure 6.5). There is almost no drag penalty at low angles of attack, up to $\alpha = 0°$. Beyond, the spoiler operates at a significantly higher C_{D} than the no spoiler case.

Figure 6.5 – Drag coefficient polar for the radial position R6 ($r/R = 0.13$). The blue square (■) shows the C_D for the no spoiler case and the orange dot (●) shows the C_D for the spoiler case.

In summary, the impact of the spoiler is a redistribution of the global forces so that the thick root sections become more efficient in terms of lift force at the cost of drag penalty. This known conclusion is in good agreement with the literature of sub-boundary layer GF, except that the lift gain and the drag penalty are much more important and quantified here ($\Delta C_\mathrm{L} = 1.34$ and $\Delta C_\mathrm{D} = 0.0825$ for $\alpha = 6°$). Globally, in terms of lift gain, adding a spoiler is found to be detrimental for the negative angles of attack while of high interest for higher angles of attack. Another drawback of the spoiler addition is the unsteady effects such as shown by the waviness in the instantaneous streamlines behind the spoiler case (see Figure 6.2) and will be detailed in the following section. The unsteadiness behind large devices at high Reynolds numbers had not yet been evaluated. Unsteady Reynolds-averaged Navier–Stokes results of such phenomena are detailed in Section 6.2.

6.2 Unsteady aerodynamics

The unsteady flow organisation behind thick aerofoil profiles with or without spoiler at high Reynolds numbers is studied here. The flow analysis focuses on such a configuration for one angle of attack first ($\alpha = 6°$), and then the aerodynamic polar ranging from $-20° < \alpha < 20°$ will be presented. Spoiler unsteady impacts mostly focus on the wake region, which will be analysed further in terms of instantaneous vorticity, Q criteria, local wall pressure (C_p) and global forces, and power spectral density (PSD) analysis.

6.2.1 Wake region

The wake can be separated into a near-wake region, from $1 < {}^{x}/_{c} < 2$, and a far-wake region, which extends to half of the computing domain (20 chords in length). This far wake is shown in a truncated illustration in Figure 6.1 and Figure 6.2 until ${}^{x}/_{c} = 5$.

Near wake region

After the convergence is reached, the spoiler case shows a periodic C_{L} and C_{D} behaviour, whereas the no spoiler case does not vary in time (see Figure 6.6a), as expected. For the spoiler case, the net area between the C_{p} curves varies progressively in synchronicity with the C_{L} extrema (the red dot illustrates $C_{L_{\max}}$ and the blue dot corresponds to $C_{L_{\min}}$ in Figure 6.6b), leading to a progressive increase and decrease in the lift and drag, as illustrated in Figure 6.8.

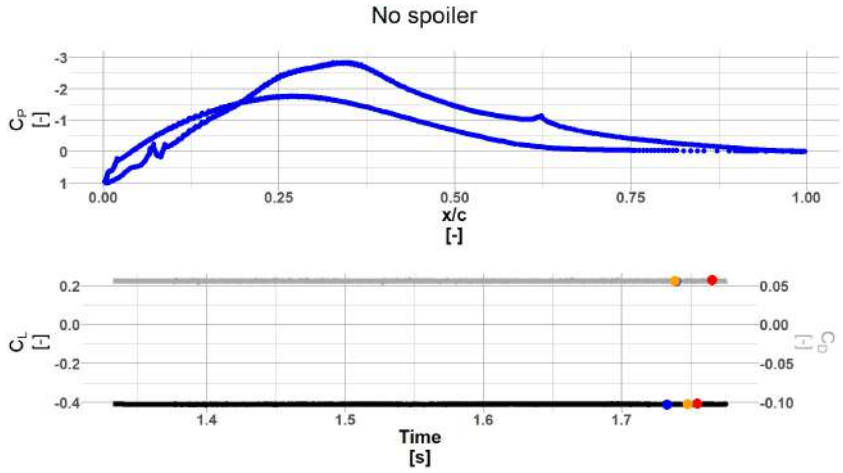

(a) No spoiler case C_L and C_p absence of synchronicity

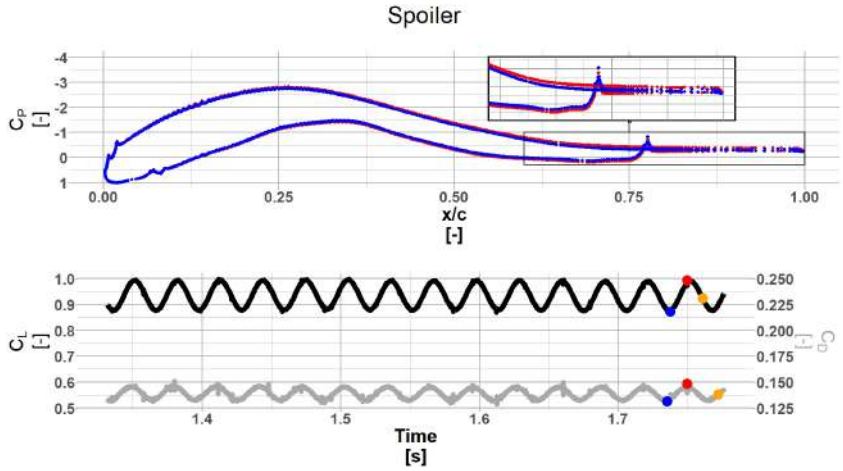

(b) Spoiler case C_L and C_p synchronicity

Figure 6.6 – C_p and aerodynamic coefficients evolution in time $\alpha = 6°$ and $Re_c = 3 \times 10^6$. For both the C_p and C_L/C_D plot, the blue dot (●) corresponds to the minimum C_L, the red dot (●) corresponds to the maximum C_L. On the C_L and C_D plot the orange dot (●) corresponds to the mean C_L.

The near-wake region is zoomed in Figure 6.7. It is illustrated by co-plotting a snapshot of the vorticity sign with the Q-criteria. Both instantaneous snapshots show vortices formed in the near-wake region due to the roll-up of the separated shear layers from both, the upper and lower sides of the aerofoil. For the no spoiler case, the black lines (isolines of $0 <$ Q criteria < 1000) clearly show that vortices are symmetric with the wake centre line. For the spoiler case, the separation of the shear layer clearly starts on the lower side of the aerofoil while the black lines are no longer symmetric with the wake centre line. The time evolution of this near-wake organisation exhibits periodic interaction of vortices from each side of the aerofoil. The vortex from the pressure side is rolling up onto the suction side, thereby forcing the upper side separation periodically.

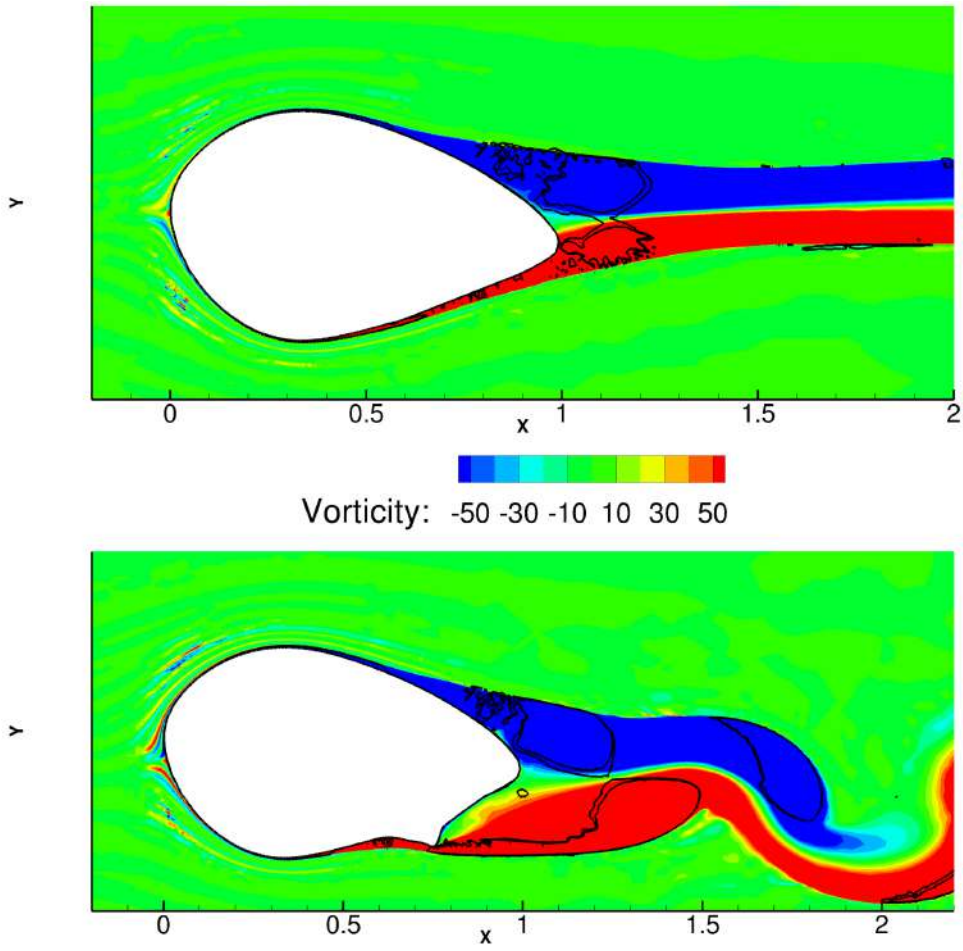

Figure 6.7 – Vorticity contour plot with Q-criteria lines for $\alpha = 6°$ and $Re_c = 3 \times 10^6$, top - no spoiler case, bottom - spoiler case. Red is counterclockwise flow rotation and blue clockwise flow rotation.

In terms of energy production, it is interesting to extract the snapshot of the near-wake organisation at $C_{L_{\max}}$. For that purpose, the different C_{L} can be analysed together with the spatial vortex organisation (see Figure 6.8). The lift is at its minimum (blue dots) when the top vortex is "far" from the trailing edge and the lower side vortex is rolling up toward the upper side. The mean C_{L} (orange dots) is characterised by having both vortices close to the trailing edge: the top side vortex already separated from the surface

and the lower one still attached to the spoiler's tip. Finally, the maximum lift (red dot) is seen when the lower side vortex is about to separate from the spoiler's tip and the upper side vortex is at its maximum size (it just left the aerofoil's surface). Consequently, it indicates that the pressure is at its lowest on the upper side. Therefore, in terms of energy production, having shed vortices at their maximum size and the closest to the trailing edge is the best flow organisation.

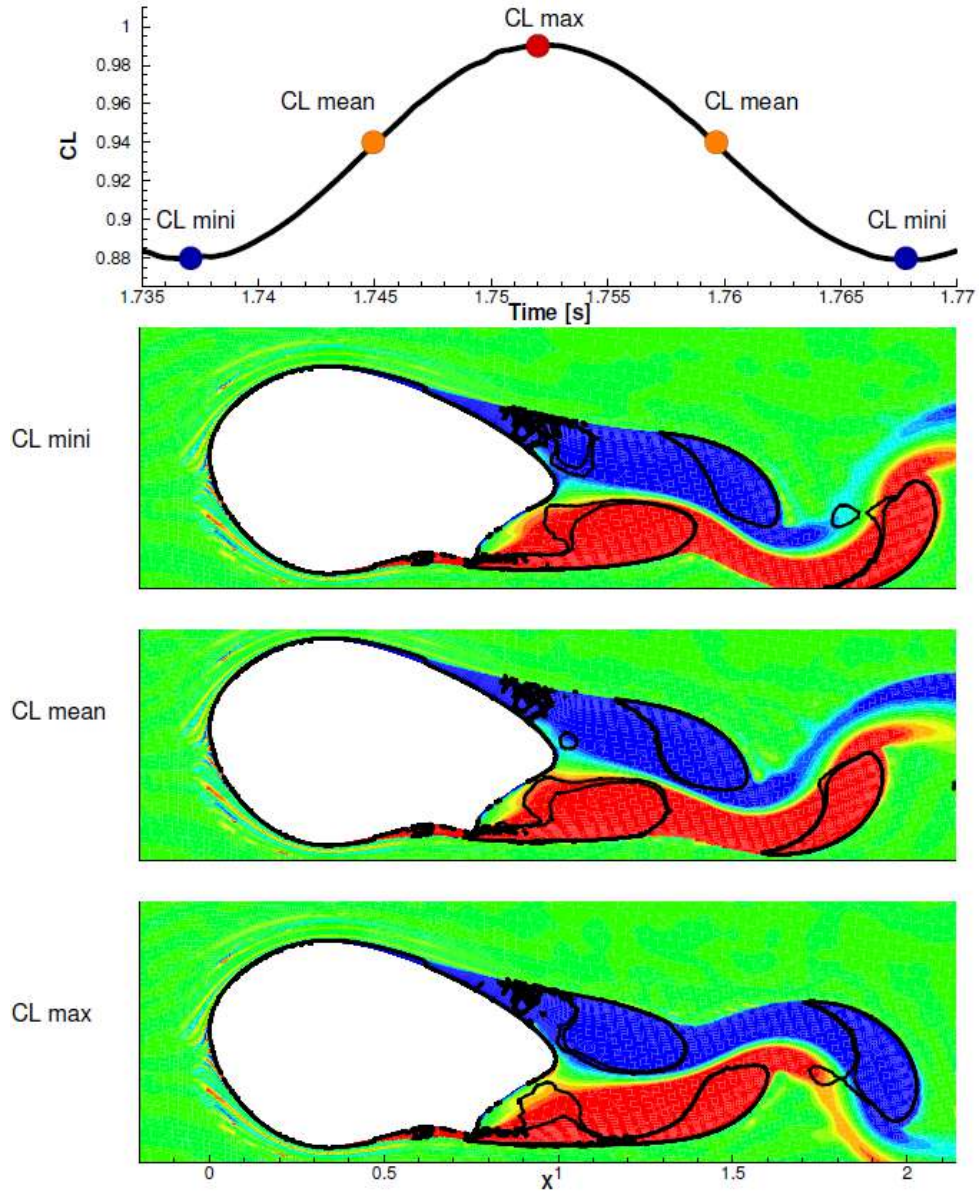

Figure 6.8 – Spoiler case illustration of vortices in the vicinity of the trailing edge in relation with the lift coefficient evolution for $\alpha = 6°$ and $Re_c = 3 \times 10^6$. The contour plots depicts instantaneous vorticity contour with Q-criteria lines.

Far wake region

In the far-wake region, a single peak frequency emerges, with its harmonics, that can be extracted at $x/c = 3.0$ using PSD analysis (see Figure 6.9). The energy content for the no spoiler case is several orders of magnitude lower than the spoiler case as expected.

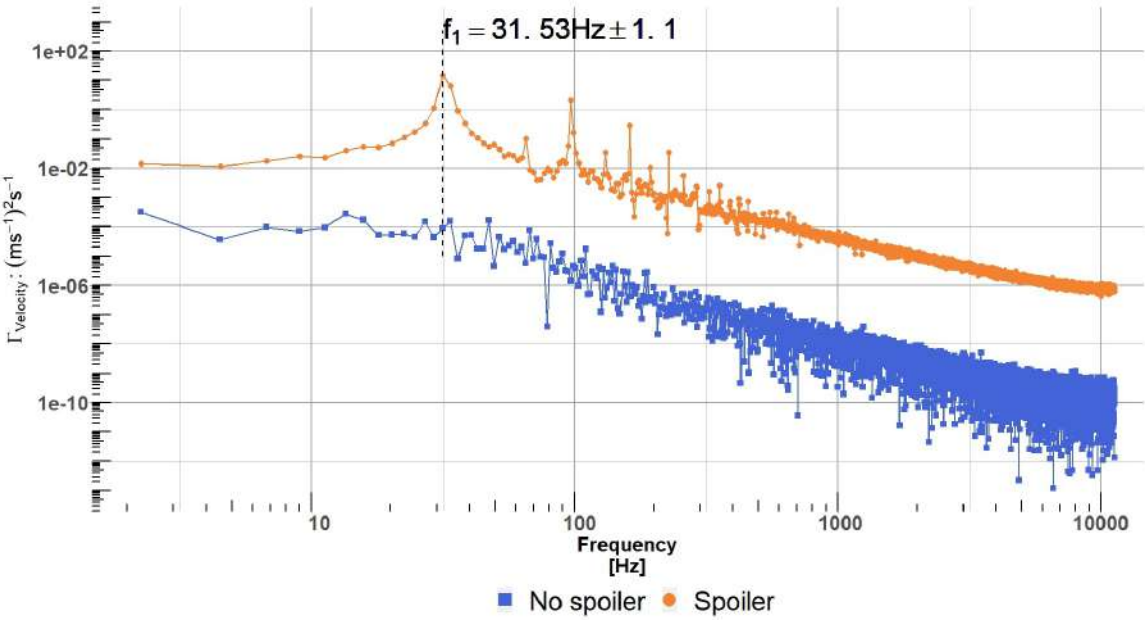

Figure 6.9 – Horizontal velocity PSD, in the wake, at $x/c = 3.0$. The blue square (■) shows the no spoiler case while the orange dot (●) shows the spoiler case.

At last, following the definition of Yarusevych et al. [159], a Strouhal number of $S^*_{t\text{-spoiler}} = 0.15$ is found. In this definition, the velocity used is the mean free stream velocity, and the characteristic length (L) is the distance between two mean horizontal velocity root mean square extrema at $x/c = 3.0$. The Root Mean Square (RMS) peaks represents the aerofoil upper side vortex centre and aerofoil lower side vortex centre. Therefore the vertical distance can be viewed as a representation of the wake width. As seen in Figure 6.10, the no spoiler case does not present two distinct peaks, only a single bell-type curve representing the velocity deficit in the wake. The spoiler case also shows a larger velocity deficit accompanied by a pair of RMS peaks showing the presence of the vortex centres.
The presented results were calculated assuming an unit chord ($c = 1$) for both the no spoiler and spoiler case. Consequently, for a real scale blade dedicated analysis are necessary. To keep the Reynolds similarity the inflow will change along with the chord. Therefore, the peak frequency calculated here will change (as seen in Chapter 8). The Strouhal number, though, remains unchanged.

$$St^*_{spoiler} = \frac{f \times L}{V_{rel}} = \frac{31.53 \times 0.2191}{45} = 0.15 \tag{6.1}$$

Where f is the main vortex shedding frequency, L is the characteristic length and V_{rel} is the incoming velocity.

This result falls in line with Yarusevych et al. study, where $S_t^* \approx 0.17$ was found, albeit in our case at a much higher Reynolds number and for a much thicker aerofoil and equipped with spoiler.

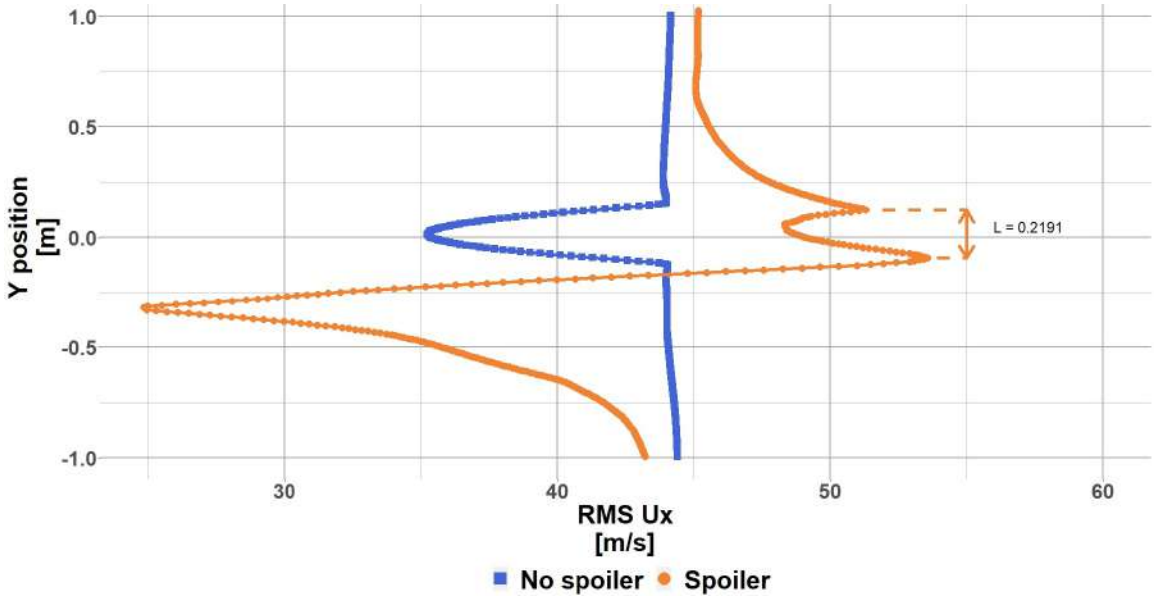

Figure 6.10 – Mean Horizontal velocity Root Mean Square value for the radial position R6 ($^r/_R = 0.13$) at $\alpha = 6°$ and at $^x/_c = 3$. The blue square (■) shows the RMS for the no spoiler case and the orange dot (●) shows the RMS for the spoiler case.

6.2.2 Unsteady aerodynamic polar

This unsteady analysis for the angle of attack: $\alpha = 6°$ is extended towards other angles of attack. The vortex shedding organisation previously described induces oscillations on the surface pressure and therefore the aerodynamic coefficients C_L and C_D.

The behaviour described for the angle of attack $\alpha = 6°$ is present throughout the polar for both cases with varying amplitude of the oscillations. The maximum and minimum of these oscillations are reported in Figure 6.11 and Figure 6.12. The no spoiler case shows a decreasing variation in lift and drag coefficients from $-20° < \alpha < -8°$. The variation in aerodynamic coefficients for the spoiler case is higher for the negative angle of attack and in the linear region. It increases drastically after 10°, showing a possible stall behaviour, as highlighted by the coloured areas. Beyond 14° the variation amplitude is similar to the actual mean aerodynamic value (for the C_L). Overall, the spoiler case adds a lot more variation in the aerodynamic loads when it becomes efficient (i.e. the lift is increased).
The peak frequency associated to the vortex shedding is changing with the angle of attack. For an increasing angle of attack the vortex shedding frequency is diminishing until reaching a plateau. The Figure 7.15 compares the vortex shedding frequency at real scale for both cases at the radial position $^r/_R = 0.13$. In the deep stall region, once the spoiler is no longer perceptible by the flow, the curves merge.

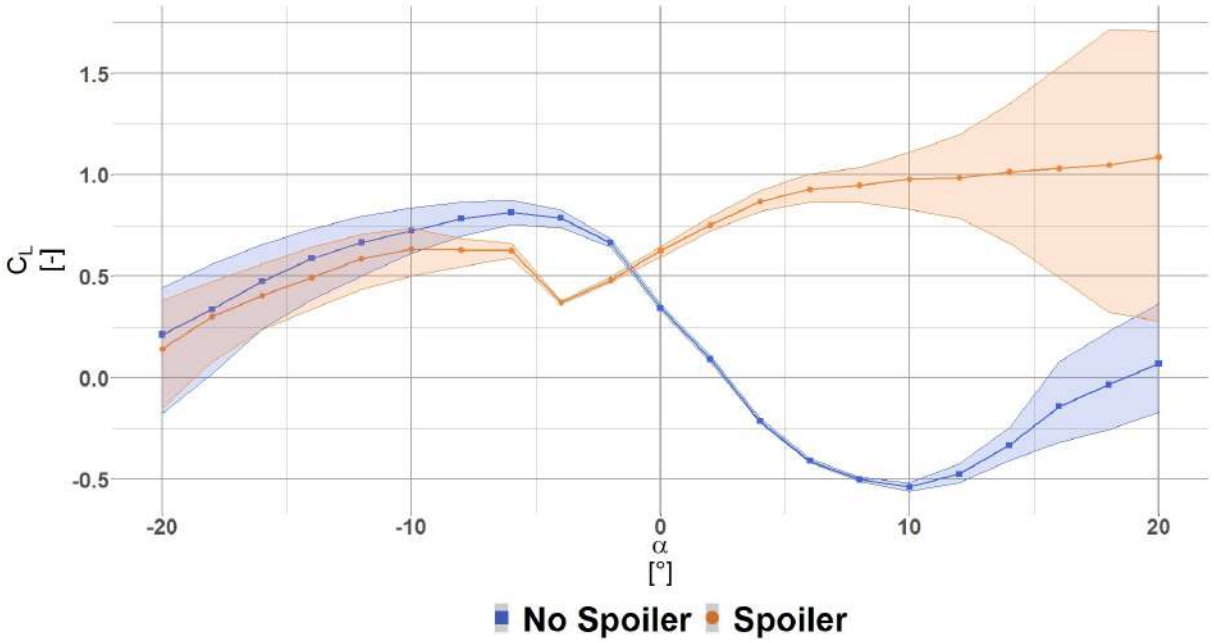

Figure 6.11 – Unsteady lift coefficient polar for the radial position R6 ($r/R = 0.13$). The blue square (■) shows the C_L for the no spoiler case and the orange dot (●) shows the C_L for the spoiler case.

Figure 6.12 – Unsteady drag coefficient polar for the radial position R6 ($r/R = 0.13$). The blue square (■) shows the C_D for the no spoiler case and the orange dot (●) shows the C_D for the spoiler case.

6.3 Summary

The Chapter 6 proposes an original 2D URANS description of the unsteady flow behind thick aerofoil (59 %) from an operating 2 MW wind turbine equipped with spoilers at high Reynolds numbers. This aerodynamic add-on is found to efficiently rearrange the mean flow, adding lift throughout the positive angles of attack. However, the drawback is a high drag penalty coupled with an increased unsteadiness of the aerodynamic forces. Without spoiler, the aerofoil wake is erratic and not organised. With spoiler, a peak frequency is dominant in the aerodynamic lift and drag coefficients, which corresponds to a vortex shedding organisation. The associated Strouhal number is almost constant $St^* = 0.15$ despite the aerodynamic coefficient variation amplitude changing with the angle of attack. The wake energy content is increased by several orders of magnitude compared to the aerofoil without spoiler. This flow reorganisation is present throughout the polar range and is accompanied by larger variation in aerodynamic forces than without spoiler. The impact of this type of excitation will be quantified further in terms of energy production and fatigue in the next chapter (see Chapter 7).

Chapter 7

A NEW METHODOLOGY TO ESTIMATE BLADE LIFETIME ACCOUNTING FOR UNSTEADINESS

Contents

The scanned wind turbine blade equipped with root spoilers is analysed using time domain aeroelastic BEM simulations to assess the impact of passive devices on the turbine AEP and lifetime. Previous 2D CFD simulations showed a large unsteadiness in aerodynamic coefficients associated with the spoiler (see Chapter 6). Such behaviour is captured by the OpenFAST simulations when all degrees of freedom are switched off. Once the turbine is fully flexible, a novel way to account for aerofoil-generated unsteadiness in the fatigue calculation is proposed and detailed. The following chapter has been published in the following article [108].

7.1 Methodology

7.1.1 Wind turbine blade and aerofoil shape

The wind turbine geometry used was acquired during a scanning campaign on an operating 2MW turbine (see [28]); the rotor diameter is 92m and the maximum height reached is 150m above ground. During the scan post-processing the chord, twist and thickness were also extracted, defining the blade geometry (see Figure 7.1a). The blade geometry is discretised more densely at the root of the blade since the spoiler is installed at this location. More details about the scan post-processing are available in [112] and in

. The scanned blade was originally equipped with root spoilers. The blade without spoiler was generated by manually removing parts of the cloud points corresponding to the spoiler location; consequently wherever the spoiler is not present both aerofoils geometries are identical (see Figure 7.1b). For the rest of the study, the simulations will take place on the real scale, i.e. using the scan outputs as blade geometry.

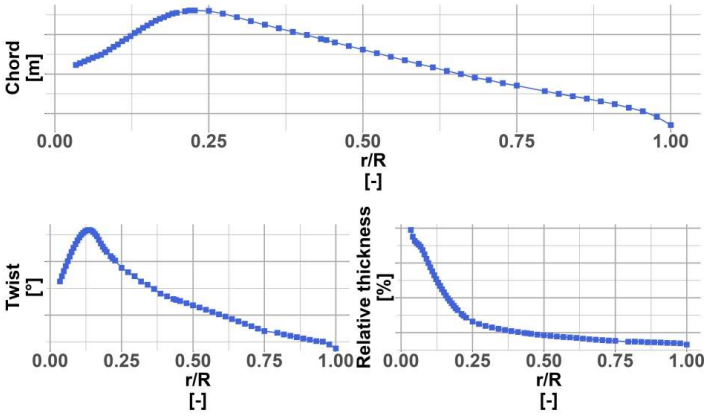

(a) The scanned blade geometry.

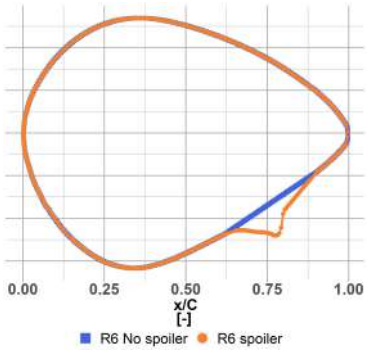

(b) Overimposed aerofoil shapes at $r/R = 0.13$.

Figure 7.1 – Left: scanned blade geometry: chord, twist and relative thickness distribution against the normalised radius. Right: overimposed aerofoil shapes at radial position R6 ($r/R = 0.13$): the blue square (■) shows the no spoiler coordinates while the orange dot (●) shows the spoiler coordinates.

7.1.2 Unsteady aerodynamic BEM inputs

The tools used to perform the spoiler impact assessment are CFD for the polar generation and blade element momentum (BEM) theory for the aerodynamic calculations. BEM is used to calculate associated loads and compute the turbine annual energy production (AEP). The BEM solver used is the AeroDyn module (see [73] and Section 2.1.3) from OpenFAST (Section 2.1.2). OpenFAST can produce a large variety of *sensors*, which are calculated outputs during the simulation. AeroDyn is a well-known tool developed by NREL and has been used in many international or academic projects. A brief step-by-step approach in Section 2.1.1 summarises the BEM iterative procedure. The procedure described relies on steady polar to perform the iterative steps; it is an inherent BEM limitation. However, as highlighted the Chapter 6, aerodynamic properties become highly unsteady at the blade root when a spoiler is present.

To overcome the single steady polar limitation and the use of steady coefficient, it was decided to generate three steady polars corresponding to the mean, minimum and maximum C_{L}, C_{D} and C_{M} for each turbine case: no spoiler and spoiler (see Table 7.1).

Table 7.1 – Turbine configurations analysed

Turbine configuration	**Aerodynamic coefficients values**
No spoiler	Mean aerodynamic coefficients
No spoiler	Maximum aerodynamic coefficients
No spoiler	Minimum aerodynamic coefficients
Spoiler	Mean aerodynamic coefficients
Spoiler	Maximum aerodynamic coefficients
Spoiler	Minimum aerodynamic coefficients

Those mean, minimum and maximum coefficients are representative of the states reached by the aerodynamic coefficients during the time series calculated using 2D CFD as found in [112] (see e.g. Figure 7.2).

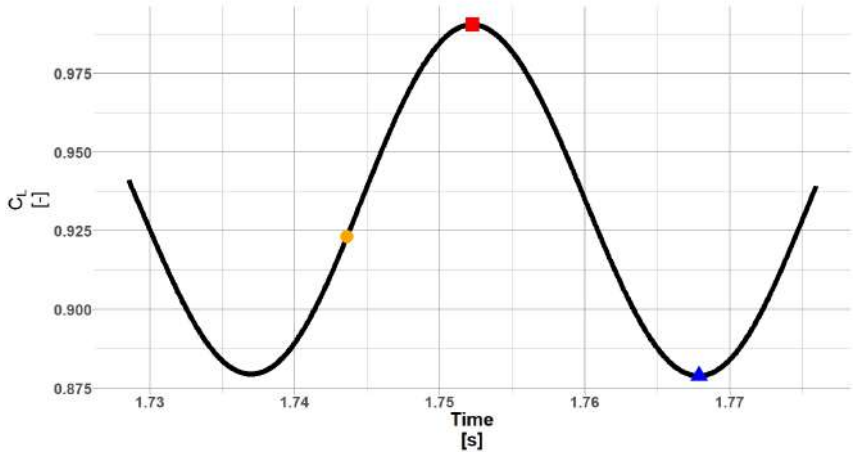

Figure 7.2 – Spoiler case C_L evolution in time $\alpha = 6°$ and $Re_c = 3 \times 10^6$ a radial position $r/R = 0.13$. The blue triangle (▲) corresponds to the minimum C_L, the red square (■) corresponds to the maximum C_L, the orange dot (●) corresponds to the mean C_L.

7.1.3 Turbine structure scaling

The scan does not give any information on the blade's material, since only the outer shell was measured. Material properties are a crucial element for turbine design, and as part of an academic or wind turbine exploiting party, this sensitive information remains classified. Therefore, for the rest of the aeroelastic study, the blade and tower mechanical properties will be scaled using the open-source NREL 5MW turbine (see [74]). Some hypotheses and assumptions had to be made and will be explained below.
Usually, scaling is made to reach the same level of stress or reach similarity in physical phenomena: Mach number, Reynolds number and Froude number (see [20]).
Here, since the stress target values are unknown and the physics similarity is already

achieved (Mach, Reynolds and Froude numbers close enough between the NREL turbine and the ENGIE Green turbine), the turbine has been scaled based on geometric properties. The NREL turbine has a 63m long blade and its tower is 87.6m heigh. In comparison the ENGIE Green turbine has a blade length of 45m and the tower height is 80m. Several scaling procedures exist and have been described in [86, 21]. In those references, the authors aimed at creating a sub-scale model for wind tunnel or field testing, where the difference between both models is large (reduction factor up to 90). In this case, the desired aim was that the ENGIE Green turbine behaves similarly to the NREL one, i.e. use the known mechanical properties and adjust them based on the smaller blade and tower length. Therefore, the method used here varies slightly compared to the literature and is described below.

The blade structural properties needed are the edgewise and flapwise local stiffnesses along the radius: EI_{xx} and EI_{yy}, as well as the linear mass M_{L}. E is the Young modulus while I_{xx} and I_{yy} are respectively the in-plane and out-of-plane sectional moment of inertia. Assuming an identical material is used to manufacture both blades, only the sectional inertiae I_{xx} and I_{yy} vary. Since the sectional inertia varies based on geometric properties, it was decided to use the chord as the main driver for the change in properties. The thickness could also have been chosen, but the chord was preferred because of its larger absolute value. Also, the edgewise stiffness could have been scaled based on the chord thickness and thickness for the flapwise stiffness. It was decided to only use the chord as a basis for the scaling for simplicity. Further studies could be done to assess the validity of the assumption. In the chosen geometric scaling, the NREL 5MW stiffnesses EI_{xx} and EI_{yy} were multiplied by the ratio of the local chord along the radius to the power of 4 (see equation 7.1), thanks to dimensional analysis. Following the same reasoning, assuming an identical material, the NREL 5MW linear mass needs to be multiplied by the chord ratio at the power of 1 (see equation 7.2). The same methodology is applied to the tower stiffnesses and mass.

$$EI_{xx_j}^{EG} = EI_{xx_j}^{NREL} \times \left(c_{r/R_j}^{NREL}/c_{r/R_j}^{EG}\right)^4 \; EI_{yy_j}^{EG} = EI_{yy_j}^{NREL} \times \left(c_{r/R_j}^{NREL}/c_{r/R_j}^{EG}\right)^4 \tag{7.1}$$

Here, E is the material Young modulus, I_{xx}^{EG} and I_{yy}^{EG} are the ENGIE Green blade local inertiae, and I_{xx}^{NREL} and I_{yy}^{NREL} are the NREL's 5MW turbine initial local inertiae. $c_{r/R}^{\mathrm{NREL}}$ and $c_{r/R}^{\mathrm{EG}}$ are the NREL's 5MW and ENGIE Green's blade chords at the same spanwise location, and the subscript j shows the analysed station.

$$M_{L_j}^{EG} = M_{L_j}^{NREL} \times \left(c_{r/R_j}^{NREL}/c_{r/R_j}^{EG}\right) \tag{7.2}$$

Where $M_{L_j}^{EG}$ and $M_{L_j}^{NREL}$ are the linear mass of both blades and the subscript j shows the analysed station. Applying the equation 7.1 and equation 7.2 yields the Figure 7.4 (mass not displayed).

Moreover, the blade and tower modal shapes, necessary OpenFAST inputs, have been recalculated using the scaled mechanical properties. A Campbell diagram illustrates that despite the difference in length and mass, both turbines behave similarly, as desired (see

Figure 7.3). All ENGIE Green blade modes follow the NREL baseline turbine trend with a little offset due to the shorter blade. Regarding the tower, the first modes (fore–aft and side-to-side) are identical between both turbines; only the second modes show a clear offset towards the highest frequencies.

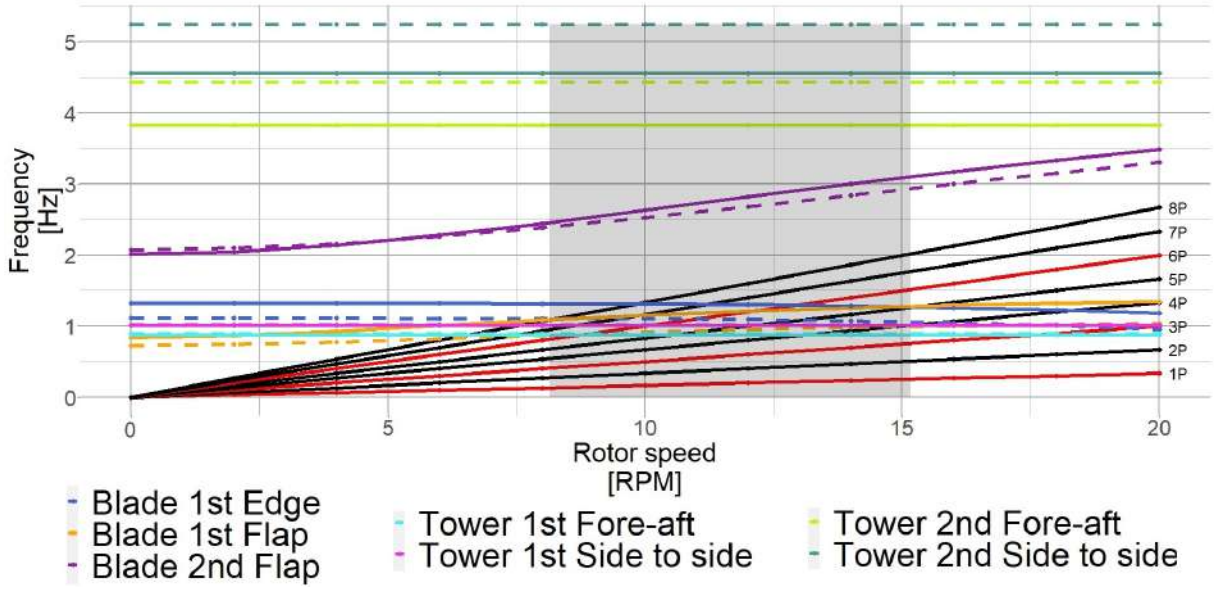

Figure 7.3 – Campbell diagram comparison between the NREL reference turbine and the ENGIE Green scaled one. The solid lines shows the NREL response and the dashed lines the ENGIE Green turbine's response. The dark shaded area illustrates the ENGIE Green's turbine range of operation.

A final sanity check was performed on the mass to assess the validity of the scaling. The blade and tower mass were respectively 0.6% and 1.3% off compared to the manufacturer's design specifications, which is small enough to be acceptable. Figures 7.4a and 7.4b show the mechanical property comparison with the original NREL 5MW turbine. Finally, the turbine characteristics publicly available and necessary for OpenFAST are gathered (see Appendix F).

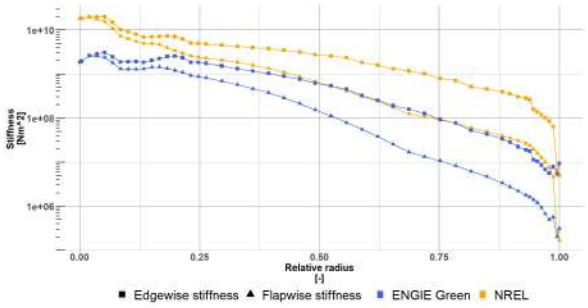

(a) Blade stiffness properties.

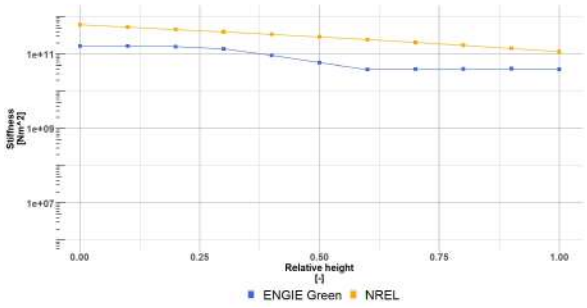

(b) Tower stiffness properties.

Figure 7.4 – The blue lines (—) shows the scaled turbine properties and the orange lines (—) the original NREL 5MW turbine properties. The square and triangle symbols (■ and ▲) show the different stiffness directions. Because fore-aft and side-to-side stiffnesses are identical only a single curve per tower is shown.

7.1.4 Unsteady polars generation

The grid independence study and polar generation methodology have already been performed and presented in Chapter 6. Then, all 16 profiles listed in Table 7.2 were simulated to extract the aerofoils' aerodynamic coefficients (lift, drag and moment coefficients) for OpenFAST computations. Thus producing six different steady polars for the turbine as described in Table 7.1. Figures 7.5 and Figure 7.6 show representative sections for the lift and drag coefficient along the blade span. The solid lines show the mean aerodynamic coefficient values, while the shaded areas illustrate the range of variation reached during each angle of attack calculation. Consequently, the polar using the maximum aerodynamic coefficients corresponds to the upper limit, and the polar using the minimum aerodynamic coefficient follows the lower limit.
Initial BEM simulations showed that high angles of attack can be reached ($\alpha > 50°$) for the inner sections; for this reason the inboard section polars have been simulated up to $\alpha = 60°$. Each polar has then been extrapolated using the Viterna extrapolation method ([153]) to cover the full 360° range ($-180° \leq \alpha \leq 180°$). Then, to account for the rotational effects, the 3D correction model derived by Chaviaropoulos was used (see [24]). Consequently, the 3D rotational model from OpenFAST has been disabled.

Table 7.2 – CFD calculated blade sections polars defining the BEM model assuming an inflow between 8m/s and 8.5m/s

Spanwise location from the hub [**m**]	**Relative spanwise location from the hub** [%]	**Aerofoil relative thickness** [%]	**Local Reynolds number** [-]
2.1	4.4%	93%	1.35×10^6
3.0	6.7%	86.8%	1.53×10^6
3.6	8.0%	81.2%	1.67×10^6
4.2	9.3%	74.9%	1.86×10^6
4.5	10.0%	71.9%	1.95×10^6
5.1	11.3%	66.2%	2.17×10^6
5.4	12.0%	63.4%	2.29×10^6
6.0	13.3%	58.6%	3.05×10^6
6.6	14.7%	53.9%	2.79×10^6
7.2	16.0%	49.6%	3.05×10^6
7.5	16.7%	47.9%	3.18×10^6
10	22.2%	35.8%	4.17×10^6
13	28.9%	29.8%	4.92×10^6
20	44.4%	24.2%	5.90×10^6
27	60.0%	21.2%	6.09×10^6
43	95.6%	17.3%	4.06×10^6

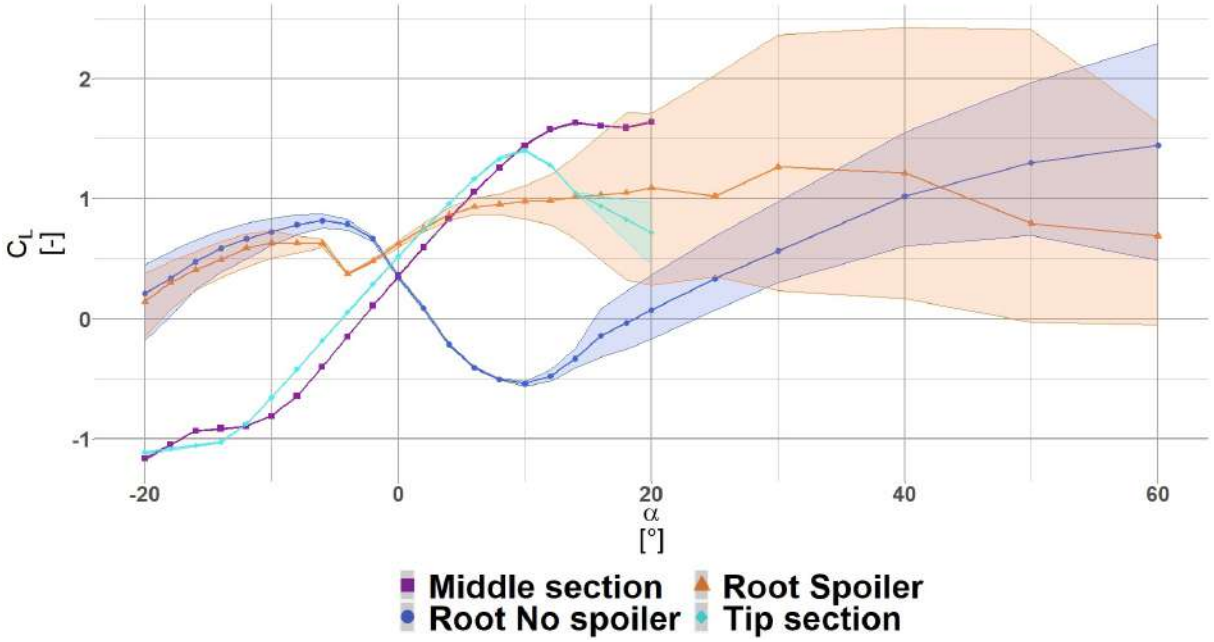

Figure 7.5 – The blue dot (●) shows the C_L for a representative root section without spoiler, the orange triangle (▲) shows the C_L for a representative root section with spoiler, the purple square (■) shows the C_L for a representative middle section and the cyan diamond (◆) shows the C_L for a representative tip section. The plotted polars have not been corrected with a rotational model.

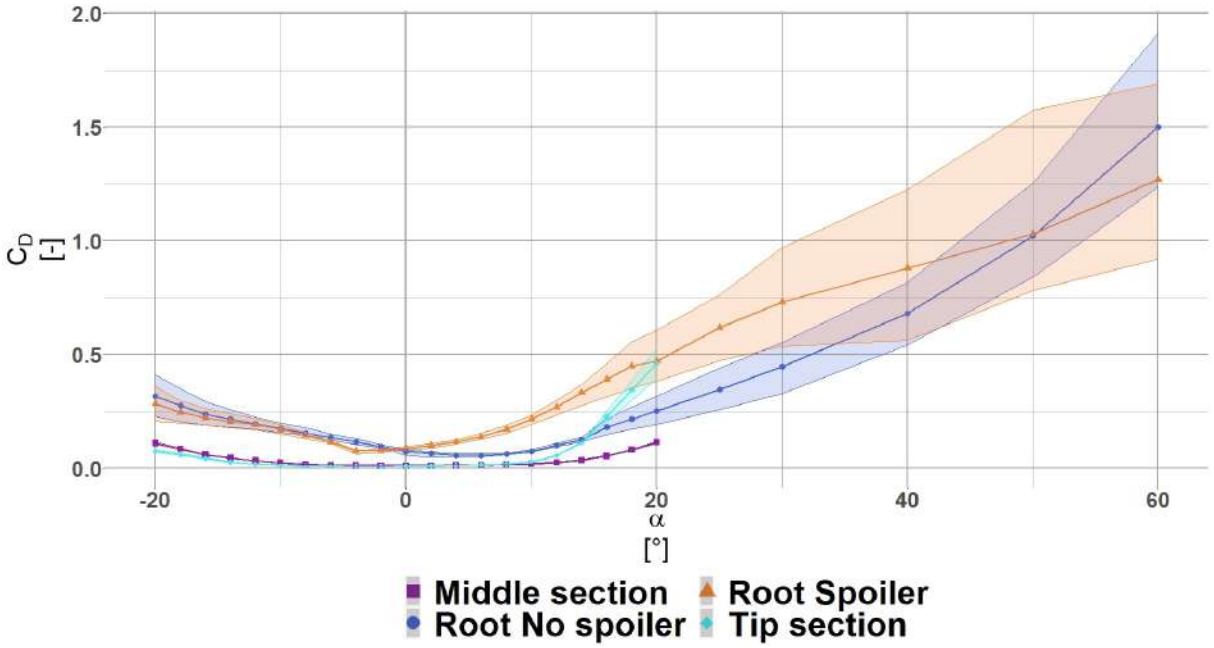

Figure 7.6 – The blue dot (●) shows the C_D for a representative root section without spoiler, the orange triangle (▲) shows the C_D for a representative root section with spoiler, the purple square (■) shows the C_D for a representative middle section and the cyan diamond (◆) shows the C_D for a representative tip section. The plotted polars have not been corrected with a rotational model.

7.1.5 BEM simulations set-up

The following sections will detail the model set-up used during the aeroelastic simulations. The first goal is to determine the maximum aerodynamic potential of spoilers compared to a bare blade, free of any constraints. A second goal is to assess the impact of the spoiler, on the turbine lifetime, when operating at maximum power extraction.

Pitch settings for maximal power production

The pitch settings for maximum power extraction are unknown. The turbine manufacturers may not recommend maximum power generation pitch settings due to potential noise, stall or load issues. Therefore, using Supervisory Control and Data Acquisition (SCADA) measurements is not sufficient, and an optimisation study is necessary. In order to reduce the optimisation space to only a single variable (the pitch settings), it is assumed that the turbine's rotational speed available thanks to averaged field measurements is optimised and will not vary. Then, a search for the optimum pitch settings was carried out for each wind speed between cut-in (3m/s) and cut-out (20m/s), by increments of 0.5m/s, and for each turbine configuration described in see Table 7.1. The optimisation constraints are described as follows: below rated wind speed (here 10.5m/s), the power production has to be maximal, whilst from rated wind speed until cut-out the turbine must regulate the generated power in order to maintain rated power (here 2.05MW).
A sweep of pitch settings for a range between $-10°$ and $10°$ below rated and between $0°$ and $20°$ above rated was tried. Figure 7.7 shows the the response surface of the optimisation procedure for the turbine with spoiler using the mean aerodynamic coefficient polar. The black dotted line shows the optimal pitch settings for maximal power production.

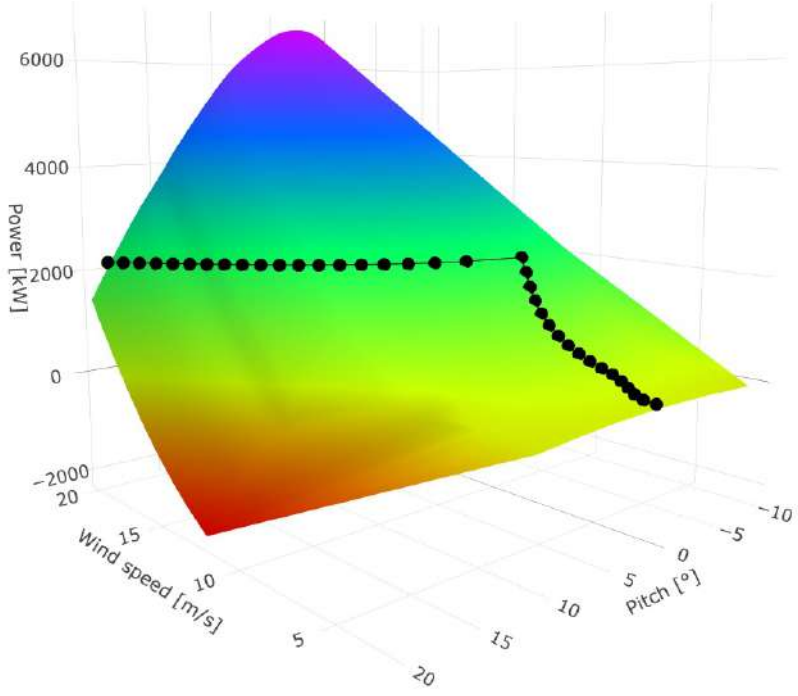

Figure 7.7 – Power surface response with varying pitch settings for different wind speed for the spoiler case using mean aerodynamic polar.

Table 7.3 shows that the blade with spoiler needs a slightly higher pitch to achieve rated power, thus reducing the angle of attack. Figure 7.8 shows the outcome of the study for all configurations tested. As can be seen, the difference between both the no spoiler and spoiler is small.

Table 7.3 – Optimal pitch settings for both no spoiler and spoiler case using mean aerodynamic polars.

Wind speed [m/s]	**No spoiler pitch settings** [°]	**Spoiler pitch settings** [°]	**Difference** [°]
3.0	-0.164	-0.059	-0.105
4.0	-0.9	-0.872	-0.028
5.0	-1.621	-1.565	-0.056
6.0	-1.549	-1.494	-0.055
7.0	-1.453	-1.405	-0.048
8.0	-1.568	-1.517	-0.051
9.0	-2.1	-2.062	-0.039
10.0	-3.046	-3.025	-0.021
11.0	0.829	0.969	-0.141
12.0	4.46	4.563	-0.104
13.0	6.998	7.095	-0.097
14.0	9.144	9.237	-0.093
15.0	11.025	11.117	-0.092
16.0	12.73	12.821	-0.092
17.0	14.322	14.417	-0.095
18.0	15.839	15.937	-0.098
19.0	17.305	17.406	-0.101
20.0	18.684	18.785	-0.102

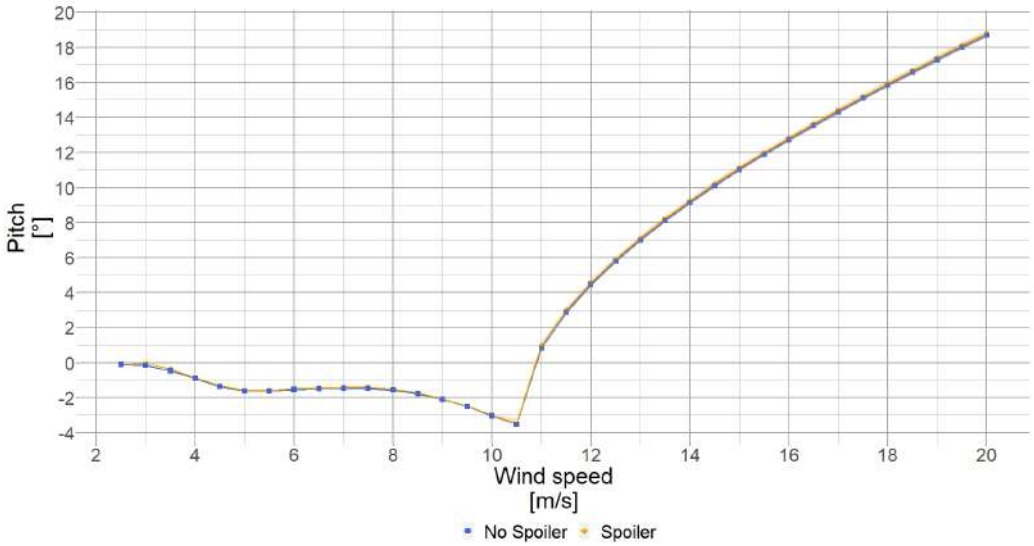

Figure 7.8 – The blue square (■) shows the pitch evolution with respect to the wind speed without spoiler, the orange dot (●) shows the with respect to the wind speed with spoiler.

Rigid turbine simulations

In the first analysis, the turbine is considered rigid (i.e. not flexible) with the hub height 80m above ground using the standalone AeroDyn module. The aerofoils associated with the CFD-calculated polars precisely define the blade discretization as detailed in Table 7.2. As the standalone AeroDyn module can only simulate steady wind profiles, the power law relation was used based on equation 1.1. The air density in the BEM calculations is considered constant in space and time and is equal to the one used for the CFD polar calculation ($\rho = 1.225$).

Flexible turbine simulations

The second analysis is a fully flexible turbine with turbulent wind using OpenFAST. The tool TurbSim (see [71]) developed by NREL is used to generate 10min long three-dimensional turbulent wind fields for each wind speed. The box representing the wind field is 150m wide and high subdivided in 50 points and 600s long. The IEC Kaimal model is used as the spectral model thanks to the directly available IEC class requirements (here IEC class II chosen). The underlying assumption is that the atmospheric conditions are considered neutral following the Monin–Obukhov similarity theory as detailed in [157, 63, 33]

7.2 Results

After running all the turbine configurations, a deep aerodynamic analysis is possible as many sensor outputs are available. For brevity reasons only a small sample of all the available results will be presented. The multiple polar "states" (mean, maxi, mini) allow for an assessment of the variation around the mean value, giving a measure of unsteadiness. First, the rigid turbine loads, power and AEP are analysed. Secondly, the flexible turbine fatigue impact is analysed.

7.2.1 Rigid turbine

In the Figure 7.9 to Figure 7.11, the x-axis represents the blade radius, the y-axis represents the considered sensor output and each subplot represents a wind speed whose value is given in the title, from 6m/s to 11m/s.

Aerodynamic parameters

Lift coefficient

The lift coefficient of the no spoiler case shows very low values inboard, as expected from very thick aerofoils. After the radial position R7.2 ($r/R = 0.16$), both curves merge, describing the end of the spoiler effect. For the spoiler case, the mean C_{L} increases to relatively high values, especially for such inboard sections, ($C_{\mathrm{L_{mean}}}^{\mathrm{spoiler}} \approx 1$). However, the associated variation increases drastically. Indeed, the variation for the no spoiler case was $C_{\mathrm{L_{mean}}}^{\mathrm{no\ spoiler}} \pm 0.3$ while in the spoiler case the variation is close to $C_{\mathrm{L_{mean}}}^{\mathrm{spoiler}} \pm 1$ (see Figure 7.9). A similar outcome is seen for the drag coefficient (not shown here). The large variation in C_{L} is a consequence of the polar unsteadiness.

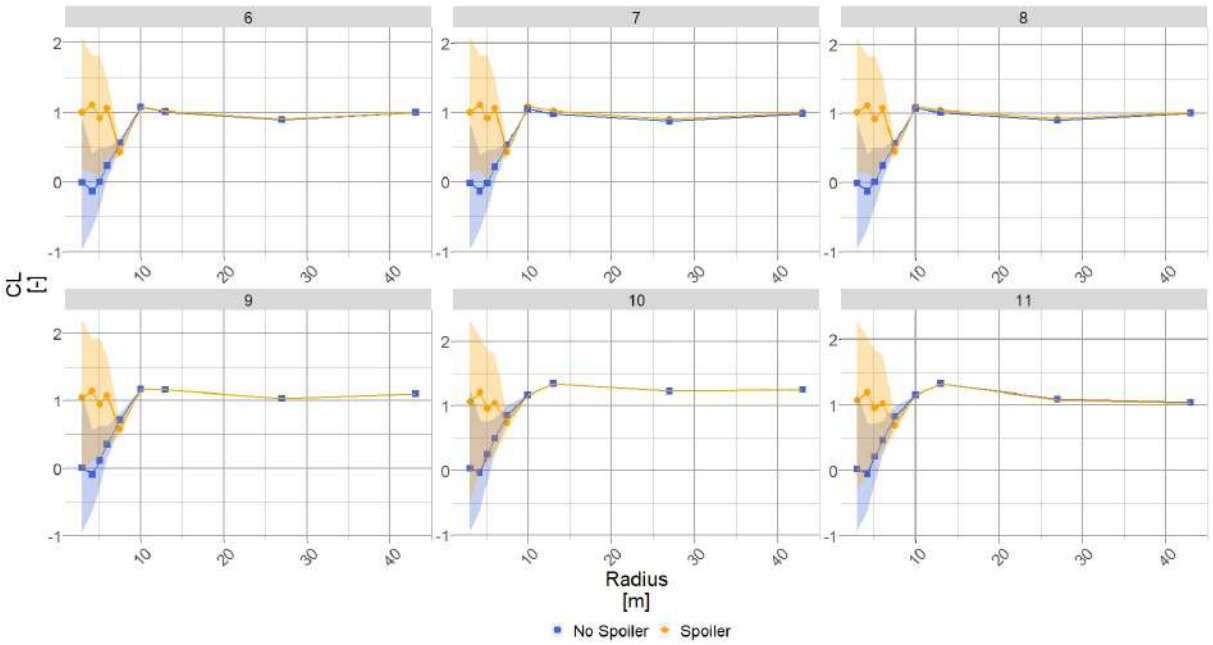

Figure 7.9 – The blue square (■) shows the C_L evolution along the blade radius without spoiler, the orange dot (●) shows the C_L evolution along the blade radius with spoiler. Each subplot shows the results for a wind speed (m/s) whose value is given in the title.

Axial induction

The axial induction, a, is a key aerodynamic metric for turbine analysis. Through this parameter it is possible to have information about the sectional energy extraction and the sectional turbine loading. The energy extraction is at its maximum when $a = 1/3$, according to the Betz limit, and the loads increase significantly beyond $a = 0.4$ following the highly loaded rotor relationship (Glauert correction). Therefore, most turbine manufacturers aim for an induction factor value close to the optimal $a = 1/3$, when in power production mode. After the pitch optimisation, the turbine runs close to optimal axial induction for the outer part of the blade.

The no spoiler case shows very low induction values at the root of the blade due to the cylinder shape: low lift coefficient and high drag values. The blade's inboard is not efficient to extract energy but the expected load level is consequently low. Where the spoiler is installed the induction increases, similarly to the lift coefficient. The upper band of the variation due to the polar unsteadiness is close to the optimal induction. The average induction level at the spoiler location is close to $a = 0.15$, which is a significant improvement compared to the no spoiler case where the induction level is close to $a = 0$ (see Figure 7.10). The relative variation area is also increased, as seen for the lift coefficient, $a_{\text{mean}}^{\text{spoiler}} \pm 0.1$ and still a lot larger than the no spoiler case.

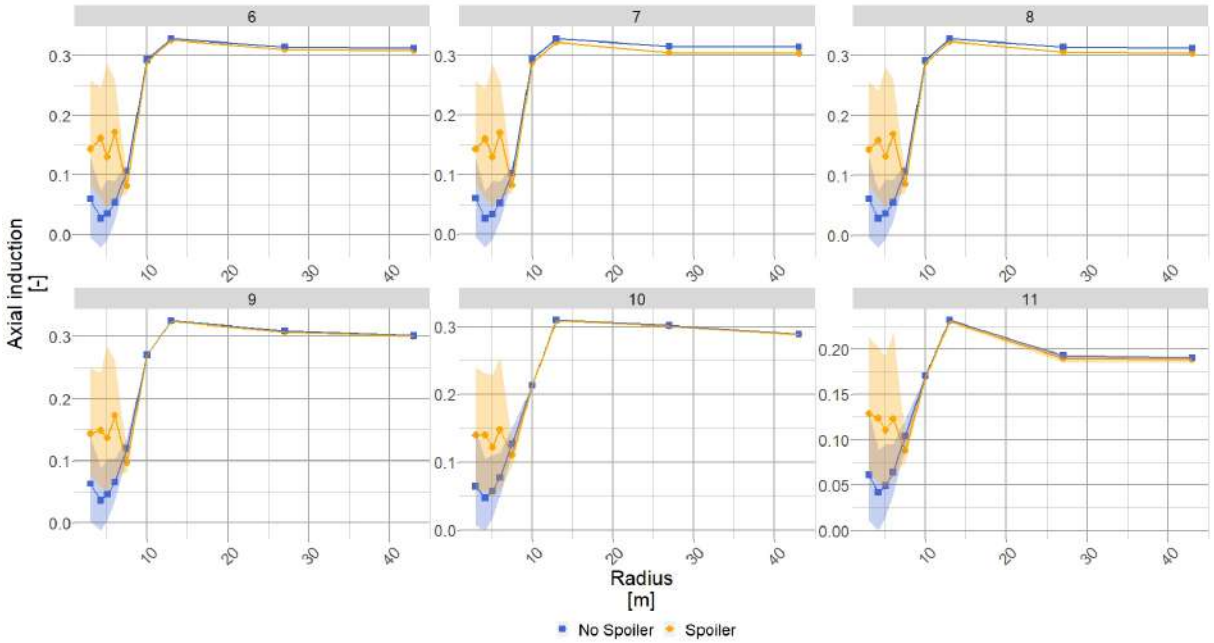

Figure 7.10 – The blue square (■) shows the a evolution along the blade radius without spoiler, the orange dot (●) shows the a evolution along the blade radius with spoiler. Each subplot shows the results for a wind speed (m/s) whose value is given in the title.

Interestingly, for 6, 7 and 8m/s, the axial induction after the radial position R10 ($r/R = 0.22$), is lower for the spoiler than for the no spoiler case. This is due to the pitch optimisation. The objective function was to maximise power and not try to reach optimal induction. The best trade-off between the spoiler power generation and the blade outboard power generation is when the blade outboard is not at its optimal point to allow for the blade inboard to play a more important role. It also means that the blade tip is slightly less loaded, as can be seen in Section 7.2.1. Nevertheless, the axial induction is still very close to its optimal value ($a = 0.3$).

Aerodynamic static loads

The local out-of-plane force (F_X) is calculated, and its evolution against the radius for several wind speeds is shown in Figure 7.11. The bare blade design intent showed very low normal forces level in the blade root vicinity with an steady increase along the span past R10 ($r/R = 0.22$). The spoiler installation lead to a significant local force increase, despite being significantly lower than the outer part of the blade. Due to the different pitch settings between both blades, the spoiler case shows a slightly lower force towards the blade tip.

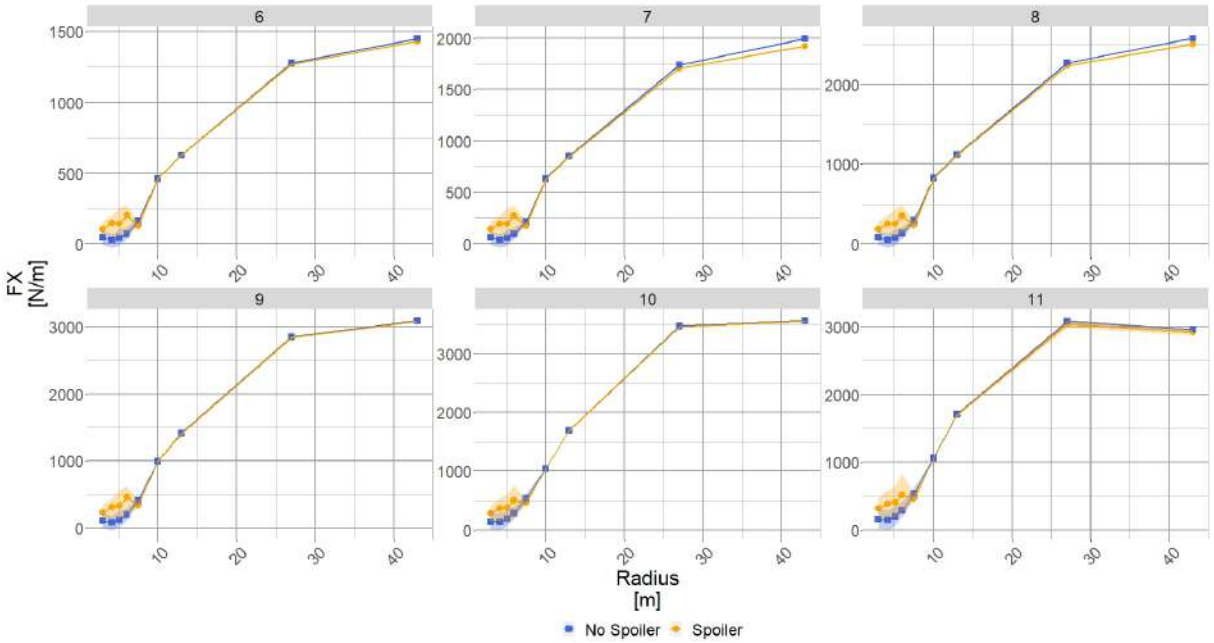

Figure 7.11 – The blue square (■) shows the force normal to the rotor plane evolution along the blade radius without spoiler, the orange dot (●) shows the the normal force to the rotor plane evolution along the blade radius with spoiler. Each subplot shows the results for a wind speed (m/s) whose value is given in the title.

Integrated load: Root Bending Moment

The previous figures showed the results at the aerofoil level, the next phase of the analysis will focus on the integrated values.
The flapwise root bending moment (RBM) is a critical parameter for blade design and is directly linked to F_X through equation (7.3).

$$\text{RBM} = \int_0^R r \times F_X(r)\mathrm{d}r, \tag{7.3}$$

Here $F_X(r)$ is the local out-of-plane force and r the local radius considered.
The unsteadiness caused by the spoiler does not seem to be reflected at rotor level, and the coloured area around the mean value is almost nonexistent. Also, because the change is very small, both curves seem overlapped in Figure 7.12. The vertical bars show the difference between the mean RBM values for the spoiler and no spoiler case. Except around 5m/s, the use of a spoiler tends to decrease the RBM slightly (right-hand side vertical axis).
The lower RBM value in the spoiler case is explained thanks to the pitch settings, and the same explanation for the out-of-plane force F_X holds for the RBM. The spoiler case pitch settings are less "aggressive" due to the higher power produced thanks to the blade inboard. The blade outboard, where most of the power is generated, experiences a lesser angle of attack than the no spoiler case. Therefore, the local load generated by the outer part of the blade is smaller in the no spoiler case than in the spoiler case. After the integration, performed using equation 7.3, the $\text{RBM}^{\text{no spoiler}}$ is higher than $\text{RBM}^{\text{spoiler}}$.

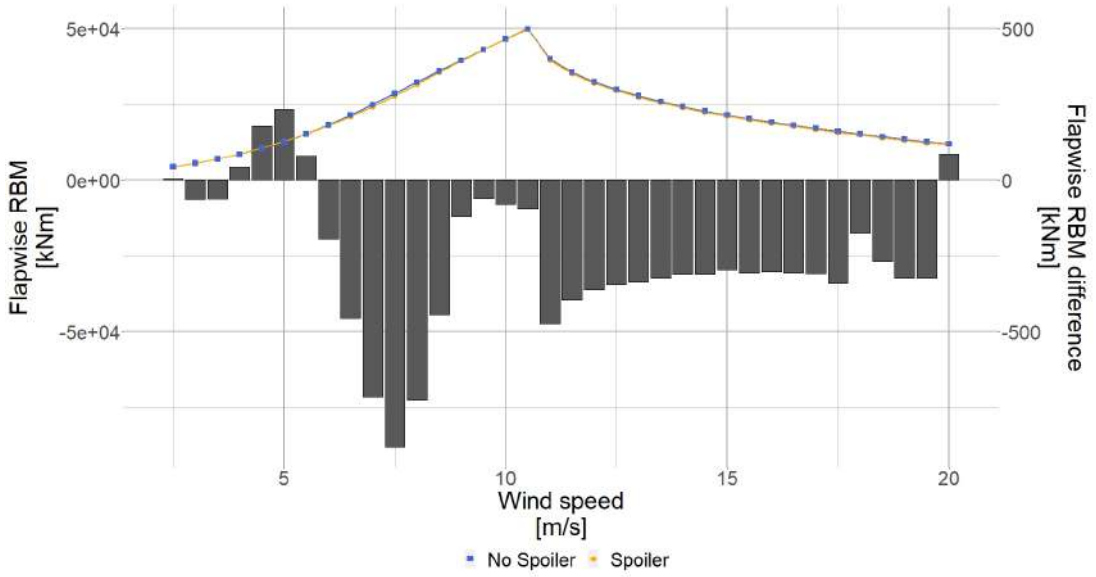

Figure 7.12 – The blue square (■) shows the flapwise root bending moment evolution without spoiler, the orange dot (●) shows the flapwise root bending moment evolution with spoiler. The black bars show the difference between the spoiler and no spoiler case for each wind speed.

Power curve and energy production

The mean power curves for the no spoiler and spoiler configuration can be plotted (see Figure 7.13). Both curves are very close to each other; the vertical bars shows that the spoiler does produce more energy on average, albeit a small amount (power difference on the right-hand axis). The error bars show the variation in power due to the different polar states used; i.e. the top of the error bar is the power difference between the spoiler and the no spoiler case using the maximum aerodynamic coefficient polar.
It is to be noted that, interestingly, the power gain of approximately 1%, for wind speeds up to up to 8m/s, is similar to the C_L gain thanks to the spoiler presented in Figure 7.9. Closer to rated power, the mean power gain reduces.

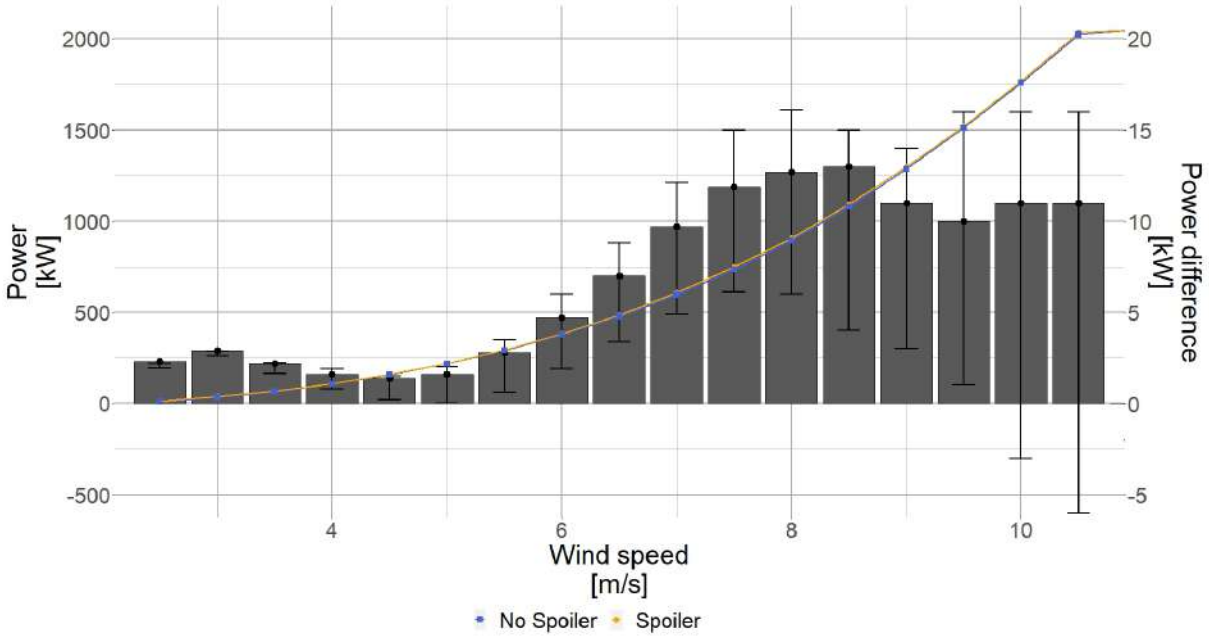

Figure 7.13 – Power curve close-up for the low wind speeds. The blue square (■) shows the power curve without spoiler, the orange dot (●) shows the power curve with spoiler. The black bars show the difference between the mean spoiler and mean no spoiler case.

After integrating the mean power curves over a year simulating a wind site condition IEC class II (Weibull shape factor = 0.2 and average wind speed = 8.5m/s), the AEP impact can be seen in the Table 7.4. On average, the spoiler produces 0.49% AEP more than the no spoiler case, assuming maximum power extraction settings and mean aerodynamic coefficient polar.

Table 7.4 – Spoiler impact on the AEP

Turbine configuration	**AEP [MWh]**	**AEP gain ratio [%]**
No spoiler	8256.5	N/A
Spoiler	8269.9	0.49

Turbine unsteadiness definition

When using BEM, one cannot use a time-varying description of each angle of attack during the iterative procedure. Using several steady-state polars representing the different possible aerodynamic coefficients allowed for a first estimation of the variation due to the unsteadiness. Analysing the loads or the different aerodynamic metrics (such as presented in Section 7.2.1) using three different polar states independently is acceptable because the data represent instantaneous "snapshot" values. However, to integrate the results in time, to calculate the mean thrust or the AEP, this assumption cannot hold. Indeed, assuming that the aerodynamic coefficient time variation is periodic, as illustrated in Figure 7.2, then after integration all oscillations cancel out. Therefore, the unsteadiness caused by the spoiler on time-integrated quantities cannot be assessed. For this reason, the following method has been applied to give a measure of the variation caused by the spoiler, using the AEP as an example.

The total variation in power for each wind speed is found by $\Delta P_{\mathrm{WS}} = P_{\mathrm{WS}}^{\mathrm{max}} - P_{\mathrm{WS}}^{\mathrm{min}}$. Where $P_{\mathrm{WS}}^{\mathrm{max}}$ and $P_{\mathrm{WS}}^{\mathrm{min}}$ are the maximum and minimum power produced for the considered wind speed. Then, knowing the Weibull site characterisation it is possible to calculate the probability of each wind speed occurring over a year: Pr(WS). Combining both, the weighted Weibull average total variation around the mean value is found (see Equation 7.4).

$$\delta E = \sum_{WS=3}^{WS=20} \Delta P_{WS} \times \Pr(WS) \tag{7.4}$$

Where δE is the Weibull weighted average energy variation, ΔP_{WS} is the power range over a wind speed, WS is the considered wind speed and Pr(WS) is the wind speed occurrence probability.

Table 7.5 shows that the spoiler addition increases the inherent variation around the mean value for the AEP.

Table 7.5 – Spoiler total AEP variation around the mean value

Turbine configuration	**AEP variation [MWh]**	**AEP variation [%]**
No spoiler	27.6	0.32
Spoiler	70.4	0.83

Figure 7.14, gives more details about the AEP variation than the Table 7.5, which gives the overview. The central symbol represents the AEP calculated using the mean aerodynamic coefficient polar. The error bars represent the AEP calculated when using the minimum and maximum aerodynamic coefficient polar as explained in Table 7.1. Comparing each configuration (black lines), the AEP gain using mean aerodynamic coefficients polar is 0.49%, the AEP gain using minimum aerodynamic coefficients polar is 0.17% and the AEP gain using maximum aerodynamic coefficients polar is 0.68%. Within each configuration (blue and orange arrows) the overall variation due to the unsteadiness also changes: the spoiler increases the variation in the AEP calculation. The AEP variation is ±0.4% in the spoiler case, while in the no spoiler case, the variation is approximately halved and no longer symmetric around the mean value (+0.23% and −0.09%).
In order to estimate the spoiler's impact boundaries, the different power curves are treated separately. The gains presented assume a single turbine operating at maximum power production, as detailed in Section 7.1.5, which is unrealistic. Consequently, the actual expected gains will be smaller.

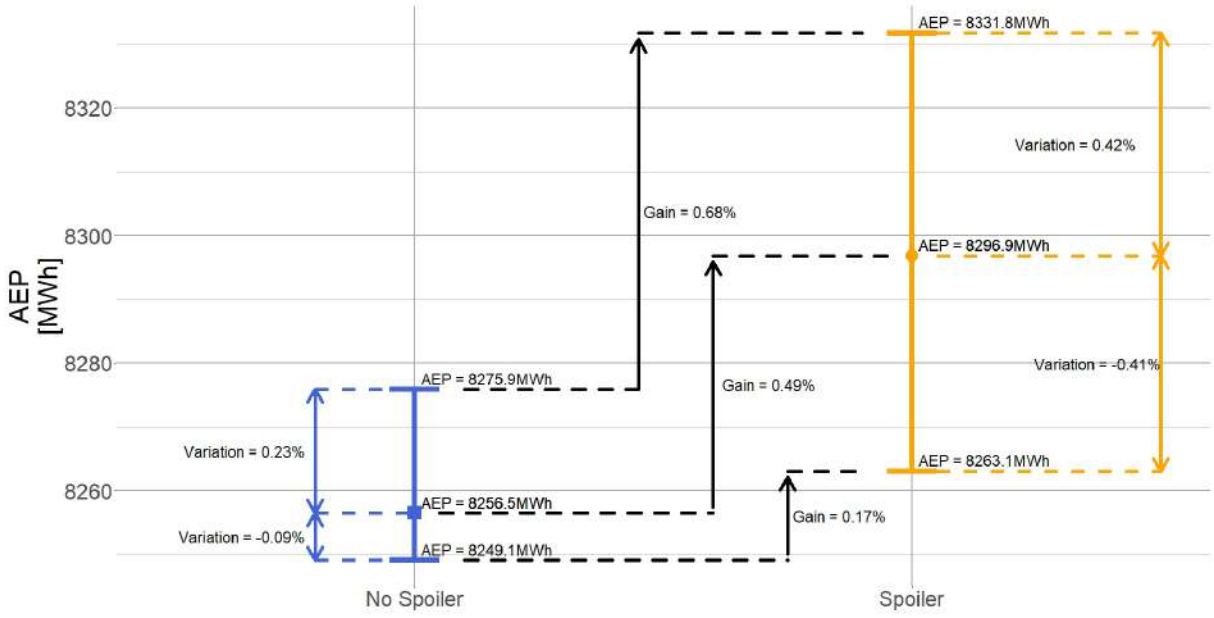

Figure 7.14 – Detailed AEP gain and variation for all configuration assuming a wind class IEC II.

7.2.2 Flexible turbine

As seen in the previous sections, the rigid modelling shows little AEP benefit of installing the spoiler. However, due to the large increase in the mean local loads and its associated variation introduced by the spoiler, it seems interesting to investigate the damage and fatigue on the turbine. The aeroelastic calculations will be performed by OpenFAST with a fully flexible turbine. The fatigue analysis will focus on the blade only but can be extended to the whole turbine.

Combination method

A method to account for unsteadiness on a rigid turbine has been presented in Section 7.2.1, but it can only simulate integrated load. In order to further analyse the spoiler unsteadiness impact, fatigue analysis is necessary. However, the same BEM limitations arise. Here again, each case (no spoiler and spoiler) is calculated using the three polars states for each wind speed (from 3 to 20m/s). Then, thanks to the previously calculated vortex shedding frequency (VSF) for each aerofoil section, a new time series is generated, as detailed below.

Vortex Shedding Frequency (VSF)
The Chapter 6 showed that a VSF can easily be found for a single aerofoil at a single angle of attack using 2D CFD velocity or 2D CFD C_L time series. Applying the same methodology for all aerofoils and for all angles of attack, the 2D CFD C_L time series were post-processed, thereby creating a database of VSF (see Figure 7.15). Using the BEM hypothesis of 2D flow, it is assumed that neither the blade rotation nor the blade deflection change the VSF. It is interesting to notice that the VSF is within range of the eigenfrequencies seen in the Campbell diagram.

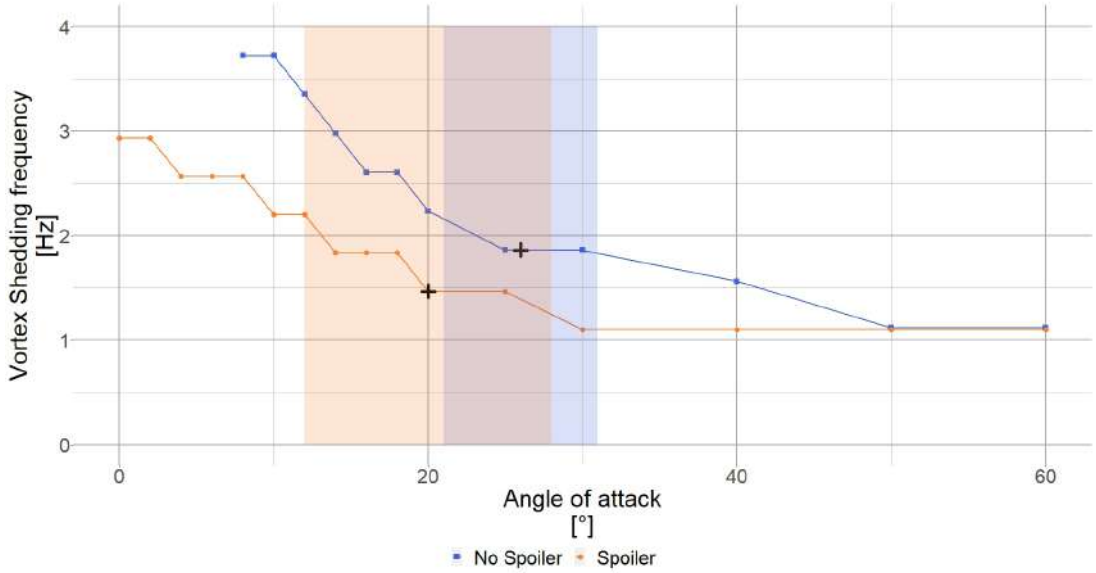

Figure 7.15 – No spoiler and spoiler case VSF evolution for a varying angle of attack, radial position R6 ($r/R = 0.13$) calculated in 2D CFD. The blue square (■) shows the no spoiler VSF, the orange dots (●) shows the no spoiler VSF. The black crosses mark the mean VSF (interpolated VSF at the mean angle of attack of the time series) for each case. The shaded area shows the standard deviation of the angle of attack time series (8m/s).

Because of the sampling theorem, the OpenFAST sampling output rate must be at least twice higher than the highest VSF. The highest calculated VSF of all sections is approximately 60Hz. To add safety margin, the OpenFAST output is set to be at 160Hz, which is equivalent to a time step of $\Delta t_{\text{OF}} = 0.0063$s.

New OpenFAST time series creation

Once all aeroelastic results are available (Figure 7.16), a mean VSF (VSF_{mean}) is determined by interpolating at the mean angle of attack of the mean polar time series the VSF (black crosses in Figure 7.15). Inverting it leads to a representative time step for the considered wind speed $\Delta t = {}^{1}/_{\text{VSF}_{\text{mean}}}$. The original results calculated using maximum, mean or minimum polars are then interpolated at new time steps using Δt (Figure 7.17). An intermediate time series is generated, for each sensor. Again, supposing a periodic variation in the lift and drag coefficients, it is assumed that the first aerodynamic coefficient "seen" by the aerofoil is from the maximum polar, and it then changes to the mean polar and finally the minimum polar and varies following this cycle for 600s. Such behaviour leads to the creation of the pink curve in Figure 7.18.

One final numerical manipulation is necessary, because all intermediate time series created possess different VSF and therefore different Δt values. To ensure further analysis, all newly created time series are re-sampled at the original OpenFAST sampling rate $\Delta t_{\text{OF}} = 0.0063$s. (Figure 7.19). The turbulent wind speed frequency spectrum is independent from the VSF, therefore it is possible to perform the interpolation in the time domain between time series rather than in the frequency domain. This method is repeated for each radial position, each wind speed and all local blade loads. The results presented in the next sections use the newly generated fatigue data.

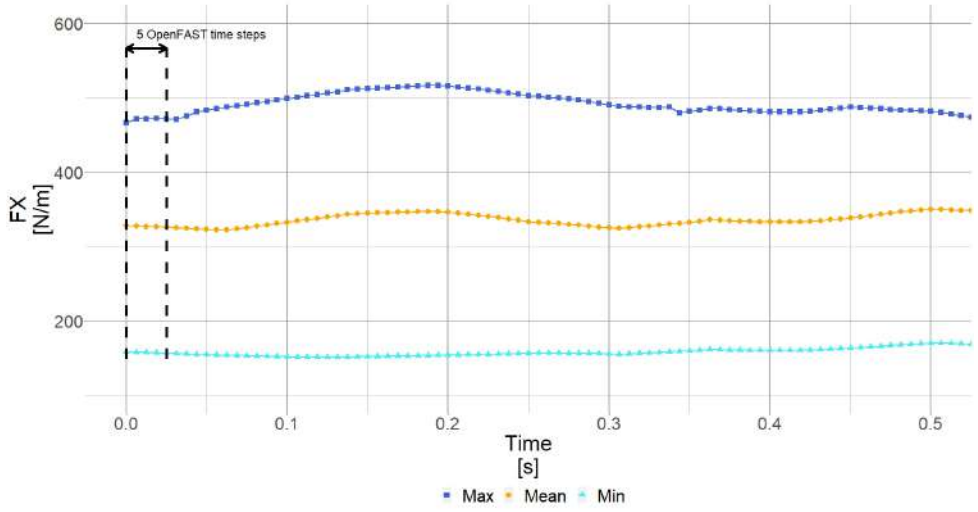

Figure 7.16 – OpenFAST time evolution of 0.5s of the local out-of-plane force (F_X) using the maximal, mean and minimal aerodynamic polar.

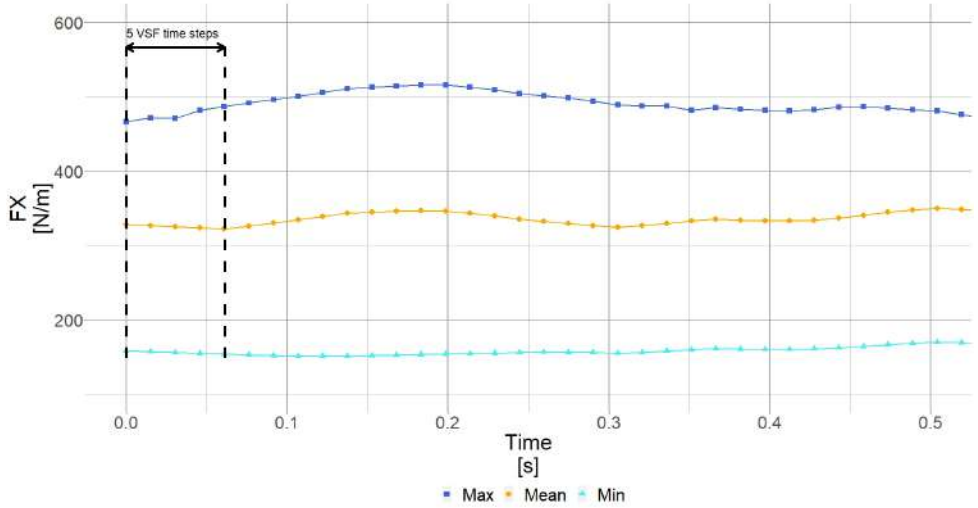

Figure 7.17 – Interpolated OpenFAST results of the local out of plane force (F_X).

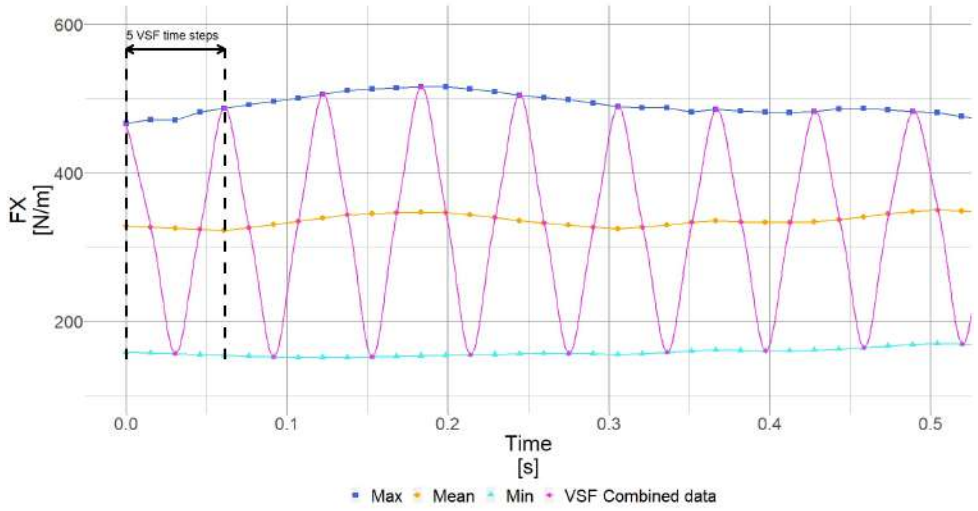

Figure 7.18 – Creation of the intermediate time series by alternating between the different interpolated time series.

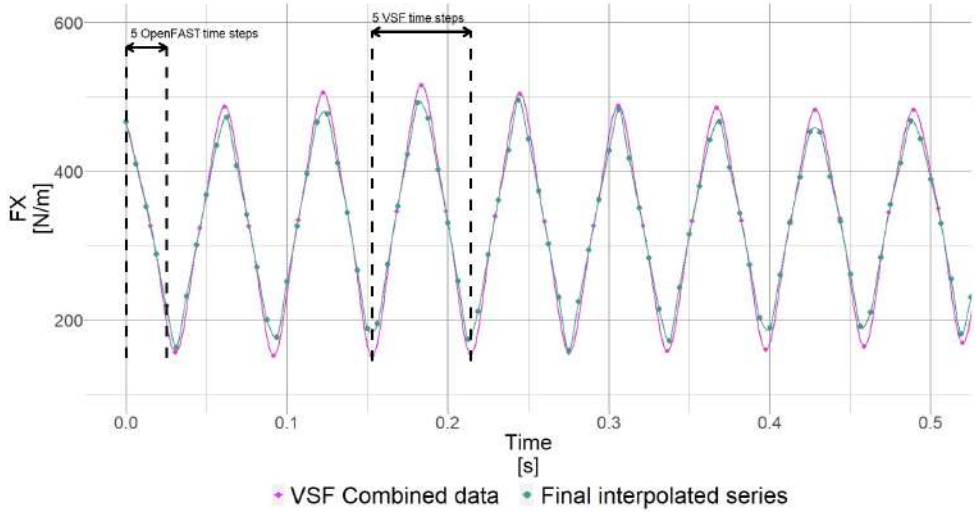

Figure 7.19 – Generation of the final time series using the sampling rate from OpenFAST ($\Delta t_{OF} = 0.0063$s).

Normal force results

Figure 7.20 shows the force normal to the rotor plane (F_X) for a 600s long OpenFAST simulation with an average horizontal wind speed of 8m/s (hub height). Each subplot shows a radial location, from $R = 3.6$ to $R = 7.5$ (from $r/R = 0.08$ to $r/R = 0.16$), and the horizontal axis shows the time spent in the simulation. F_X is clearly higher in the spoiler case regardless of the spanwise location.

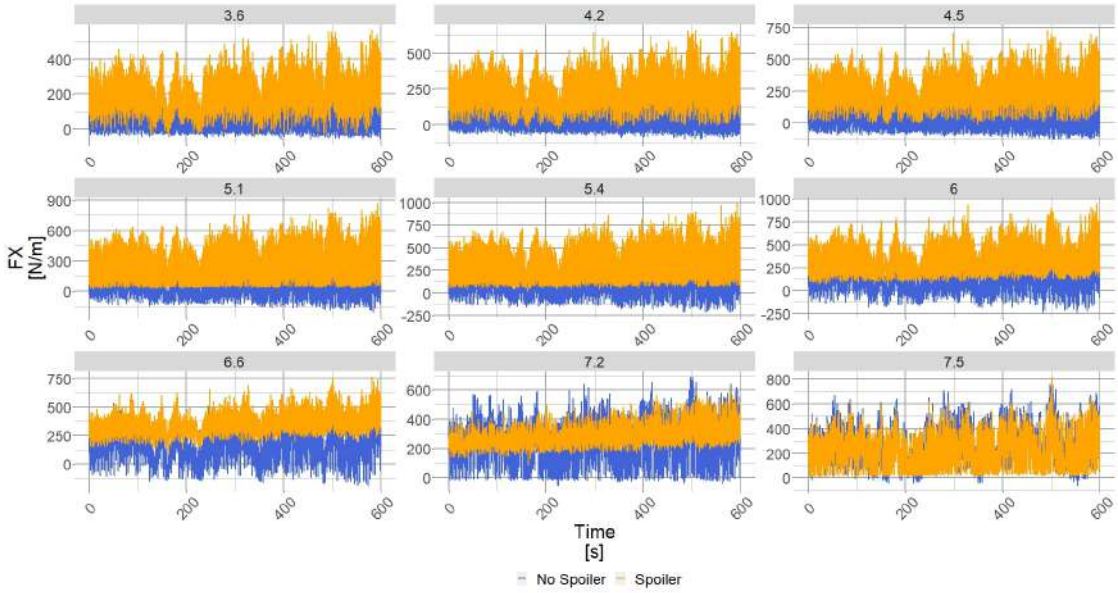

Figure 7.20 – OpenFAST output normal force to the rotor plane for an average horizontal wind speed of 8m/s (hub height). The blue square (■) shows the blade results without spoiler using the combination method, the orange dot (●) shows the blade results with spoiler using the combination method. Each subplot shows the results for a radial location (m) whose value is given in the title.

Figure 7.21 compares the power spectral density (PSD) for the spoiler case using either the mean aerodynamic polar results or the combination method results. At low frequencies the PSDs are overlapped, since the same turbulent wind speed was used in all aeroelastic simulations. However after the VSF_{mean} is reached, the combination method shows clear peaks and harmonics. The curve trend also shows the same downward behaviour at higher frequencies. The higher energy in the spectrum for the combination method hints at higher fatigue loads for the combination method than using the OpenFAST results directly.

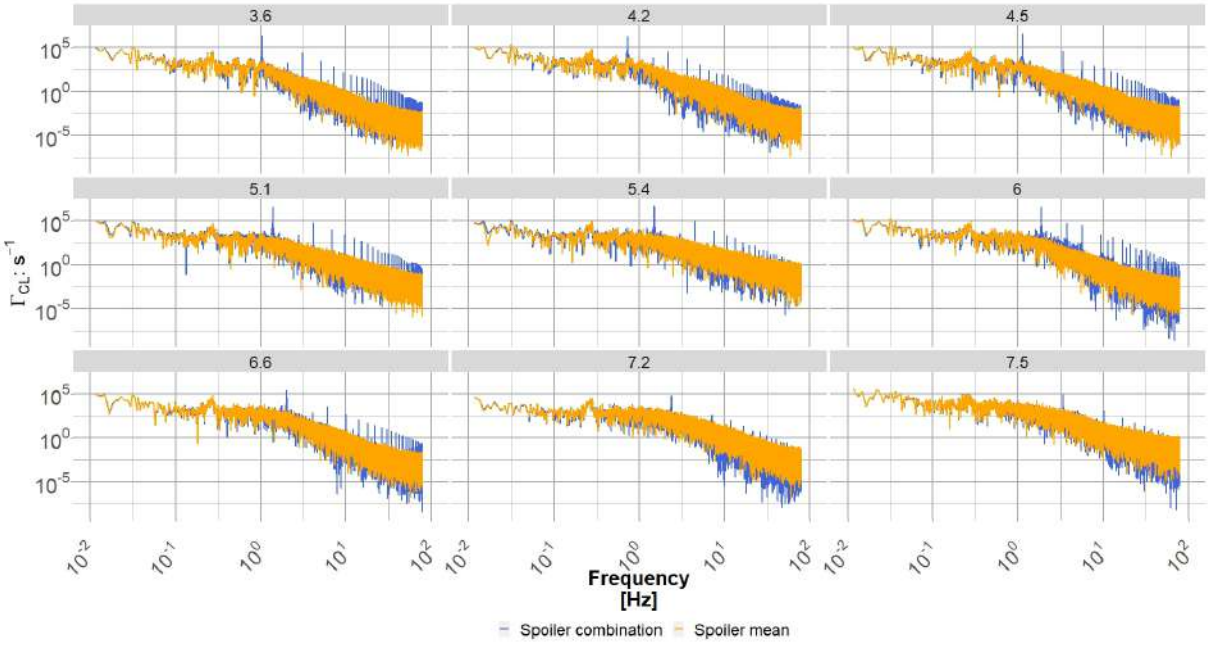

Figure 7.21 – OpenFAST output normal Power spectral Density of the normal force to the rotor plane for an average horizontal wind speed of 8m/s (hub height). The blue square (■) shows the blade results with combination method for the spoiler, the orange dot (●) shows the blade results for the mean spoiler. Each subplot shows the results for a radial location (m) whose value is given in the title.

Fatigue results

After running in OpenFAST all wind speeds for both turbine configurations and generating the new time series as described in Section 7.2.2, it is possible to determine the lifetime impact of the spoiler and its associated unsteadiness on the turbine. The tool used is Mlife, also developed by NREL (see [56]). Similarly to the AEP calculation, it is assumed that the generated OpenFAST outputs follow a Weibull distribution of an IEC site B (shape factor = 2 and average wind speed = 8.5m/s).

The method developed can only account for sectional loads since it relies on vortex shedding frequency. The integrated load such as RBM cannot be associated with any particular VSF

In order to calculate the blade lifetime with the predefined pitch and RPM settings, an ultimate load before rupture for each analysed sensor must be given. Since the material

properties are unknown, MExtreme was used (see [55]) to extract the highest sectional loads of interest seen by the turbine of both cases as first approximation (here F_X and F_Y). To assess the lifetime evolution with respect to the ultimate load, three distinct load values were selected. Using those values for the no spoiler and spoiler cases, it is now possible to plot the lifetime evolution with respect to the ultimate load for the local out-of-plane force (see Figure 7.22) and the local in-plane forces (see Figure 7.23). The horizontal dashed line shows the usual 25 years design lifetime. The lowest symbol of each coloured line represents the turbine lifetime if it were designed based on the highest load found by MExtreme. The following two points are calculated lifetimes using the initial highest load multiplied by a factor of 2 and 3. As expected, the behaviour is highly non-linear and can reach unrealistic lifetime expectancy. To avoid running fatigue simulation with a very low life expectancy, loads from the multiplication factor of 2 were chosen as baseline for the rest of the analysis (see Table F.6). The Wöhler exponent was kept constant throughout the study to a representative wind turbine blade material: m = 10 (see [85]). The symbols definition in Figure 7.22 and Figure 7.23 is detailed in Table 7.6.

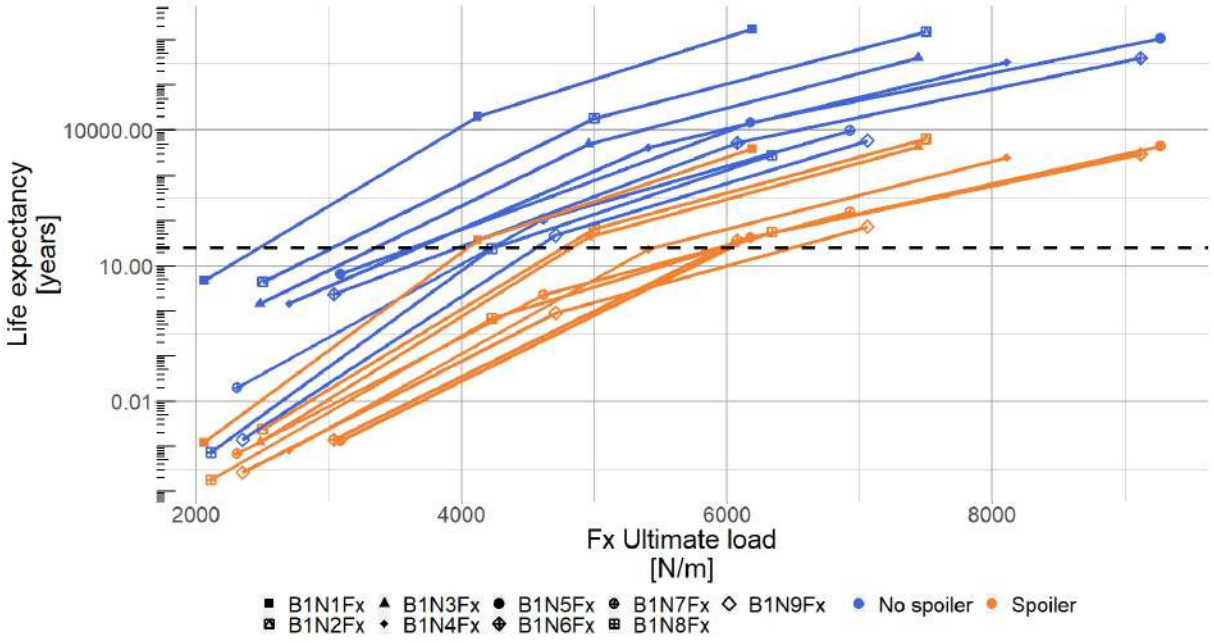

Figure 7.22 – Life time expectancy evolution with respect to out of plane local load. The blue square (■) shows the blade results without spoiler, the orange dot (●) shows the blade results with spoiler and each symbol represent a blade nodal output ($8.0\% < {}^{r}/_{R} < 16.7\%$)

Because of the different hypotheses taken, presenting the direct Mlife results would lead to results difficult to conclude from. Therefore a life index (Li) is created by normalising the outputs of the no spoiler case to create a baseline; i.e. for each sensor $Li^{\text{no spoiler}} = 1$. Then the spoiler case results are normalised by the previously created baseline.

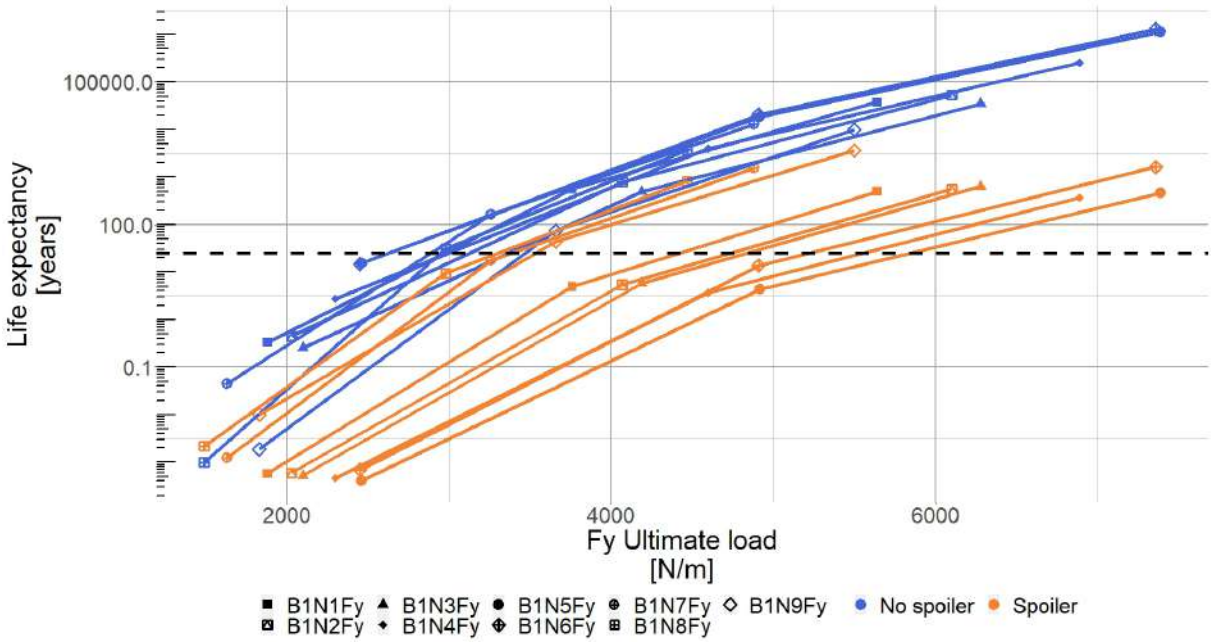

Figure 7.23 – Life time expectancy evolution with respect to the in plane local load. The blue square (■) shows the blade results without spoiler, the orange dot (●) shows the blade results with spoiler and each symbol represent a blade nodal output ($8.0\% < {}^{r}/_{R} < 16.7\%$)

Table 7.6 summarises the outcome of the fatigue calculation. The second column shows the life index impact of the considered sensor when adding a spoiler.

$$Li_j^{no\ spoiler} = \frac{T_{life_j}^{no\ spoiler}}{T_{life_j}^{no\ spoiler}} = 1 \qquad Li_j^{spoiler} = \frac{T_{life_j}^{spoiler}}{T_{life_j}^{no\ spoiler}} \tag{7.5}$$

Here, Li is the life index of the no spoiler or spoiler case, j is the section considered. Reading equation 7.5, it is apparent that $Li^{\text{spoiler}} < Li^{\text{no spoiler}}$ indicates that this specific section will fail before the no spoiler turbine. As suspected in Section 7.2.1, all local forces see a negative impact after installing the spoilers.
Despite the hypotheses and assumptions, the method employed captures the negative impact of the spoiler on the local sections well, which is in line with the blade failures (cracks), seen at the spoiler's end in the field. It is to be noted that BEM aeroelastic simulations can model neither the spoiler's glue joint nor the internal elements of the blade (such as spar or web). A dedicated finite element analysis (FEA) would be required to answer the question fully, but such a study is out of the scope of the PhD.

To compare the results of the proposed method, Table 7.7 shows the same life index calculation when using the steady polar. In some cases the fatigue calculation predicts much higher residual lifetime when adding a spoiler. It is in clear contradiction with the analysis performed so far and the damaged blades in the field. It highlights the risk of installing such AAO without knowing the aerodynamic impact and structural consequences.

Table 7.6 – Life index of the spoiler case

Sensor output	Life index [-]	Description
B1N1Fx	0.00	r/R = 8.0% normal force (flap)
B1N2Fx	0.00	r/R = 9.3% normal force (flap)
B1N3Fx	0.01	r/R = 10.0% normal force (flap)
B1N4Fx	0.01	r/R = 11.3% normal force (flap)
B1N5Fx	0.00	r/R = 12.0% normal force (flap)
B1N6Fx	0.01	r/R = 13.3% normal force (flap)
B1N7Fx	0.03	r/R = 14.7% normal force (flap)
B1N8Fx	0.03	r/R = 16.0% normal force (flap)
B1N9Fx	0.02	r/R = 16.7% normal force (flap)
B1N1Fy	0.01	r/R = 8.0% tangential force (edge)
B1N2Fy	0.01	r/R = 9.3% tangential force (edge)
B1N3Fy	0.02	r/R = 10.0% tangential force (edge)
B1N4Fy	0.00	r/R = 11.3% tangential force (edge)
B1N5Fy	0.00	r/R = 12.0% tangential force (edge)
B1N6Fy	0.00	r/R = 13.3% tangential force (edge)
B1N7Fy	0.23	r/R = 14.7% tangential force (edge)
B1N8Fy	0.39	r/R = 16.0% tangential force (edge)
B1N9Fy	0.50	r/R = 16.7% tangential force (edge)

Table 7.7 – Life index of the spoiler case assuming steady polars

Sensor output	Life index min polar [-]	Life index mean polar [-]	Life index max polar [-]	Description
B1N1Fx	7.23	0.00	0.00	r/R = 8.0% normal force (flap)
B1N2Fx	4.16	0.00	0.00	r/R = 9.3% normal force (flap)
B1N3Fx	7.79	0.12	0.00	r/R = 10.0% normal force (flap)
B1N4Fx	3.07	1.79	0.00	r/R = 11.3% normal force (flap)
B1N5Fx	0.08	0.27	0.00	r/R = 12.0% normal force (flap)
B1N6Fx	0.16	0.41	0.00	r/R = 13.3% normal force (flap)
B1N7Fx	0.19	18.74	0.83	r/R = 14.7% normal force (flap)
B1N8Fx	0.37	704.85	1704.08	r/R = 16.0% normal force (flap)
B1N9Fx	0.70	2.73	2.05	r/R = 16.7% normal force (flap)
B1N1Fy	0.00	0.01	0.00	r/R = 8.0% tangential force (edge)
B1N2Fy	0.00	0.01	0.00	r/R = 9.3% tangential force (edge)
B1N3Fy	0.00	0.02	0.00	r/R = 10.0% tangential force (edge)
B1N4Fy	0.00	0.31	0.01	r/R = 11.3% tangential force (edge)
B1N5Fy	0.00	0.20	0.01	r/R = 12.0% tangential force (edge)
B1N6Fy	0.00	0.42	0.02	r/R = 13.3% tangential force (edge)
B1N7Fy	0.01	3.22	1.02	r/R = 14.7% tangential force (edge)
B1N8Fy	0.00	287.13	372.88	r/R = 16.0% tangential force (edge)
B1N9Fy	0.01	3.42	2.58	r/R = 16.7% tangential force (edge)

7.3 Summary

The Chapter 7 analysed the impact of an installed root spoiler on the AEP and loads from a 2MW turbine. Regarding the AEP gain and rotor integrated load the spoiler impact is marginal. The AEP increases by a small amount ($\approx 0.5\%$) with a large variation associated. So far, all the efforts to measure in the field, the AEP led to inconclusive results due to the small absolute difference and large dispersion in the power curve measuring method. The integrated loads remain approximately constant, a small decrease in flapwise root bending moment has even been noted. However, the local root loads increase significantly with a large variation around the mean value.
A fatigue analysis has been performed using a novel way of capturing the aerodynamic unsteadiness due to the aerofoil's behaviour. It uses 2D CFD flow characteristics (Vortex Shedding Frequency) as well as the results calculated from three different steady polars (maximum, mean and minimum aerodynamic coefficients). The spoiler increases the already locally present unsteadiness and should not be neglected in the turbine's structural design. The spoiler can be detrimental to the turbine lifetime, retrofitting such devices should be done with care and the turbine's mechanical properties should be re-evaluated prior to installing the spoiler. Finally, the presented method currently relies on 2D assumptions and BEM calculations, further studies involving 3D CFD verifying the assumptions made will be presented in Chapter 8.

Chapter 8

Blade root spoilers effect comparison: 2D vs 3D unsteady simulations

Contents

Previous chapters were dedicated to develop a method to estimate fatigue loading introduced by root spoilers, or add-ons in general, from 2D CFD simulations. The present chapter focuses on estimating differences between 2D and 3D CFD flow physics at the root spoiler and ultimately ensures the correctness of the method introduced in Chapter 7. It is important to emphasise here that, using the described method of Chapter 7 with 3D CFD polar would be the best approach. However, it is unreachable in term of computational cost within the PhD duration and even more inaccessible in the design phase for blade manufacturer. The present simulations do not include the full turbine geometry (no tower and no nacelle) with rigid blades. The inflow is simplified to a steady and uniform case. Only one operating conditions is performed and chosen from the optimisation procedure presented in Chapter 7, the domain size and AGR are chosen after validation the simulation parameters using the DANAERO database (see Section 4.2 and Section 4.3). The results presented after are limited to the following operating conditions:

- Inflow: 8m/s
- Pitch: -1.568°
- Rotation speed: 14.1 RPM

At last, results from the root spoiler configuration are systematically presented against simulations of the no spoiler configuration for comparison purposes. It should be noted that 2D simulations from Chapter 6 were not performed at the exact same angle of attack as 3D simulations because this quantity is only known after computation of the induction (see Section 8.1.1 for more details on the evaluation of the angle of attack). For comparison purposes, it was thus necessary to rerun 2D simulations corresponding to the local

angle of attack from 3D simulations.
Results are separated in two parts. The first part presents results at the rotor scale including two sections. The first section gives an overview of the far wake organisation using the refinement method described in Section 4.3. In the following section the zone impacted by the spoiler is presented. In the second section, results focus on the blade aerodynamics. Starting from the 3D blade organisation to the unsteady pressure distribution in the blade root area. These 3D results are compared to the 2D simulations and BEM computations when possible.
Because of the blade scan orientation and CFD set-up (see Figure 4.11), the main velocity is following the z-axis (U_z), the x-axis represents the chordwise velocity (U_x) and the y-axis the spanwise velocity (U_y).

8.1 Analysis of the spoiler impact in 3D simulations

In this chapter the impact of the spoiler is analysed for the first time using 3D URANS simulations. The first sections give a description of the spoiler effect at the rotor scale: upstream in the induction zone, downstream in the rotor near and far wake area and finally in the rotor plane (the axial and tangential induction and the angle of attack). Major impacts are expected in the blade root area and are detailed later. The impacted area is first identified using the mean wall shear stress quantity, then the blade root mean flow organisation is described. The loads associated to the spoiler addition are analysed by means of the C_p and C_L. Finally, the unsteady flow and loads are characterised using spectrum analysis.
The following table highlights the main operating conditions for the 3D simulations.

Table 8.1 – 3D operational conditions for the no spoiler and spoiler at the radial position $^r/_R = 0.13$

Conditions	**No spoiler**	**Spoiler**
Rotation speed	14.1 RPM	
Relative velocity	11.5m/s	11.4m/s
Angle of attack	27°	19.3°
Reynolds number	2.42×10^6	2.39×10^6
Chord	3.1m	

8.1.1 At the rotor scale

Upstream and downstrean the rotor

The upstream region of the turbine is dominated by the induction zone. It is defined by the wind inflow reduction when approaching the turbine. The induction zone is defined here where the velocity is below 99% of the inflow. In Figure 8.1, the rotor centre of rotation is located in $[^X/_D = 0; {}^Y/_D = 0; {}^Z/_D = 0]$, where X, Y and Z are the Cartesian coordinate system used with the rotor plane located in the $X - Z$ plane. The induction

extent can be highlighted using isocontour of the streamwise velocity in the $Z-Y$ plane (see Figure 8.1). It clearly shows, for the spoiler and the no spoiler case, that the induction area extends $2D$ upstream of the rotor plane, with D the rotor diameter. Also this induction zone progressively decreases, for both cases, from $^{Y}/_{D} = 0$ to $^{Y}/_{D} \approx 1.25$ (light orange and yellow zone ahead of the rotor plane). In the defined induction area, the mean streamwise velocity reduces by up to 20%. All these observations are in good agreement with both the experimental [129] and the numerical literature [18, 149] without spoiler. Since the induction area is identical in both cases, it indicates that, as expected, the spoiler has no effect on this area.

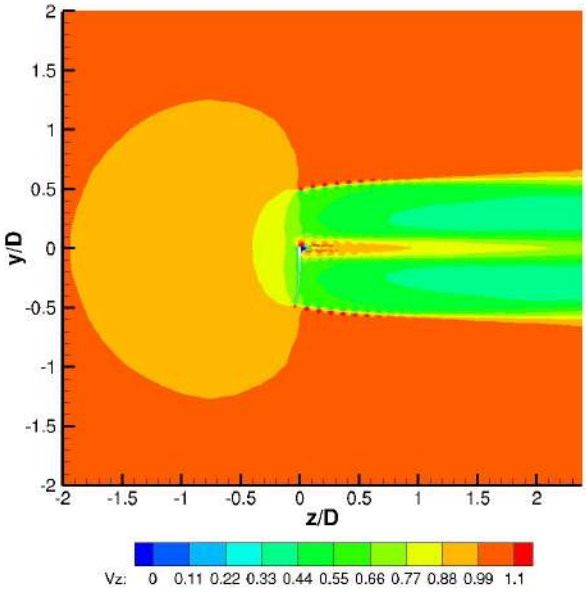

(a) Axial inflow reduction, no spoiler case (close up).

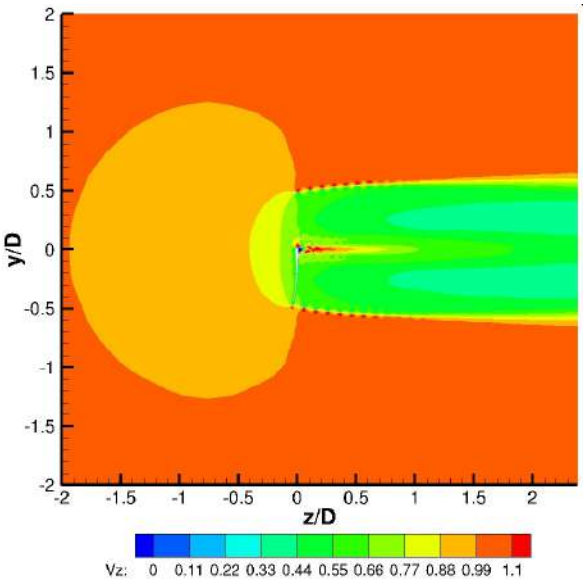

(b) Axial inflow reduction, spoiler case (close up).

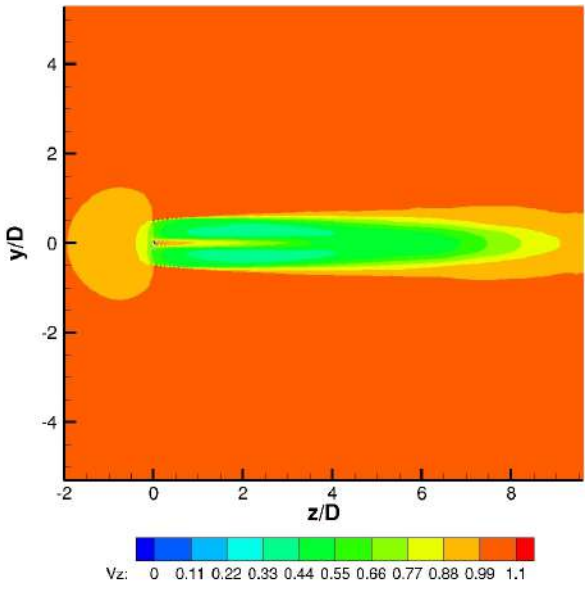

(c) Axial inflow reduction, no spoiler case (full wake).

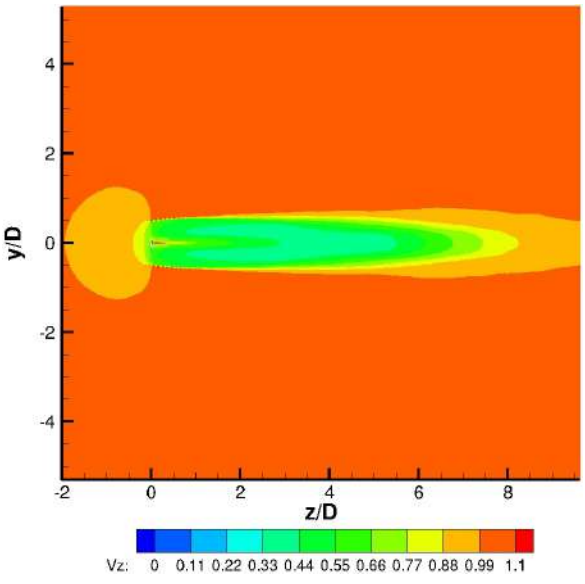

(d) Axial inflow reduction, spoiler case (full wake).

Figure 8.1 – Effect of the spoiler on the induction zone, near and far wake mixing. The inflow is dimensionless (V_z) and flows from left to right.

Behind the rotor, a near wake organisation develops in two main areas: a centred cone area, starting at $^{Z}/_{D} = 0$ and ending at $^{Z}/_{D} = 3$, in the no spoiler case, (see Figure 8.1a). Outside of the cone area, there exists a constant velocity deficit bounded by the well-known tip vortices (see the wavy surfaces of Figure 8.2a or the Q-critera iso-contour of the Figure 8.2b). This global organisation found with and without spoiler agrees well with the existing literature (see e.g. [12]). In the presence of the spoiler, the cone size is largely decreased from more than $3D$ diameters down to less than $1D$ (estimated at the threshold level $V_z = 0.66$ of the dimensionless streamwise velocity from Figure 8.1b). This is expected as the spoiler improves the blade root energy extraction and increases the flow mixing, thus reduces further the wind velocity in the near wake. Consequently, it increases the root loads, in good agreement with the flow reorganisation observed in 2D simulations of Chapter 6. A slight overspeed is also noted for the root spoiler case, which might be attributed to the flow circumvention at the spoiler location. However, this local organisation would certainly be highly influenced by the presence of the nacelle and would need further investigations.

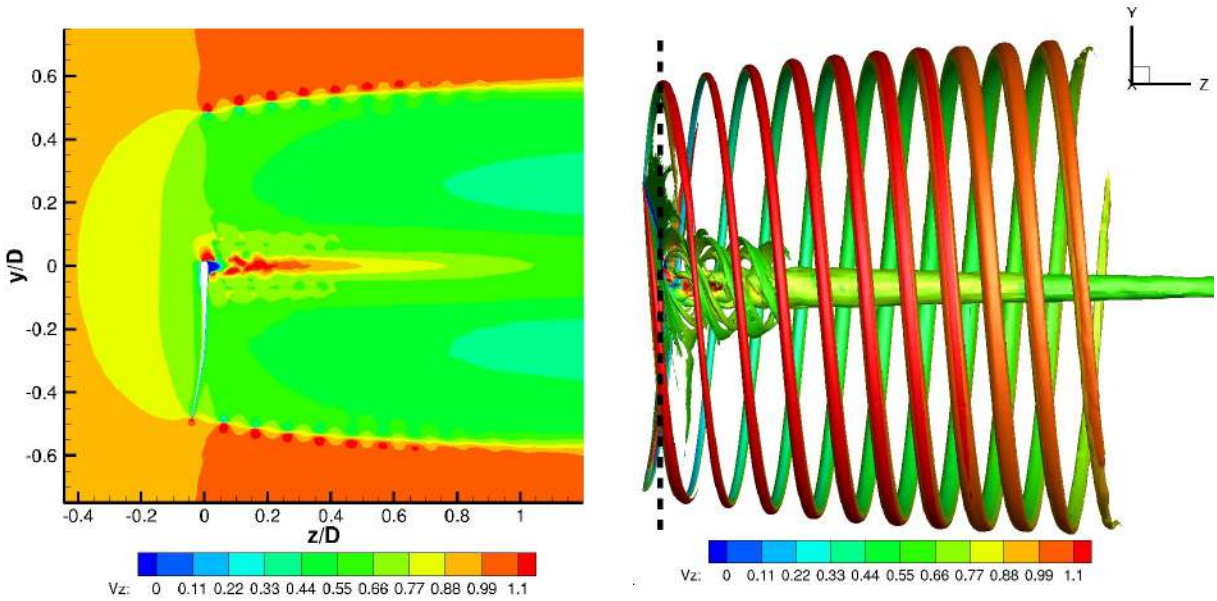

(a) Near wake axial inflow reduction for the spoiler case

(b) Isosurface of the Q-criteria illustrating the tip vortices. The dashed line represents the rotor plane.

Figure 8.2 – Near wake description of the spoiler case.

Further along the blade span, the near wake deficit for the no spoiler case is as important as in the spoiler case (approximately 60% of the inflow), meaning that blades are working efficiently to extract kinetic energy from the wind with or without spoiler.

In the far wake, the recovery distance (taken at 99% of the streamwise velocity) without spoiler is around $z/D = 9$, while it is $8.5D$ for the spoiler case (see green lines on Figure 8.3a and Figure 8.3b). This impact is four times smaller than the one observed in the near wake (cone reduction from $3D$ to $1D$). These results are showing similar tendency as what is generally underlined in the literature about the independence of the blade aerodynamic with the far wake [147, 136].

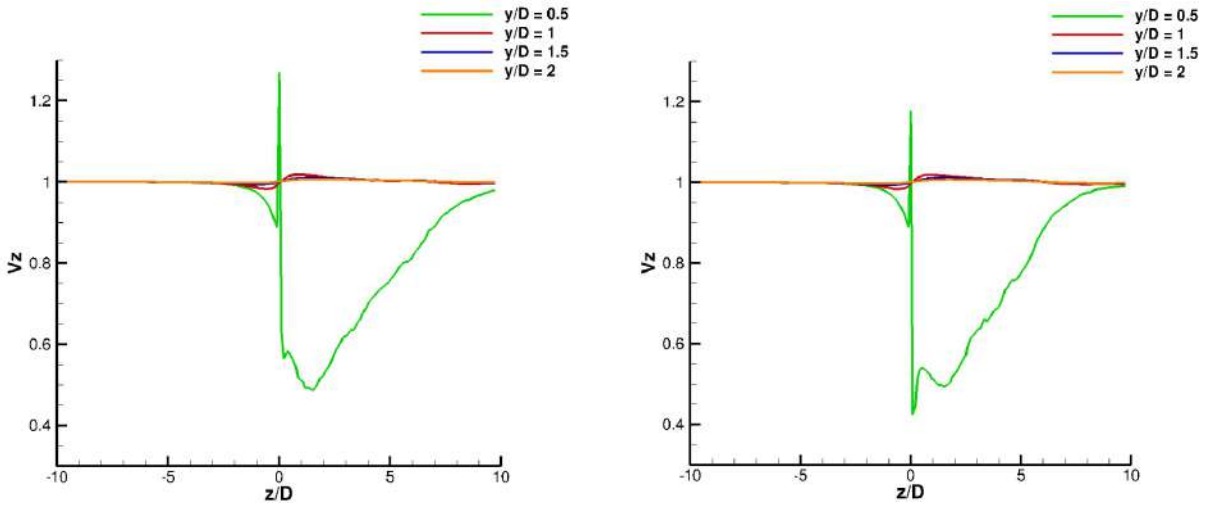

(a) No spoiler (b) Spoiler

Figure 8.3 – Axial dimensionless velocity deficit at different rotor spanwise positions for the no spoiler and spoiler case.

In the rotor plane

After investigating upstream and downstream the rotor, the following sections will focus on the rotor plane region with observations of the spoiler impact on the local axial and tangential inductions and on the local angle of attack.

Axial induction

Following the classical BEM theory (see [53, 19] and Section 2.1) the axial induction is defined as: $a = 1 - \frac{U_z}{V_0}$, where U_z is the velocity in the z-direction and V_0 the free-stream velocity. The axial induction evolution along the blade radius shows its efficiency to extract energy (see Figure 8.5). According to the BEM theory, the optimal induction along the blade radius is $a = 1/3$. The extraction of the blade related velocities using the AAT method described in 4.3.3 can be used to obtain the inductions in the rotor plane.

Figure 8.4 shows the axial induction in the rotor plane for the spoiler case. It clearly highlights that the highest energy extraction is located in mid-span and outer part of the blade. The energy extraction at the root and tip area is degraded due to respectively the tip vortices and the 3D flow organisation at the root, as described in [61].

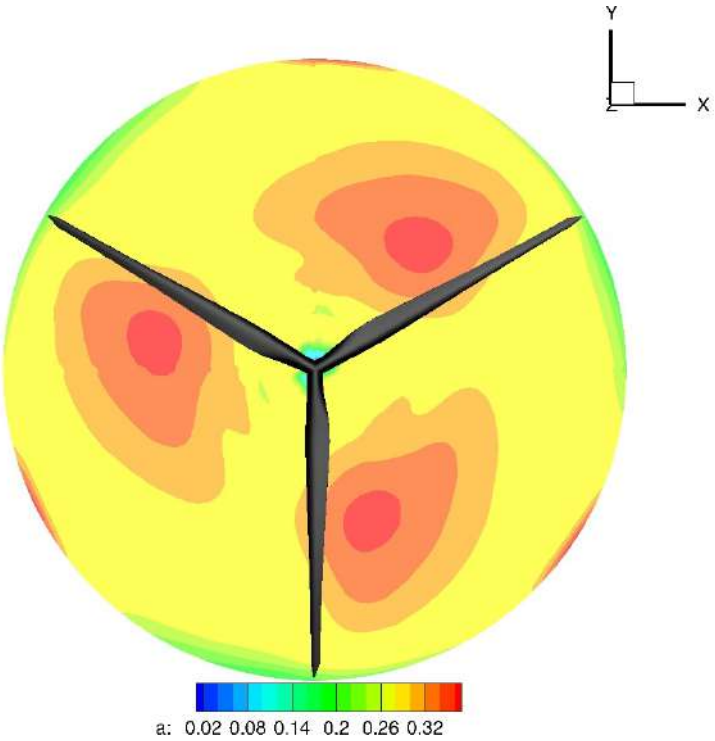

Figure 8.4 – Axial induction over the rotor plane for the spoiler case.

The spoiler effect is seen on the blade inboard on Figure 8.5: the induction increases significantly where the spoiler is installed (from $0.03 < {}^{r}/_{R} < 0.17$). The end of the spoiler is marked by a drop in induction before an increase where the blade becomes more aerodynamic.

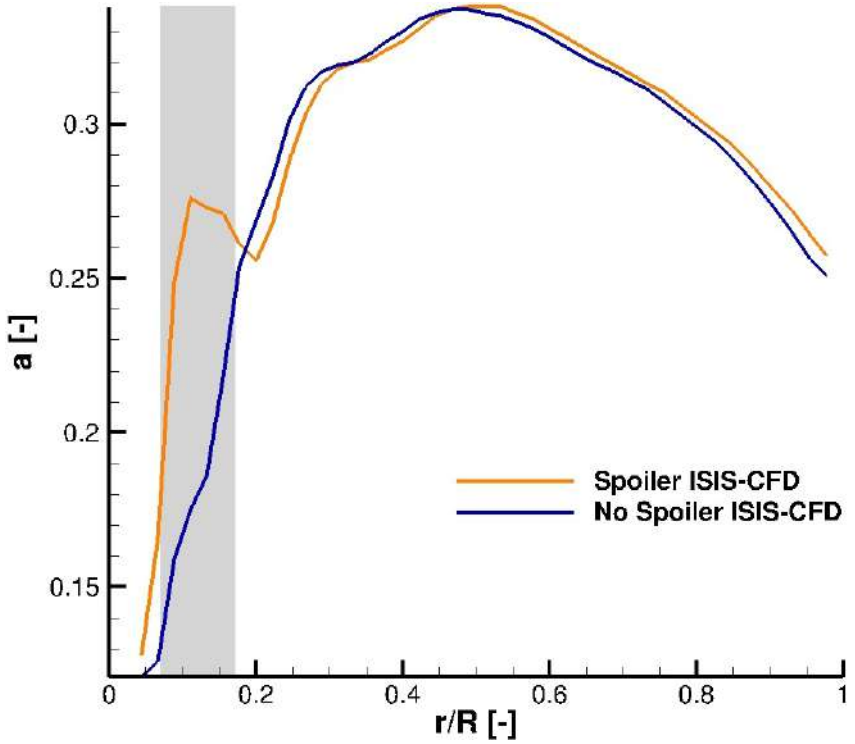

Figure 8.5 – Effect of the spoiler on the local axial induction along the blade radius.

Tangential induction

Regarding the tangential induction, it can be obtained from the ratio between the local tangential flow velocity and the local rotational speed, i.e. $a' = -U_x/\omega r$, where U_x is the induced tangential flow velocity, ω the blade rotational speed and r the considered radius ([60]). Figure 8.6a shows its evolution along the blade radius without and with the spoiler. Similarly to the axial induction, the tangential induction is significantly increased at the blade root with a spoiler. This increase is linked to the extent of the cone area behind the rotor detailed in the Section 8.1.1.

At this stage, it is interesting to evaluate the angle of attack modification from these two induction quantities.

Angle of attack

The Figure 2.3 in Section 2.1, illustrates the relationship between the inductions and the angle of attack which translates into: $\alpha = \varphi - \theta$ where φ is the inflow angle and θ is the sum of the blade pitch and local twist. The inflow angle is calculated using the axial and tangential induction : $\varphi = \arctan \frac{U_z(1-a)}{\omega r(a'+1)}$. The Figure 8.6b shows the computation of the angle of attack evolution along the blade radius without and with spoiler using previous axial and tangential inductions. As expected, the blade inboard experiences high angles of attack without spoiler where the local section operates in the stall region. The spoiler tends to reduce the local operating angle of attack where installed, although the section still operates in the stall region. This is mostly due to the axial induction increase and partly thanks to the tangential induction increase. Lowering the angle of attack would mean that the local sections will operate at lower C_L and C_D. It will also operate closer to the linear region, thereby limiting the harmful effects of the stall region. However, as it is shown the in following sections, the spoiler effect is not strong enough to remove the flow separation region.

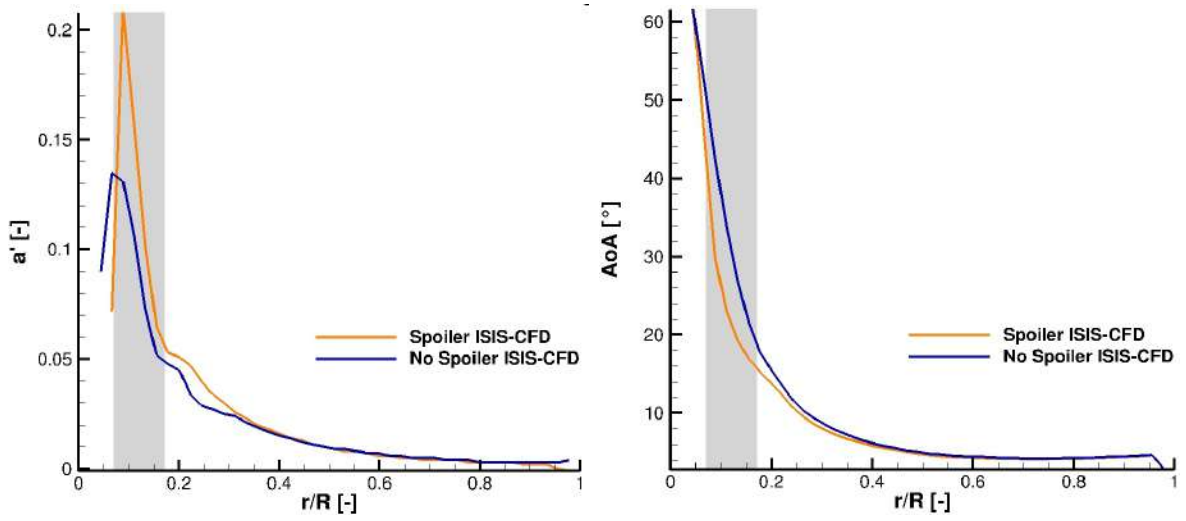

(a) Effect of the spoiler on the local tangential induction along the blade radius.

(b) Effect of the spoiler on the local angle of attack along the blade radius.

Figure 8.6 – Tangential induction and angle of attack evolution for both no spoiler and spoiler case.

8.1.2 At the blade scale

This section aims at understanding the spoiler impact at blade level. Locating first the modified area, the flow reorganisation is then described. Impact on local loads is presented and the description of the blade wake dynamics reorganisation follows.
The coordinate system used in the following is attached to the blade, with its centre at the intersection of the three blade axis. The x-axis is along chordwise direction, the y-axis is along the blade length and the z-axis is orthonormal to the x-axis and y-axis.

Identification of the impacted area

The 3D flow organisation at the root area is first analysed in this section through the mean wall shear stress (WSS) quantity in the chordwise direction, τ_x, and in the spanwise direction, τ_y, to have a global overview of the impacted area by the spoiler. It is defined by the following equations and its unit is in $[N/m^2]$:

$$\tau_x = \mu \left(\frac{\partial U_x}{\partial z} \right) \Big|_{z=0} \qquad \tau_y = \mu \left(\frac{\partial U_y}{\partial z} \right) \Big|_{z=0} \tag{8.1}$$

U_x is the x-axis velocity component, U_y is the y-axis velocity component, z the direction normal to the rotor surface and μ is the dynamic viscosity.
Wall shear stress isocontours for the two directions are plotted on the inboard region of the blade in Figure 8.7a and Figure 8.7b for the no spoiler and the spoiler cases. The WSS_x shows a clear region where its value is negative and thus lower than the rest of the blade (in cyan), indicating a reverse flow region of the U_x component. This region extends until $r/R \approx 20\%$ in both cases in good agreement with the literature (see e.g. [25, 98]). This region is bounded by transitional regions where the WSS is no longer negative but still lower than rest of the blade (in yellow). The spoiler does not remove the reverse flow region, on the contrary, it increases slightly.
On the other hand, the wall shear stress value component along the blade length, WSS_y, in Figure 8.7b underlines a region in red, until $r/R \approx 0.3$, where the WSS is positive. This region remains almost unchanged when a spoiler is installed and is related to the well-known crossflow due to the rotation as described in Section 8.2.1.
It should be noted that both WSS components are calculated using URANS simulations and exhibit a beating movement in the radial direction that will be discussed further in the unsteady investigation of Section 8.2. To understand in more details the wall shear stress distribution, it is analysed in the next section with respect to the velocity field organisation.

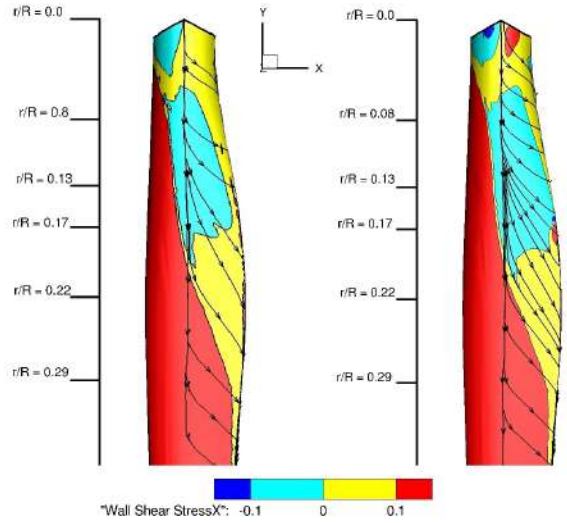

(a) Wall Shear Stress (WSS_x) comparison for both case. Left: no spoiler - right: spoiler.

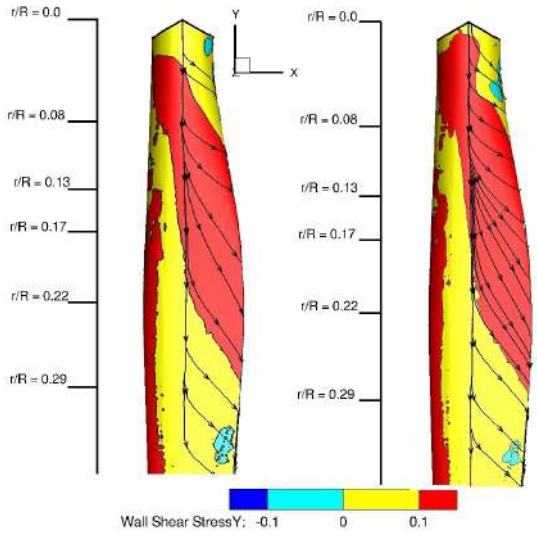

(b) Wall Shear Stress (WSS_y) comparison for both case. Left: no spoiler - right: spoiler.

Figure 8.7 – Wall Shear Stress comparison for both case in the following the x and y directions.

The blade root flow organisation

Figure 8.8 and Figure 8.9 show respectively isocontours of the velocity U_x and velocity U_y at the radial position $r/R = 0.13$ in an isometric view, overimposed with the previously illustrated wall shear stress. The figures show the blade from $r/R = 0.13$ to $r/R = 0.4$. Isocontour of the chordwise velocity (U_x) clearly evidences the flow separation region in good agreement with the negative wall shear stress region shown in the previous section. Moreover, the other velocity component (the spanwise velocity U_y), in Figure 8.8b highlights the Himmelskamp (or Coriolis) effect (also seen on Figure 8.7b). This last flow organisation induces an increase of the wall shear stress spanwise component that is found responsible of a pressure increase on the blade suction side noticed in the following section (see Figure 8.17b). Indeed, the chordwise velocity component exhibits a flow separation and thus normally a zero pressure gradient evolution. This Coriolis beneficial effect is retrieved and described in the literature (see e.g. [61]). The spoiler does not impact significantly this phenomenon, the cross-flow region being only slightly increased (see Figure 8.9a) and the separated region is almost unchanged. Therefore, the previously observed impact of the spoiler in Section 8.1.1: the cone reduction, the angle of attack reduction and the axial and tangential induction increase cannot be attributed to the improvement of the flow separation by the spoiler, nor the increase of the beneficial cross-flow effect. It should be rather linked to the spoiler ability to reorganise the pressure distribution around the aerofoil which is investigated in the next section.

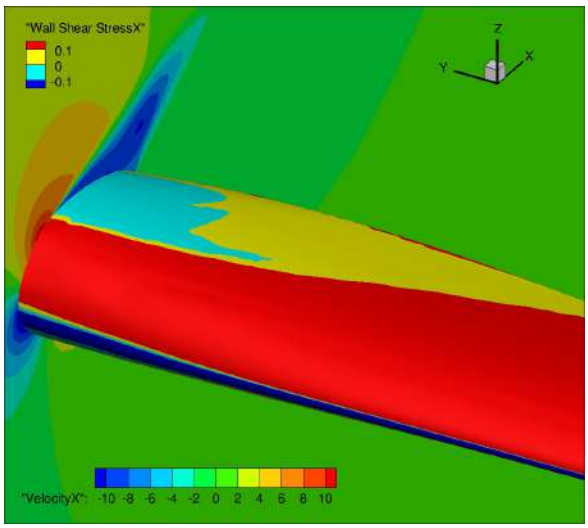

(a) No spoiler R6 - WSS_x and U_x velocity field

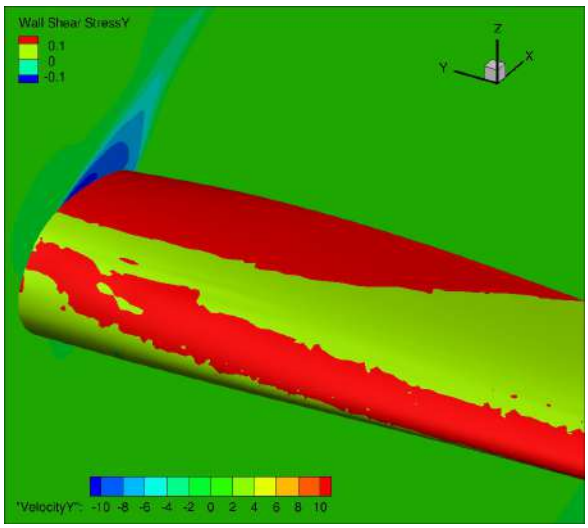

(b) No spoiler R6 - WSS_y and U_y velocity field

Figure 8.8 – Wall Shear Stress and velocity field for the no spoiler cases following the x-axis and y-axis. Respectively the chordwise and spanwise direction. The velocity field intersects the blade at $^r/_R = 0.13$, the blade can be seen up to $^r/_R = 0.4$.

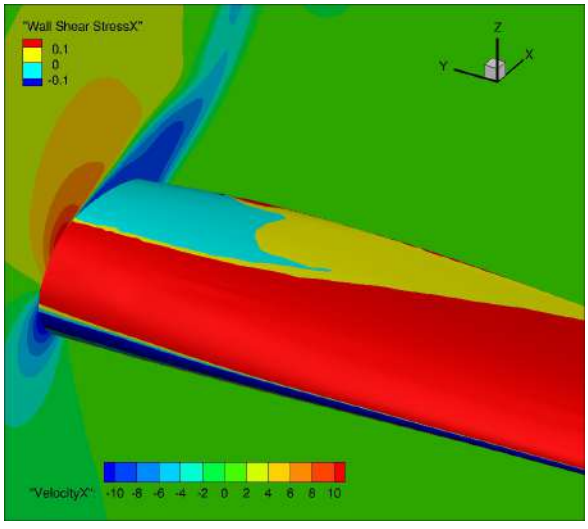

(a) Spoiler R6 - WSS_x and U_x velocity field

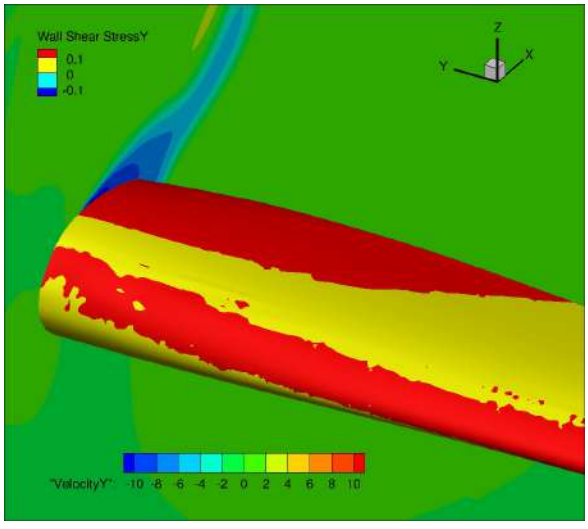

(b) Spoiler R6 - WSS_y and U_y velocity field

Figure 8.9 – Wall Shear Stress and velocity field for the spoiler cases following the x-axis and y-axis. Respectively the chordwise and spanwise direction. The velocity field intersects the blade at $^r/_R = 0.13$, the blade can be seen up to $^r/_R = 0.4$.

Impact on blade loads

The following section will detail the spoiler impact on the mean local wall pressure coefficient (C_p) and lift coefficient evolution in 3D for the radial position $r/R = 0.13$. In both spoiler and no spoiler cases, the separated flow region does not exhibit a flat C_p distribution (zero pressure gradient) in the trailing edge region. This is to be attributed to the beneficial Coriolis effect described in the previous section. As a reminder, the spoiler is installed on the pressure (bottom) side of the aerofoil. When the spoiler is installed, the impact on the pressure is mostly found on the pressure side (bottom curve), the C_p being only slightly increased in the suction side. This induces an increase of the mean C_L value (see Figure 8.10b) and a decrease of the moment coefficient as the aerofoil loading is more evenly distributed rather than front loaded (not shown here). The lift is not steady due to two phenomena observed in simulations (see short movies available online [110, 109]): vortex shedding from the unsteady blade wake organisation and transverse flow unsteadiness. The spoiler increases significantly these lift oscillations, similarly to the findings in 2D simulations (see Chapter 6). The following section will examine in more detail this unsteady organisation.

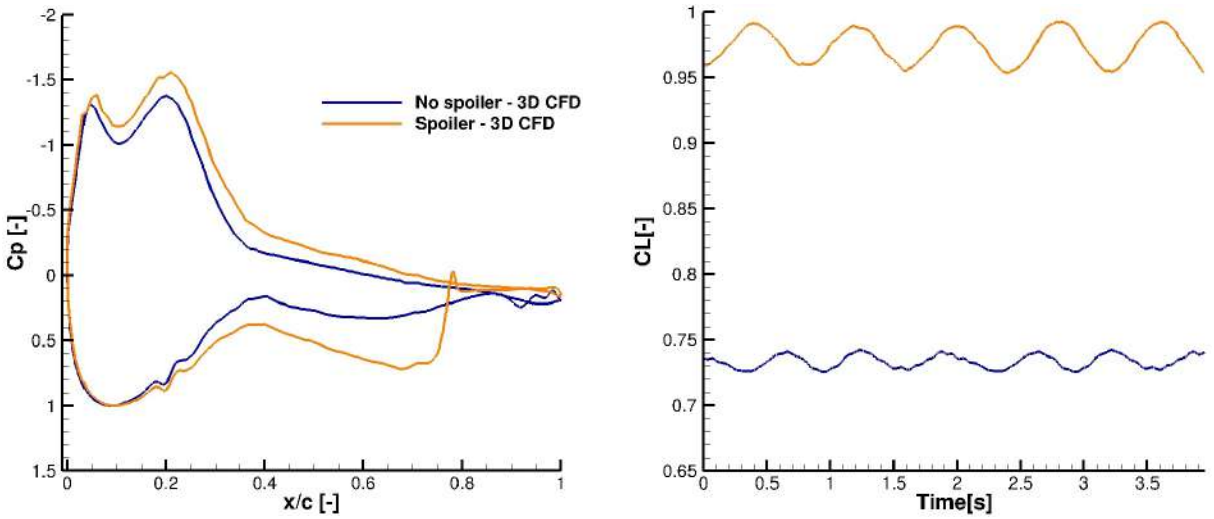

(a) Pressure coefficient, C_p, comparison between the no spoiler and spoiler case in 3D

(b) Lift coefficient, C_L, comparison between the no spoiler and spoiler case in 3D

Figure 8.10 – Comparison of the C_p and C_L in 3D for the no spoiler and spoiler case.

Unsteady investigation

The following section will first investigate the possible sources of unsteadiness responsible of the lift fluctuations. In the following, the focus will be on the radial location $r/R = 0.13$.

The main known source of unsteadiness is the vortex shedding from the blade wake organisation. The Figure 8.11 shows for both cases, no spoiler and spoiler, the 3D simulations outcome of the vorticity and Q-criteria. The Q-criteria is illustrated by black lines following a logarithmic increment between 0.1 and 1000. Due to the blade rotation the

vortices are elongated and no longer circular as described later in section 8.2.1 in more details. They are however present and tend to move "upward", following, the main inflow direction. This behaviour is thus creating the cone noticed near the centre of rotation in Figure 8.2b.
The spoiler case exhibits a wider wake than the no spoiler case, similar to previous 2D simulations (see Chapter 6). The vortex shedding organisation seems to be also impacted. In the following plots (Figure 8.12 to Figure 8.15), a spectral analysis is performed in the wake region from a probing point located after the trailing edge. It is located 10% of the local chord after the trailing edge and aligned with the blade's section chord (see Figure 8.11). It is compared with the spectral analysis of the lift fluctuation at this section, for the no spoiler and spoiler cases.

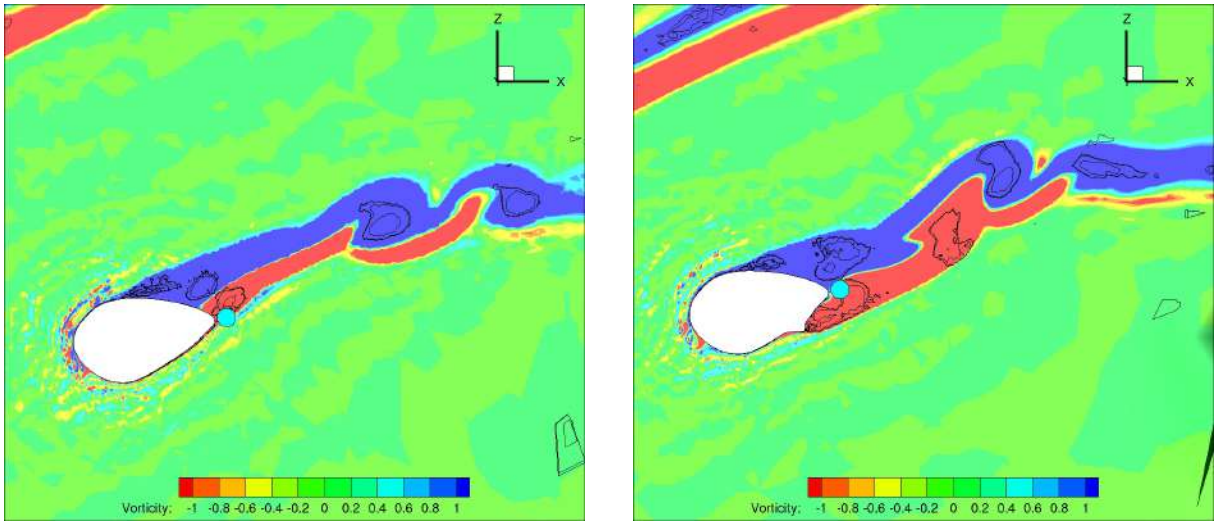

(a) 3D No spoiler case Vorticity and Q-criteria. (b) 3D Spoiler case Vorticity and Q-criteria.

Figure 8.11 – No spoiler and spoiler case 3D vorticity and Q-criteria, operating following the conditions of Table 8.1. The probing point is shown as the cyan dot (●) near the aerofoil's trailing edge.

The no spoiler case shows that both main peak frequencies from the sample signal in the aerofoil's wake and from the lift signal happen around 1.5Hz (see Figure 8.12). The C_L PSD fails to capture the first harmonic seen in the wake velocity signal. Although the aerofoil is 60% thick, this behaviour falls in line with the well known cylinder behaviour: the C_L carries the main frequency while the C_D carries the first harmonics and is always twice as high as the peak frequency [66]. In the wake both information are available through the air velocity and therefore the main frequency and harmonics are seen. In the following figures, "3D CL" refers to the lift coefficient calculated by integrating the pressure coefficient around the aerofoil from 3D CFD simulations. "3D Inflow" refers to the measured data through a probing point positioned in the wake of the 3D blade.
Aside from the main inflow direction (U_z), the main component of the peak frequency is U_y. It corresponds to the cross-flow pulsing from the blade root toward the tip as clearly seen on Figure 8.13. The blue square (■) on Figure 8.13 and Figure 8.15 corresponds to the vectorial sum of U_x, U_y and U_z, i.e. the velocity vector $\mathbf{U}$.

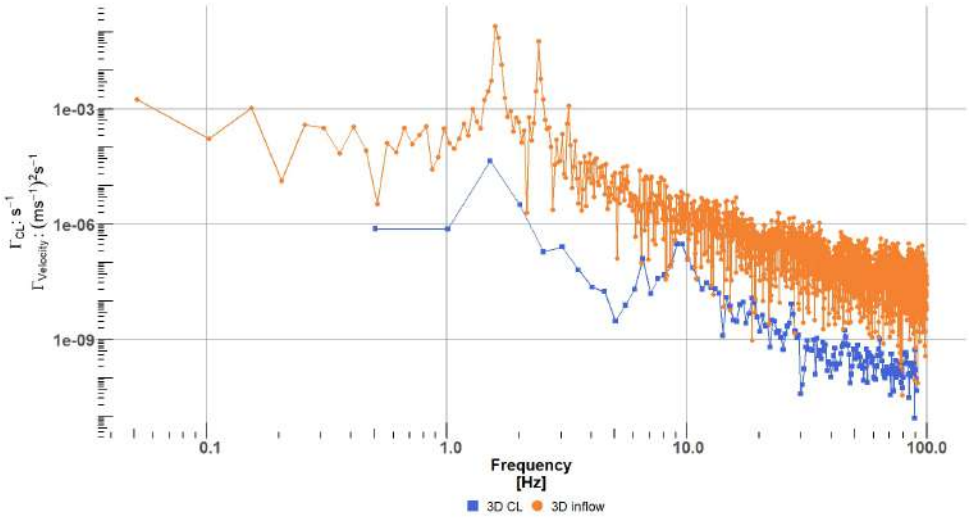

Figure 8.12 – C_L and relative velocity power spectral density of the no spoiler case in 3D. The blue square (■) shows the 3D C_L results and the orange dot (●) shows the 3D relative velocity results.

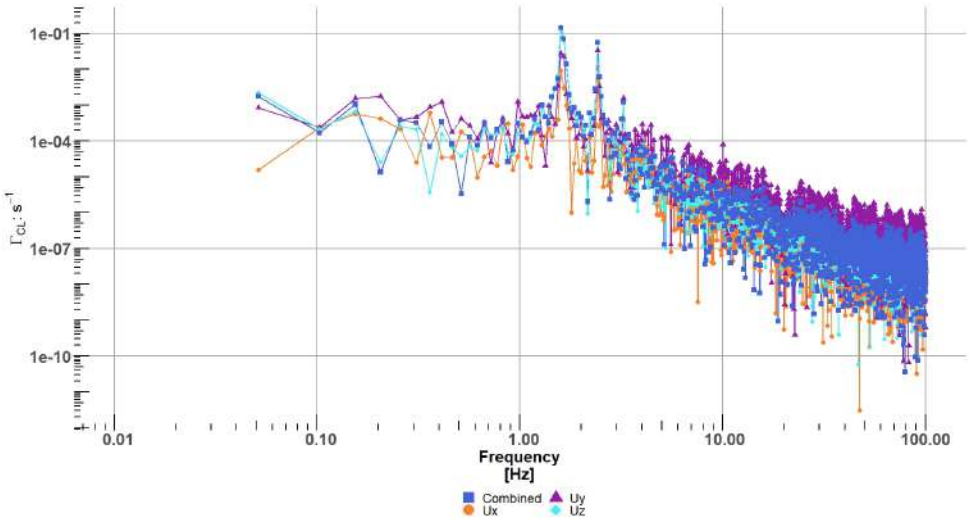

Figure 8.13 – Comparison of the power spectral density for the relative velocity and its components in the three dimensions for the no spoiler case. The blue square (■) shows the relative velocity, the orange dot (●) shows x-axis velocity component, the purple triangle (▲) shows y-axis velocity component and the cyan diamond (◆) shows z-axis velocity component.

In the spoiler case, the peak frequency measured in the wake of the aerofoil is much broader than the one from the lift coefficient and occurs at a slightly lower frequency level, ≈ 1Hz (see Figure 8.14). The wake being broader in the spoiler case, the associated vortices are larger. It induces a slower convective velocity of these vortices and thus a lower shedding frequency. The broader peak frequency can be explained by either a merging of vortices or the perceived area by the flow is "less smooth" due to the spoiler's presence. However, the most probable scenarii are either a different contribution from other velocity

components or because the probe in the wake is capturing trailing flow from previous radial positions as illustrated by the inclined streamlines on the Figure 8.7a. Indeed, no vortex merging were observed and the vortices do not leave the trailing edge in a similar fashion. As shown in Figure 8.11, for the no spoiler case, the probing point is at the edge of the wake, while in the spoiler case it is in the middle of the bottom vortex.
Similar to the no spoiler case, U_z and U_y are the main contributors of the peak frequency. Dedicated studies to discriminate the influence of the rotation and the blade span would be necessary to identify the independent effects on the spectral broadening.

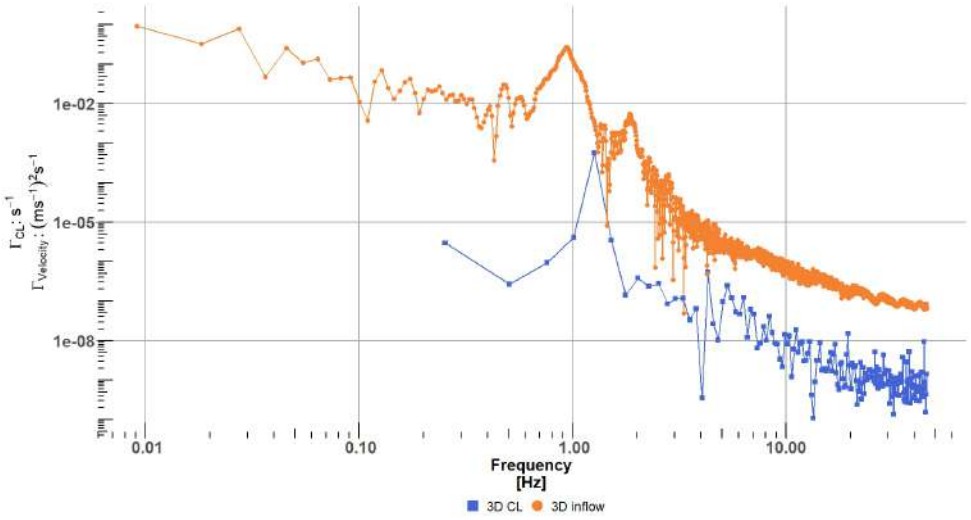

Figure 8.14 – C_L and relative velocity power spectral density of the spoiler case in 3D. The blue square (■) shows the 3D C_L results and the orange dot (●) shows the 3D relative velocity results.

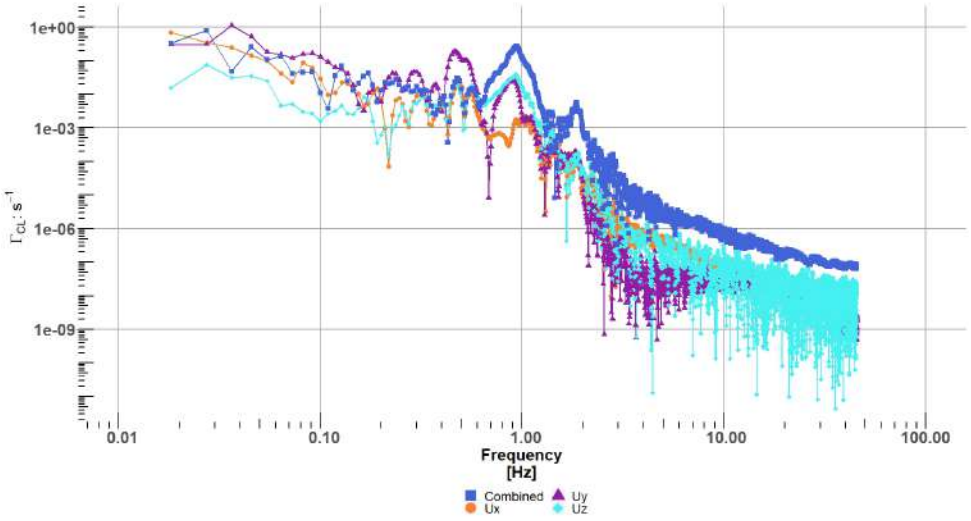

Figure 8.15 – Comparison of the power spectral density for the relative velocity and its components in the three dimensions for the spoiler case. The blue square (■) shows the relative velocity, the orange dot (●) shows x-axis velocity component, the purple triangle (▲) shows y-axis velocity component and the cyan diamond (◆) shows z-axis velocity component.

The main difference between choosing the wake velocity or the C_L for performing a PSD analysis is the energy within the spectrum. The energy contained in the lift spectrum is much lower than the energy captured in the relative velocity as indicated by the difference in the levels of the power spectrum in Figure 8.12 and Figure 8.14. Otherwise the predicted VSF in both methods is quite similar. Because the goal is the fatigue analysis, the case without and with the spoiler are compared using loads, here the sectional C_L, in Figure 8.16. It shows that, in 3D, the addition of the spoiler to a blade section does not change significantly the VSF, despite the different angle of attacks. Indeed both peak frequencies are close to each others ($f_1 = 1.26$Hz and $f_2 = 1.52$Hz). Two main contradicting effects can explain the differences in VSF: the change in angle of attack and the wake widening due to the spoiler addition. The spoiler reduces the local angle of attack which tends to increase the VSF. However, the spoiler's other characteristics is that it widens the wake behind the aerofoil which tends to reduce the VSF. The Figure 8.16 indicates that the wake widening effect is stronger than the angle of attack reduction.

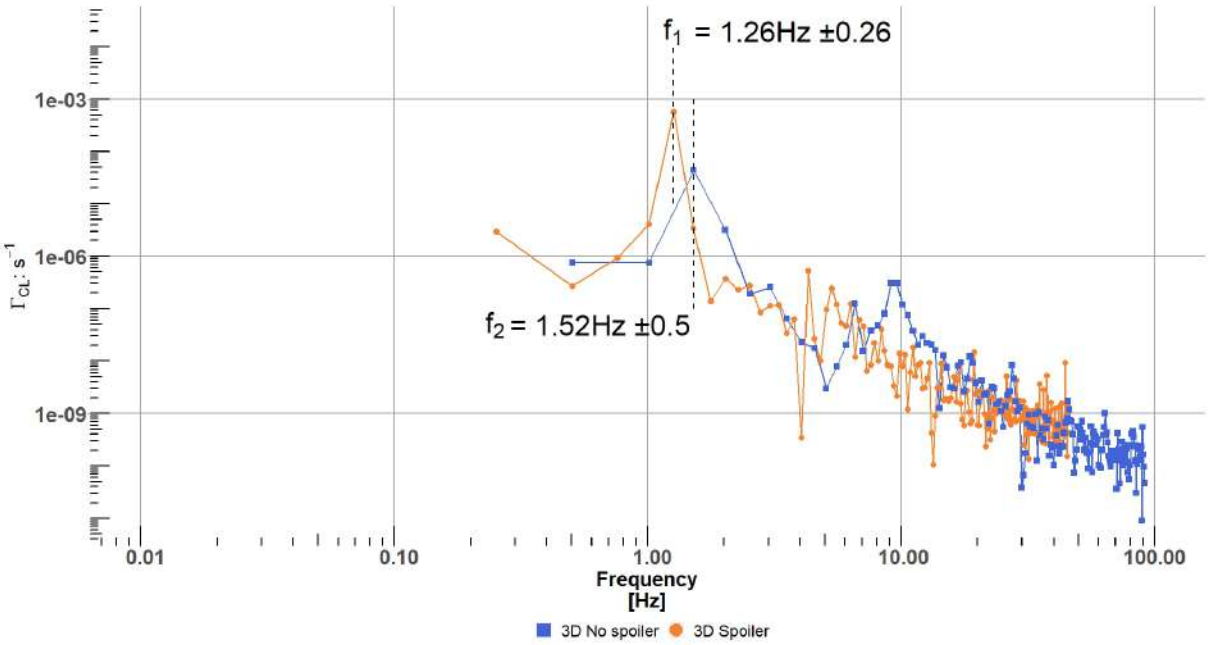

Figure 8.16 – C_L power spectral density for both cases in 3D. The blue square (■) shows the C_L results for the no spoiler case in 3D and the orange dot (●) shows the C_L results for the spoiler case in 3D. The "±" symbol corresponds to the spectral discretisation used.

8.2 Impact of the simulation fidelity on the spoiler effect

Increasing simulation fidelity increases the computational time. Using polars from 2D simulated aerofoil sections together with a BEM approach is reasonable in the design phase in term of computational cost. However, this may induce bias that is not always known. The impact of fidelity simulations on the spoiler effect is evaluated here. The difference in simulation fidelity is first presented at the aerofoil scale by comparing 2D URANS simulations with aerofoil cross sections of 3D URANS simulations. Then, it is shown at the rotor scale, by comparing BEM simulations, using 2D URANS simulations as aerodynamic polar inputs, with 3D URANS simulations. Finally 3D URANS simulations are briefly compared with DDES simulations.

8.2.1 At aerofoil scale

3D simulations previously described are presented below at $^{r}/_{R} = 0.13$, while 2D simulations have been redone to match the exact same angle of attack and Reynolds number perceived in 3D (see Table 8.1).

Aerofoil local and global loads

The wall pressure coefficient, C_p, is used to help define the possible separation along the aerofoil. Flow separation occurs after a sharp adverse pressure gradient and can be observed on a C_p plot in the region exhibiting a plateau. Such example occurs at $^{x}/_{c} = 0.25$ on the Figure 8.17b for the 2D case while it is not present in 3D simulations, for both cases (without and with spoiler). Also, integrating the area comprised between the two C_p curve (suction side and pressure side) allows for the calculation of the local lift coefficient C_L and drag coefficient C_D. The velocities used to calculate the different metrics have been extracted using the AAT method described in Section 4.3.3.
Figure 8.17 and Figure 8.18 show the differences at aerofoil level between 2D and 3D CFD simulations through the comparison of the mean local wall pressure coefficient, C_p, and the instantaneous lift coefficient, C_L. For both cases, the no spoiler and the spoiler case, the pressure coefficient distribution exhibits a plateau and thus a separated flow area in 2D that is not present in 3D simulations. It is due to the cross-flow and the Coriolis effect in good agreement with the stall delay phenomenon found in the literature [27, 128] and already discussed in Section 8.1.2. For the no-spoiler case, the impact of the mean lift level due to this Coriolis effect is found to be almost tripled, from $C_L^{2D} \approx 0.25$ to $C_L^{3D} \approx 0.75$ (see Figure 8.17b).

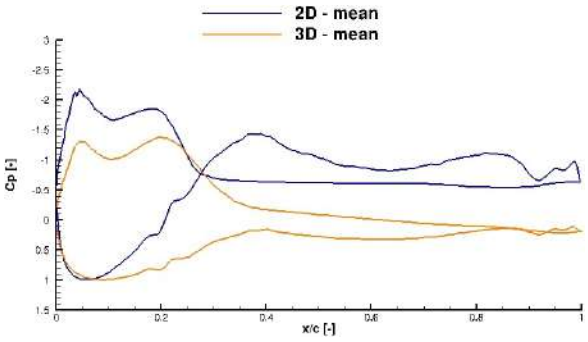

(a) No spoiler case - C_p comparison between 2D and 3D simulations

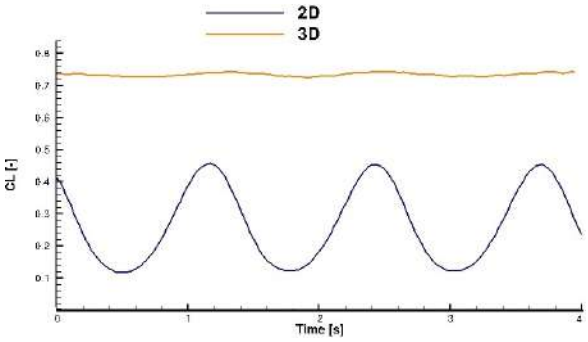

(b) No spoiler case - C_L comparison between 2D and 3D simulations

Figure 8.17 – Comparison of the wall pressure coefficient, C_p, (left) and the lift coefficient C_L, (right) for the no spoiler case, in 2D and 3D.

The difference between the 2D and 3D simulations in terms of mean lift coefficient is less important for the spoiler case, $C_L^{2D} \approx 0.92$ and $C_L^{3D} \approx 0.97$ (see Figure 8.18b). It is to be noticed that even if the mean lift value is similar, there is a significant difference in the pressure distribution, that is more balanced in the chordwise direction in 3D than in 2D simulations. The results also show that 3D simulations significantly dampen the amplitude of oscillations in both spoiler and no spoiler case (Figure 8.17b and Figure 8.18b). To understand further, the unsteady aerofoil wake organisation is analysed in the following section.

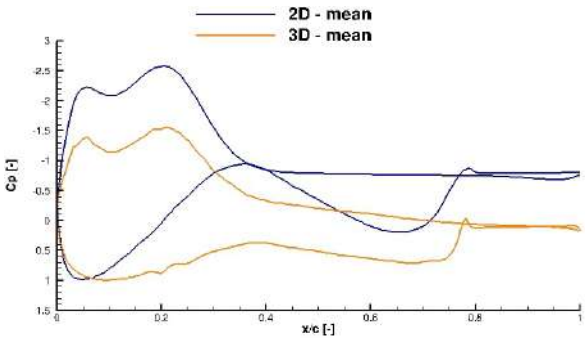

(a) Spoiler case - C_p comparison between 2D and 3D simulations

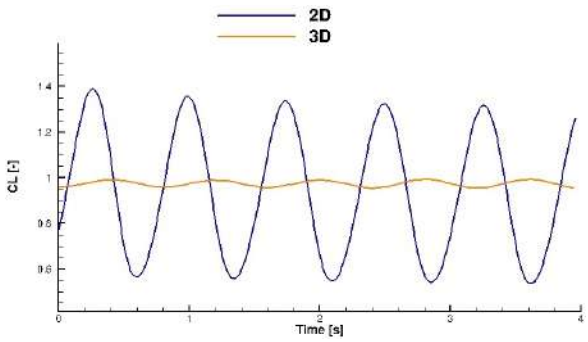

(b) Spoiler case - C_L comparison between 2D and 3D simulations

Figure 8.18 – Comparison of the wall pressure coefficient, C_p, (left) and the lift coefficient C_L, (right) for the spoiler case, in 2D and 3D.

Aerofoil unsteady wake investigation

The following section will verify the validity of the assumption that the VSF is affected neither by the blade's span nor its rotation and that 2D simulations can, in a first design approach, represent the unsteady behaviour of the flow past the aerofoil. The Figure 8.19 highlights differences between 2D and 3D simulations on the aerofoil wake flow organisation. Globally, with or without spoiler, vortices in the 2D wake are well formed (Figure 8.19a and 8.19c), homogeneous in their size and with a proper alternation of the vortex sign. This results in a clear peak frequency. In the 3D wake, the vortices are not round (highlighted with black isocontours of the Q-criteria), not formed regularly and with a high vorticity level (in red and blue) between them (Figure 8.19b and figure 8.19d).

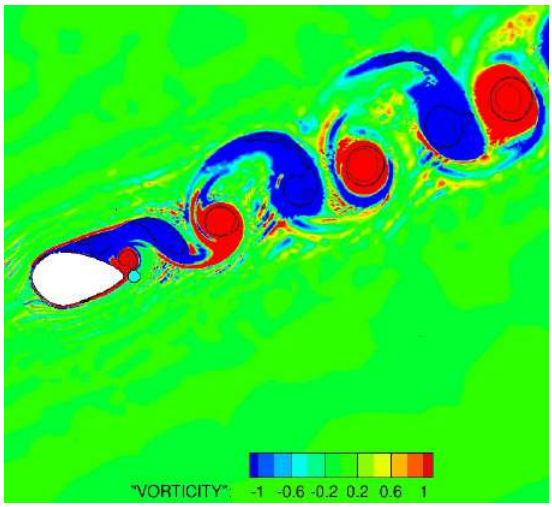

(a) 2D No spoiler case Vorticity and Q-criteria.

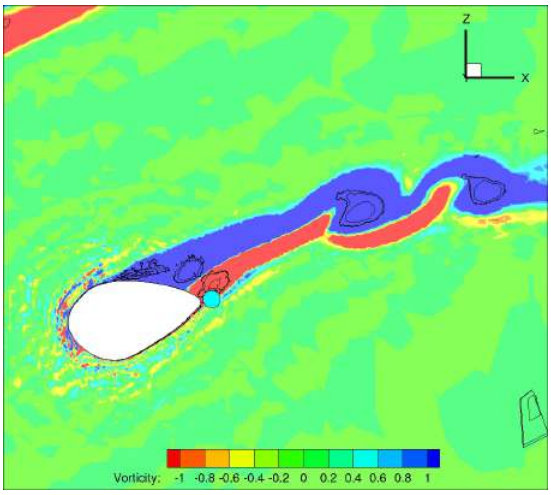

(b) 3D No spoiler case Vorticity and Q-criteria.

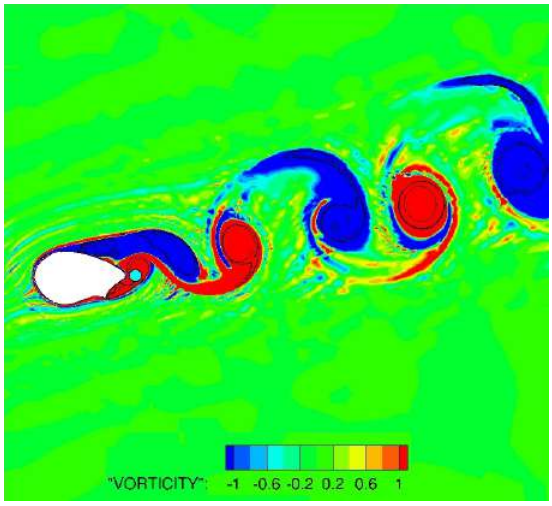

(c) 2D Spoiler case Vorticity and Q-criteria.

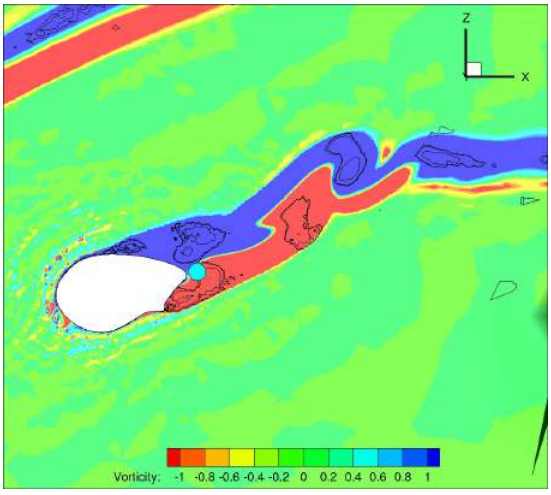

(d) 3D Spoiler case Vorticity and Q-criteria.

Figure 8.19 – No spoiler and spoiler case vorticity and Q-criteria comparison between 2D and 3D, operating following the conditions of Table 8.1. The probing point is shown as the cyan dot near the aerofoil's trailing edge.

The Figure 8.20a and Figure 8.20b compare the 2D and 3D spectrum of the relative velocity in the aerofoil's wake for both cases. Similarly to the outcome when comparing the lift coefficients and wake velocity in 3D (see Figure 8.12 and Figure 8.14), the no spoiler case shows a good agreement in peak frequencies for the 2D and 3D simulations. However, in the spoiler case, the 2D simulation does not catch the first peak below 1Hz, but detects the higher ones. It may be due to the too large frequency step chosen in 2D. In the following figures, "2D CL" refers to the lift coefficient calculated by integrating the pressure coefficient around the aerofoil from 2D CFD simulations. "2D Inflow" refers to the measured data through a probing point positioned in the wake of the 2D aerofoil.

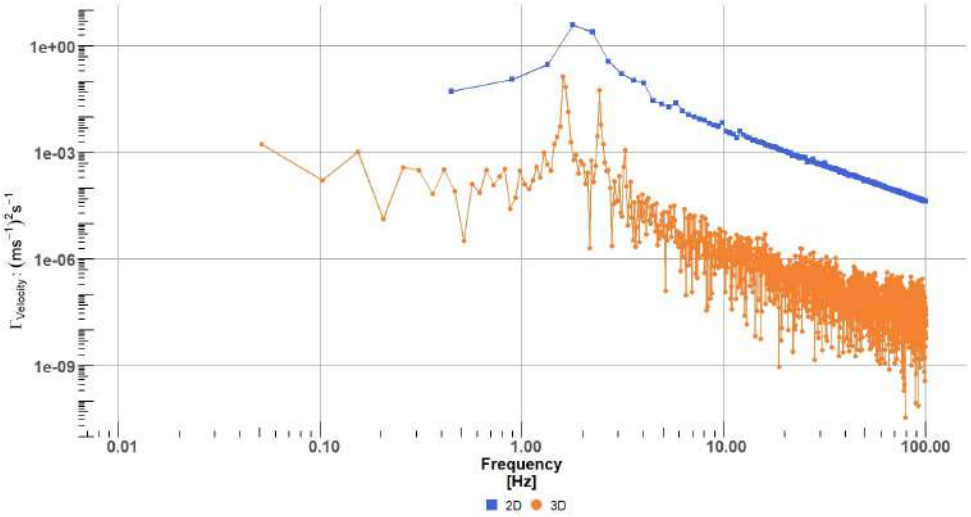

(a) Relative velocity Power Spectral Density of the no spoiler case in 2D and 3D.

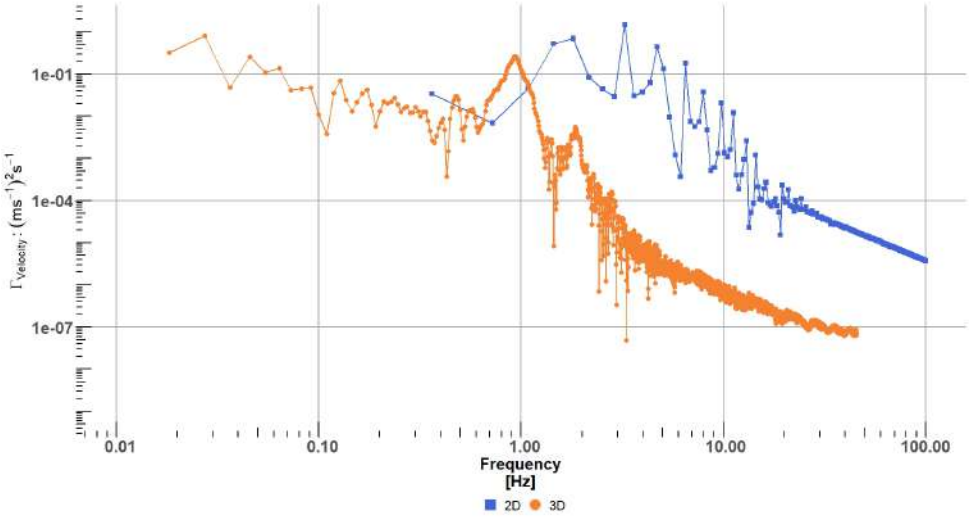

(b) Relative velocity Power Spectral Density of the spoiler case in 2D and 3D.

Figure 8.20 – Relative velocity Power Spectral Density of the no spoiler and spoiler case in 2D and 3D. The blue square (■) shows the 2D relative velocity results and the orange dot (●) shows the 3D relative velocity results.

Focusing now on the C_L spectrum, the differences between 2D and 3D organisation without and with spoiler is mostly reflected by the decrease in the energy in the spectrum, while the VSF remains almost unchanged (see Figure 8.21 and Figure 8.22). This validates the use of 2D simulations to compute VSF values in a first design approach regarding the fatigue evaluation introduced in Chapter 7. The investigation at the aerofoil scale shows a significant difference between 2D and 3D simulations on the pressure distribution and thus local aerofoil loads in the inboard area. These differences are found less important in the evaluation of the VSF for fatigue computation (see Chapter 7), even if the 2D simulations significantly overpredict the peak frequency energy.

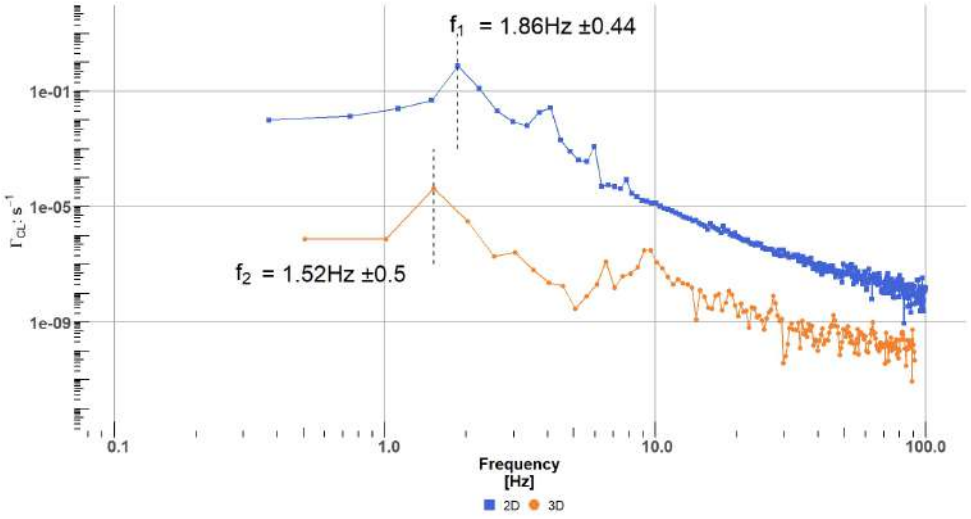

Figure 8.21 – No spoiler power spectral density comparison of the C_L. The blue square (■) shows the 2D C_L results and the orange dot (●) shows the 3D C_L results. The "±" symbol corresponds to the spectral discretisation used.

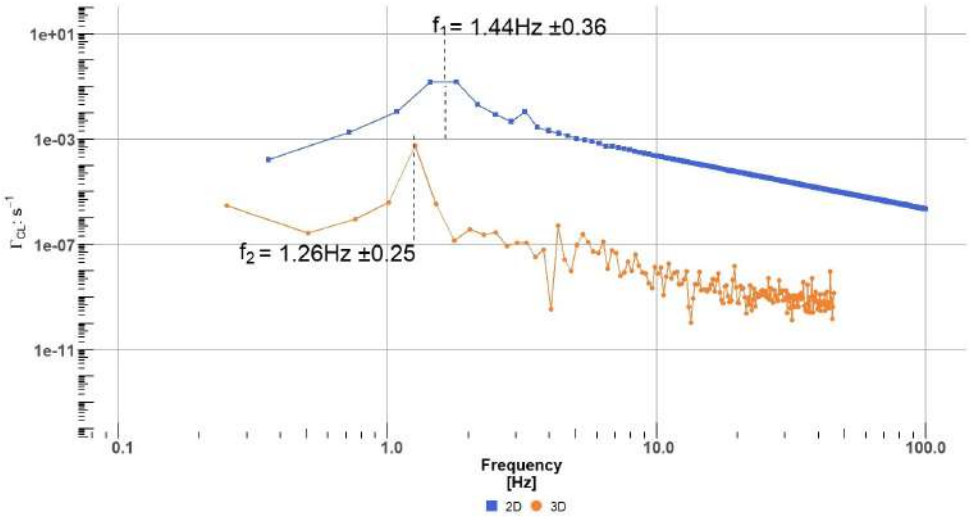

Figure 8.22 – Spoiler power spectral density comparison of the C_L. The blue square (■) shows the 2D C_L results and the orange dot (●) shows the 3D C_L results. The "±" symbol corresponds to the spectral discretisation used.

8.2.2 At the rotor scale

It is now interesting to evaluate the subsequent impact on loads at the rotor scale. For that purpose, 2D aerofoil simulations are taken as inputs for a BEM solver. AeroDyn, developed by NREL (see Section 2.1.3 and Chapter 7), is used and compared to the 3D CFD simulations described above, using the same operating conditions (see Table 8.1). Then, 3D URANS simulations are briefly compared to DDES results.

BEM - 3D URANS

The Table 8.2 shows the radii available for the BEM and 3D CFD comparison.

Table 8.2 – Available radial positions for the different solvers

Solver	Radii
3D CFD	$0 < r/R < 1$ (quasi-continuous data)
BEM	$r/R = 0.07$, $r/R = 0.09$, $r/R = 0.13$, $r/R = 0.17$, $r/R = 0.22$, $r/R = 0.29$, $r/R = 0.60$, $r/R = 0.96$ (discrete data)

The Figure 8.23 to the Figure 8.26 show the comparison between the high fidelity results (3D URANS using ISIS-CFD solver) and the low fidelity results (BEM using AeroDyn) of several metrics along the blade radius with error bars corresponding to extreme polar values from unsteady 2D simulations (see Table 7.1). The results were calculated for an 8m/s wind speed and the optimal pitch settings from the "mean aerodynamic polar - spoiler case" from Table 7.3. In the following plots (from Figure 8.23 to Figure 8.26), the grey area represents the spoiler location.

Induction and angle of attack

The Figure 8.23 shows the evolution of the axial induction along the blade radius without and with spoiler. Differences are described below from the tip (outbard), $r/R = 1$, to the root (inboard), $r/R = 0$.

From $r/R = 1$ to $r/R = 0.8$, the BEM results show higher induction values than the 3D simulation results. This may be attributed to the different way to account for the prebend shape in both fidelity simulations. In BEM simulations, the blade is considered contained within the rotational plane. While blades from 3D simulations keep the initial prebend shape from the scan. As the prebend plays a role in the local speed calculations, it consequently impacts the induction values.

From $r/R = 0.26$ to $r/R = 0.8$, BEM results are constants with $a \approx 1/3$. While the 3D CFD simulations results evolve as a concave arc along the blade radius, peaking above the BEM distribution at $r/R \approx 0.5$. This is certainly to be attributed to the prebend shape that progressively decreases along the radius towards the blade root. The differences from $r/R = 0.26$ to $r/R = 0$ are attributed to the differences between the model fidelity themselves since the prebend is non-existent inboard. The differences on the blade's outboard, mainly due to the prebend, do not have a large influence at the root. In the spoiler installation

area, the BEM method consistently underpredicts the induction compared to the 3D CFD in both the spoiler and no spoiler case. Interestingly, the spoiler effect can be highlighted in both fidelity simulations, with however a significantly reduced impact on the mean induction for the spoiler case of BEM simulations. In the BEM simulations the induction level is almost constant ($a \approx 0.15$), while in 3D URANS the values increases with the radius up to $a \approx 0.27$ (see Figure 8.23b). However, the highest value of the error bars (i.e. polar using the maximum aerodynamic coefficients) is found to yield similar results than the 3D CFD for the spoiler case.

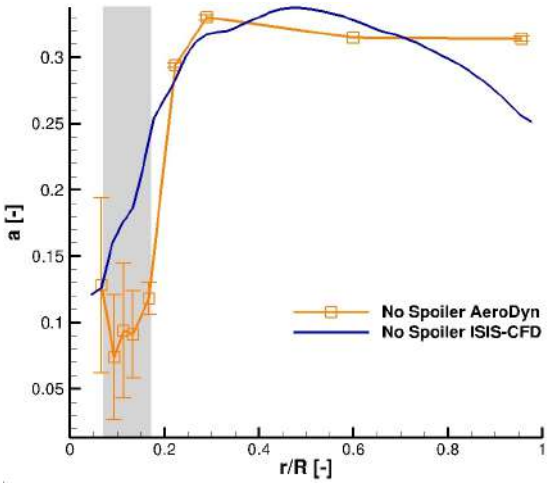

(a) No spoiler case - Axial induction.

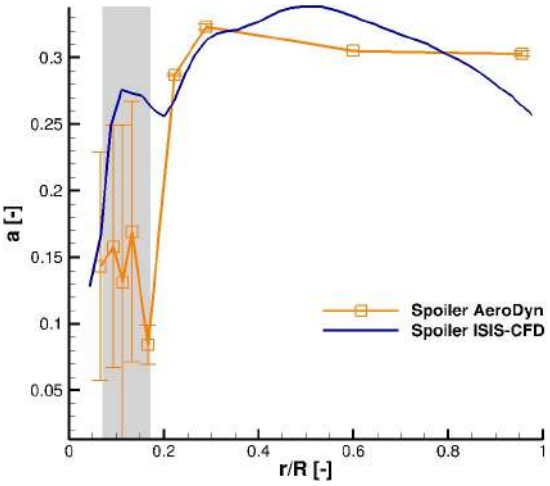

(b) Spoiler case - Axial induction.

Figure 8.23 – Axial induction comparison between ISIS-CFD and AeroDyn. The orange square (□) shows the BEM results and the solid blue line the ISIS-CFD results.

The same trends are found for the tangential induction for the inboard region in Figure 8.24, while outboard both fidelity models converge on the same close to zero value.

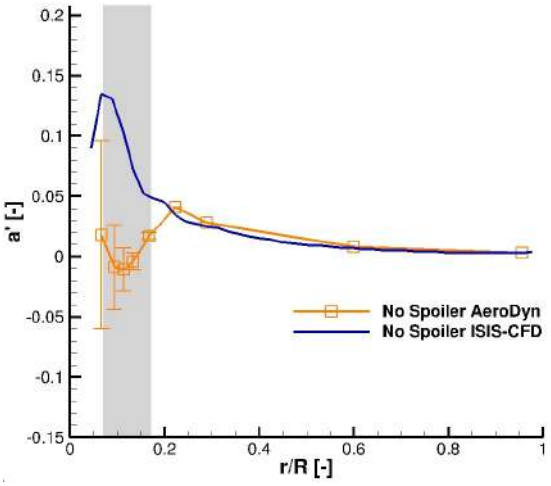

(a) No spoiler case - Tangential induction.

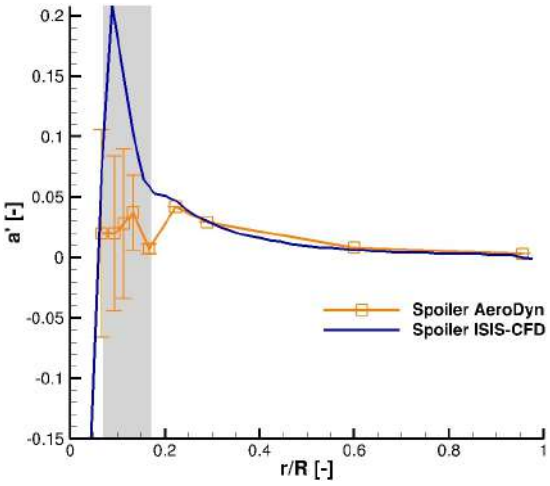

(b) Spoiler case - Tangential induction.

Figure 8.24 – Tangential induction comparison between ISIS-CFD and AeroDyn. The orange square (□) shows the BEM results and the solid blue line the ISIS-CFD results.

This has a natural impact on the computed angle of attack, as seen in Figure 8.25, that is systematically underpredicted without spoiler and with almost no impact with spoiler.

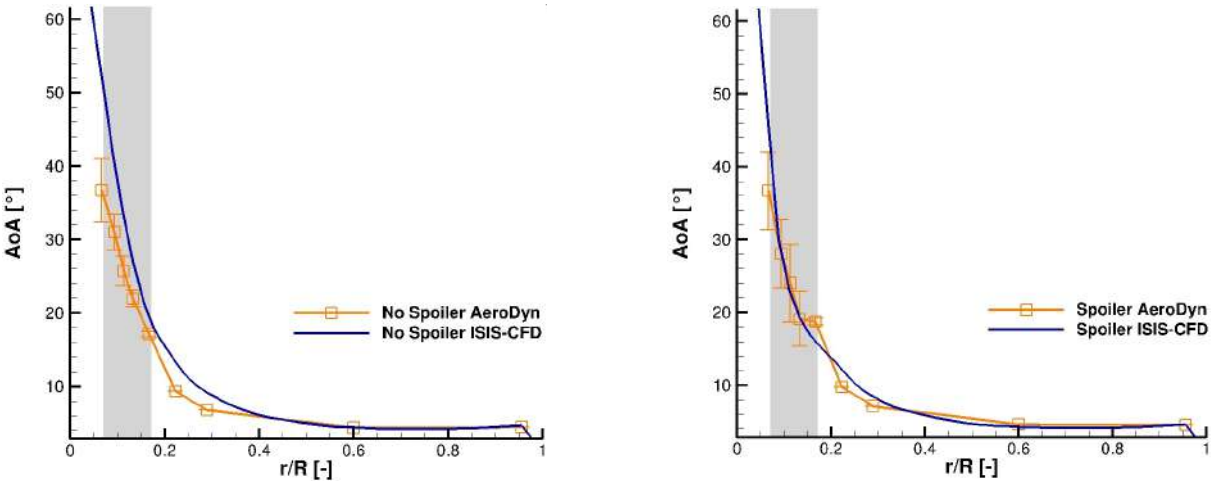

(a) No spoiler case - Angle of attack.

(b) Spoiler case - Angle of attack.

Figure 8.25 – Angle of attack comparison between ISIS-CFD and AeroDyn. The orange square (□) shows the BEM results and the solid blue line the ISIS-CFD results.

Aerodynamic thrust

The Figure 8.26 illustrates the aerodynamic thrust along the blade radius associated to the previously computed inductions and angle of attack. As expected, the outer part of the blade shows similar discrepancies noted for the induction namely: similar load trend evolution but not an actual match in values (see Figure 8.23b and Figure 8.24b). Also, the drop in aerodynamic thrust for the last radius locations is not seen when using the BEM output because the last section outputted was $r/R = 0.96$ and not the very tip of the blade.

Focusing on the area of the spoiler installation, from $r/R = 0$ to $r/R = 0.16$, despite a small underprediction for the BEM compared to the 3D CFD results, the spoiler effect trend is well captured: the thrust values increases with the spoiler in both 2D and 3D simulations in the same order of magnitude. The end of the spoiler in the BEM simulations is marked by a large drop in the aerodynamic thrust which is not seen in 3D CFD. This discrepancy is attributed to the 3D nature of the flow that BEM cannot capture fully due to the blade element discretisation and 3D spoiler shape

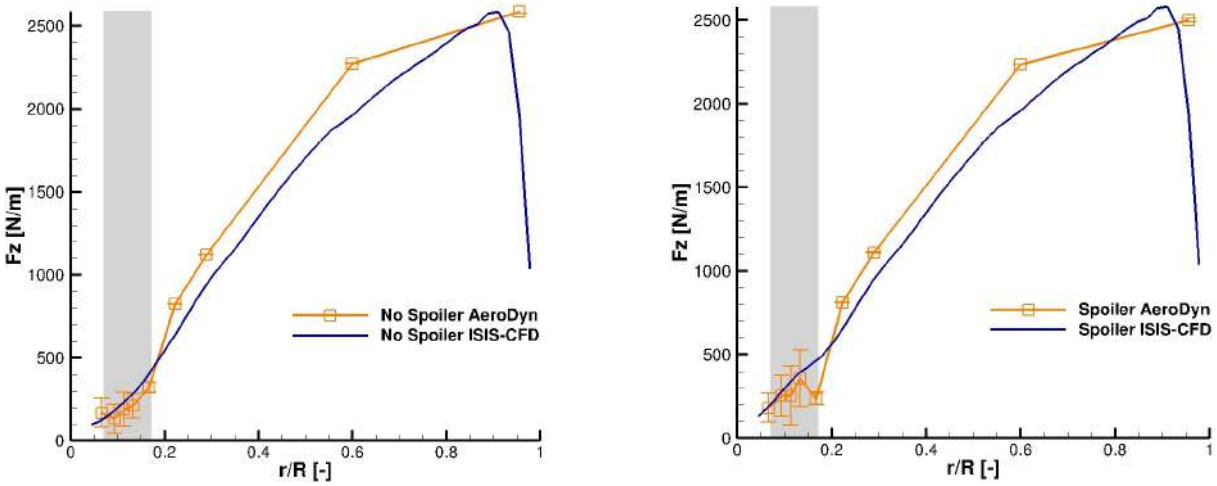

(a) No spoiler case - Aerodynamic thrust.

(b) Spoiler case - Aerodynamic thrust.

Figure 8.26 – Aerodynamic thrust comparison between ISIS-CFD and AeroDyn. The orange square (□) shows the BEM results and the solid blue line the ISIS-CFD results.

URANS - DDES

There are known difficulties associated to Unsteady Reynolds Average Navier Stokes (URANS) model to simulate highly swirling flows that has led to the development of more advanced turbulence model e.g.: Delayed Detached Eddy Simulation (DDES) model. DDES model combines the best aspects of LES and URANS model. Indeed, Large Eddy Simulation (LES) is well known as a better model compared to the URANS model in terms of accuracy for highly separated flow, but its computational cost is high especially near the wall, in the viscous boundary layer. The best aspects of DDES is the hybrid calculation approach: URANS is applied near the wall and the LES model applied far from the body.

In previous results, the $k-\omega$ SST URANS model (or SST model as later named) has been used. It can be extended easily in ISIS-CFD by selecting the DDES model. Only the blade equipped with the spoiler has been ran, due to the high CPU cost because of the finer mesh and smaller time step required. The Figure 8.27 shows differences in the relative velocity wake spectrum at the radial position $^r/_R = 0.13$. As expected, the energy in the spectrum is well distributed over all frequency values in DDES simulations, while the SST simulations has a single dominant frequency ($\approx$ 1Hz). Regarding its use for fatigue analysis, the DDES presents a completely different excitation pattern. It may call into question the use of a single VSF methodology as presented in Chapter 7. The increase of the energy level using DDES simulations brings it closer to the energy content using 2D simulations. More investigations are necessary to draw any further conclusions, especially regarding the convergence of DDES simulations which needs to be improved. However, it is interesting to notice that, after the spoiler position both the SST and DDES model produce a similar spectrum as seen on Figure 8.28.

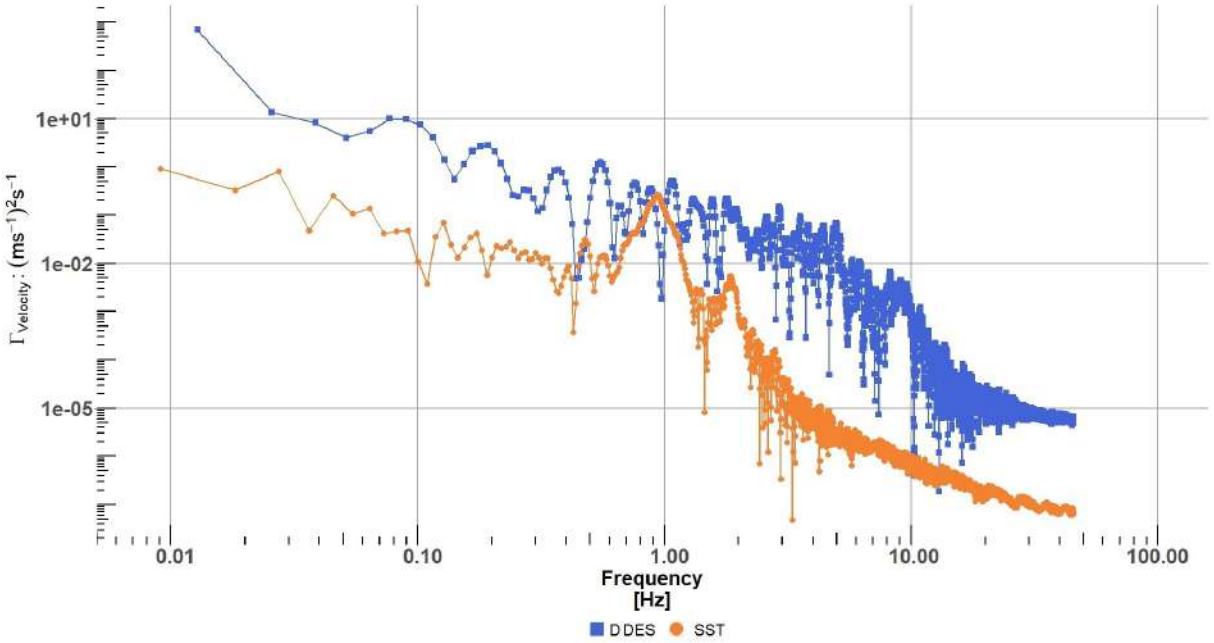

Figure 8.27 – Comparison of the power spectral density relative velocity for the DDES and SST model at $r/R = 0.13$ for the spoiler case. The blue square (■) shows the 3D relative velocity results for the DDES model and the orange dot (●) shows the 3D relative velocity results for the SST model.

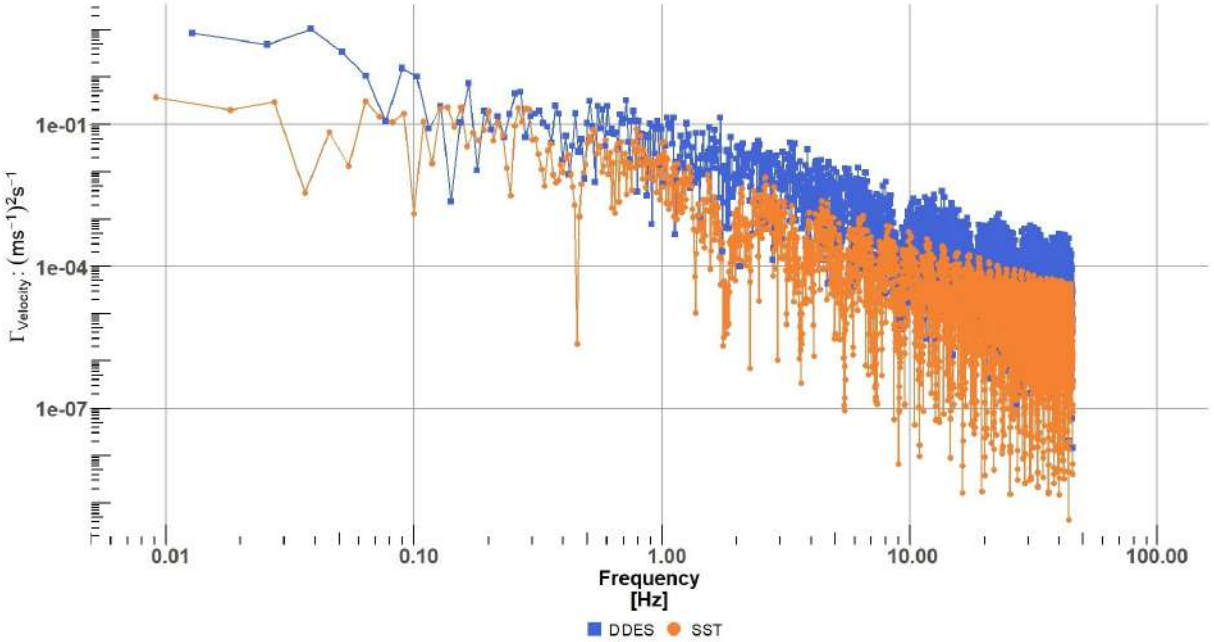

Figure 8.28 – Comparison of the power spectral density relative velocity for the DDES and SST model at $r/R = 0.28$ for the spoiler case. The blue square (■) shows the 3D relative velocity results for the DDES model and the orange dot (●) shows the 3D relative velocity results for the SST model.

The DDES model is able to capture a much broader array of turbulence structure which is confirmed by the presence of numerous vortices of different sizes in DDES simulations compared to simulations of the SST model in the inboard region of the rotor wake (see Figure 8.29a and Figure 8.29b). It should be noted that these vortices are more persistent in the rotor wake for the DDES model than the vortices from the SST model.

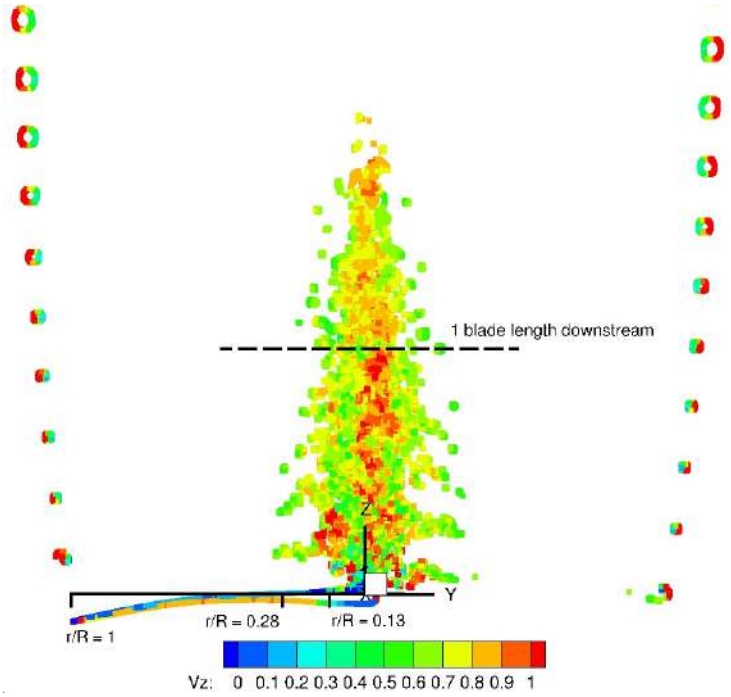

(a) Spoiler case - Q-criteria coloured by the dimensionless velocity V_z for the DDES model.

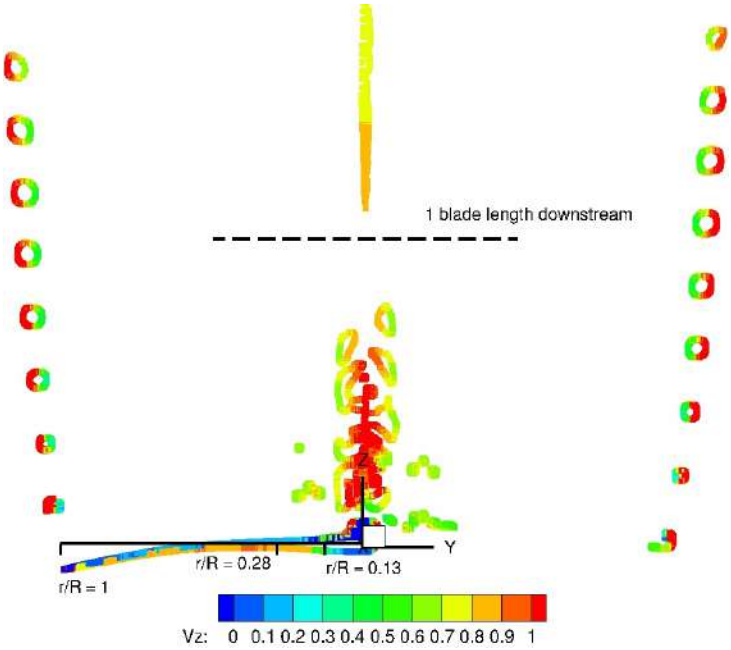

(b) Spoiler case - Q-criteria coloured by the dimensionless velocity V_z for the SST model.

Figure 8.29 – Comparison of vortices in the wake of the turbine for different turbulence models.

8.3 Summary

The previous chapter highlighted the spoiler impact using 3D simulations. The findings can be summarised as follow: the addition of the spoiler influences the near wake by means of reducing the size of the cone region, however its influence on the far wake velocity recovery is limited. Similarly the induction area upstream the rotor is not impacted by the spoiler. The local inboard blade quantities however, i.e.: the axial and tangential induction and angle of attack are very much impacted. The axial induction and the tangential induction increases, leading to a reduction of the local angle of attack. When analysing the flow locally, this can be explained by a redistribution of the pressure around the blade with the spoiler case. However, it cannot be due to a modification of the separation area nor by modification of crossflow region which are almost identical in both cases. Local loads with a spoiler are increased, mostly due to the lift and drag increase following the pressure redistribution. A positive side effect is the more balanced loads in the chordwise direction. Overall, the 3D CFD simulation confirms that the energy extraction is improved by the spoiler in the inboard region. The counterpart is an increase of the flow oscillations with two major sources of excitation: the blade shedding frequency and the crossflow oscillations. These oscillations are found to be transferred to the structure through the lift variation. The energy content in the C_L spectrum is higher in the spoiler case despite the no spoiler case having similar peak frequencies.
In 3D, the spoiler presence produces similar overall effect as in 2D simulations (see Chapter 6), with a redistribution of the pressure, an increase of the wake area and the level of the lift oscillations, with no impact on the flow separation. However, major differences exist between 3D and 2D simulations at the aerofoil scale for inboard regions such as: the wake and vortices organisation and the presence of the cross-flow due to Coriolis effects.
At the aerofoil scale, for the no spoiler case, the mean lift is significantly different between 2D and 3D simulations because of the crossflow benefit from Coriolis effects. Where the spoiler is installed, similar mean lift is observed between 2D and 3D simulations. Regarding the aerofoil wake unsteadiness, 3D simulations are found to significantly dampen the lift oscillations, leading to a significant decrease of the lift spectrum energy and thus on its transmission to the structure. No significant modification of the peak frequency value is found, without and with the spoiler both in 2D and 3D. At the rotor scale, all quantities (induction, angle of attack, thrust) evolve similarly when a spoiler is introduced with both fidelity models (BEM and SST model). However, the values found with BEM simulations are significantly underpredicted, except for the angle of attack where both model present similar results. Also, at radial distances near the end of the spoiler location, the BEM simulations present significant discrepancies caused by the 3D flow organisation there.
To conclude this study, DDES simulations were briefly compared with SST model results. They present a broader frequency range in the blade inboard wake with a higher energy level than 3D URANS simulations. It suggests a completely different structure excitation scenario and may call into question the use of a single VSF methodology as presented in Chapter 7. Such findings needs to be investigated further as part of dedicated studies.

CONCLUSION

The main objective of the thesis is to characterise the role of the local aerodynamic unsteadiness on the turbine lifetime and turbine energy production. To that end a definition and description of the wind and wind turbines are given in Chapter 1. Then, the most state-of-the-art modelling techniques and underlying theory have been introduced in the Chapter 2. It appears that a gap exists between the capabilities of high fidelity tools and design tools (engineering models). Indeed, the atmospheric turbulence is well understood and accounted for in both high and low fidelity method, however only in CFD the aerodynamic unsteadiness is captured. The present thesis helps bridging the gap using the strengths of both numerical methods and then assess the spoiler impact on the turbine lifetime.

A large dataset comprising experimental (field and wind tunnel test) and numerical data (2D and 3D high and low fidelity simulations) have been made available as part of the thesis and presented in Chapter 3. The DANAERO database has been used extensively to validate and verify an in-house developed Unsteady Inverse BEM code to analyse wind turbine field data. It has also been used as a numerical benchmark so as to verify ISIS-CFD, a solver developed by Centrale Nantes and CNRS. The validation activities are presented in the Chapter 4. This work allowed to show the solver versatility since it was already well-known for its marine and automotive applications.

The in-house developed Unsteady Inverse BEM code managed to show the limits of the current BEM theory and associated corrections and add-ons models as presented in Chapter 5. Steady BEM equations are not sufficient to capture the right wind turbine field behaviour. Applying the atmospheric unsteady equations are necessary for integrated data. However, analysing local phenomenon showed that more complex behaviour occur at the aerofoil scale that BEM cannot yet capture.

The following chapters (namely Chapter 6 and Chapter 7) built upon the previously gained knowledge. They were dedicated to create, run and analyse an aeroelastic model of a scanned blade equipped with root spoiler. First, the scan was post-processed to generated usable 2D sections using Bezier curves as interpolating technique. Then, assuming the mean wind speed for an IEC II site, the aerodynamic polar were calculated for all sections composing the blade. The unknown turbine structural properties have been extrapolated from the existing literature. The 2D CFD simulated root sections exhibited a large unsteady behaviour, which was enhanced by the spoiler addition even at low angles of attack. As expected, the spoiler increased drastically the lift coefficient in the positive range of angles of attack for a high drag penalty cost. The aerofoil's wake with the spoiler

addition exhibits a vortex shedding organisation with a main peak frequency even at low angles of attack. Whereas, it only occurs in the stall region for the bare aerofoil.
After running an optimisation procedure to derive the most energy producing pitch and RPM settings, power curves assuming rigid turbine were ran for all possible aerodynamic states caused by the unsteady behaviour. In idealised conditions, the spoiler will increase the AEP at most by 0.5% with a large variation associated. The integrated loads such as the blade flapwise root bending moment is slightly reduced with the spoiler thanks to the less aggressive pitch settings (due to the inboard's higher energy extraction). However, the inboard local loads increase significantly with a large variation around the mean value. Rendering the wind turbine fully flexible a novel fatigue analysis has been performed. The proposed method makes use of the vortex shedding frequency calculated in the 2D simulations and combines multiple time series following each local section's vortex shedding frequency. The outcome is that, if poorly designed the spoiler can be detrimental to the turbine's lifetime and the blade structural properties should account for the extra loading. This conclusion could be extended to any aerodynamic add-on generating similar amount of unsteadiness, however dedicated studies would be necessary. Also, more studies would be required to quantify the impact height and chordwise position of the spoiler.

Finally, full 3D URANS simulations for the 8m/s operating condition in both cases (rotor with and without spoiler) were ran. Using a quantitative approach, the 3D CFD simulation showed that the spoiler did not influence the induction zone in front of the rotor nor the far wake recovery. However, the spoiler does have an influence on the near wake behind the rotor. Similarly, the well-known cross-flow related to the Coriolis force and separation zone are not changed by the pressure redistribution due to the spoiler. The cross-flow oscillations and vortex shedding near the aerofoil's trailing edge, are found to be transferred to the structure through the lift variation. The energy associated to those vibration is higher is the spoiler case despite appearing at similar frequencies.
A comparison with the state-of-the-art BEM model was also made as part of the thesis. All calculated quantities (induction, angle of attack, thrust) evolve similarly for both fidelity models: BEM and 3D CFD model, regardless of the spoiler's presence. It is to be noted, however, that the BEM results significantly underpredict the metrics compared to the 3D CFD. The only exception is the angle of attack which present similar results. Another BEM limitation was found as part of this comparison, the highly 3D flow near the end of the spoiler cannot be captured using the BEM 2D geometry.
Despite the relative good agreement with BEM results, the main aim was to verify that the vortex shedding frequency calculated in 2D did not vary due to the rotation and blade span. More in-depth comparison between the 2D and 3D simulations were performed, especially regarding the pressure and lift coefficient distribution. The 3D simulations showed, similar to the 2D cases, a pressure redistribution around the aerofoil leading to a more balanced loading and reduction of the moment coefficient and a wider wake in the spoiler case. The main difference comes from the dampening, in 3D, of the unsteady activity noticed in 2D, both for the pressure coefficient and the lift. The 2D mean lift

value with a spoiler is however increased reaching similar level as in 3D.
This is also another limitation found to the current BEM rotational correction model. Indeed, the rotational correction model used in BEM are supposedly reproducing the enhanced behaviour at the blade root due to the rotation (so called *stall delay*). When a spoiler is installed, the main gain is from the pressure redistribution around the aerofoil rather than the stall delay. Dedicated studies to investigate the add-ons impact on the rotational effects would be necessary to propose updated 3D correction models. Moreover, 3D simulations with non rotating blade conditions would be necessary to discriminate clearly the effect of the radial flow on the local separation and vortex shedding frequency. This vortex organisation would certainly be highly influenced by the presence of the nacelle and of the tower; it would need further investigations to account these additional geometries.
Finally, the comparison of 2D and 3D vortex shedding frequencies showed that using 2D simulations to define wake organisation is sufficient for the fatigue analysis proposed here. It should be noted that using 2D calculated polar in a BEM aeroelastic code may lead to conservative results due to the larger unsteadiness inherent to 2D simulations. A higher fidelity model, DDES, was also compared against the previous 3D CFD URANS simulations. The preliminary spectral analysis showed that at the spoiler location, the wake and vortices organisation differs greatly. Several distinct peak frequencies are seen, while only one appears in 3D CFD URANS. This suggest a completely different excitation scenario that needs to be investigated further.

BIBLIOGRAPHY

[1] International Energy Agency, *World Energy Outlook 2020*, en, p. 464.

[2] Jörg Alber et al., « Aerodynamic effects of Gurney flaps on the rotor blades of a research wind turbine », en, *in*: *Wind Energy Science* 5.*4* (Nov. 2020), pp. 1645–1662, ISSN: 2366-7451, DOI: 10.5194/wes-5-1645-2020, URL: https://wes.copernicus.org/articles/5/1645/2020/ (visited on 01/13/2021).

[3] John D. Anderson, *Computational fluid dynamics: the basics with applications*, McGraw-Hill series in mechanical engineering, New York: McGraw-Hill, 1995, ISBN: 978-0-07-001685-9.

[4] Bengt Andersson, ed., *Computational fluid dynamics for engineers*, en, OCLC: ocn751752493, Cambridge ; New York: Cambridge University Press, 2012, ISBN: 978-1-107-01895-2.

[5] *atmospheric circulation (meteorology) - Images | Britannica*, en, URL: https://www.britannica.com/science/atmospheric-circulation/images-videos (visited on 01/28/2022).

[6] Alena Berit Bach, « Gurney flaps and micro-tabs for load control on wind turbines », en, PhD thesis, Technischen Universität Berlin, 2016.

[7] Christian Bak, Niels Troldborg, and Helge Aagaard Madsen, « DAN-AERO MW: Measured Airfoil Characteristics for a MW Rotor in Atmospheric Conditions », *in*: *Scientific Proceedings*, European Wind Energy Association (EWEA), 2011, pp. 171–175, URL: https://orbit.dtu.dk/en/publications/dan-aero-mw-measured-airfoil-characteristics-for-a-mw-rotor-in-at (visited on 2020-06-02).

[8] Christian Bak et al., « DAN-AERO MW: Comparisons of Airfoil Characteristics for Two Airfoils Tested in Three Different Wind Tunnels », *in*: *Torque 2010: The Science of Making Torque from Wind*, Torque 2010, 2010, pp. 59–70, URL: https://orbit.dtu.dk/en/publications/dan-aero-mw-comparisons-of-airfoil-characteristics-for-two-airfoi (visited on 2020-08-04).

[9] Christian Bak et al., *DANAERO MW: Measurement Campaigns on the NM80 2.3MW Wind Turbine at Tjæreborg 2009*, 2010, p. 49.

[10] Christian Bak et al., *DANAERO MW: Wind tunnel tests*, en, 2010, p. 19.

[11] Galih Bangga, « Three-Dimensional Flow in the Root Region of Wind Turbine Rotors », 2018.

[12] P. Benard et al., « Large-Eddy Simulation of Wind Turbines Wakes Including Geometrical Effects », *in*: *Computers & Fluids* 173 (Sept. 2018), pp. 133–139, ISSN: 00457930, DOI: 10.1016/j.compfluid.2018.03.015.

[13] Franck Bertagnolio et al., « Aerodynamic Noise Characterization of a Full-Scale Wind Turbine through High-Frequency Surface Pressure Measurements », *in*: *International Journal of Aeroacoustics* 14.*5-6* (2015), pp. 729–766, ISSN: 1475-472X, DOI: 10.1260/1475-472X.14.5-6.729, URL: https://orbit.dtu.dk/en/publications/aerodynamic-noise-characterization-of-a-full-scale-wind-turbine-t (visited on 2020-05-25).

[14] Franck Bertagnolio et al., « Experimental Characterization of Stall Noise Toward Its Modelling », *in*: *Proceedings of the 6th International Conference on Wind Turbine Noise*, 6th International Conference on Wind Turbine Noise, 2015, URL: https://orbit.dtu.dk/en/publications/experimental-characterization-of-stall-noisetoward-its-modelling (visited on 2020-06-02).

[15] F Blondel et al., « Improving a BEM Yaw Model Based on NewMexico Experimental Data and Vortex/CFD Simulations », en, *in*: Lille, France: *23eCongrès Français de Mécanique*, 2017, p. 14.

[16] C.S. Boeije et al., « Fluidic load control for wind turbines blades », English, *in*: *Proceedings of the 47th AIAA Aerospace Sciences Meeting, 5-8 January, 2009, Orlando, Florida, USA*, ed. by xx Maureen Hand, 47th AIAA Aerospace Sciences Meeting, January 5-8, 2009, Orlando, FL, USA ; Conference date: 05-01-2009 Through 08-01-2009, United States: American Institute of Aeronautics and Astronautics Inc. (AIAA), 2009, pp. 1–8.

[17] K Boorsma and J G Schepers, *New MEXICO experiment Preliminary overview with initial validation*, en, 2014, p. 63.

[18] Emmanuel Simon Pierre Branlard and Alexander Raul Meyer Forsting, « Using a cylindrical vortex model to assess the induction zone infront of aligned and yawed rotors », English, *in*: *Proceedings of EWEA Offshore 2015 Conference*, EWEA Offshore 2015 Conference ; Conference date: 10-03-2015 Through 12-03-2015, European Wind Energy Association (EWEA), 2015.

[19] Tony Burton, ed., *Wind Energy: Handbook*, Chichester ; New York: J. Wiley, 2001, 617 pp., ISBN: 978-0-471-48997-9.

[20] Filippo Campagnolo, « WIND TUNNEL TESTING OF SCALED WIND TURBINE MODELS: AERODYNAMICS AND BEYOND », en, PhD thesis, POLITECNICO DI MILANO, 2013.

[21] Helena Canet, Pietro Bortolotti, and Carlo L. Bottasso, *On the scaling of wind turbine rotors*, en, preprint, Design methods, reliability and uncertainty modelling, Mar. 2020, DOI: 10.5194/wes-2020-66, URL: https://wes.copernicus.org/preprints/wes-2020-66/wes-2020-66.pdf (visited on 07/30/2021).

[22] P. Cathalifaud et al., « The flow structure behind vortex generators embedded in a decelerating turbulent boundary layer », en, *in*: *Journal of Turbulence* 10 (Jan. 2009), N42, ISSN: 1468-5248, DOI: 10.1080/14685240903273881, URL: http://www.tandfonline.com/doi/abs/10.1080/14685240903273881 (visited on 02/10/2020).

[23] Bruno Chaouat, « The State of the Art of Hybrid RANS/LES Modeling for the Simulation of Turbulent Flows », *in*: *Flow, Turbulence and Combustion* 99.*2* (Sept. 2017), pp. 279–327, ISSN: 1386-6184, 1573-1987, DOI: 10.1007/s10494-017-9828-8.

[24] P. K. Chaviaropoulos and M. O. L. Hansen, « Investigating Three-Dimensional and Rotational Effects on Wind Turbine Blades by Means of a Quasi-3D Navier-Stokes Solver », en, *in*: *Journal of Fluids Engineering* 122.*2* (June 2000), pp. 330–336, ISSN: 0098-2202, 1528-901X, DOI: 10.1115/1.483261, URL: https://asmedigitalcollection.asme.org/fluidsengineering/article/122/2/330/459646/Investigating-ThreeDimensional-and-Rotational (visited on 01/29/2021).

[25] Raymond Chow and C. P. van Dam, « Verification of Computational Simulations of the NREL 5 MW Rotor with a Focus on Inboard Flow Separation: Computational Simulations of the NREL 5 MW Rotor », *in*: *Wind Energy* 15.*8* (Nov. 2012), pp. 967–981, ISSN: 10954244, DOI: 10.1002/we.529.

[26] Julia A. Cole et al., « Experimental Investigation into the Effect of Gurney Flaps on Various Airfoils », en, *in*: *Journal of Aircraft* 50.*4* (July 2013), pp. 1287–1294, ISSN: 0021-8669, 1533-3868, DOI: 10.2514/1.C032203, URL: https://arc.aiaa.org/doi/10.2514/1.C032203 (visited on 07/02/2021).

[27] Gustave P Corten, « Flow Separation on Wind Turbine Blades », PhD thesis, Universiteit Utrecht, 2001, p. 170.

[28] Gauthier Dambrine, « Impact of Blade Aging on Wind Turbine Production », en, MA thesis, European Master in Renewable Energy, 2010, p. 39.

[29] Swagata Das, Neeraj Karnik, and Surya Santoso, « Time-Domain Modeling of Tower Shadow and Wind Shear in Wind Turbines », en, *in*: *ISRN Renewable Energy* 2011 (Oct. 2011), pp. 1–11, ISSN: 2090-7451, 2090-746X, DOI: 10.5402/2011/890582, URL: https://www.hindawi.com/journals/isrn/2011/890582/ (visited on 01/29/2021).

[30] D. De Tavernier et al., « Controlling dynamic stall using vortex generators on a wind turbine airfoil », en, *in*: *Renewable Energy* (Mar. 2021), S0960148121003736, ISSN: 09601481, DOI: 10.1016/j.renene.2021.03.019, URL: https://linkinghub.elsevier.com/retrieve/pii/S0960148121003736 (visited on 03/31/2021).

[31] G B Deng, P Queutey, and M Visonneau, « A code verification exercise for the unstructured finite-volume CFD solver ISIS-CFD », en, *in*: *European Conference on Computational Fluid Dynamics ECCOMAS CFD 2006*, 2006, p. 18.

[32] G B Deng et al., « Ship Flow Simulations with the ISIS CFD Code », en, *in*: *CFD Workshop Tokyo 2005 (CFDWS2005)*, 2005, pp 474–482.

[33] Alfredo Pena Diaz, Sven-Erik Gryning, and Jakob Mann, « On the Length-Scale of the Wind Profile », *in*: *Quarterly Journal of the Royal Meteorological Society* 136.*653* (2010), pp. 2119–2131, ISSN: 0035-9009, DOI: 10.1002/qj.714, URL: https://orbit.dtu.dk/en/publications/on-the-length-scale-of-the-wind-profile (visited on 08/05/2020).

[34] Norman E. Dowling, Stephen L. Kampe, and Milo V. Kral, *Mechanical behavior of materials: engineering methods for deformation, fracture, and fatigue*, eng, Fifth edition, global edition, Harlow: Pearson, 2020, ISBN: 978-1-292-27935-0.

[35] S.D. Downing and D.F. Socie, « Simple rainflow counting algorithms », *in*: *International Journal of Fatigue* 4.*1* (1982), pp. 31–40, ISSN: 0142-1123, DOI: https://doi.org/10.1016/0142-1123(82)90018-4, URL: https://www.sciencedirect.com/science/article/pii/0142112382900184.

[36] Mark Drela, « XFOIL: An Analysis and Design System for Low Reynolds Number Airfoils », *in*: *Low Reynolds Number Aerodynamics*, ed. by C. A. Brebbia et al., vol. 54, Series Title: Lecture Notes in Engineering, Berlin, Heidelberg: Springer Berlin Heidelberg, 1989, pp. 1–12, ISBN: 978-3-540-51884-6, DOI: 10.1007/978-3-642-84010-4_1, URL: http://link.springer.com/10.1007/978-3-642-84010-4_1 (visited on 01/26/2022).

[37] Stefan Emeis, *Wind Energy Meteorology*, Green Energy and Technology, Berlin, Heidelberg: Springer Berlin Heidelberg, 2013, ISBN: 978-3-642-30522-1, DOI: 10.1007/978-3-642-30523-8, URL: http://link.springer.com/10.1007/978-3-642-30523-8 (visited on 01/28/2022).

[38] A. Fatemi and L. Yang, « Cumulative fatigue damage and life prediction theories: a survey of the state of the art for homogeneous materials », *in*: *International Journal of Fatigue* 20.*1* (1998), pp. 9–34, ISSN: 0142-1123, DOI: https://doi.org/10.1016/S0142-1123(97)00081-9, URL: https://www.sciencedirect.com/science/article/pii/S0142112397000819.

[39] Joel H Ferziger and Milovan Peric, *Computational Methods for Fluid Dynamics*, English, OCLC: 1120912802, 2002, ISBN: 978-3-642-56026-2.

[40] A Fischer and H A Madsen, « Investigation of the Maximum Load Alleviation Potential Using Trailing Edge Flaps Controlled by Inflow Data », *in*: *Journal of Physics: Conference Series* 555 (2014), p. 012037, ISSN: 1742-6588, 1742-6596, DOI: 10.1088/1742-6596/555/1/012037, URL: https://iopscience.iop.org/article/10.1088/1742-6596/555/1/012037 (visited on 2020-05-25).

[41] Andreas Fischer and Helge Aagaard Madsen, « Load Alleviation Potential with Trailing Edge Flaps for Turbines in Wake Operation », *in*: *Proceedings of the 2013 International Conference on Aerodynamics of Offshore Wind Energy Systems and Wakes (ICOWES2013)*, ICOWES, Technical University of Denmark, 2013, URL: https://orbit.dtu.dk/en/publications/load-alleviation-potential-with-trailing-edge-flaps-for-turbines- (visited on 2020-06-02).

[42] Andreas Fischer et al., « Analyses of the Mechanisms of Amplitude Modulation of Aero-Acoustic Wind Turbine Sound », *in*: *Proceedings of European Wind Energy Association Conference and Exhibition 2014*, European Wind Energy Conference & Exhibition 2014, 2014, URL: https://orbit.dtu.dk/en/publications/analyses-of-the-mechanisms-of-amplitude-modulation-of-aero-acoust-2 (visited on 2020-06-02).

[43] Th. Foken and B. Wichura, « Tools for Quality Assessment of Surface-Based Flux Measurements », *in*: *Agricultural and Forest Meteorology* 78.*1-2* (1995), pp. 83–105, ISSN: 01681923, DOI: 10.1016/0168-1923(95)02248-1, URL: https://linkinghub.elsevier.com/retrieve/pii/0168192395022481 (visited on 2020-02-27).

[44] Sten Frandsen et al., « Analytical Modelling of Wind Speed Deficit in Large Offshore Wind Farms », *in*: *Wind Energy* 9.*1-2* (2005), pp. 39–53, ISSN: 1095-4244, 1099-1824, DOI: 10.1002/we.189, URL: http://doi.wiley.com/10.1002/we.189 (visited on 2020-03-09).

[45] Linyue Gao et al., « Effects of vortex generators on a blunt trailing-edge airfoil for wind turbines », en, *in*: *Renewable Energy* 76 (2014), pp. 303–311, ISSN: 09601481, DOI: 10.1016/j.renene.2014.11.043, URL: https://linkinghub.elsevier.com/retrieve/pii/S0960148114007587 (visited on 02/14/2020).

[46] P Giguere, J Lemay, and G Dumas, « Gurney flap effects and scaling for low-speed airfoils », en, *in*: *13th Applied Aerodynamics Conference*, San Diego,CA,U.S.A.: American Institute of Aeronautics and Astronautics, June 1995, DOI: 10.2514/6.1995-1881, URL: https://arc.aiaa.org/doi/10.2514/6.1995-1881 (visited on 07/02/2021).

[47] G. Godard and M. Stanislas, « Control of a decelerating boundary layer. Part 1: Optimization of passive vortex generators », en, *in*: *Aerospace Science and Technology* 10.*3* (Apr. 2006), pp. 181–191, ISSN: 12709638, DOI: 10.1016/j.ast.2005.11.007, URL: https://linkinghub.elsevier.com/retrieve/pii/S127096380500163X (visited on 07/02/2021).

[48] Alvaro Gonzalez-Salcedo, « Aerodynamic flow control final report », en, *in*: *AdVanced Aerodynamic Tool for lArge Rotors*, European project AVATAR, 2016, p. 86.

[49] E. Guilmineau et al., « Assessment of hybrid RANS-LES formulations for flow simulation around the Ahmed body », en, *in*: *Computers & Fluids* 176 (2017), pp. 302–319, ISSN: 00457930, DOI: 10.1016/j.compfluid.2017.01.005, URL: https://linkinghub.elsevier.com/retrieve/pii/S0045793017300051 (visited on 02/10/2020).

[50] E. Guilmineau et al., « Numerical Simulations for the Wake Prediction of a Marine Propeller in Straight-Ahead Flow and Oblique Flow », en, *in*: *Journal of Fluids Engineering* 140.*2* (Feb. 2018), p. 021111, ISSN: 0098-2202, 1528-901X, DOI: 10.1115/1.4037984, URL: https://asmedigitalcollection.asme.org/fluidsengineering/article/doi/10.1115/1.4037984/374183/Numerical-Simulations-for-the-Wake-Prediction-of-a (visited on 11/06/2020).

[51] M. M. Hand et al., *Unsteady Aerodynamics Experiment Phase VI: Wind Tunnel Test Configurations and Available Data Campaigns*, en, tech. rep. NREL/TP-500-29955, 15000240, NREL, Dec. 2001, NREL/TP–500–29955, 15000240, DOI: 10.2172/15000240, URL: http://www.osti.gov/servlets/purl/15000240-1FhaHo/native/ (visited on 03/09/2020).

[52] M.H. Hansen, Mac Gaunaa, and Helge Aagaard Madsen, *A Beddoes-Leishman type dynamic stall model in state-space and indicial formulations*, English, Denmark. Forskningscenter Risoe. Risoe-R, 2004, ISBN: 87-550-3090-4.

[53] Martin Hansen, *Aerodynamics of Wind Turbines*, 3rd ed., London: Routledge, May 2015, ISBN: 978-1-315-76998-1, DOI: 10.4324/9781315769981.

[54] Martin O. L. Hansen et al., « Extraction of Lift, Drag and Angle of Attack from Computed 3-D Viscous Flow around a rotating Blade », English, *in*: *Proceedings of the European wind energy conference*, ed. by R. Watson, 1997 European Wind Energy Conference , EWEC '97 ; Conference date: 06-10-1997 Through 09-10-1997, Vindenergi og atmosfæriske processer, Irish Wind Energy Association, 1998, pp. 499–502, ISBN: 0-9533922-0-1.

[55] G. J. Hayman, *MExtreme User's Guide*, en, tech. rep., National Renewable Energy Laboratory, 2015, URL: https://www.nrel.gov/wind/nwtc/assets/downloads/MCrunch_MLife_MExtremes/MExtremesManual.pdf.

[56] G. J. Hayman, *Mlife user's guide*, tech. rep., National Renewable Energy Laboratory, 2012, URL: https://www.nrel.gov/wind/nwtc/assets/pdfs/mlife-theory.pdf.

[57] Kris Hectors and Wim De Waele, « Cumulative Damage and Life Prediction Models for High-Cycle Fatigue of Metals: A Review », en, *in*: *Metals* 11.*2* (Jan. 2021), p. 204, ISSN: 2075-4701, DOI: 10.3390/met11020204, URL: https://www.mdpi.com/2075-4701/11/2/204 (visited on 01/25/2022).

[58] Bumsuk Kim Heejeon Im Seongkeon Kim, « Numerical analysis of the effect of vortex generator on inboard region of wind turbine blade », *in*: *Journal of Renewable and Sustainable Energy* 13.*6* (2021), p. 063306, DOI: 10.1063/5.0065108.

[59] Manuel Helbig et al., « Integrating Continuous Atmospheric Boundary Layer and Tower-Based Flux Measurements to Advance Understanding of Land-Atmosphere Interactions », *in*: *Agricultural and Forest Meteorology* 307 (Sept. 2021), p. 108509, ISSN: 01681923, DOI: 10.1016/j.agrformet.2021.108509.

[60] Iván Herráez, Elia Daniele, and J. Gerard Schepers, « Extraction of the Wake Induction and Angle of Attack on Rotating Wind Turbine Blades from PIV and CFD Results », *in*: *Wind Energy Science* 3.*1* (Jan. 2018), pp. 1–9, ISSN: 2366-7451, DOI: 10.5194/wes-3-1-2018.

[61] Iván Herráez et al., « Detailed Analysis of the Blade Root Flow of a Horizontal Axis Wind Turbine », *in*: *Wind Energy Science* 1.*2* (2016), pp. 89–100, ISSN: 2366-7451, DOI: 10.5194/wes-1-89-2016, URL: https://www.wind-energ-sci.net/1/89/2016/ (visited on 2020-02-12).

[62] H. Himmelskamp, *Profile Investigations on a Rotating Airscrew*, Ministry of Aircraft Production, 1947.

[63] M C Holtslag, W A A M Bierbooms, and G J W van Bussel, « Estimating Atmospheric Stability from Observations and Correcting Wind Shear Models Accordingly », *in*: *Journal of Physics: Conference Series* 555 (2014), p. 012052, ISSN: 1742-6588, 1742-6596, DOI: 10.1088/1742-6596/555/1/012052, URL: https://iopscience.iop.org/article/10.1088/1742-6596/555/1/012052 (visited on 2020-05-20).

[64] C Hur, T Berdowski, and C Ferreira, « A Review of Momentum Models for the Actuator Disk in Yaw », *in*: San Diego, United States of America: AIAA Scitech 2019 Forum, 2019, p. 16, DOI: 10.2514/6.2019-1799.

[65] International Renewable Energy Agency, *FUTURE OF WIND Deployment, investment, technology, grid integration and socio-economic aspects*, en, International Renewable Energy Agency, 2019, p. 88, ISBN: 978-92-9260-155-3, URL: https://www.irena.org/publications/2019/Oct/Future-of-wind.

[66] Shams-Ul. Islam et al., « A Computational Study of Drag Reduction and Vortex Shedding Suppression of Flow Past a Square Cylinder in Presence of Small Control Cylinders », *in*: *AIP Advances* 7.*4* (Apr. 2017), p. 045119, ISSN: 2158-3226, DOI: 10.1063/1.4982696.

[67] R.I. Issa, « Solution of the implicitly discretised fluid flow equations by operator-splitting », *in*: *Journal of Computational Physics* 62.*1* (1986), pp. 40–65, DOI: 10.1016/0021-9991(86)90099-9.

[68] Cory S. Jang, James C. Ross, and Russell M. Cummings, « Numerical investigation of an airfoil with a Gurney flap », en, *in*: *Aircraft Design* 1.*2* (June 1998), pp. 75–88, ISSN: 13698869, DOI: 10.1016/S1369-8869(98)00010-X, URL: https://linkinghub.elsevier.com/retrieve/pii/S136988699800010X (visited on 11/24/2020).

[69] V. Jaunet and C. Braud, « Experiments on lift dynamics and feedback control of a wind turbine blade section », en, *in*: *Renewable Energy* 126 (Oct. 2018), pp. 65–78, ISSN: 09601481, DOI: 10.1016/j.renene.2018.03.017, URL: https://linkinghub.elsevier.com/retrieve/pii/S0960148118303227 (visited on 02/10/2020).

[70] N. O Jensen, *A Note on Wind Generator Interaction*, Roskilde, Denmark: Risø National Laboratory, 1983, ISBN: 978-87-550-0971-4.

[71] B J Jonkman and Jr. Buhl M. L., *TurbSim User's Guide*, tech. rep., National Renewable Energy Laboratory, Sept. 2005, DOI: 10.2172/15020326, URL: https://www.osti.gov/biblio/15020326.

[72] J M Jonkman, *Modeling of the UAE Wind Turbine for Refinement of FAST{_}AD*, en, tech. rep. NREL/TP-500-34755, 15005920, Dec. 2003, NREL/TP–500–34755, 15005920, DOI: 10.2172/15005920, URL: http://www.osti.gov/servlets/purl/15005920/ (visited on 02/01/2022).

[73] J M Jonkman et al., *AeroDyn v15 User's Guide and Theory Manual*, en, 2015, p. 46.

[74] J. Jonkman et al., *Definition of a 5-MW Reference Wind Turbine for Offshore System Development*, en, tech. rep. NREL/TP-500-38060, 947422, National Renewable Energy Laboratory, Feb. 2009, NREL/TP–500–38060, 947422, DOI: 10.2172/947422, URL: http://www.osti.gov/servlets/purl/947422-nhrlni/ (visited on 04/28/2021).

[75] Jason Jonkman and Marshall Buhl, « New Developments for the NWTC's FAST Aeroelastic HAWT Simulator », en, *in*: *42nd AIAA Aerospace Sciences Meeting and Exhibit*, Reno, Nevada: American Institute of Aeronautics and Astronautics, Jan. 2004, ISBN: 978-1-62410-078-9, DOI: 10.2514/6.2004-504, URL: https://arc.aiaa.org/doi/10.2514/6.2004-504 (visited on 02/01/2022).

[76] J. C. Kaimal and J. J. Finnigan, *Atmospheric Boundary Layer Flows: Their Structure and Measurement*, New York: Oxford University Press, 1994, ISBN: 978-0-19-506239-7.

[77] Thomas R Kane and David A Levinson, *Dynamics, theory and applications*, McGraw Hill, 1985.

[78] Lars Landberg, ed., *Meteorology for Wind Energy: An Introduction*, en, Chichester, UK: John Wiley & Sons, Ltd, Nov. 2015, ISBN: 978-1-118-91345-1, DOI: 10.1002/9781118913451, URL: http://doi.wiley.com/10.1002/9781118913451 (visited on 01/28/2022).

[79] J. G. Leishman and T. S. Beddoes, « A Semi-Empirical Model for Dynamic Stall », *in*: *Journal of the American Helicopter Society* 34.*3* (1989), pp. 3–17, DOI: 10.4050/JAHS.34.3.3.

[80] Yachen Li, Jinjun Wang, and Panfeng Zhang, « Effects of Gurney Flaps on a NACA0012 Airfoil », en, *in*: *Flow, Turbulence and Combustion* (2002), pp. 27–39.

[81] Robert H. Liebeck, « Design of Subsonic Airfoils for High Lift », en, *in*: *Journal of Aircraft* 15.*9* (Sept. 1978), pp. 547–561, ISSN: 0021-8669, 1533-3868, DOI: 10.2514/3.58406, URL: https://arc.aiaa.org/doi/10.2514/3.58406 (visited on 01/11/2021).

[82] John C Lin, « Review of research on low-profile vortex generators to control boundary-layer separation », en, *in*: *Progress in Aerospace Sciences* 38.*4-5* (May 2002), pp. 389–420, ISSN: 03760421, DOI: 10.1016/S0376-0421(02)00010-6, URL: https://linkinghub.elsevier.com/retrieve/pii/S0376042102000106 (visited on 02/10/2020).

[83] C Lindenburg, *Investigation into Rotor Blade Aerodynamics*, 2003, p. 114.

[84] C Lindenburg, « Modelling of Rotational Augmentation Based on Engineering Considerations and Measurements », *in*: European Wind Energy Conference, London, 2004, p. 12.

[85] Germanischer Lloyd, *Guideline for the Certification of Wind Turbine*, en, 2010, p. 384.

[86] Eric Loth et al., « Gravo-Aeroelastically Scaling for Extreme-Scale Wind Turbines », en, *in*: *35th AIAA Applied Aerodynamics Conference*, Denver, Colorado: American Institute of Aeronautics and Astronautics, June 2017, ISBN: 978-1-62410-501-2, DOI: 10.2514/6.2017-4215, URL: https://arc.aiaa.org/doi/10.2514/6.2017-4215 (visited on 07/30/2021).

[87] H. Aa. Madsen et al., « Blade Element Momentum Modeling of Inflow with Shear in Comparison with Advanced Model Results: BEM Modeling of Inflow with Shear », *in*: *Wind Energy* 15.*1* (2012), pp. 63–81, ISSN: 10954244, DOI: 10.1002/we.493, URL: http://doi.wiley.com/10.1002/we.493 (visited on 2020-04-10).

[88] Helge Aagaard Madsen, Franck Bertagnolio, and Andreas Fischer, « Measurement of High Frequency Surface Pressure Fluctuations for Blade Noise Characterization », *in*: IQPC Conference and o, 2012, URL: https://orbit.dtu.dk/en/publications/measurement-of-high-frequency-surface-pressure-fluctuations-for-b (visited on 2020-06-02).

[89] Helge Aagaard Madsen et al., « Correlation of Amplitude Modulation to Inflow Characteristics », *in*: *Proceedings of 43rd International Congress on Noise Control Engineering: Internoise 2014*, 43rd International Congress on Noise Control Engineering, The Australian Acoustical Society, 2014, URL: https://orbit.dtu.dk/en/publications/correlation-of-amplitude-modulation-to-inflow-characteristics (visited on 2020-06-02).

[90] Helge Aagaard Madsen et al., « Implementation of the Blade Element Momentum Model on a Polar Grid and Its Aeroelastic Load Impact », *in*: *Wind Energy Science* 5.*1* (2020), ISSN: 2366-7451, DOI: 10.5194/wes-5-1-2020, URL: https://www.wind-energ-sci.net/5/1/2020/ (visited on 2020-04-14).

[91] Helge Aagaard Madsen et al., *The DAN-AERO MW Experiments: Final report*, English, DTU Wind Energy, 2010, ISBN: 978-87-550-3809-7, URL: https://orbit.dtu.dk/en/publications/the-dan-aero-mw-experiments-final-report (visited on 08/04/2020).

[92] Jakob Mann, « Wind Field Simulation », *in*: *Probabilistic Engineering Mechanics* 13.*4* (Oct. 1998), pp. 269–282, ISSN: 02668920, DOI: 10.1016/S0266-8920(97)00036-2.

[93] James F Manwell, *Wind Energy Explained: Theory, Design and Application*, en, 2. ed., p. 705, ISBN: 978-0-470-01500-1.

[94] Michael K. McWilliam et al., « Aero-elastic wind turbine design with active flaps for AEP maximization », en, *in*: *Wind Energy Science* 3.*1* (May 2018), pp. 231–241, ISSN: 2366-7451, DOI: 10.5194/wes-3-231-2018, URL: https://wes.copernicus.org/articles/3/231/2018/ (visited on 08/02/2021).

[95] Muralikrishnan Gopalakrishnan Meena, Kunihiko Taira, and Keisuke Asai, « Airfoil-Wake Modification with Gurney Flap at Low Reynolds Number », en, *in*: *AIAA Journal* (2017), p. 12.

[96] F. Menter, « Zonal Two Equation k-w Turbulence Models For Aerodynamic Flows », *in*: *23rd Fluid Dynamics, Plasmadynamics, and Lasers Conference*, Fluid Dynamics and Co-located Conferences, American Institute of Aeronautics and Astronautics, July 1993, DOI: 10.2514/6.1993-2906, URL: https://arc.aiaa.org/doi/10.2514/6.1993-2906 (visited on 11/09/2020).

[97] Milton A. Miner, « Cumulative Damage in Fatigue », *in*: *Journal of Applied Mechanics* 12.*3* (Mar. 2021), A159–A164, ISSN: 0021-8936, DOI: 10.1115/1.4009458, URL: https://doi.org/10.1115/1.4009458 (visited on 01/25/2022).

[98] Jang-Oh Mo and Young-Ho Lee, « CFD Investigation on the Aerodynamic Characteristics of a Small-Sized Wind Turbine of NREL PHASE VI Operating with a Stall-Regulated Method », *in*: *Journal of Mechanical Science and Technology* 26.*1* (Jan. 2012), pp. 81–92, ISSN: 1738-494X, 1976-3824, DOI: 10.1007/s12206-011-1014-7.

[99] Mohammad Mohammadi, Ali Doosttalab, and Mehdi Doosttalab, « The effect of various gurney flaps shapes on the performace of wind turbine airfoils », *in*: *Proceedings of the ASME Early Career Technical Conference, Atlanta, GA, USA*, 2012, pp. 2–3.

[100] P J Moriarty and A C Hansen, *AeroDyn Theory Manual*, NREL/TP-500-36881, 15014831, 2005, NREL/TP-500–36881, 15014831, DOI: 10.2172/15014831, URL: http://www.osti.gov/servlets/purl/15014831/ (visited on 2020-02-10).

[101] O S Ozçakmak et al., « Inflow Turbulence and Leading Edge Roughness Effects on Laminar-Turbulent Transition on NACA 63-418 Airfoil », en, *in*: *Journal of Physics: Conference Series* 1037 (June 2018), p. 022005, ISSN: 1742-6588, 1742-6596, DOI: 10.1088/1742-6596/1037/2/022005, URL: https://iopscience.iop.org/article/10.1088/1742-6596/1037/2/022005 (visited on 03/18/2021).

[102] O. S. Özçakmak et al., « Laminar-Turbulent Transition Characteristics of a 3-D Wind Turbine Rotor Blade Based on Experiments and Computations », *in*: *Wind Energy Science Discussions* 2020 (2020), pp. 1–29, DOI: 10.5194/wes-2020-54, URL: https://www.wind-energ-sci-discuss.net/wes-2020-54/.

[103] Arvid Palmgren, « Die lebensdauer von kugellargern », *in*: *Zeitshrift des Vereines Duetsher Ingenieure* 68.*4* (1924), p. 339.

[104] Mayuresh Patil, Donghoon Lee, and Dewey Hodges, « Multi-flexible-body dynamic analysis of horizontal-axis wind turbines », en, *in*: *20th 2001 ASME Wind Energy Symposium*, Reno,NV,U.S.A.: American Institute of Aeronautics and Astronautics, Jan. 2001, DOI: 10.2514/6.2001-64, URL: https://arc.aiaa.org/doi/10.2514/6.2001-64 (visited on 02/01/2022).

[105] Georgios Pechlivanoglou, « Passive and Active Flow Control Solutions for Wind Turbine Blades », en, PhD thesis, Technischen Universität Berlin, 2013.

[106] YG Perivolaris and SG Voutsinas, « A cfd performance analysis of vortex generators used for boundary layer control on wind turbine blades », *in*: *Proceedings of the European Wind Energy Conference, Copenhagen, Denmark*, 2001.

[107] T. Potentier et al., « Comparison between 3D and 2D CFD unsteady simulations of the DANAERO blade », en, *in*: Nantes, France: *25^{e}Congrès Français de Mécanique*, 2022, (visited on 01/09/2022).

[108] T. Potentier et al., « High-Reynolds-number wind turbine blade equipped with root spoilers – Part 2: Impact on energy production and turbine lifetime », *in*: *Wind Energy Science* 7.*4* (2022), pp. 1771–1790, DOI: 10.5194/wes-7-1771-2022.

[109] Thomas Potentier, *R6 Qcriteria and vorticity*, Copernicus Publications, Last accessed: 07 Sep 2022, 2022, DOI: 10.5446/58972.

[110] Thomas Potentier, *R6 Uy and WSSy*, Copernicus Publications, Last accessed: 07 Sep 2022, 2022, DOI: 10.5446/58973.

[111] Thomas Potentier et al., « Analysis of the DANAERO wind turbine field database to assess the importance of different state-of-the-art blade element momentum (BEM) correction models », en, *in*: *Energy Science and Engineering* (2021), p. 24, DOI: 10.1002/ese3.908.

[112] Thomas Potentier et al., « High-Reynolds-number Wind Turbine Blade Equipped with Root Spoilers – Part 1: Unsteady Aerodynamic Analysis Using URANS Simulations », *in*: *Wind Energy Science* (2022), p. 11, DOI: https://doi.org/10.5194/wes-7-647-2022.

[113] Ludwig Prandtl and Albert Betz, *Vier Abhandlungen zur Hydrodynamik und Aerodynamik*, vol. 3, Göttinger Klassiker der Strömungmechanik, Göttingen: Göttingen University Press, 1927, ISBN: 978-3-941875-75-3, DOI: 10.17875/gup2010-106, URL: http://resolver.sub.uni-goettingen.de/purl?isbn-978-3-941875-75-3 (visited on 2020-05-25).

[114] P. Queutey and M. Visonneau, « An Interface Capturing Method for Free-Surface Hydrodynamic Flows », *in*: *Computers and Fluids* 36 (2007), pp. 1481–1510, DOI: 0.1016/j.compfluid.2006.11.007.

[115] Hamid Rahimi et al., « Evaluation of Different Methods for Determining the Angle of Attack on Wind Turbine Blades with CFD Results under Axial Inflow Conditions », *in*: *Renewable Energy* (2018), DOI: 10.1016/j.renene.2018.03.018, arXiv: 1709.04298, URL: http://arxiv.org/abs/1709.04298 (visited on 2020-02-10).

[116] *Renewable energy sources and climate change mitigation: special report of the Intergovernmental Panel on Climate Change*, en, 11, July 2012, pp. 49–6309–49–6309, DOI: 10.5860/CHOICE.49-6309, URL: http://choicereviews.org/review/10.5860/CHOICE.49-6309 (visited on 01/31/2022).

[117] C. M. Rhie and W. L. Chow, « A Numerical Study of the Turbulent Flow Past an Airfoil with Trailing Edge Separation », *in*: *AIAA Journal* 21.*11* (1983), pp. 1525–1532, DOI: 10.2514/6.1982-998.

[118] Zohaib Saleem, « Investigation of passive root flaps on HAWT », en, MA thesis, TU Delft, 2019.

[119] Saptarshi Sarkar and Breiffni Fitzgerald, « Use of Kane's Method for Multi-Body Dynamic Modelling and Control of Spar-Type Floating Offshore Wind Turbines », en, *in*: *Energies* 14.*20* (Oct. 2021), p. 6635, ISSN: 1996-1073, DOI: 10.3390/en14206635, URL: https://www.mdpi.com/1996-1073/14/20/6635 (visited on 02/01/2022).

[120] Peter Schaffarczyk and Chuichi Arakawa, « A thick aerodynamic profile with regions of negative lift slope and possible implications on profiles for wind turbine blades », en, *in*: *Wind Energy* (Aug. 2020), we.2565, ISSN: 1095-4244, 1099-1824, DOI: 10.1002/we.2565, URL: https://onlinelibrary.wiley.com/doi/abs/10.1002/we.2565 (visited on 09/01/2020).

[121] J G Schepers and K Boorsma, *Final Report of IEA Wind Task 29: Mexnext (Phase 2)*, p. 257.

[122] J.G Schepers, *Advanced aerodynamic modelling, design and testing for large rotor blades*, English, Final report FP7-ENERGY-2013.2.3.1/ n°608396, European Comission, 2017, p. 77, URL: https://www.eera-avatar.eu/fileadmin/avatar/user/AVATAR_final_report_v26_2_2018.pdf (visited on 06/28/2021).

[123] J.G. Schepers et al., *IEA Wind TCP Task 29, Phase IV: Detailed Aerodynamics of Wind Turbines*, tech. rep., Zenodo, May 2021, DOI: 10.5281/ZENODO.4925963, URL: https://zenodo.org/record/4925963 (visited on 06/15/2021).

[124] Jan Gerhard Schepers, « Engineering Models in Wind Energy Aerodynamics: Development, Implementation and Analysis Using Dedicated Aerodynamic Measurements. », Netherlands: TU Delft, 2012.

[125] Jaap Schijve, *Fatigue of structures and materials*, eng, 2. ed. [Nachdr.], Dordrecht: Springer, 2010, ISBN: 978-1-4020-6807-2.

[126] G. B. Schubauer and W. G. Spangenberg, « Forced mixing in boundary layers », en, *in*: *Journal of Fluid Mechanics* 8.*01* (May 1960), p. 10, ISSN: 0022-1120, 1469-7645, DOI: 10.1017/S0022112060000372, URL: http://www.journals.cambridge.org/abstract_S0022112060000372 (visited on 08/02/2021).

[127] Walter Schütz, « A history of fatigue », *in*: *Engineering Fracture Mechanics* 54.*2* (1996), pp. 263–300, ISSN: 0013-7944, DOI: https://doi.org/10.1016/0013-7944(95)00178-6, URL: https://www.sciencedirect.com/science/article/pii/0013794495001786.

[128] C. Sicot et al., « Rotational and Turbulence Effects on a Wind Turbine Blade. Investigation of the Stall Mechanisms », *in*: *Journal of Wind Engineering and Industrial Aerodynamics* 96.*8-9* (Aug. 2008), pp. 1320–1331, ISSN: 01676105, DOI: 10.1016/j.jweia.2008.01.013.

[129] Eric Simley et al., « Characterization of Wind Velocities in the Upstream Induction Zone of a Wind Turbine Using Scanning Continuous-Wave Lidars », *in*: *Journal of Renewable and Sustainable Energy* 8.*1* (Jan. 2016), p. 013301, ISSN: 1941-7012, DOI: 10.1063/1.4940025.

[130] D Simms et al., *NREL Unsteady Aerodynamics Experiment in the NASA-Ames Wind Tunnel: A Comparison of Predictions to Measurements*, en, tech. rep. NREL/TP-500-29494, 783409, June 2001, NREL/TP–500–29494, 783409, DOI: 10.2172/783409, URL: http://www.osti.gov/servlets/purl/783409/ (visited on 01/21/2022).

[131] Witold Skrzypiński, Mac Gaunaa, and Christian Bak, « The Effect of Mounting Vortex Generators on the DTU 10MW Reference Wind Turbine Blade », en, *in*: *Journal of Physics: Conference Series* 524 (June 2014), p. 012034, ISSN: 1742-6596, DOI: 10.1088/1742-6596/524/1/012034, URL: http://stacks.iop.org/1742-6596/524/i=1/a=012034?key=crossref.54b36d594b93e12c30aaea5e828c8f1e (visited on 02/10/2020).

[132] Vaclav Smil, *Energy transitions: global and national perspectives*, Second edition, Santa Barbara, California: Praeger, an imprint of ABC-CLIO, LLC, 2017, ISBN: 978-1-4408-5324-1.

[133] H Snel, J G Schepers, and B Montgomerie, « The MEXICO project (Model Experiments in Controlled Conditions): The database and first results of data processing and interpretation », en, *in*: *Journal of Physics: Conference Series* 75 (July 2007), p. 012014, ISSN: 1742-6596, DOI: 10.1088/1742-6596/75/1/012014, URL: https://iopscience.iop.org/article/10.1088/1742-6596/75/1/012014 (visited on 01/21/2022).

[134] H Snel, J. G Schepers, and Stichting Energieonderzoek Centrum Nederland, *Joint Investigation of Dynamic Inflow Effects and Implementation of an Engineering Method*, Petten, Netherlands: Netherlands Energy Research Foundation ECN, 1995.

[135] Herman Snel, *Joint Investigation of Dynamic Inflow Effects and Implementation of an Engineering Method.Pdf*, ECN publication ECN-C–94-107, TNO, 1995, p. 326, URL: https://publications.ecn.nl/E/1995/ECN-C--94-107.

[136] Jens N. Sørensen et al., « Simulation of Wind Turbine Wakes Using the Actuator Line Technique », *in*: *Philosophical Transactions of the Royal Society A: Mathematical, Physical and Engineering Sciences* 373.*2035* (Feb. 2015), p. 20140071, ISSN: 1364-503X, 1471-2962, DOI: 10.1098/rsta.2014.0071.

[137] Niels N Sørensen et al., « Prediction of the Effect of Vortex Generators on Airfoil Performance », en, *in*: *Journal of Physics: Conference Series* 524 (June 2014), p. 012019, ISSN: 1742-6596, DOI: 10.1088/1742-6596/524/1/012019, URL: http://stacks.iop.org/1742-6596/524/i=1/a=012019?key=crossref.cb688acdfc81344405660a9873fa9a0b (visited on 02/10/2020).

[138] Niels N. Sørensen, « General purpose flow solver applied to flow over hills », English, Publisher: Risø National Laboratory, PhD thesis, DTU, 1995, URL: https://orbit.dtu.dk/en/publications/general-purpose-flow-solver-applied-to-flow-over-hills (visited on 11/09/2020).

[139] Niels N. Sorensen et al., « CFD code comparison for 2D airfoil flows », en, *in*: *Journal of Physics: Conference Series* 753 (Sept. 2016), p. 082019, ISSN: 1742-6588, 1742-6596, DOI: 10.1088/1742-6596/753/8/082019, URL: https://iopscience.iop.org/article/10.1088/1742-6596/753/8/082019 (visited on 11/19/2020).

[140] Bruce L. Storms and Cory S. Jang, « Lift enhancement of an airfoil using a Gurney flap and vortex generators », en, *in*: *Journal of Aircraft* 31.*3* (May 1994), pp. 542–547, ISSN: 0021-8669, 1533-3868, DOI: 10.2514/3.46528, URL: https://arc.aiaa.org/doi/10.2514/3.46528 (visited on 02/10/2020).

[141] Roland B. Stull, « Mean Boundary Layer Characteristics », *in*: *An Introduction to Boundary Layer Meteorology*, ed. by Roland B. Stull, Dordrecht: Springer Netherlands, 1988, pp. 1–27, DOI: 10.1007/978-94-009-3027-8_1.

[142] Nikola Sucevic and Zeljko Djurisic, « Influence of atmospheric stability variation onuncertainties of wind farm production estimation », en, *in*: Copenhagen, Denmark: European Wind Energy Conference and Exhibition, Apr. 2012.

[143] Herbert J. Sutherland, *On the Fatigue Analysis of Wind Turbines*, en, tech. rep. SAND99-0089, 9460, June 1999, SAND99–0089, 9460, DOI: 10.2172/9460, URL: http://www.osti.gov/servlets/purl/9460-L0Udei/webviewable/ (visited on 01/25/2022).

[144] Harold D Taylor et al., « The elimination of diffuser separation by vortex generators », *in*: *Research department report no. r-4012-3, United Aircraft Corporation, East Hartford, Connecticut* 103 (1947).

[145] Kirt & Thomsen, *Bladena, Wind Turbine Blades Handbook*, en, 2019, ISBN: 978-87-971709-0-8.

[146] SP Timoshenko and JM Gere, « Mechanics of Materials. van Nordstrand Reinhold Company », *in*: *New York* (1972).

[147] Luis A. Martinez Tossas and Stefano Leonardi, *Wind Turbine Modeling for Computational Fluid Dynamics: December 2010 - December 2012*, tech. rep. NREL/SR-5000-55054, 1089598, July 2013, NREL/SR-5000–55054, 1089598, DOI: 10.2172/1089598.

[148] Niels Trodborg et al., *DANAERO MW II Final Report*, English, DTU Wind Energy E 0027(EN), DTU Wind Energy, 2013, URL: https://orbit.dtu.dk/en/publications/danaero-mw-final-report.

[149] Niels Troldborg and Alexander Raul Meyer Forsting, « A simple model of the wind turbine induction zone derived from numerical simulations », English, *in*: *Wind Energy* 20.*12* (2017), pp. 2011–2020, ISSN: 1095-4244, DOI: 10.1002/we.2137.

[150] Niels Troldborg et al., « Experimental and numerical investigation of 3D aerofoil characteristics on a MW wind turbine », English, *in*: *Proceedings - European Wind Energy Conference & Exhibition 2013*, tex.ids: troldborgExperimentalNumericalInvestigation2013, European Wind Energy Association (EWEA), 2013, URL: https://orbit.dtu.dk/en/publications/experimental-and-numerical-investigation-of-3d-aerofoil-character (visited on 08/05/2020).

[151] H. K. Versteeg and Weeratunge Malalasekera, *An introduction to computational fluid dynamics - the finite volume method*, 2007, p. 520, ISBN: 0131274988.

[152] *Vestas*, URL: http://nozebra.ipapercms.dk/Vestas/Communication/Productbrochure/ProductImprovements/AerodynamicUpgrades/.

[153] L A Viterna and D C Janetzke, *Theoretical and experimental power from large horizontal-axis wind turbines*, en, tech. rep. DOE/NASA/20320-41, NASA-TM-82944, 6763041, National Aeronautics and Space Administration, Sept. 1982, DOI: 10.2172/6763041, URL: http://www.osti.gov/servlets/purl/6763041/ (visited on 06/22/2021).

[154] Jeroen Wackers et al., « Can adaptive grid refinement produce grid-independent solutions for incompressible flows? », en, *in*: *Journal of Computational Physics* 344 (Sept. 2017), pp. 364–380, ISSN: 00219991, DOI: 10.1016/j.jcp.2017.04.077, URL: https://linkinghub.elsevier.com/retrieve/pii/S0021999117303650 (visited on 06/15/2021).

[155] Jeroen Wackers et al., « Combined refinement criteria for anisotropic grid refinement in free-surface flow simulation », en, *in*: *Computers & Fluids* 92 (Mar. 2014), pp. 209–222, ISSN: 00457930, DOI: 10.1016/j.compfluid.2013.12.019, URL: https://linkinghub.elsevier.com/retrieve/pii/S0045793013005112 (visited on 06/15/2021).

[156] J.J. Wang, Y.C. Li, and K.-S. Choi, « Gurney flap—Lift enhancement, mechanisms and applications », en, *in*: *Progress in Aerospace Sciences* 44.*1* (Jan. 2008), pp. 22–47, ISSN: 03760421, DOI: 10.1016/j.paerosci.2007.10.001, URL: https://linkinghub.elsevier.com/retrieve/pii/S0376042107000784 (visited on 02/10/2020).

[157] Sonia Wharton and Julie K. Lundquist, « Assessing Atmospheric Stability and Its Impacts on Rotor-Disk Wind Characteristics at an Onshore Wind Farm », *in*: *Wind Energy* 15.*4* (2012), pp. 525–546, ISSN: 1099-1824, DOI: 10.1002/we.483, URL: https://onlinelibrary.wiley.com/doi/abs/10.1002/we.483 (visited on 2020-08-04).

[158] Guangxing Wu et al., « Uncertainty Prediction on the Angle of Attack of Wind Turbine Blades Based on the Field Measurements », *in*: *Energy* (2020), DOI: 10.1016/j.energy.2020.117515, URL: https://linkinghub.elsevier.com/retrieve/pii/S0360544220306228 (visited on 2020-04-10).

[159] Serhiy Yarusevych, Pierre E. Sullivan, and John G. Kawall, « On vortex shedding from an airfoil in low-Reynolds-number flows », en, *in*: *Journal of Fluid Mechanics* 632 (Aug. 2009), pp. 245–271, ISSN: 0022-1120, 1469-7645, DOI: 10.1017/S0022112009007058, URL: https://www.cambridge.org/core/product/identifier/S0022112009007058/type/journal_article (visited on 02/10/2021).

[160] Ye Zhang et al., « Effects of Root Gurney Flaps on the Aerodynamic Performance of a Horizontal Axis Wind Turbine », *in*: *Energy* 187 (Nov. 2019), p. 115955, ISSN: 03605442, DOI: 10.1016/j.energy.2019.115955.

Appendix A

Résumé substantiel

A.1 Principes de l'éolien

Le premier chapitre du manuscrit de thèse relate l'historique de l'énergie éolienne : il commence par une description et caractérisation du vent puis s'en suit une brève description de l'évolution des éoliennes.
Le vent perçu à la surface du globe est le résultat de déplacement de larges masses d'air. De par la rotondité de la Terre, son inclinaison et sa différente composition, la densité d'énergie solaire absorbée varie on fonction de la position sur Terre. Ces différences entraînent de larges déplacements d'air. Plus localement, à l'échelle continentale, des cellules convectives dues à la force de Coriolis créées des « boucles » de recirculation de l'air. Enfin, proche du sol les éoliennes opèrent dans la couche limite atmosphérique, celle-ci varie en épaisseur en fonction de l'ensoleillement mais aussi de la rugosité du terrain. La difficulté des simulations éoliennes tient à prendre en compte toutes ces échelles (kilomètre jusqu'au micromètre) pour les résoudre et les lier convenablement. Le vent peut être caractérisé grâce à sa valeur moyenne et les variations associées autour de la moyenne : la turbulence. Typiquement la vitesse moyenne et la direction servent à caractériser un gisement en suivant la classification de l'IEC. La turbulence sert à décrire de nombreux facteurs, dans notre cas seules la stationnarité et la stabilité seront utilisées.

L'Homme a appris à apprivoiser le vent depuis l'antiquité : des moulins à vent utilisés pour moudre le grain ont été retrouvés en Iran datant de IXème siècle avant notre ère. C'est en 1887 que la première éolienne à production électrique a été créée en Ecosse par un professeur écossais James Blyth. En 1931, l'ingénieur Georges Jean-Marie Darrieus a repris le concept de machine à axe vertical et a breveté l'utilisation d'aérofoils. De nos jours, les turbines suivent un design similaire : axe horizontal, trois pales tournant de le sens horaire, une tour et nacelle. Malgré une similitude de design l'énergie générée, a augmentée considérablement de quelques kW à maintenant 15MW pour les plus grandes machines en mer. Cependant, le pied de pale reste une zone de perte pour les turbiniers, en effet dû au contraintes mécaniques importantes la forme n'est pas optimisée aérodynamiquement. Pour cela une panoplie de solution existe, notamment les ajouts aérodynamiques passifs. Dans cette thèse, l'ajout passif étudié est le « spoiler ». Le spoiler est installé proche du centre de rotation, entre 60% et 80% de la corde locale et sur plusieurs mètres de long. ENGIE Green est un exploitant d'énergies renouvelables, au cours d'une maintenance de routine des fissures ont été remarquées sur les pales étant équipées de spoilers. Cette thèse cherche à comprendre les causes aérodynamiques des dommages structurels en utilisant

des outils de simulations numériques les plus modernes. De plus une nouvelle méthode de calcul de durée de vie est proposée prenant en compte l'instationnarité aérodynamique liée à la présence du spoiler. Enfin, le calcul d'énergie annuel sera aussi analysé afin de quantifier l'impact théorique maximal du spoiler sur la courbe de puissance.

A.2 Description des outils de modélisation

Le chapitre suivant décrit la théorie des différents outils utilisés : des codes d'ingénierie (OpenFAST et AeroDyn) et codes de calculs haute fidélité (ISIS-CFD).

A.2.1 Théorie de l'élément de pale

La théorie de l'élément de pale, plus communément appelée BEM (Blade Element Momentum) est une théorie où de nombreuses simplifications sont appliquées à l'écoulement afin de résoudre rapidement et facilement les différentes équations.
En partant de l'hypothèse de la conservation de quantité de mouvement le rotor est modélisé par un disque poreux, sans friction et statique. La poussée aérodynamique est déduite. Ensuite, en appliquant le théorème de Bernouilli au contrôle de volume et en conservant les précédentes hypothèses on peut trouver la pression et la vitesse de l'écoulement proche de disque. La puissance extraite est calculée grâce à la conservation de masse et en gardant constante la pression le long des parois extérieures du volume de contrôle. Le facteur d'induction, a, est alors introduit comme un fraction de l'écoulement incident. La puissance et poussée peuvent ainsi être réécrites en fonction de l'induction. Utilisant les éléments précédemment introduits, la BEM inclut la transformation du disque poreux en rotor avec un nombre fini de pales, la géométrie de la pale (discrétisation en 2D éléments indépendants) et la rotation du rotor. Au final un procédé itératif de quelques équations et relations analytiques permettent aux industriels et au monde de la recherche de calculer les charges appliquées à la turbine ainsi que la production énergétique. L'avantage de la rapidité de calcul et relative simplicité de mise en œuvre vient avec l'inconvénient d'hypothèses simplificatrices. En effet, dans la théorie BEM, l'écoulement est considéré stationnaire et 2D, les éléments de pales sont indépendants les uns des autres et les effets de la rotations sont négligés. C'est pourquoi depuis les années 1900 de nombreux modèles de corrections ont été ajouté à la BEM. Ces différents modèles ont été trouvé grâce à de nombreuses expériences en soufflerie et/ou en plein air, mais aussi ces dernières années grâce à des simulations numériques précises.

A.2.2 Mécanique des Fluides Numériques

La Mécanique de Fluides Numériques, plus communément appelée CFD (pour Computational Fluid Dynamics), est un vaste sujet d'expertise même si l'on considère seulement l'aérodynamique externe. On peut appeler CFD un solveur 2D simple utilisant une formulation non-visqueuse comme XFOIL mais aussi l'utilisation de simulations directes

(Direct Numerical Simulation – DNS) qui résout toutes les échelles de la turbulence sans modélisation. Même la BEM présentée plus haut peut rentrer dans la catégorie de la CFD puisqu'elle permet de traiter des problèmes appliquées de la mécanique des fluides. Dans ce manuscrit, CFD, fera référence à la résolution des équations de Navier-Stokes utilisant un maillage. De nombreux ouvrages considérés comme classiques explicitent en détails les tenant et aboutissants des divers modèles, ici on se contentera d'une brève explication afin de poser les bases de la compréhension pour la suite du manuscrit.

Les équations de la CFD représentent sous forme mathématiques les différentes lois physiques :

- Conservation de la masse
- Principe fondamental de la dynamique en translation (deuxième loi de Newton appliquée à une particule fluide)
- Conservation de l'énergie (première principe de thermodynamique appliquée à une particule fluide)

Différents niveaux de précisions existent, le plus précis (DNS) permet la résolution à toute échelle des différentes équations mais son utilisation reste principalement dans la recherche de part le temps de calcul nécessaire (proportionnel au cube du nombre de Reynolds). Ensuite les simulations aux grands tourbillons (LES) permettent une résolution plus grossières mais nécessite malgré tout l'utilisation intensive de supercalculateurs pendant plusieurs jours pour converger vers une solution. Le plus bas niveau de précision est l'utilisation de la moyenne de Reynolds (RANS). En moyennant les fluctuations dans le temps, le problème est mathématiquement ouvert et nécessite ainsi une approximation via modélisation pour le fermer. Différents modèles de turbulence existent dans la littérature. De récents modèles utilisant à la fois des solutions RANS et LES sont maintenant disponible : DES et DDES.

A.2.3 Charges et structures

Grâce à sa forme et sa fabrication, une pale d'éolienne peut être approximée comme un poutre ayant une section et des propriétés mécaniques variables. Les propriétés structurelles nécessaire à OpenFAST sont les raideurs dans le plan et hors plan de rotation (EI_{xx} et EI_{yy} respectivement) ainsi que la masse linéique (M_L). Un première approximation d'équilibre permet d'intégrer des équations de poutres afin de trouver la déformée de la pale. Cependant pour un degré de précision accrue, les déformations calculées dépendent du chargement aérodynamique qui lui-même dépend des charges et déformations, le problème est couplé. Pour cette raison, un modèle de structure dynamique est nécessaire.

Plusieurs méthodes existent pour modéliser la structure d'une turbine, celle employée par OpenFAST utilise un couplage entre une approche modale et une formulation muticorps dynamique. En utilisant le superposition des premiers modes propres et en utilisant l'équation de Kane, OpenFAST permet de réduire le nombre de degrés de liberté au prix d'une perte d'information minime comparé à la méthode des éléments finis.

A.2.4 Fatigue

Le calcul de durée de vie et de tenue en fatigue des éoliennes est un sujet relativement récent. A partir de 2009 le nombre de publications augmente significativement pour atteindre plus de 1000 par an en 2021. La règle de Miner (ou règle de Palgrem-Miner) malgré sa simplicité est le standard de calcul accepté et implémenté dans les différentes normes de certifications. La méthode de comptage rainflow est un ajout nécessaire à la règle de Miner car elle prend en compte l'élément aléatoire des charges aérodynamiques. La correction de Goodman est aussi appliquée car elle prend en compte l'utilisation d'une plage de valeur moyenne plutôt qu'une valeur fixe.

A.3 Base de données

A.3.1 Base de données DANAERO

La base de donnée DANAERO est un ensemble de données unique. En effet, un vaste projet de collaboration entre industriels et universités de 2003 à 2010 a permis la mise en commun de données expérimentales et numériques.
Les données utilisées au cours de cette thèse proviennent d'une éolienne de 2MW instrumentée spécialement afin de mesurer, dans des conditions réelles d'opérations, les forces appliquées le long du rayon. Des mesures plus conventionnelles en soufflerie ont aussi été réalisées sur quatre aérofoils utilisés sur la pale instrumentée. Enfin, de nombreuses études numériques 2D et 3D dans diverses conditions d'opérations sont disponibles. Ces études numériques ont permis de valider l'utilisation du solveur ISIS-CFD pour une application dédiée à l'éolien.

A.3.2 Base de données ENGIE Green

ENGIE Green possède un scan 3D d'une éolienne réalisé en 2010 dans le cadre d'un autre projet. Le scan étant ancien certaines zones de la géométrie n'ont pas été capturées. Ainsi plusieurs étapes de lissages utilisant des courbes de Bézier ont été utilisées afin de garantir une géométrie continue pour chaque tronçon. Le spoiler étudié est installé en pied de pale entre les rayons R3 et R7.5. Les deux derniers mètres de la pale scannée étant inexploitables, ils ont été extrapolés à partir de la dernière section utilisée (R43) pour rendre la géométrie conforme à un design traditionnel.

A.4 Vérification des outils et méthodologie de post-process

A.4.1 UiBEM

La méthode UiBEM développée compare deux modèles d'induction issus de la littérature ainsi qu'un troisième où l'utilisation de l'induction axial du premier est couplé au modèle d'induction tangentiel du deuxième. Après utilisation de la base de données DANAERO numérique dans des conditions de vent axial, le dernier modèle « hybride » a été jugé le plus fidèle. Par la suite, la partie instationnaire, notamment le modèle d'orientation axial (yaw), a aussi comparé trois modèles existants. Au final, le modèle étant le plus proche des résultats issus de la CFD a été choisi et implémenté dans le solveur UiBEM développé.

A.4.2 ISIS-CFD 2D

Une première étude utilisant les données de soufflerie et numérique de la base de données DANAERO a permis de déterminer l'influence de la taille du domaine calcul. Pour ce faire le procédé « Design of Experiment » issu de la méthodologie 6-Sigma a été utilisé. La taille du domaine de calcul étant définie pour un aérofoil de corde 1, il suffit par la suite de multiplier le domaine par la corde de l'aérofoil pour une étude à taille réelle. Ensuite, une étude d'indépendance de maillage et d'indépendance du pas de temps a été faite pour générer des polaires aérodynamiques utilisées par OpenFAST.

A.4.3 ISIS-CFD 3D

Suivant la méthodologie établie en 2D, une première étude concernant la taille du domaine a été faite en utilisant la base de données DANAERO. Ensuite, afin d'optimiser le nombre de cellules dans le domaine de calcul une étude concernant la discrétisation de la pale a été menée. Une discrétisation grossière couplée au raffinement automatique de maillage d'ISIS-CFD permet d'obtenir des résultats similaire à la littérature tout en limitant à 80M le nombre de cellules.

A.5 Preuves des limites de la BEM pour le calcul de fatigue d'une pale

Le Chapitre 5 du manuscrit de thèse résume les résultats de l'analyse aérodynamique de la base de données expérimentale de DANAERO en utilisant le code UiBEM développé. Les séries temporelles analysées correspondent à 30min continues, échantillonnées à 35Hz, de mesures de forces et SCADA. Afin de reproduire les cas se rapprochant des hypothèses de la BEM de nombreux filtres et modèles de correction des données d'entrée ont été rajouté aux équations traditionnelles de la BEM instationnaire. Les effets du gradient verti-

cal, du sillage d'éoliennes voisines, de désalignement axial, de position de l'anémomètre ont été ajoutés. Le résultat principal de cet étude montre que la BEM stationnaire est insuffisante pour décrire le comportement dynamique d'une éolienne. L'utilisation d'équations instationnaires est nécessaire pour la prise en compte de phénomènes transitoires et dynamiques. Ces phénomènes sont, aujourd'hui, pour parti ignorés lors du calcul de durée de vie de l'éolienne.

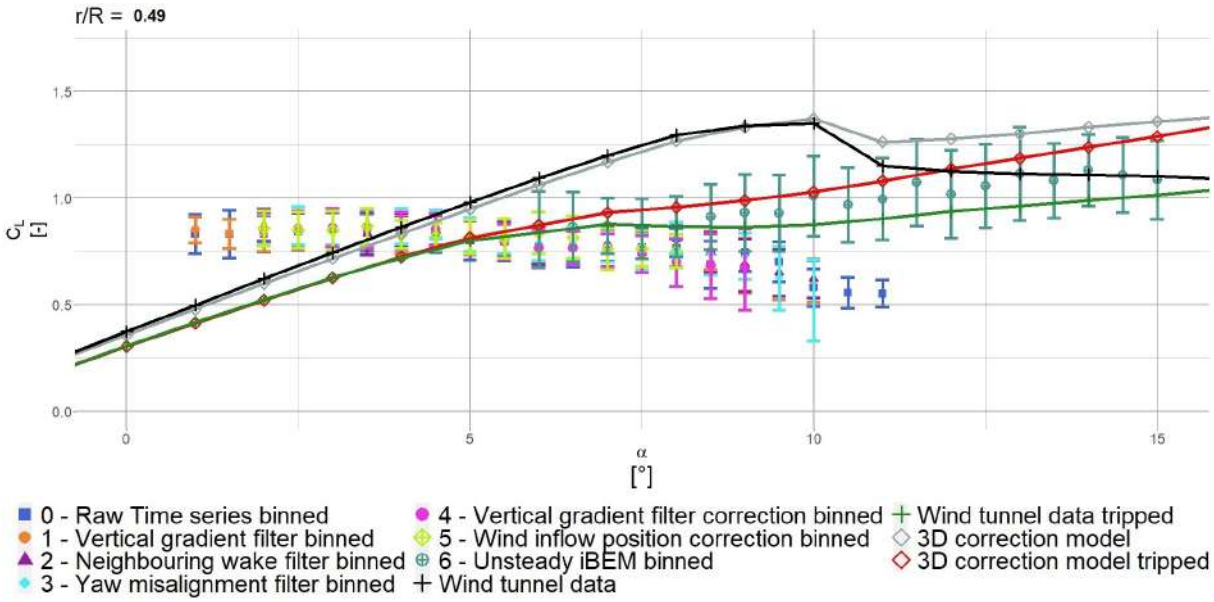

Figure A.1 – Comparaison des C_L en fonction des différents modèles

A.6 Estimation de l'impact d'un spoiler à l'aide de simulation 2D instationaires

Le Chapitre 6 propose une étude 2D URANS nouvelle de l'écoulement instationnaire derrière un aérofoil épais équipé (ou non) d'un spoiler provenant d'une éolienne de 2MW. Le spoiler réarrange l'écoulement et la pression moyenne augmentant ainsi la portance moyenne aux angles d'attaque positifs. Cependant, une forte pénalité sur le coefficient de traînée est aussi constatée. Une forte instationnarité est aussi générée. Sans spoiler, le sillage est erratique et non organisé alors qu'avec l'installation du spoiler une fréquence de lâcher tourbillonnaire émerge. Le nombre de Strouhal calculé reste cohérent avec la littérature ($S_t = 0.15$) malgré la variation d'amplitude des coefficients aérodynamiques avec l'angle d'attaque. Aussi, le contenu énergétique spectral est augmenté de plusieurs ordres de grandeurs avec l'ajout d'un spoiler. Les prochains chapitres permettront l'évaluation en terme de fatigue et d'énergie de l'ajout du spoiler.

Figure A.2 – Coefficient de portance pour la position radiale R6 ($r/R = 13\%$).

Figure A.3 – Coefficient de traînée pour la position radiale R6 ($r/R = 13\%$).

A.7 Une nouvelle méthode pour estimer la durée de vie d'une pale en prenant en compte l'instationnarité

La pale scannée est analysée au moyen d'un code BEM aéroélastique dans le domaine temporel pour vérifier l'impact des ajouts passifs sur la production annuelle d'énergie et la durée de vie. La chapitre précédent montre l'instationnarité des coefficients aérodynamique, cette instationnarité est bien capturée par OpenFAST lorsque la turbine est rigide. Une fois rendue flexible, un nouveau mode de prise en compte de l'instationnarité dans le calcul de fatigue est proposé.
Concernant le gain énergétique, dans des conditions optimales, il n'est que de 0.5% auquel une forte amplitude est associée. Les charges intégrées le long du rayon de la pale restent constantes malgré une légère réduction du moment fléchissant en pied de pale lorsque le spoiler est installé. Cependant, les efforts locaux augmentent de façon significative en valeur moyenne ainsi que l'amplitude associée. Une analyse en fatigue a été faite utilisant la fréquence de lâcher tourbillonnaire et les résultats de trois séries temporelles distinctes pour inclure l'effet instationnaire. Le spoiler augmente l'instationnarité déjà présente au pied de pale et ne doit pas être négligé lors du design structurel de la turbine. Si mal dimensionné, le spoiler peut avoir des conséquences néfastes sur la durée de vie de la turbine.
Enfin, la méthode présentée suppose que les hypothèses BEM et les simulations 2D sont suffisantes. Une analyse 3D sera présentée lors du chapitre suivant afin de vérifier la validité de ces hypothèses.

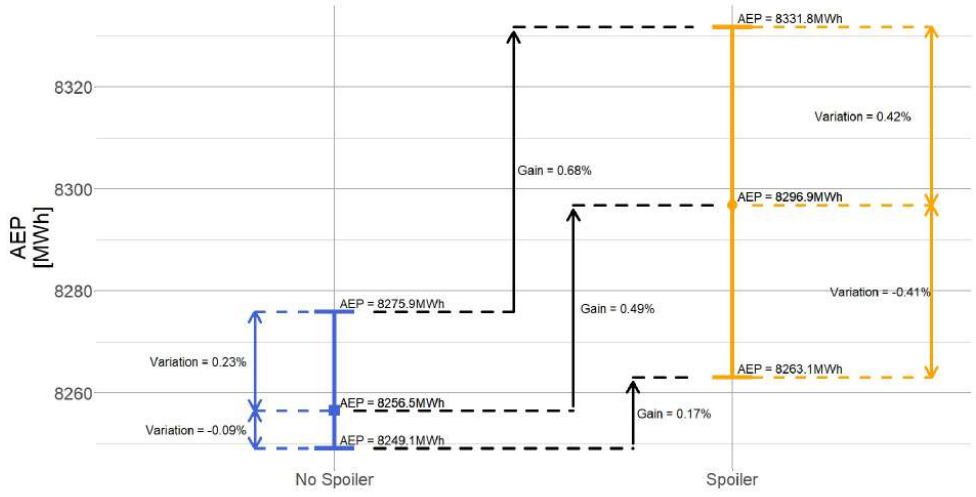

Figure A.4 – Gain énergétique ainsi que les variations associées pour toutes les configurations utilisant un vent de classe IEC II

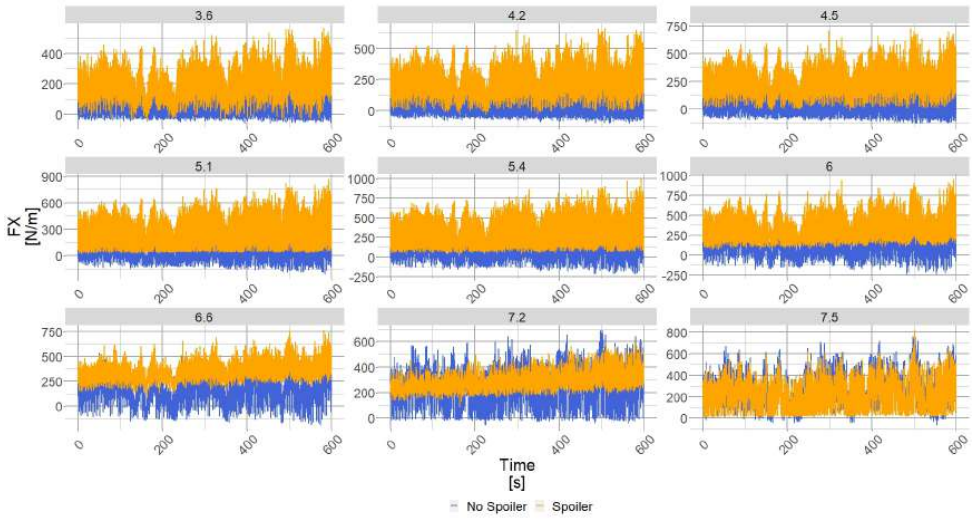

Figure A.5 – Résultat OpenFAST de la force normale au plan de rotation pour une vitesse de vent horizontale de 8m/s. Les carrés bleus (■) montrent les résultats pour une pale sans spoiler, les points oranges (●) montrent les résultats pour une pale sans spoiler. Les deux cas utilisent la méthode de combination développée pour le calcul de fatigue. Chaque sous figure montre les résultats pour un rayon dont la valeur est donnée en titre.

A.8 Comparaison des effets du spoiler : simulations instationnaires 2D vs 3D

Les chapitres précédents ont permis de développer et d'utiliser une méthode pour estimer la durée de vie lors d'ajout de spoiler grâce à des simulations CFD 2D. Le Chapitre 8 se concentre sur l'estimation des différences entre des simulations 2D et 3D au niveau du spoiler et s'assurer de la justesse de la méthode développée au Chapitre 7. Pour cause de manque de temps au cours de ce doctorat, les simulations 3D seront faites sans tour ni nacelle. De plus, l'écoulement incident est considéré stationnaire et constant. Une seule vitesse de vent a pu être analysée, les conditions d'opérations sont rappelées ci-dessous :

- Vitesse: 8m/s
- Pitch: -1.568°
- RPM: 14.1

Les résultats peuvent être séparés en deux parties. La première partie présente des résultats à l'échelle du rotor et comprend deux sections. La première section donne un aperçu de l'organisation du sillage lointain en tenant compte de la méthode de raffinement utilisée précédemment. Dans la section suivante la zone impactée par le spoiler est présentée. Ensuite, les résultats se sont concentrés sur l'aérodynamique de la pale, de l'organisation 3D de l'écoulement sur la pale à la répartition instationnaire de la pression dans la zone du pied de pale. Ces résultats 3D sont comparés aux simulations 2D et aux calculs BEM lorsque cela est possible.
L'ajout du spoiler influence le sillage proche en réduisant la taille du cône, mais son influence sur la récupération de la vitesse de sillage lointain est limitée. De même la zone

d'induction en amont du rotor n'est pas impactée par le spoiler. Les grandeurs locales en pied de pales: l'induction axiale et tangentielle et l'angle d'attaque sont en revanche très impactés. L'induction axiale augmente et l'induction tangentielle diminue, entraînant une réduction de l'angle d'attaque local. En analysant l'écoulement local, cela peut s'expliquer par une redistribution de la pression autour de l'aerofoil avec le spoiler. Une modification de la zone de décollement ou par une modification de la zone d'écoulement transverse ne pouvant pas être incriminées. Les charges locales avec un spoiler sont augmentées, principalement en raison de l'augmentation de la portance suite à la redistribution de la pression. Un effet secondaire positif est la meilleure répartition des charges dans le sens de la corde. Dans l'ensemble, l'extraction d'énergie est améliorée par le spoiler dans la région en pied de pale. La contrepartie est une augmentation des oscillations d'écoulement avec deux sources majeures d'excitation et donc de fatigue : le sillage de la pale avec sa fréquence de lâcher tourbillonnaire et les oscillations liées à l'écoulement transversal. Toutes ces oscillations se retrouvent transférées à la structure par la variation de portance. Malgré la proximité de fréquence émergente dans le cas sans et avec spoiler, ce dernier produit des amplitudes plus élevées. En 3D, la présence du spoiler produit un effet global similaire à celui des simulations 2D, avec une redistribution de la pression, une augmentation de la taille du sillage et du niveau des oscillations de portance, sans impact sur la séparation de l'écoulement. Cependant, des différences majeures existent à l'échelle de l'aérofoil pour les régions au pied de pale telles que : l'organisation du sillage et des tourbillons et la présence de l'écoulement transversal dû aux effets de Coriolis.
L'impact de la fidélité de la simulation sur l'effet de spoiler a aussi été étudié dans ce chapitre. À l'échelle de l'aérofoil, pour le cas sans spoiler, la portance moyenne est significativement différente entre les simulations 2D et 3D en raison du bénéfice de l'écoulement radial et des effets de Coriolis. Lorsque le spoiler est installé, des portances moyennes similaires sont observées entre les simulations 2D et 3D, car le bénéfice 2D obtenu avec le spoiler est plus important que le gain 3D. En ce qui concerne l'instabilité du sillage de la pale, les simulations 3D atténuent considérablement les oscillations de portance, entraînant une diminution significative de l'énergie de son spectre et donc de sa transmission à la structure. En revanche, aucune modification significative de la valeur de fréquence crête n'est constatée, sans et avec le spoiler en 2D ou 3D.
A l'échelle du rotor, toutes les grandeurs (induction, angle d'attaque, poussée aérodynamique) évoluent de manière similaires lorsqu'un spoiler est introduit avec les deux modèles de fidélité (modèle BEM et SST). Cependant, les valeurs issues des simulations BEM sont significativement sous-estimées, sauf pour l'angle d'attaque où les deux modèles présentent des résultats similaires. De plus, à des distances radiales proches de l'extrémité de l'emplacement du spoiler, les simulations BEM présentent des écarts importants comparés aux simulations 3D, certainement causés par un écoulement hautement tridimensionnel.
Pour conclure cette étude, des simulations DES ont été brièvement comparées aux modèles SST. Ils présentent une gamme de fréquences beaucoup plus large dans le sillage en pied de pale avec un niveau d'énergie plus élevé que les simulations URANS 3D. Cela

suggère un scénario d'excitation de structure complètement différent. L'utilisation de la VSF uniquement pour l'évaluation de la fatigue doit encore être étudié.

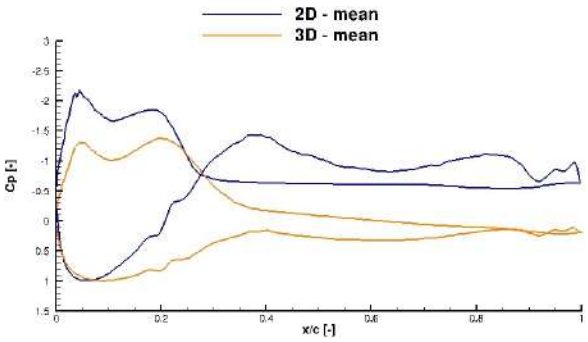

(a) Cas sans spoiler - Comparaison du C_p entre simulations 2D and 3D

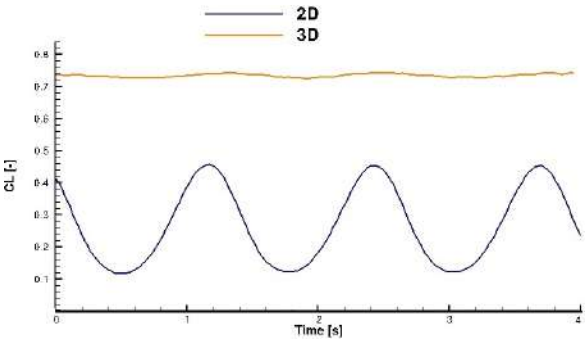

(b) Cas sans spoiler - Comparaison du C_L entre simulations 2D and 3D

Figure A.6 – Comparaison du coefficient de pression pariétal , C_p, (gauche) et du coefficient de portance C_L, (droite) pour le cas sans spoiler en 2D et 3D.

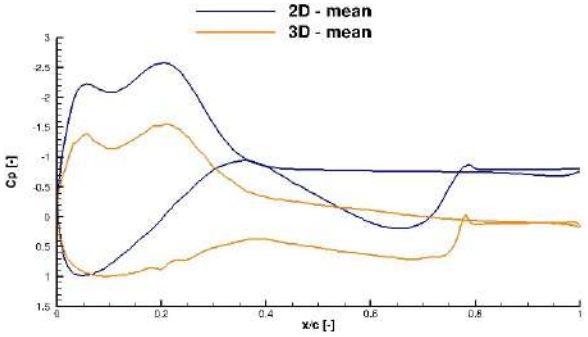

(a) Cas avec spoiler - Comparaison du C_p entre simulations 2D and 3D

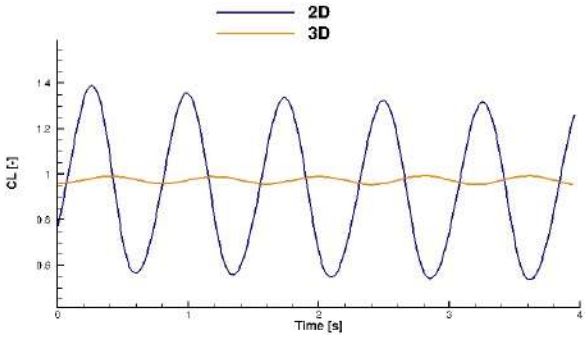

(b) Cas avec spoiler - Comparaison du C_L entre simulations 2D and 3D

Figure A.7 – Comparaison du coefficient de pression pariétal , C_p, (gauche) et du coefficient de portance C_L, (droite) pour le cas avec spoiler en 2D et 3D.

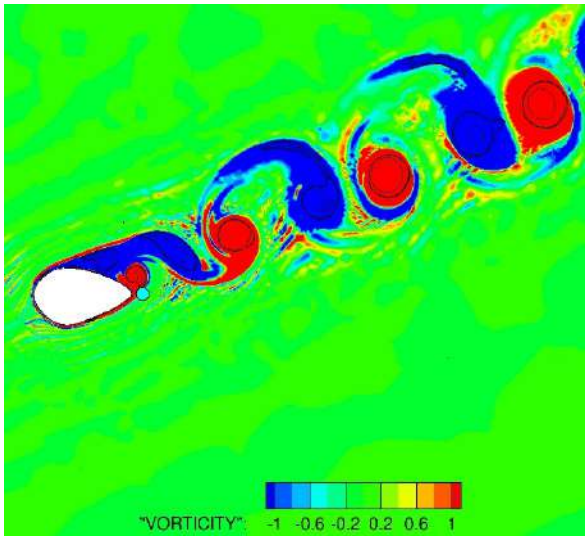

(a) Cas sans spoiler 2D : vorticité et critère Q.

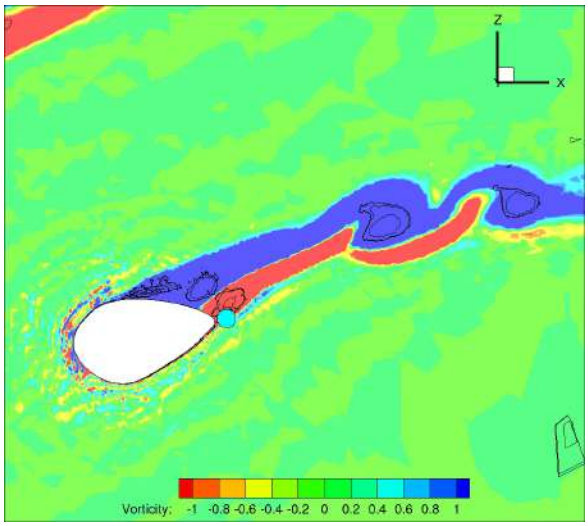

(b) Cas sans spoiler 3D : vorticité et critère Q.

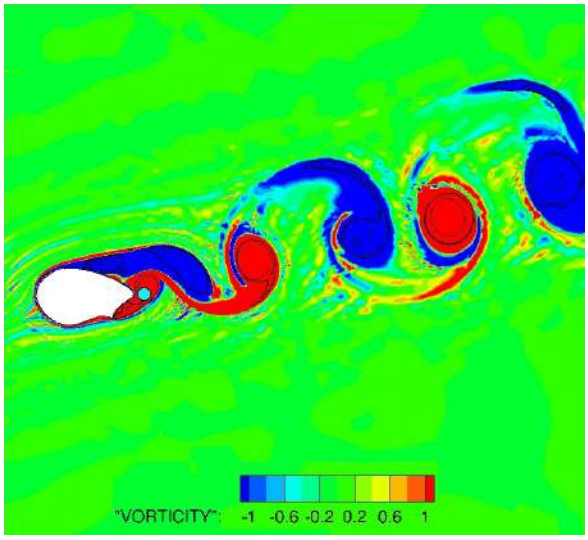

(c) Cas avec spoiler 2D : vorticité et critère Q.

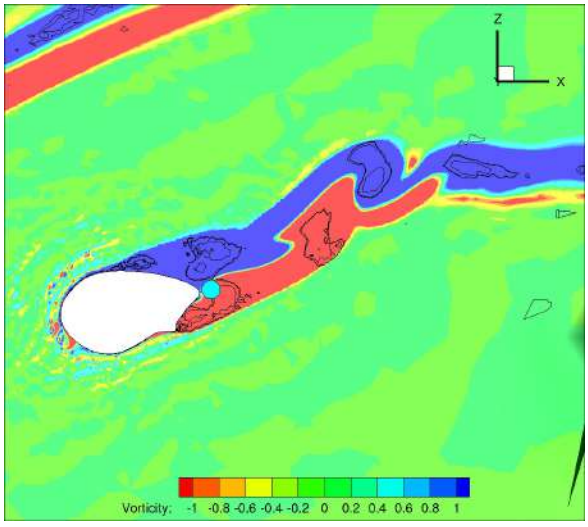

(d) Cas avec spoiler 3D : vorticité et critère Q.

Figure A.8 – Cas sans et avec spoiler de la vorticité et du critère Q en 2D et 3D. Le point de sondage est montré en cyan proche du bord de fuite de la section.

A.9 Conclusion

L'objectif principal de la thèse est de caractériser le rôle de l'instationnarité aérodynamique locale sur la durée de vie de la turbine et la production d'énergie de la turbine. À cette fin, une définition et une description du vent et des éoliennes sont d'abord données. Ensuite, les techniques de modélisation les plus avancées et la théorie sous-jacente ont été introduites dans le Chapitre 2. Il apparaît qu'un écart existe entre les capacités des outils haute fidélité et les outils utilisés par l'industrie (modèles d'ingénierie). En effet, la turbulence atmosphérique est bien comprise et prise en compte dans les méthodes haute et basse fidélité, mais ce n'est qu'en CFD que l'instationnarité aérodynamique est capturée. L'objectif de la thèse est d'aider à combler l'écart en utilisant les points forts des deux méthodes numériques, puis d'évaluer l'impact sur la durée de vie de la turbine.

Les Chapitre 6 et Chapitre 7 s'appuient sur les connaissances issues de l'analyse de données expérimentales (détaillé au Chapitre 5). Ils sont consacrés à la construction et à l'analyse d'un modèle aéroélastique d'une pale scannée équipée d'un spoiler. Les propriétés structurelles inconnues de la turbine ont été extrapolées à partir de la littérature existante. Les sections de pied de pale simulées par CFD 2D présentaient un comportement instable qui a été accrût par l'ajout de spoiler. Comme prévu, le spoiler a considérablement augmenté le coefficient de portance dans la plage positive des angles d'attaque pour une pénalitée élevée sur le coefficient de traînée. Le sillage de l'aérofoil avec l'ajout du spoiler présente une organisation de détachement de vortex avec une fréquence principale même à de faibles angles d'attaque. Alors que cela ne se produit que dans la région de décrochage pour un aérofoil sans ajout passif.

La turbine étant totalement flexible, une analyse de fatigue a été réalisée. La nouvelle méthode proposée ici utilise la fréquence de détachement des tourbillons calculée dans les simulations 2D. Elle propose de combiner plusieurs séries temporelles en utilisant la fréquence de détachement des vortex de chaque section pendant une série temporelle de 10 minutes. A la suite de l'analyse, le résultat est que, s'il est mal conçu, le spoiler peut être préjudiciable à la durée de vie de la turbine et les propriétés structurelles de la pale devraient tenir compte de la charge supplémentaire. Cette conclusion pourrait être étendue à tout ajout aérodynamique générant une quantité similaire d'instationnarité, mais des études dédiées seraient nécessaires. De plus, d'autres études seraient nécessaires pour quantifier la hauteur et la position du spoiler dans le sens de la corde.

Enfin, des simulations 3D complètes pour la condition de fonctionnement de 8 m/s pour les deux cas (rotor avec et sans spoiler) ont été exécutées. Malgré le bon accord relatif avec les résultats BEM, l'objectif principal était de vérifier que la fréquence de détachement des tourbillons calculée en 2D ne variait pas en raison de la rotation et de l'envergure des pales. Des comparaisons plus approfondies entre les simulations 2D et 3D ont aussi été effectuées, notamment en ce qui concerne la distribution des coefficients de

pression et de portance. Enfin, la comparaison des fréquences de détachement des tourbillons 2D et 3D a montré que l'utilisation de simulations 2D pour définir l'organisation du sillage est suffisante pour l'analyse de fatigue proposée ici.
Il convient de noter que l'utilisation des polaires calculées en 2D dans un code aéroélastique BEM peut conduire à des résultats conservateurs en raison de la plus grande instationnarité inhérente aux simulations 2D.

Appendix B

List of publications

The following list shows the papers, conferences proceedings and presentations published as part of the PhD:

- J.G. Schepers et al., 'IEA Wind TCP Task 29, Phase IV: Detailed Aerodynamics of Wind Turbines', Zenodo, May 2021. doi: 10.5281/ZENODO.4925963.
- T. Potentier, C. Braud, E. Guilmineau, A. Finez, and C. L. Bourdat, 'Analysis of the DANAERO wind turbine field database to assess the importance of different state-of-the-art blade element momentum (BEM) correction models', p. 24., in: Energy Science and Engineering ,https://doi.org/10.1002/ese3.908, 2021
- T. Potentier, E. Guilmineau, and C. Braud, 'CFD solver and meshing techniques verification using the DANAERO database', p. 8, 2020., https://phd2020.eawe.eu/site-phd2020/assets/files/Book_of_Proceedings.pdf
- T. Potentier, E. Guilmineau, and C. Braud. CFD solver and meshing techniques verification using the DANAERO database. In *16th PhD Seminar*, Online, 2020.
- T. Potentier, E. Guilmineau, C. Le Bourdat, A. Finez, and C. Braud. 2D unsteady results with and without spoiler on a thick aerofoil section. In Wind Energy Science Conference, Online, 2021.
- Potentier, T., Guilmineau, E., Finez, A., Le Bourdat, C., and Braud, C.: High-Reynolds-number wind turbine blade equipped with root spoilers – Part 1: Unsteady aerodynamic analysis using URANS simulations, Wind Energ. Sci., 7, 647–657, https://doi.org/10.5194/wes-7-647-2022, 2022
- Potentier, T., Guilmineau, E., Finez, A., Le Bourdat, C., and Braud, C.: High-Reynolds-number wind turbine blade equipped with root spoilers – Part 2: Impact on energy production and turbine lifetime, Wind Energ. Sci., 7, 1771–1790, https://doi.org/10.5194/wes-7-1771-2022, 2022.
- T. Potentier, E. Guilmineau, C. Le Bourdat, A. Finez, and C. Braud. Comparison between 3D and 2D CFD unsteady simulations of a scanned blade equipped with root spoilers In *25^{e}Congrès Français de Mécanique*, Nantes, France, 2022.
- T. Potentier, E. Guilmineau, C. Le Bourdat, A. Finez, and C. Braud. Comparison between 3D and 2D CFD unsteady simulations of the DANAERO blade. In *25^{e}Congrès Français de Mécanique*, Nantes, France, 2022.

Appendix C

UiBEM figures

C.1 UiBEM Validation

The following plots (from Figure C.1 to Figure C.3) show the different wind speed validations of the UiBEM tool developped.

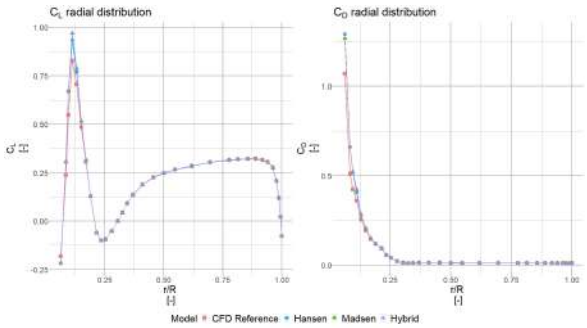

(a) UiBEM Verification for different induction models at 3m/s for the C_L and C_D.

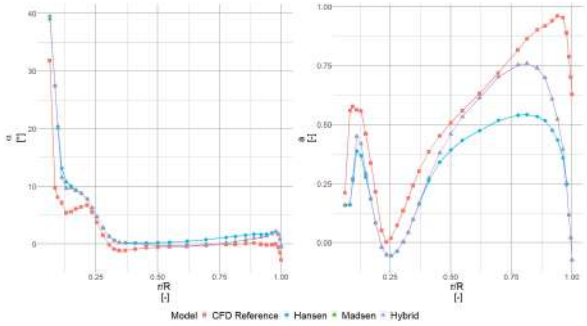

(b) UiBEM Verification for different induction models at 3m/s for the angle of attack and axial induction.

Figure C.1 – UiBEM Verification for different induction models at 3m/s.

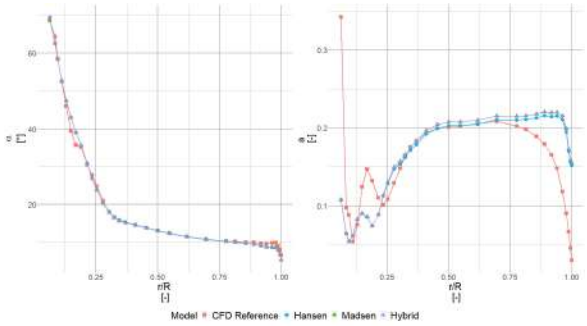

(a) UiBEM Verification for different induction models at 10m/s for the C_L and C_D.

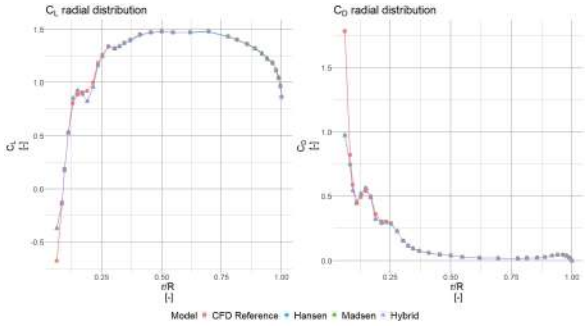

(b) UiBEM Verification for different induction models at 10m/s for the angle of attack and axial induction.

Figure C.2 – UiBEM Verification for different induction models at 10m/s.

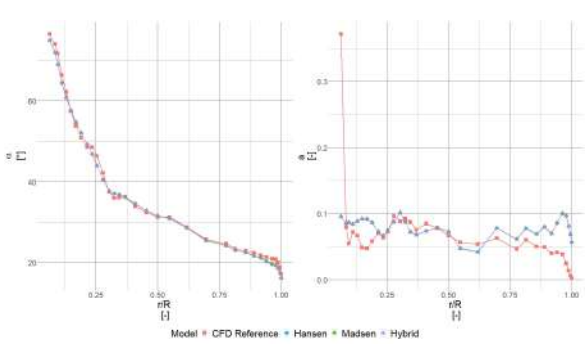

(a) UiBEM Verification for different induction models at 20m/s for the C_L and C_D.

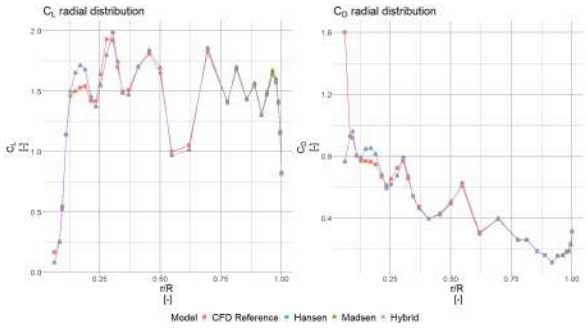

(b) UiBEM Verification for different induction models at 20m/s for the angle of attack and axial induction.

Figure C.3 – UiBEM Verification for different induction models at 20m/s.

C.2 Filters and corrections

The following plots (from Figure C.4 to Figure C.10) show the different effect of each filter and correction model implemented as part of the UiBEM procedure.
In the following plots, the black crosses show the clean 2D wind tunnel data, the grey crosses show the tripped 2D wind tunnel data. The error bars represent the C_L standard deviation in the analysed time series. The red diamonds show the 3D correction model applied to the clean 2D wind tunnel data, the green diamonds show the 3D correction model applied to the tripped 2D wind tunnel data. The error bars represent the C_L standard deviation in the analysed time series.

C.2.1 Vertical gradient filter

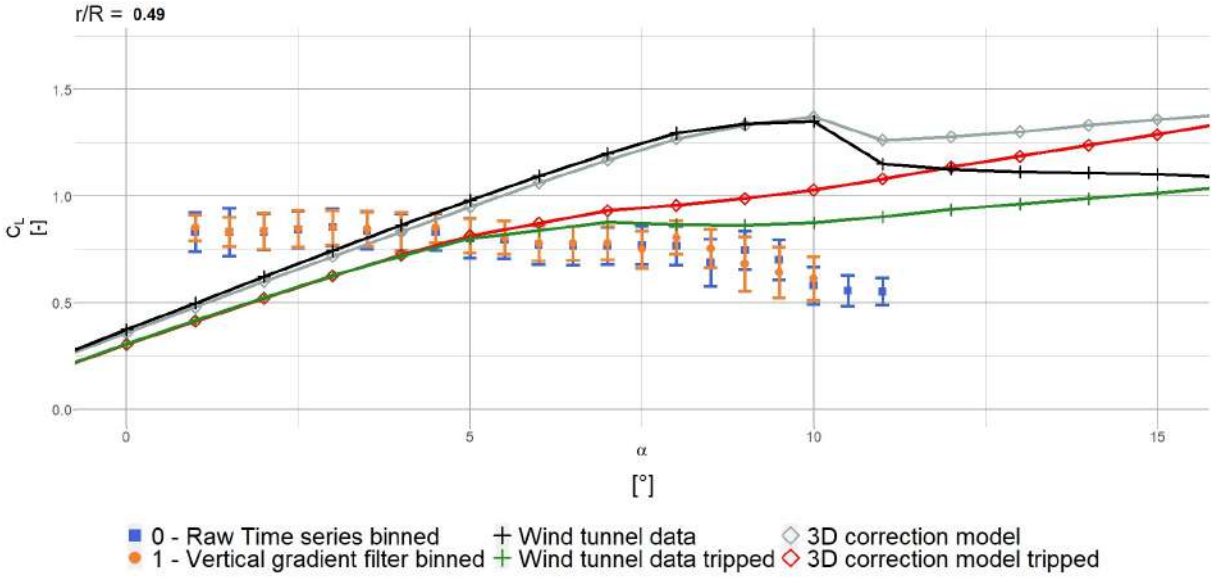

Figure C.4 – Binned averaged C_L comparison between raw time series and gradient selection for the radial location $r/R = 49\%$. The blue square (■) represents the average coefficients for the raw data and the orange circle (●) the average coefficients when the mean vertical gradient filter is used.

C.2.2 Neighbouring wake filter

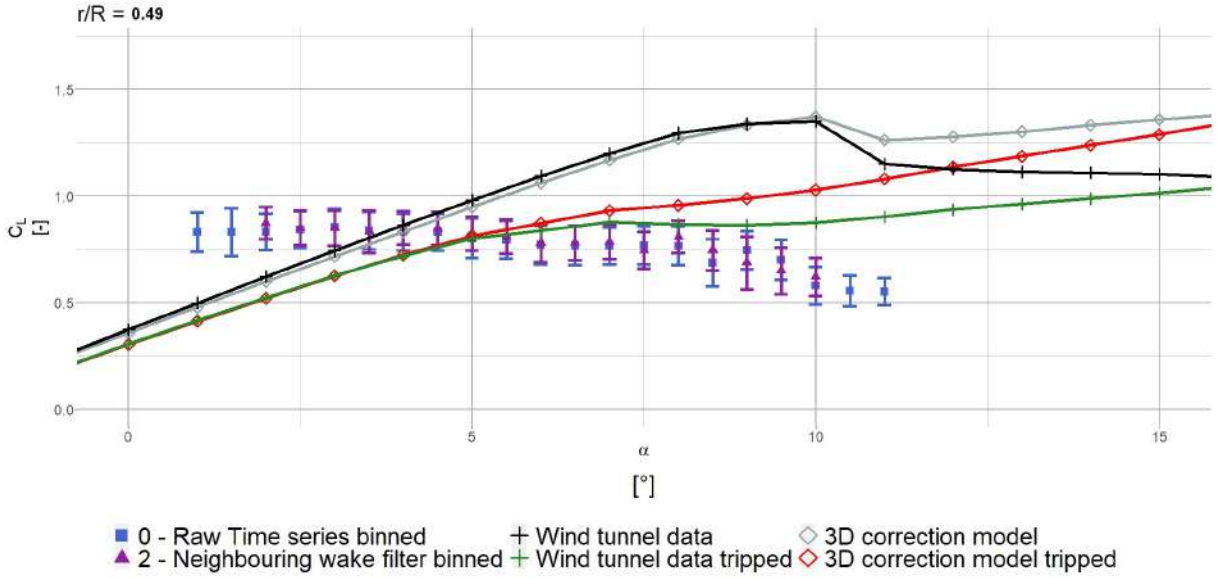

Figure C.5 – Binned averaged C_L comparison between raw time series and wake effect selection for the radial location $^r/_R = 49\%$. The blue square (■) represents the average coefficients for the raw data and the purple triangle (▲) the average coefficients when the neighbouring wake filter is used.

C.2.3 Yaw misalignment filter

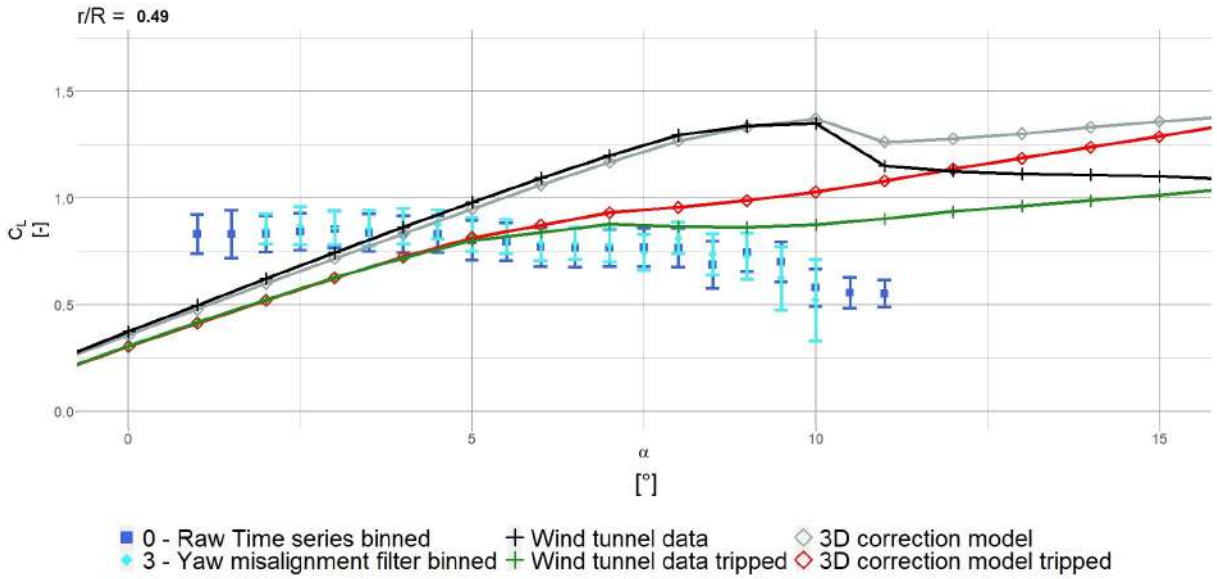

Figure C.6 – Binned averaged C_L comparison between raw time series and yaw error selection for the radial location $^r/_R = 49\%$. The blue square (■) represents the average coefficient for the raw data and the cyan diamond (◆) the average coefficient when the yaw misalignment filter is used.

C.2.4 Vertical gradient correction

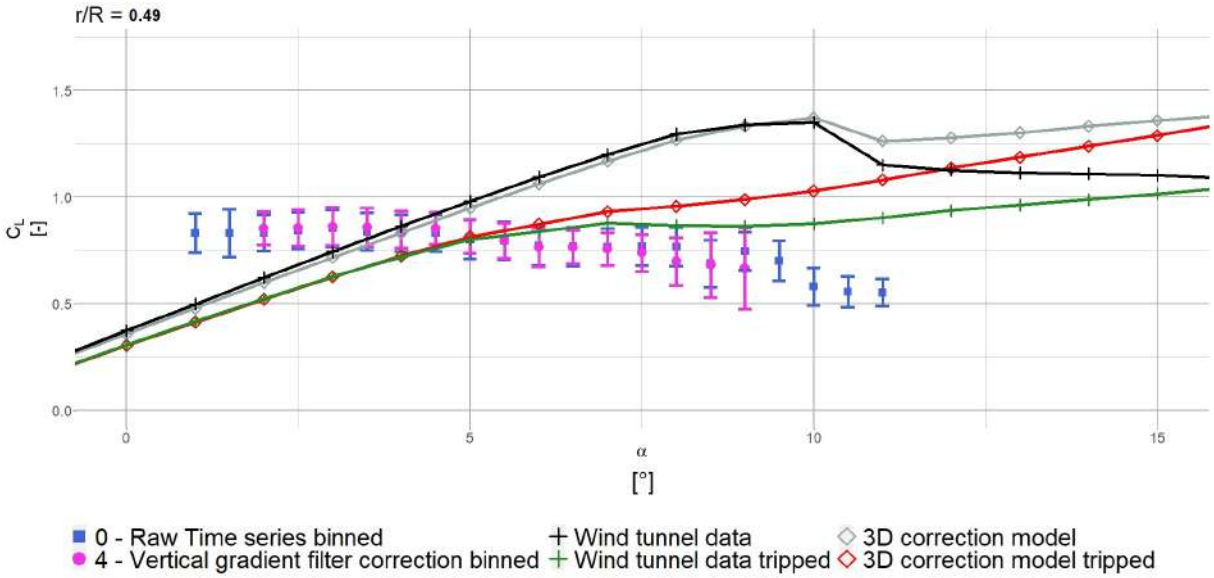

Figure C.7 – Binned averaged C_L comparison between the raw time series and the vertical gradient velocity correction for the radial location $r/R = 49\%$. The blue square (■) represents the average coefficient for the raw data and the pink circle (●) the average coefficient when the vertical gradient velocity correction is used.

C.2.5 Wind inflow location correction

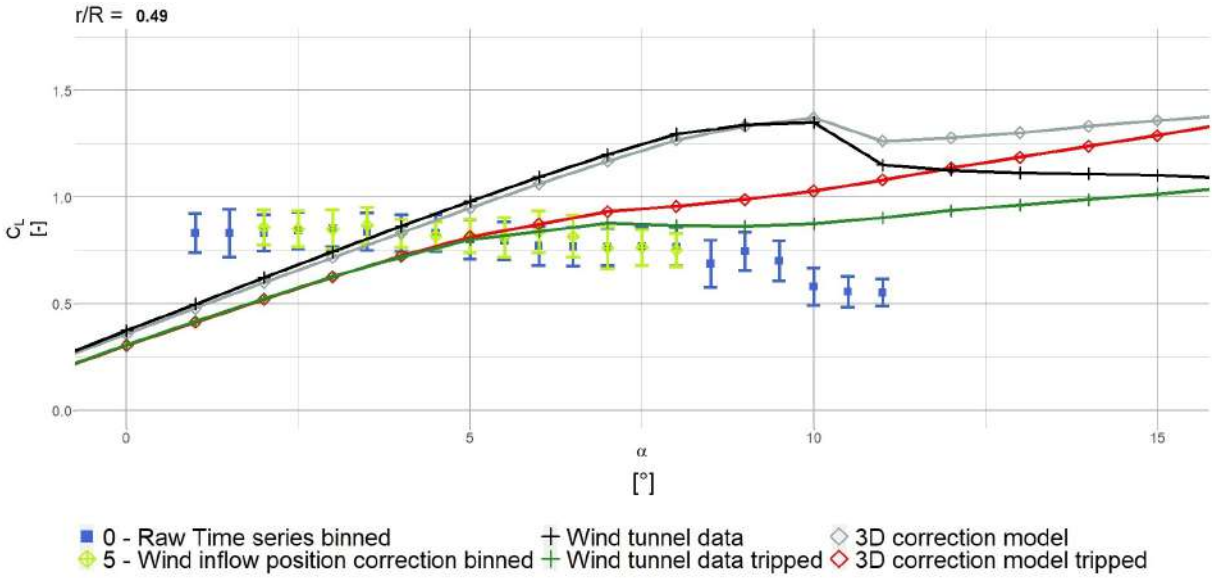

Figure C.8 – Binned averaged C_L comparison between the raw time series and the vertical gradient velocity correction for the radial location $r/R = 49\%$. The blue square (■) represents the average coefficient for the raw data and the green hollow circle (⊕) the average coefficient when the wind inflow location correction is used.

C.2.6 Unsteady Inverse Blade Element Momentum (UiBEM)

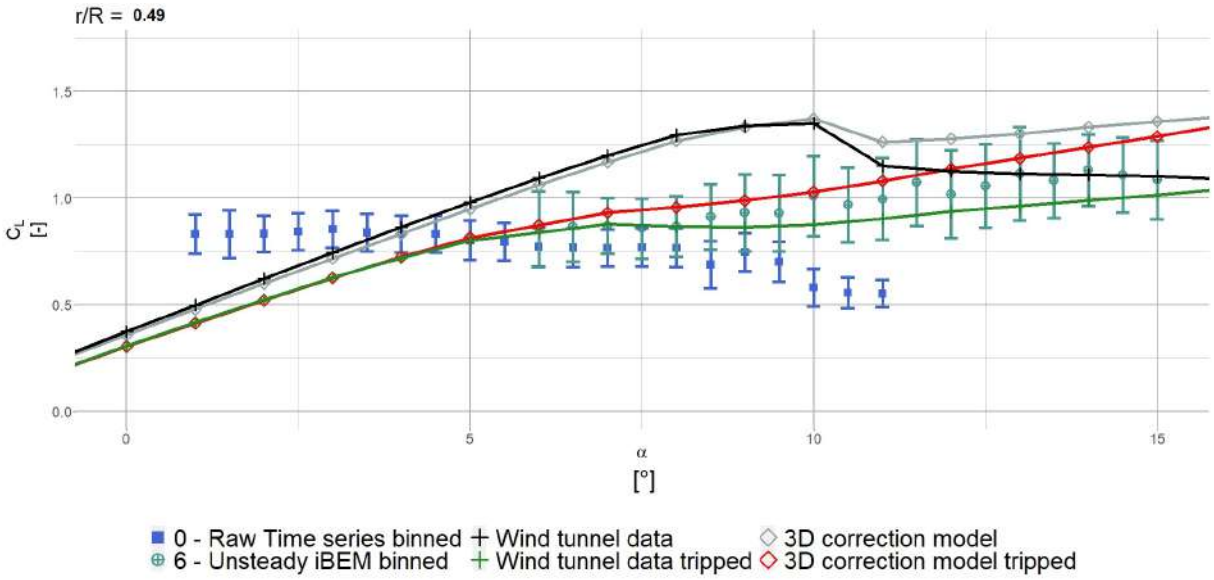

Figure C.9 – Binned averaged C_L comparison between the raw time series and the vertical gradient velocity correction for the radial location $r/R = 49\%$. The blue square (■) represents the average coefficient for the raw data and the blue crossed circles (⊕) the average coefficients when the unsteady BEM equations are used.

C.2.7 Tangential force measurement correction

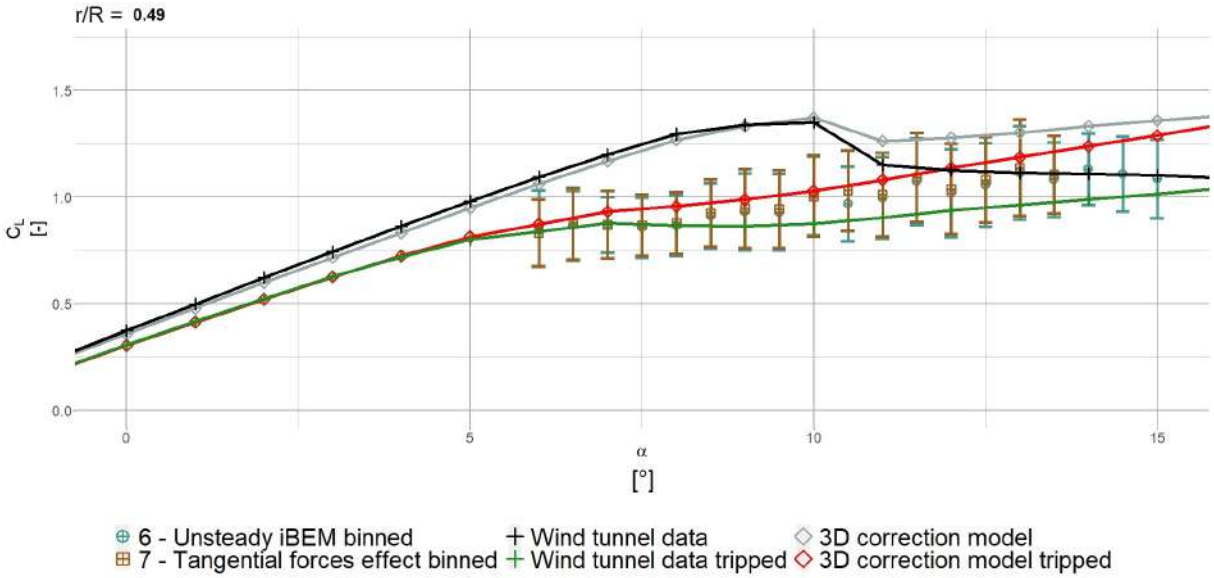

Figure C.10 – Binned averaged C_L comparison for the radial location $r/R = 49\%$. The blue crossed circles (⊕) represent the average coefficients when the unsteady BEM equations are used, the brown crossed squares (⊞) the average coefficients when the tangential force measurement are increased by 65%.

C.3 Dynamic stall investigation

Previous data were presented using an angle of attack binning method. The blade azimuthal position impact were therefore compensated. In the following, the lift hysteresis is now investigated. The rapid variation of angle of attack during the blade rotation does not enable the flow around the aerofoil to reach a steady state organisation. In particular, dynamic stall can locally occur and may cause deviation from the mean $C_L(\alpha)$ curve. Figure C.11 shows the $C_L(\alpha)$ evolution when the data is averaged by azimuthal position ($\Delta\Phi = 5°$). The dynamic stall behaviour is modelled using the adapted Beddoes-Leishman model from DTU [52]. Some parameters need to be chosen for this model: the reduced frequency k has been defined by the blade rotational speed (since the pitch is constant throughout the time series), the mean angle of attack α_m is extracted from the UiBEM simulation of the considered time series, while the amplitude of the angle of attack oscillations α_a is the difference between the highest quadrant averaged angle of attack and lowest quadrant averaged angle of attack.
The quadrant average results follow the overall shape described by the instantaneous cloud of points. In Figure C.11, the numbers written on the plot show some azimuthal blade position (0° being the instrumented blade pointing upwards). We can clearly see the effect of the ABL vertical gradient, which decreases the angle of attack and the C_L when the blade is close to the ground (between 90° to 270°). Then, the tower shadow effect is visible between 90° to 180°, because when the blade goes down, the angle of attack does not linearly change with the blade azimuth but loops back. Despite using a crude assumption for the reduced frequency, the dynamic stall model captures the essence of both the instantaneous data and the quadrant average data.

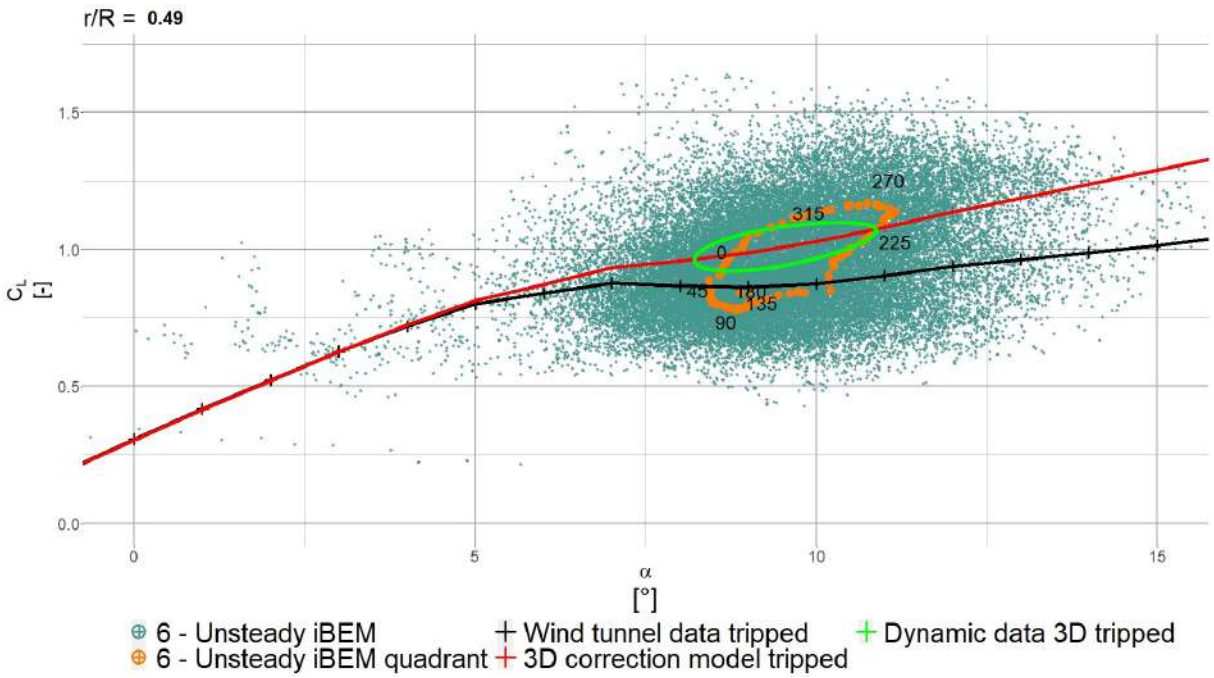

Figure C.11 – Quadrant averaged C_L comparison for the radial location $^r/_R = 49\%$.

Appendix D

3D SCAN POST-PROCESSING

D.1 3D scan post-processing

The blade has been scanned at rest on the ground as seen on Figure 1.13a. The outcome of the scan is a point cloud composing of millions of [X, Y, Z] coordinates in seemingly random order. The supplier's initial processing allowed to order the data by increasing radial position. The data is then manually sliced along the blade neutral axis (following the blade curvature in its supports) to ensure a normal sectional cut. Such cut can be seen in Figure D.1.

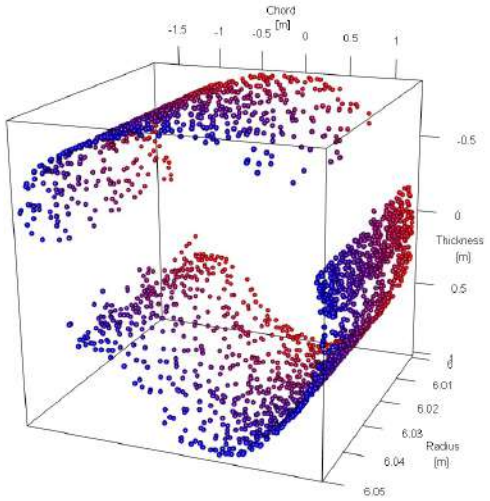

Figure D.1 – Raw 3D scan at radius $r/R = 0.13$.

Several steps are necessary to apply to the slice so as to be used by any 2D CFD or any further analysis (see Figure D.2):

1. All the data points are projected onto a single reference plane (here at $r/R = 0.13$)
2. The section is de-twisted
3. The section is flipped to have the suction side facing up
4. The section is moved to coincide the leading edge with the coordinates system origin

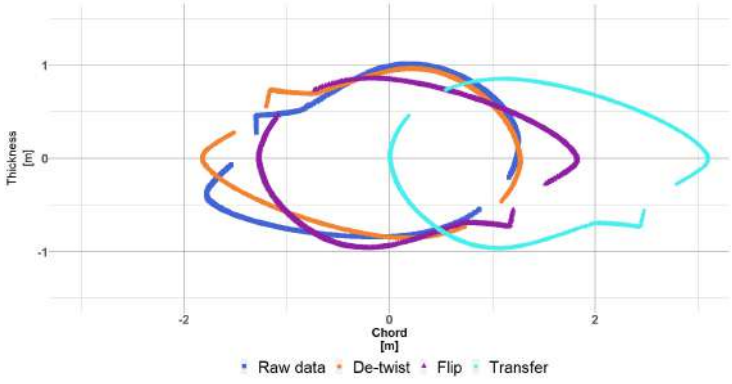

Figure D.2 – Necessary steps for 3D scan post-processing.

Once the leading edge is at the origin, the section is normalised using its local chord. One has to bear in mind, that the data point forming the aerofoil perimeter are still in random order. It is mandatory to order them in sequential order to perform any operation to fill-in the gaps in the geometry. Using the cross-product and the separation line displayed in orange in the Figure D.3a the pressure side and suction side can be discriminated. The final step is the interpolation of missing data in order to produced a closed

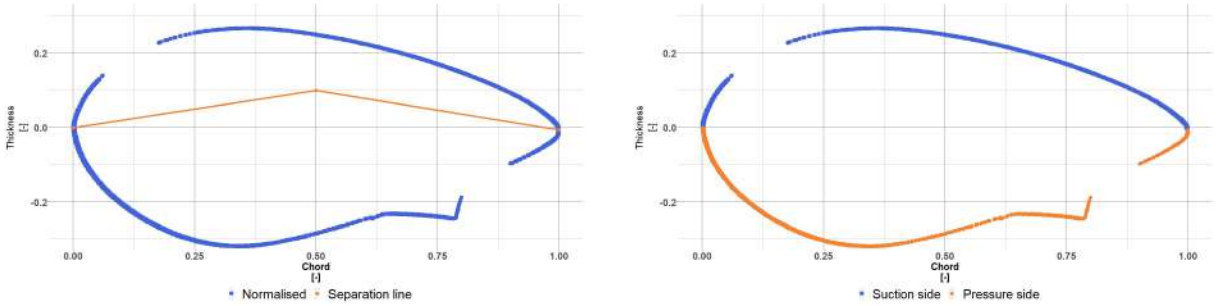

(a) Raw data normalised with separation line.

(b) Suction side and pressure side split.

Figure D.3 – $^{r}/_{R} = 0.13$ data points sorted.

geometry, without altering the overall aerofoil shape (see Figure D.4b). High order Bezier approximation curves have been used on several "patches" defining the aerofoil geometry (see Figure D.4a).

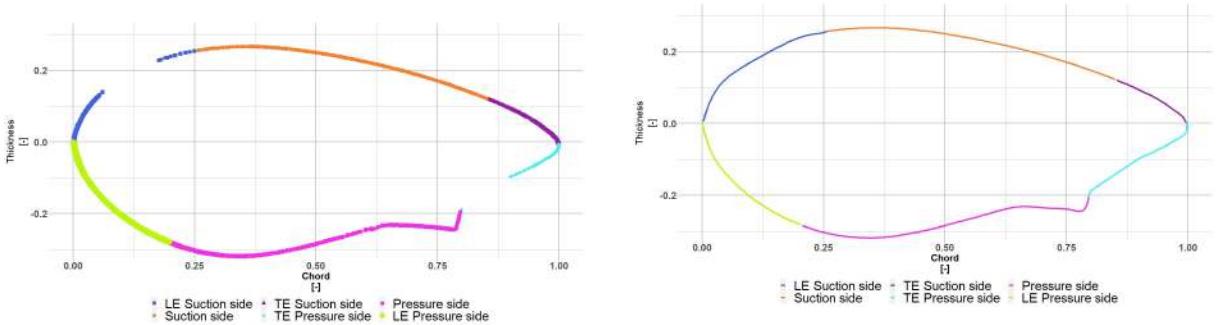

(a) Aerofoil patches for Bezier interpolation..

(b) Bezier curves interpolation through patches.

Figure D.4 – Closed aerofil geometry

Finally, this procedure is repeated for all slices along the blade radius where the blade geometry (chord, thickness and twist) is also extracted.

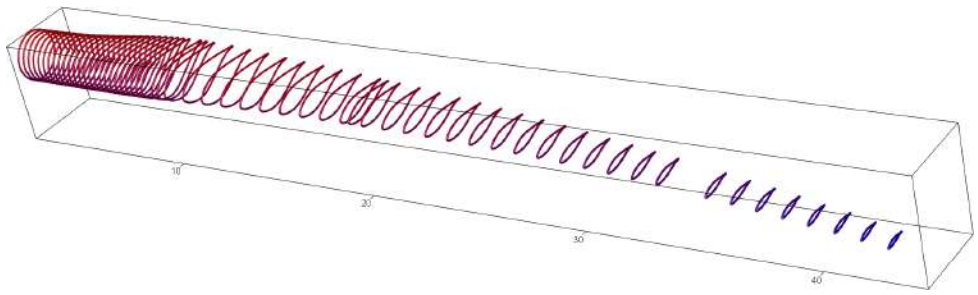

Figure D.5 – Full blade 3D scan.

Appendix E

3D CFD outputs

E.1 Surface force

The law of momentum conservation in fluid mechanics is defined by equation E.1:

$$\int_{V(t)} \rho \mathbf{U} dV \tag{E.1}$$

Where, $\mathbf{U}$ is the velocity vector and V the considered volume. Following the fundamental principle of dynamics applied to a small volume particle, the total force exerted on the surface is defined by equation E.2:

$$\frac{d}{dt} \int_{V(t)} \rho \mathbf{U} dV = \mathbf{F} \tag{E.2}$$

Where $\mathbf{F}$ is the sum of all applied forces on the considered volume. The total force $\mathbf{F}$ can be split into volume force and surface force (see equation E.3).

$$\mathbf{F} = \underbrace{\int_{S(t)} \bar{\bar{T}} \mathbf{n} dS}_{\text{Surface force}} + \underbrace{\int_{V(t)} \rho \mathbf{g} dV}_{\text{Volume force}} \tag{E.3}$$

Where $\bar{\bar{T}}$ is the stress tensor, $\mathbf{n}$ is the vector normal in each point to the surface, $\mathbf{g}$ is the acceleration due to gravity and ρ the density.
The volume force due to gravity is unchanged in both cases, the main change comes the pressure and viscous forces applied on the surface. For this reason, we will focus on the surface force. The stress tensor, $\bar{\bar{T}}$, can be rewritten into the sum of the hydrostatic force (or pressure force) and the force due to viscous stress as defined in equation E.4:

$$\bar{\bar{T}} = \alpha \bar{\bar{I}} \mathbf{n} + \bar{\bar{T}}' \mathbf{n} \Leftrightarrow \begin{bmatrix} \sigma_{xx} & \tau_{xy} & \tau_{xz} \\ \tau_{yx} & \sigma_{yy} & \tau_{yz} \\ \tau_{zx} & \tau_{zy} & \sigma_{zz} \end{bmatrix} = \underbrace{\alpha \begin{bmatrix} 1 & 0 & 0 \\ 0 & 1 & 0 \\ 0 & 0 & 1 \end{bmatrix}}_{\text{Hydrostatic force}} \begin{Bmatrix} n_x \\ n_y \\ n_z \end{Bmatrix} + \underbrace{\begin{bmatrix} \tau_{xx} & \tau_{xy} & \tau_{xz} \\ \tau_{yx} & \tau_{yy} & \tau_{yz} \\ \tau_{zx} & \tau_{zy} & \tau_{zz} \end{bmatrix}}_{\text{Viscous stress}} \begin{Bmatrix} n_x \\ n_y \\ n_z \end{Bmatrix} \tag{E.4}$$

The first term on the right hand side of the equation is applied normal to the surface, it is the pressure force. Finally, when applied on each point along the surface the local force $\bar{\bar{T}}$ can be written as the sum of the pressure and viscous part:

$$\bar{\bar{T}} = -p\bar{\bar{I}}' + \bar{\bar{T}}' \tag{E.5}$$

The following plots illustrates the evolution of the local surface loads in the blade inboard. First a comparison at the radial position $r/R = 0.13$ in 2D and 3D is given, then all sections where the spoiler is installed will be shown in 3D.
The Figure E.1a and Figure E.1b show the local surface force $\bar{\bar{T}}$ in 2D. The force distribution with the addition of the spoiler differs from the no spoiler case. The suction side shows a higher local force in the spoiler case. As expected, the pressure side force distribution is highly disturbed on the spoiler case. The higher load applied on the surface is a consequence of the pressure reorganisation around the section. In 3D (as seen in the Figure E.1c and Figure E.1d), the difference between spoiler and no spoiler is less pronounced. Indeed, in 2D the addition of a spoiler changes drastically the force magnitude in the first half of the aerofoil. In 3D, this behaviour is dampened and both cases (no spoiler and spoiler) are relatively close to each other in term of magnitude. It is well in line with the C_L and C_p behaviour described in Chapter 7.

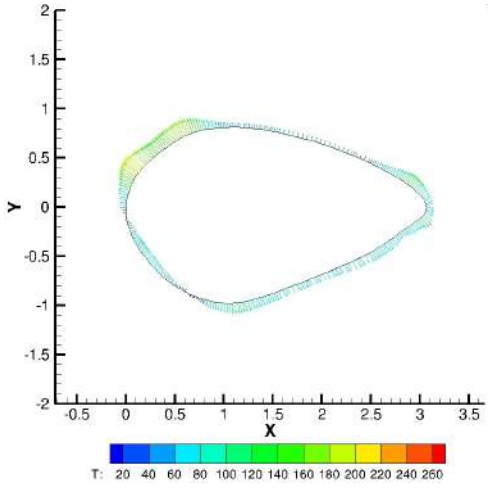

(a) No spoiler $r/R = 0.13$ - 2D local force

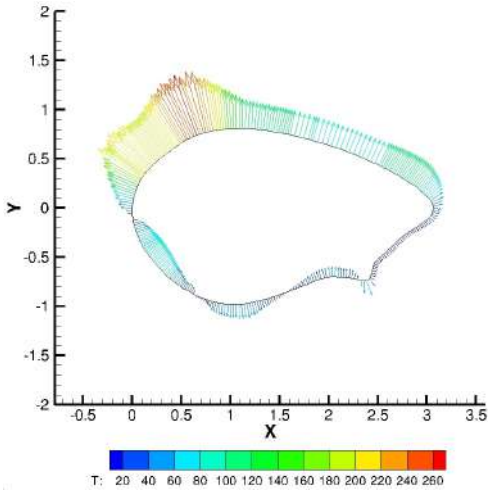

(b) Spoiler $r/R = 0.13$ - 2D local force

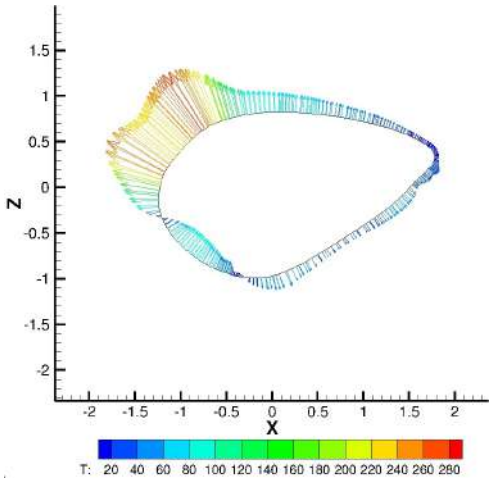

(c) No spoiler $r/R = 0.13$ - 3D local force

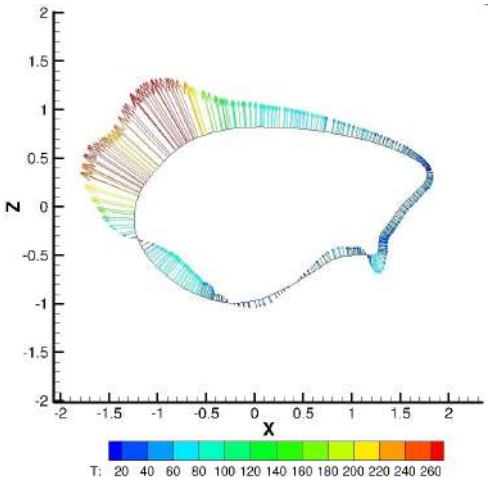

(d) Spoiler $r/R = 0.13$ - 3D local force

Figure E.1 – Comparison of the 2D and 3D CFD calculated local surface force $\bar{\bar{T}}$ along the aerofoil surface at $r/R = 0.13$.

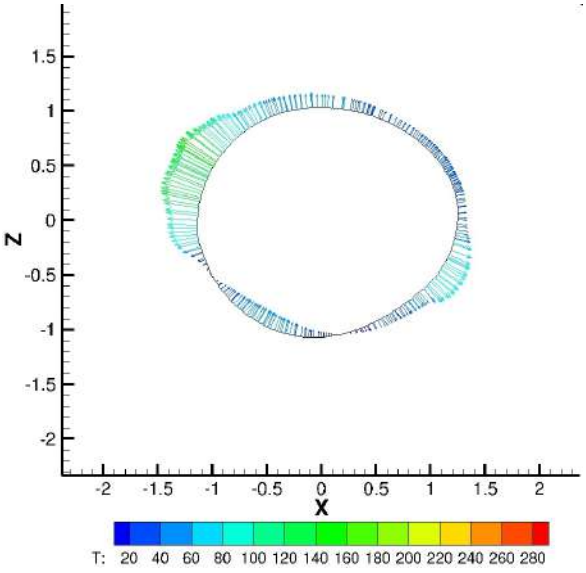

(a) No spoiler $r/R = 0.07$ - local force.

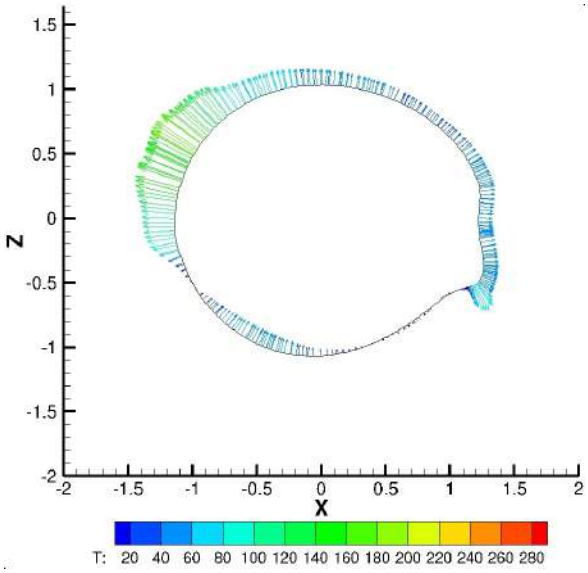

(b) Spoiler $r/R = 0.07$ - local force.

Figure E.2 – Local surface force $\bar{\bar{T}}$ along the aerofoil surface ($r/R = 0.07$).

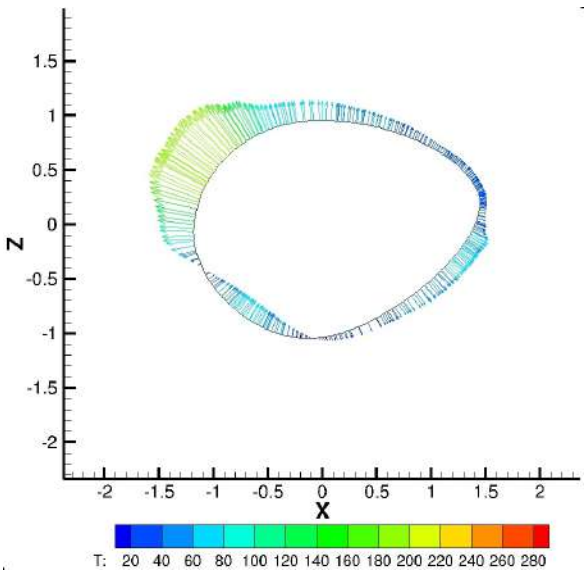

(a) No spoiler $r/R = 0.09$ - local force.

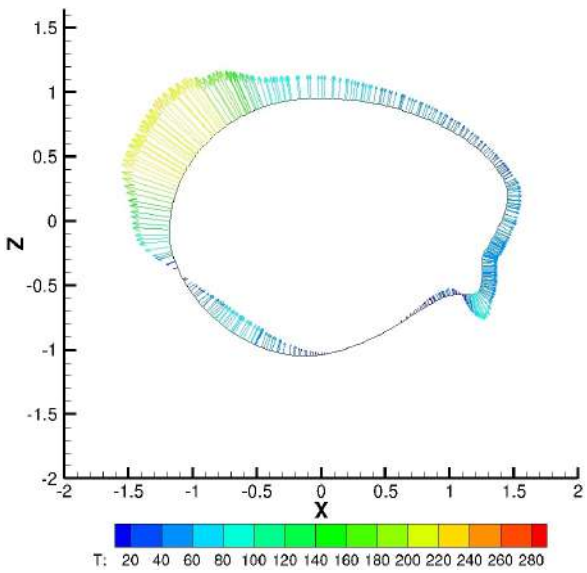

(b) Spoiler $r/R = 0.09$ - local force.

Figure E.3 – Local surface force $\bar{\bar{T}}$ along the aerofoil surface ($r/R = 0.09$).

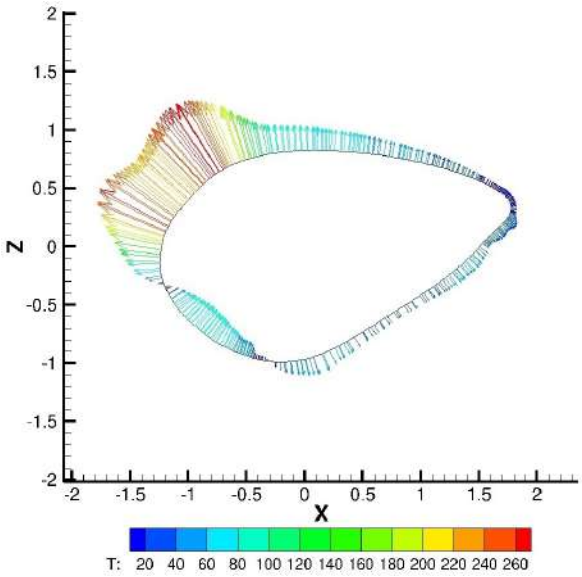

(a) No spoiler $r/R = 0.11$ - local force.

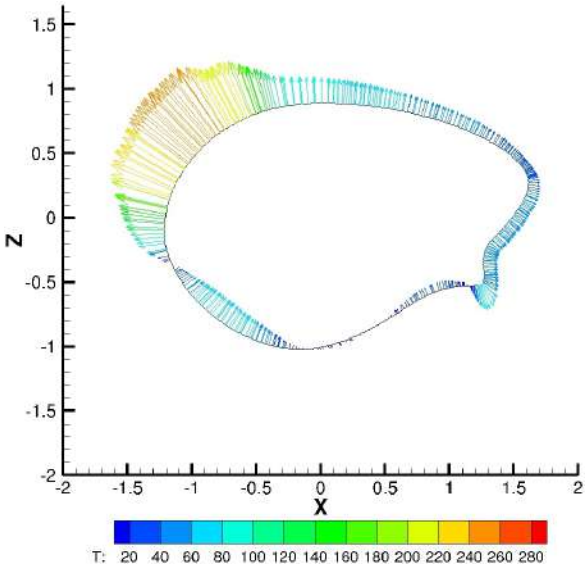

(b) Spoiler $r/R = 0.11$ - local force.

Figure E.4 – Local surface force $\bar{\bar{T}}$ along the aerofoil surface ($r/R = 0.11$).

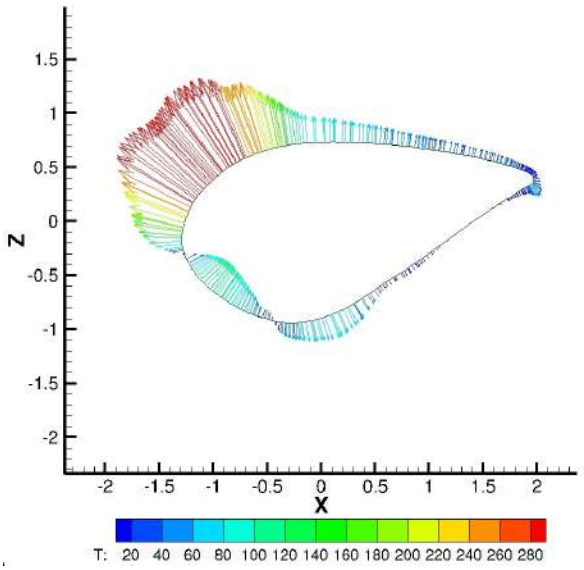

(a) No spoiler $r/R = 0.16$ - local force.

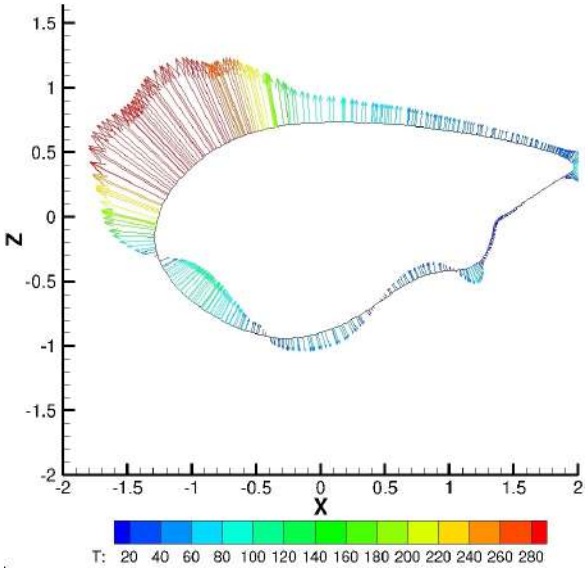

(b) Spoiler $r/R = 0.16$ - local force.

Figure E.5 – Local surface force $\bar{\bar{T}}$ along the aerofoil surface ($r/R = 0.16$).

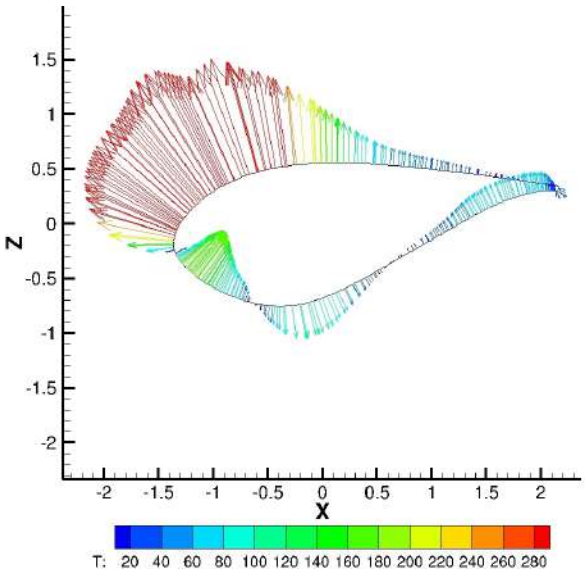

(a) No spoiler $r/R = 0.22$ - local force.

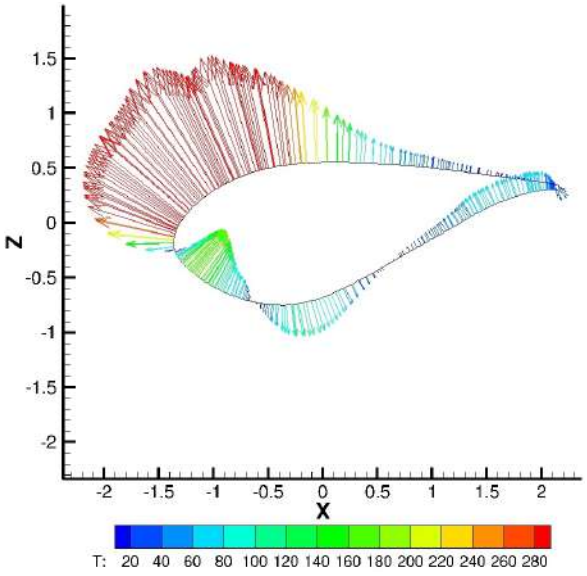

(b) Spoiler $r/R = 0.22$ - local force.

Figure E.6 – Local surface force $\bar{\bar{T}}$ along the aerofoil surface ($r/R = 0.22$).

E.2 No spoiler near wake

The Figure E.7 illustrates the near wake area of the no spoiler case.

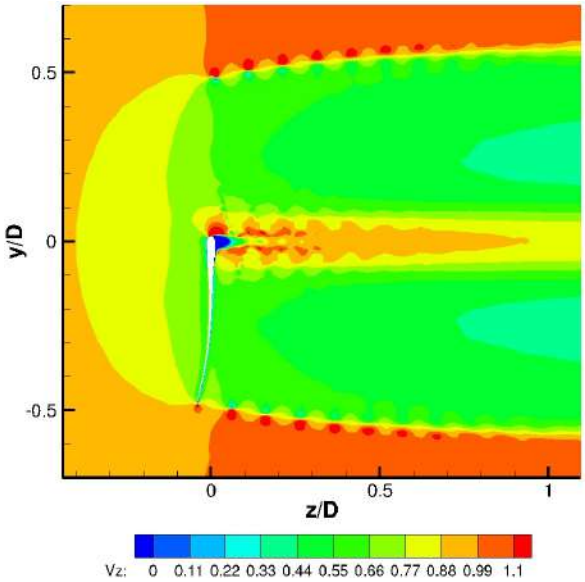

(a) Near wake axial inflow reduction for the no spoiler case

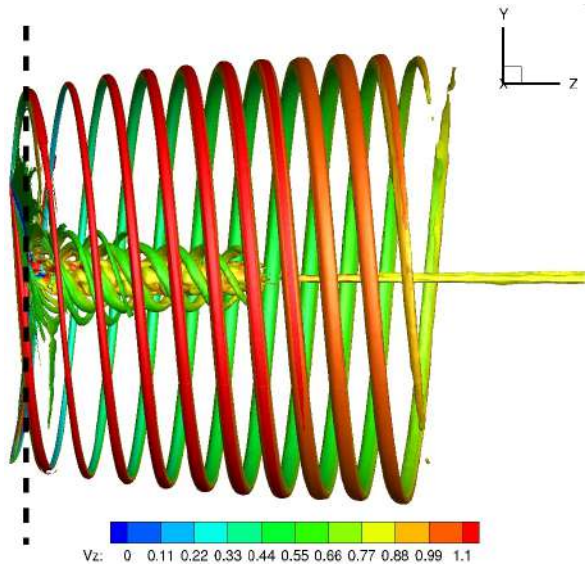

(b) Isosurface of the Q-criteria illustrating the tip vortices

Figure E.7 – Near wake description of the no spoiler case.

E.3 Vortex Shedding Frequency

The Figure E.8 shows that both in 2D and 3D without or with spoiler, using either the relative velocity in the wake or the C_L to extract the VSF is accurate. The small discrepancies introduced using only 2D CFD simulations are deemed acceptable for the level of analysis performed here.

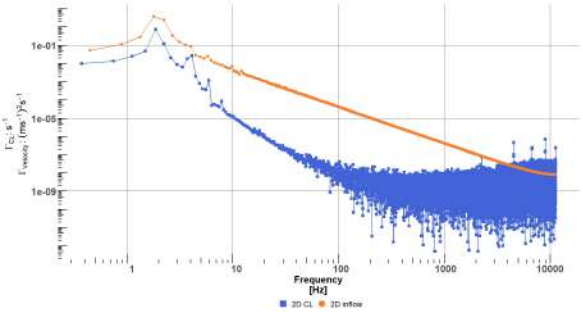

(a) No spoiler - Power Spectral Density of the relative velocity in the wake and the C_L in 2D.

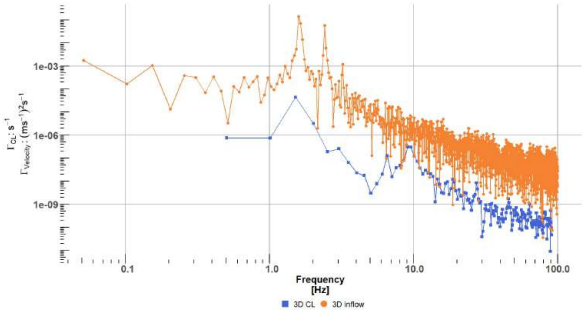

(b) No spoiler - Power Spectral Density of the relative velocity in the wake and the C_L in 3D.

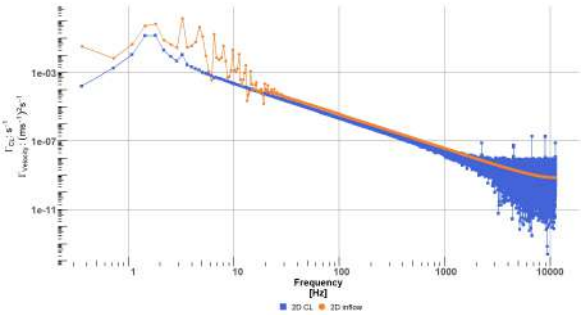

(c) Spoiler - Power Spectral Density of the relative velocity in the wake and the C_L in 2D.

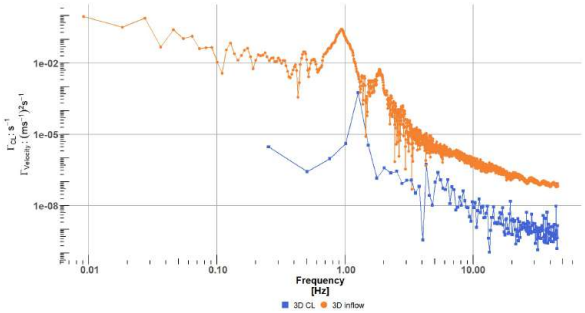

(d) Spoiler - Power Spectral Density of the relative velocity in the wake and the C_L in 3D.

Figure E.8 – Power Spectral Density of the relative velocity in the wake and the C_L in 2D and 3D for the no spoiler and spoiler case.

Appendix F

ENGIE Green turbine related data for aeroelastic modelling

Below are some publicly available turbine related data necessary to build an aeroelastic model.

F.1 ENGIE Green turbine's characteristics

Table F.1 – Blade characteristics

Metric	Value	Unit
Mass	8100	kg
Length	45.2	m
Maximum chord	5	m
Rotor diameter	92.5	m

Table F.2 – Hub characteristics

Metric	Value	Unit
Mass	18700	kg
Diameter	4.5	m
Height	3.4	m
Overhang	1.89	m
Mass moment of inertia about rotor axis	47334	$kg.m^2$

Table F.3 – Nacelle characteristics

Metric	Value	Unit
Mass	69200	kg
Length	10.3	m
Depth	3.8	m
Height	3.9	m
Mass moment of inertia about yaw axis	170982	$kg.m^2$

Table F.4 – Drive train characteristics

Metric	Value	Unit
Mass	25646	kg
Length	4.9	m
Depth	3.0	m
Height	2.4	m
Mass moment of inertia about high speed shaft axis	170982	$kg.m^2$
Gearbox ratio	120	-

Table F.5 – Tower characteristics

Metric	Value	Unit
Mass	129700	kg
Height	80	m

Table F.6 – Ultimate loads for various sensors

Sensor output	Ultimate load	Description
B1N1Fx	4124	r/R = 8.0% normal force (flap)
B1N2Fx	5002	r/R = 9.3% normal force (flap))
B1N3Fx	4958	r/R = 10.0% normal force (flap))
B1N4Fx	5407	r/R = 11.3% normal force (flap))
B1N5Fx	6178	r/R = 12.0% normal force (flap)
B1N6Fx	6079	r/R = 13.3% normal force (flap)
B1N7Fx	4618	r/R = 14.7% normal force (flap)
B1N8Fx	4226	r/R = 16.0% normal force (flap)
B1N9Fx	4708	r/R = 16.7% normal force (flap)
B1N1Fy	3757	r/R = 8.0% tangential force (flap)
B1N2Fy	4067	r/R = 9.3% tangential force (flap))
B1N3Fy	4190	r/R = 10.0%tangential force (flap))
B1N4Fy	4595	r/R = 11.3%tangential force (flap))
B1N5Fy	4924	r/R = 12.0%tangential force (flap)
B1N6Fy	4908	r/R = 13.3%tangential force (flap)
B1N7Fy	3255	r/R = 14.7%tangential force (flap)
B1N8Fy	2979	r/R = 16.0% tangential force (flap)
B1N9Fy	3665	r/R = 16.7% tangential force (flap)

Titre : Evaluation de l'impact de grands spoilers sur une pale d'éolienne en utilisant des simulations CFD instationnaires pleines échelles

Mots clés : Eolienne, aérodynamique, instationnaire, fatigue, spoiler

Résumé : Le premier objectif de la thèse est de caractériser le rôle de l'instationnarité aérodynamique locale introduite par les profils aérodynamiques épais équipés d'ajouts passifs. Un accent particulier sera mis sur les charges aérodynamiques, la durée de vie de la turbine et la production d'énergie. La thèse vise à comprendre les causes aérodynamiques de la défaillance structurelle en utilisant des méthodes de calcul de pointe. L'utilisation d'outils de haute fidélité tels que la CFD, à la fois en 2D et en 3D, a permis une meilleure compréhension du phénomène instationnaire. Une nouvelle façon de tenir compte de l'instationnarité dans le calcul de la fatigue aéroélastique BEM est ainsi proposée.

Peu de références disponibles dans la littérature ciblent les aérofoils épais et/ou les conditions de fonctionnement des éoliennes. La thèse vise également à combler le vide dans la littérature en fournissant une analyse de profils épais simulés avec et sans spoilers. Enfin, les principaux résultats de la thèse sont : l'impact négatif du spoiler sur la durée de vie de la turbine, le conservatisme des polaires aérodynamiques simulées en 2D utilisées pour la simulation aéroélastique BEM et le calcul de la fatigue, l'indépendance de la fréquence de détachement des tourbillons avec la rotation et l'envergure des pales. Une analyse dédiée de l'effet d'amortissement 3D sur le comportement instationnaire permettrait une meilleure corrélation entre 2D et 3D.

Title : Impact of large spoilers on a wind turbine blade using full scale and unsteady CFD simulations

Keywords : Wind turbine, aerodynamics, unsteadiness, fatigue, spoiler

Abstract : The first objective of the thesis is to characterise the role of the local aerodynamic unsteadiness introduced by thick aerofoils equipped with root aerodynamic add-on. A special focus will be on the aerofoil loads, turbine lifetime and turbine energy production. The thesis aims at understanding the aerodynamic causes of the structural failure using state of the art calculation methods. The use of high fidelity tool such as CFD, both in 2D and 3D, allowed for a better understanding of the unsteady phenomenon. A novel way of accounting for unsteadiness in the BEM aeroelastic fatigue calculation is proposed.

Few references available in the literature are targeting thick aerofoils and/or large wind turbine operating conditions. The present thesis aims also at bridging the gap in the literature by providing an analysis of simulated thick profiles with and without spoilers. Finally, the main findings of the thesis are: the negative impact of the spoiler upon the turbine lifetime, the conservativeness of 2D simulated aerodynamic polars used for BEM aeroelastic simulation and fatigue calculation, the independence of the vortex shedding frequency with the blade rotation and span. A dedicated analysis about the 3D dampening effect on the unsteady behaviour would allow a better correlation between 2D and 3D.